Coherence properties of third and fourth generation x-ray sources. Theory and experiment

Dissertation
zur Erlangung des Doktorgrades des Department Physik der Universität Hamburg

vorgelegt von
Andrej Singer

Hamburg
2012

Gutachter der Dissertation:	Prof. Dr. E. Weckert
	Prof. Dr. I. A. Vartanyants
	Dr. I. McNulty
Gutachter der Disputation:	Prof. Dr. E. Weckert
	Prof. Dr. W. Wurth
Datum der Disptutation:	20.12.2012
Vorsitzender des Prüfungsausschusses:	Prof. Dr. G. Huber
Vorsitzender des Promotionsausschusses:	Prof. Dr. P. Hauschild
Leiterin des Departments Physik:	Prof. Dr. D. Pfannkuche
Dekan der Fakultät Mathematik, Informatik und Naturwissenschaften:	Prof. Dr. H. Graener

Contents

1 High brilliance x-ray sources **1**
- 1.1 Synchrotron sources . . . 5
- 1.2 Next generation synchrotron sources . . . 9
- 1.3 Free-electron lasers . . . 10

2 Theory of optical coherence **14**
- 2.1 Propagation of electromagnetic waves . . . 14
- 2.2 Coherence: Basic Equations . . . 17
- 2.3 Correlation functions of stationary wave-fields . . . 20
  - 2.3.1 Propagation of the wave-field correlation functions . . . 20
  - 2.3.2 Coherent mode representation of correlation functions . . . 22
  - 2.3.3 Gaussian Schell-model sources . . . 24
  - 2.3.4 Propagation of Gaussian Schell-model beams in free space . . . 25
  - 2.3.5 Coherent mode representation of a Gaussian Schell-model source . . . 30
  - 2.3.6 Young's double pinhole experiment . . . 34
- 2.4 Correlation functions of non-stationary wave-fields . . . 38
  - 2.4.1 Propagation of the wave-field correlation functions in free space . . . 39
  - 2.4.2 Statistical properties of pulsed sources . . . 40

3 Coherence properties of third and fourth generation x-ray sources in the frame of statistical optics **44**
- 3.1 Synchrotron sources . . . 44
  - 3.1.1 Transverse coherence properties of the PETRA III source . . . 47
- 3.2 Next generation synchrotron sources . . . 54
- 3.3 Free-electron lasers . . . 56
  - 3.3.1 Transverse coherence properties of the European XFEL source . . . 56
  - 3.3.2 Transverse coherence properties of the FLASH source . . . 60

4 Thin optical elements at third and fourth generation x-ray photon sources **62**
- 4.1 Focusing of partially coherent Gaussian Schell-model beams . . . 64
- 4.2 Focusing of x-ray beams at PETRA III beamline P10 . . . 70
- 4.3 Modelling of partially coherent radiation based on the coherent mode decomposition . . . 73

5 Transverse coherence measurements at free-electron lasers **80**
- 5.1 Young's double pinhole measurements at LCLS . . . 80
  - 5.1.1 Determination of the spatial coherence properties . . . 82

5.1.2 Determination of the temporal coherence properties 88
5.2 Young's double pinhole measurements at FLASH 89
5.3 Young's double slit measurements at FLASH 94
5.4 Coherence measuremens at FLASH using a uniformly redundant array . . 97
5.5 Intensity correlations 106

6 Summary **112**

7 List of Abbreviations **116**

8 List of Symbols **117**

9 Own publications **118**

A Appendix **131**
A.1 Numerical implementation of the wave propagation in free space 131
A.2 The degree of transverse coherence 132
A.3 Simulations of single pulses in the frame of Gaussian statistics 133
A.4 Synchrotron radiation 137
A.5 Propagation of a GSM beam through the thin lenses 139
A.5.1 The magnification factor 140
A.5.2 Distance from the lens to the focus 142
A.6 Numerical mode decomposition 143
A.7 Degeneracy parameter 147
A.8 Analysis of the Young's measuremens at LCLS 148
A.9 Beam width characterization 148
A.9.1 Measurements at SXR beamline at LCLS 148
A.9.2 Measurements at BL2 beamline at FLASH 149
A.9.3 Measurements at PG2 beamline at FLASH 153

Abstract

Interferenzeffekte gehören zu den faszinierendsten optischen Phänomenen. Als Beispiel, verdanken Schmetterlinge und Seifenblasen ihre Farbenpracht der Interferenz von Licht. Diese Erscheinung ist eine Folge des Superpositionsprinzips, das seine Gültigkeit von der Linearität der Wellengleichung der Elektrodynamik bezieht. Wenn zwei elektromagnetische Wellen interferieren, wird das Gesamtfeld zur Summe dieser beiden Felder und wird maßgeblich durch die relativen Phasen bestimmt. Die Schwingungsfrequenz vom optischen oder gar von Röntgenstrahlen ist zu groß, daher können die Felder mit dem menschlichen Auge oder einem anderen Detektor nicht direkt beobachtet werden. Die Phasendifferenzen dieser interferierenden Felder können allerdings deutlich langsamer oszillieren und sind als Variation der Feldstärke messbar. Daher stellt Interferenz eine hervorragende Messmöglichkeit der Phasendifferenzen von Licht dar, welche detaillierte Informationen über die Lichtquelle oder ein Streuobjekt tragen können.

Ob zwei Wellen imstande sind zu interferieren, hängt stark vom Grad der Korrelation zwischen diesen beiden Wellen ab, d.h. ihrer Kohärenz. Bis zur Mitte des 20. Jahrhunderts war die Kohärenz aller bekannten Quellen niedrig. Es musste ein erheblicher Aufwand betrieben werden, um den Grad der Kohärenz zu steigern, und das Interferenzprinzip zur direkten Phasenmessung zu instrumentalisieren. Erst durch die revolutionäre Entdeckung des Lasers, welcher höchst kohärent ist, wurden Methoden wie Holographie, welche eine direkte Messung vom elektromagnetischen Feld ist, möglich gemacht. Wichtige Beiträge zur Entwicklung der Interferenzmethoden lieferten auch Astronomen, da das Licht von den Sternen aufgrund von sehr großen Abständen zur Erde große transversale Kohärenz aufweist.

Der Bau neuartiger Synchrotronquellen eröffnete Zugang zu partiell kohärenten Strahlen im Röntgenbereich. Neue Forschungsmöglichkeiten mit diesen Strahlen sind entstanden, einschließlich X-ray Photon Correlation Spectroscopy (XPSC), Röntgen Holographie, und Coherent X-Ray Diffractive Imaging (CXDI). In der ersten Methode wird die Dynamik eines Systems erforscht während die zweite und dritte Bildgebungsverfahren von vorwiegend statischen Objekten sind. Die höchst brillianten, kohärenten und ultrakurzen Röntgenpulse an den sogenannten Freie-Elektronen Röntgenlaser versprechen durch Ausnutzung genannter Techniken bahnbrechende Einblicke in Biologie, Festkörperphysik, Magnetismus und andere korrelierte Systeme zu liefern.

Die Interferenz der Felder, die am Objekt gestreut wurden, bildet die Grundlage vieler dieser Methoden. Als solches, ist das Verständnis der Kohärenz neuartiger Röntgenquellen von entscheidender Bedeutung. Dieses Verständnis kann sogar genutzt werden, um die Methoden zu verfeinern. In dieser Arbeit untersuchen wir Kohärenzeigenschaften der Röntgenstrahlen an neuartigen Röntgenquellen. Bestehende theoretische und experimentelle Methoden werden beschrieben und durch neu entwickelte Methoden ergänzt.

Abstract

Interference effects are among the most fascinating optical phenomena. For instance, the butterflies and soap bubbles owe their beautiful colors to interference effects. They appear as a result of the superposition principle, valid in electrodynamics due to the linearity of the wave equation. If two waves interfere, the total radiation field is a sum of these two fields and depends strongly on the relative phases between these fields. While the oscillation frequency of individual fields is typically too large to be observed by a human eye or other detection systems, the phase differences between these fields manifest themselves as relatively slowly varying field strength modulations. These modulations can be detected, provided the oscillating frequencies of the superposed fields are similar. As such, the interference provides a superb measure of the phase differences of optical light, which may carry detailed information about a source or a scattering object.

The ability of waves to interfere depends strongly on the degree of correlation between these waves, i.e. their mutual coherence. Until the middle of the 20th century, the coherence of light available to experimentalists was poor. A significant effort had to be made to extend the degree of coherence, which made the electromagnetic field determination using of the interference principle very challenging. Coherence is the defining feature of a laser, whose invention [1] initiated a revolutionary development of experimental techniques based on interference, such as holography. Important contributions to this development were also provided by astronomists, as due to enormous intergalactic distances the radiation from stars has a high transverse coherence length at earth [2].

With the construction of third generation synchrotron sources (see for example [3]), partially coherent x-ray sources have become feasible. New areas of research utilizing highly coherent x-ray beams have emerged, including x-ray photon correlation spectroscopy (XPCS) [4], x-ray holography [5], and coherent x-ray diffractive imaging (CXDI) [6]. In the former, the dynamics of a system are explored whereas in the latter two predominantly static real space images of the sample are obtained by phase retrieval techniques [7]. Using the intense, coherent, and ultrashort x-ray pulses produced by so-called x-ray free-electron lasers [8] and energy recovery linacs [9] these techniques promise new insights in structural biology, condensed matter physics, magnetism and other correlated systems [6].

The key feature of all these methods is the interference between the field scattered by different parts of the sample under study. As such, spatial coherence across the sample is essential and understanding the coherence properties of the beams generated at new generation x-ray sources is of vital importance for the scientific community. This understanding can even be used to improve the applied methods [10].

In this thesis we aim to describe existing and develop new techniques to study transverse coherence properties of x-ray beams at third and fourth generation sources.

1 High brilliance x-ray sources

Since their discovery by Wilhelm Conrad Röntgen in 1895 [11] x-rays have been used to determine the structure of matter[1]. Exploiting the weak interaction of x-rays with matter Röntgen, for the first time, visualized the structure of bones in a living human. Due to the higher density bones absorb a higher fraction of the radiation than the soft tissue surrounding them and a shadow of the bones is visible on the photograph.

According to Max von Laue [12] "Die Röntgenstrahlen sind elektromagnetische Wellen gleich dem Licht, nur von weit kürzerer Wellenlänge λ und entsprechend grösserer Schwingungszahl ν. Man kann ihren spektralen Bereich etwa abgrenzen durch die Angaben $5 \cdot 10^{-7}$ cm $< \lambda < 1 \cdot 10^{-11}$ cm oder wegen $\nu = c/\lambda$ durch $6 \cdot 10^{16} s^{-1} < \nu < 3 \cdot 10^{21} s^{-1}$"[2]. The wavelength of x-ray radiation is comparable with the size of inter atomic distances in a crystal. Due to interference of the light scattered from a large number of identical scatterers in a crystal the scattered signal is significantly enhanced in certain directions and investigations of the atomic structure of crystals are possible. This last property was discovered by M. von Laue [13, 14]. Shortly after Laue's discovery, W. H. Bragg and W. L. Bragg were able to find the structure of several salts and molecules on atomic level [15, 16, 17, 18]. These pioneering experiments have initiated a remarkably successful field, called x-ray crystallography, which has been extensively utilized during the last century up to now. In cristallography the resolution is comparable to the wavelength of the radiation and can even be smaller than the size of a single atom. Being used to solve small structures consisting of a few atoms in the early stage, recently crystallographers were able to map the ribosome - one of the cell's most complex machineries - at atomic level [19]. Twenty six nobel prizes, including four nobel prizes in chemistry in the last ten years, were awarded to scientists for their scientific achievements directly related to, or involving the use of, crystallographic methods and techniques.

Another striking feature of x-rays has been discovered by C. G. Barkla. If the inner shell electrons are liberated from an atom, element specific characteristic x-ray radiation –fluorescence– is emitted by the atom. It happens while electrons from the outer shells refill the vacancies in the inner shell. By analyzing the wavelength of the fluorescent radiation emitted by a specimen under study it is possible to determine the type of the elements present in the sample. These and other properties of x-ray radiation have stimulated a continuous development of x-ray sources.

[1] Röntgen called this new type of radiation x-rays: "Der Kürze halber möchte ich den Ausdruck "Strahlen" und zwar zur Unterscheidung von anderen den Namen "X-Strahlen" gebrauchen."[11]

[2] X-rays are electromagnetic waves, like the visible light, but with a much shorter wavelength λ or equivalently a higher frequency ν. The spectral width might be limited by the values $5 \cdot 10^{-7}$ cm $< \lambda < 1 \cdot 10^{-11}$ cm or due to $\nu = c/\lambda$ by $6 \cdot 10^{16}$ s$^{-1} < \nu < 3 \cdot 10^{21}$ s^{-1}.

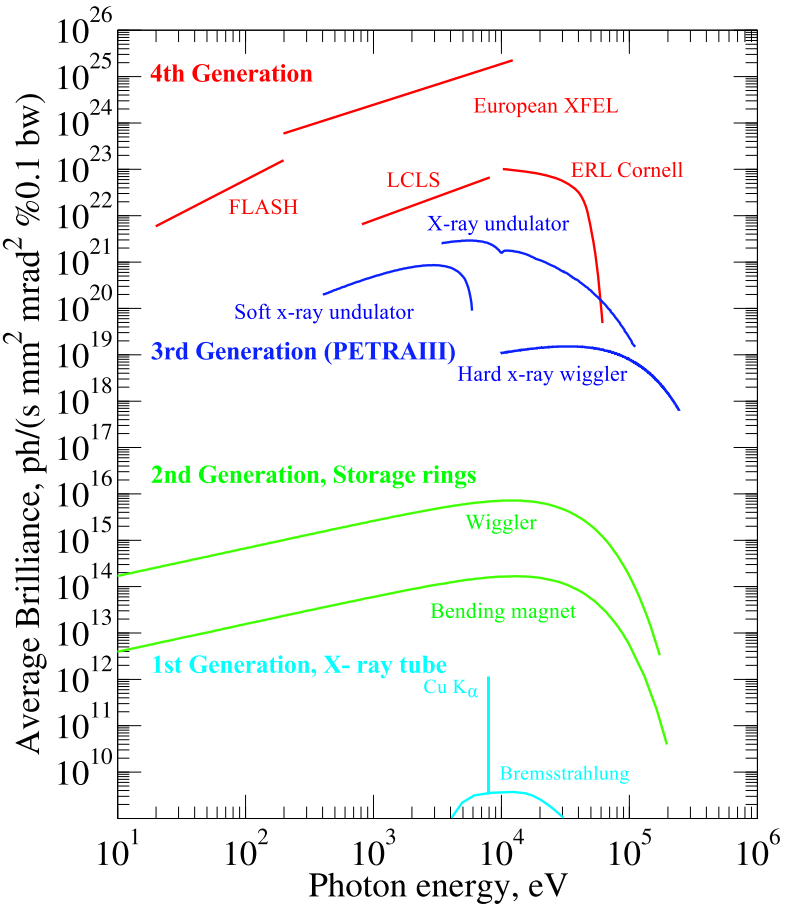

Figure 1.1: Average brilliance of available and planned x-ray radiation radiation sources as a function of photon energy. Third and fourth generation sources situated at DESY (PETRA III, FLASH and European XFEL), the first operating hard x-ray FEL LCLS in Stanford and the planned ERL in Cornell are shown. For comparison the brilliance from the first and second generation sources is also shown. All plots were taken from [3], except for the planned linear undulator source at an ERL [9].

First x-ray experiments were performed with x-ray tubes, where free-electrons are produced through heating of a negatively charged metal wire (cathode) and accelerated by a static electromagnetic field towards a positively charged metal plate (anode). If the electrons are accelerated to an energy of a few tens of keV x-ray radiation is emitted at the anode. The radiation spectrum consists of two components (see Figure 1.1).

- Due to the deceleration in the anode the electrons loose their energy and are eventually stopped. This gives rise to the continuous bremsstrahlung spectrum with its maximum energy being the energy of the electrons.

- During a collision with an atom in the anode the electron may also remove an electron from an inner shell of the atom. The refilling of these vacancies with outer shell electrons gives rise to characteristic sharp lines, which are superimposed on the bremsstrahlung spectrum. The characteristic lines are orders of magnitude stronger than the bremsstrahlung spectrum (see Figure 1.1) and are typically used in experiments.

Due to the weak interaction of x-rays with matter the amount of the photon flux available to the experimentalist is crucial for most applications. It can be characterized by the spectral photon flux [20]

$$F(\lambda) = \frac{\text{number of photons}}{(\text{s})(0.1\%\text{bandwidth})},$$

which is the number of photons per second within a bandwidth (typically 0.1%). A more convenient measure of the source brightness is, however, the brilliance

$$B(\lambda) = \frac{F(\lambda)}{(2\pi)^2 \varepsilon_x \varepsilon_y}, \tag{1.1}$$

where $\varepsilon_{x,y} = \sigma_{x,y}\sigma'_{x,y}$ is the emittance, and $\sigma_{x,y}$ and $\sigma'_{x,y}$ are the size and divergence of the x-ray source, respectively. The brilliance is defined as the number of photons per $(\,\text{s} \cdot \text{mm}^2 \cdot \text{mrad}^2 \cdot 0,1\%\text{bandwidth})$. It is well known that the brilliance can be used to calculate the transverse coherent flux

$$F_{\text{coh}} = B(\lambda) \left(\frac{\lambda}{2}\right)^2, \tag{1.2}$$

which is the number coherent photons in the beam. The coherent fraction is often introduced as

$$\zeta = F_{\text{coh}}(\lambda)/F(\lambda) = \left(\frac{\lambda}{4\pi}\right)^2 \frac{1}{\varepsilon_x \varepsilon_y}. \tag{1.3}$$

Since x-ray tubes are totally incoherent sources and radiate in all directions, they have a comparably low brilliance and low coherent flux. The brilliance is significantly larger at synchrotron sources, which due to relativistic effects radiate into a narrow cone of angles. As a matter of fact, due to invention of synchrotron sources and their further development the brilliance could be increased by about 10 orders of magnitude. The average brilliance at the so called fourth generation x-ray sources like free-electron lasers is another few orders of magnitude higher (see Figure 1.1).

The experimentalists benefit to a great extend from the high brilliance of these sources, which assures that a large number of photons are within the transverse coherence area. In structure determination using crystallography this area determines how many unit cells scatter coherently and give rise to Bragg peaks. At low brilliance sources the signal from the coherently illuminated area (or volume) is rather poor, since the number of coherent photons is small. Comparably large crystals are used to utilize as much flux as possible. Because the scattered intensity from different coherently illuminated parts

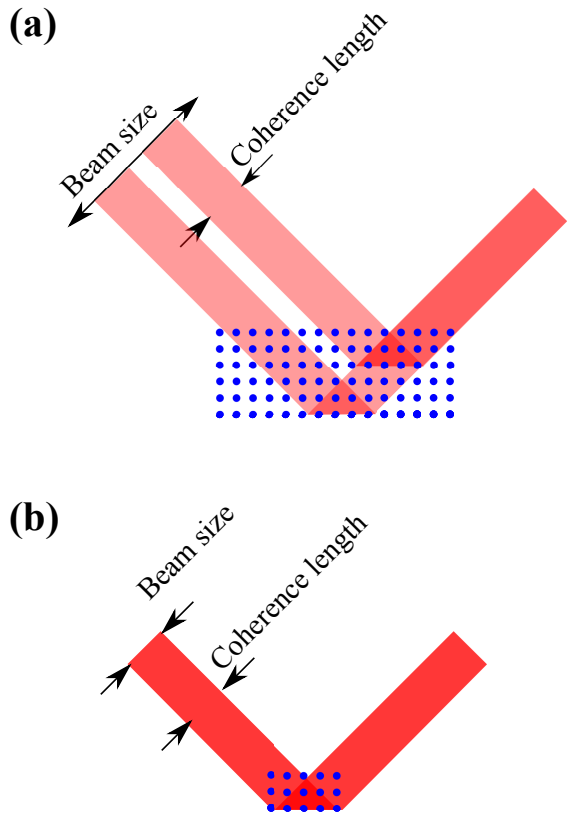

Figure 1.2: Crystallography using low (a) and high (b) coherent flux. The unit cell of the crystal is shown by the blue circle. The coherence area is indicated by the red color. With low coherent flux (a) large crystal is used and the scattered intensity from different regions from the sample sum up in the total signal. With high coherent flux (b) similarly strong signal can be measured with the same total photon flux but with a smaller crystal.

of a large perfect crystal are identical, the intensity in the Bragg peaks grows linearly with the volume of the crystal (see Figure 1.2 (a)). The lack of coherent flux, that is able to interfere, is compensated by the periodicity of the crystal. If the structure is to obtain from a smaller crystal, more photons per coherence area are required. First the beam has to be focused to a smaller size, to utilize the full photon flux and second the coherence area of the focused beam has to be large enough to create interference. As will be shown later, this only can be achieved if the beam has a high coherent flux $F_{\mathrm{coh}}(\lambda)$. This means that if the coherent flux is large, the structure of the unit cell can be determined from a much smaller crystal (see Figure 1.2 (b)).

As a consequence a larger flux per unit cell volume, stronger radiation damage occurs, in particular for biological samples. However, simulations using a single molecule [21] and experiments using small crystals [22] at x-FELs indicate, that the radiation damage due to a large flux per unit cell can be mitigated using pulses briefer than the timescale

of relevant damage processes. At x-ray free-electron lasers the structure determination from the so called nano crystals, consisting of about ten to hundred single constituents in each dimension has been achieved [22].

With the advent of highly brilliant x-ray sources new type of experiments became available, which utilize the high degree of coherence of x-ray beams. One of these new techniques is coherent x-ray diffraction imaging (CXDI) (for a review see [6]), where coherent radiation illuminates the sample and a far-field diffraction pattern is recorded. Because only intensities are measured on the detector, phase retrieval techniques [7, 23] are required to recover the missing phase and at the same time the structure of the object. Since its first experimental demonstration [24], this method has been successfully used to determine the structure of small crystals [25, 26, 27, 28] and biological samples [29, 30]. However, contrary to crystallography, a periodic structure is not mandatory for the CXDI technique. Therefore this method has the potential to image non-periodic sample. First successful experimental steps towards single molecule imaging [21] were reported [31].

Another technique, which uses coherent x-rays is x-ray photon correlation spectroscopy (XPCS) [4]. It is based on the analysis of 'speckle' patterns, which appear in the scattering of transversely coherent light from an non-translation periodic object. The time correlation of consecutively measured diffraction patterns reveals the time dynamics of the sample under study. This method has been applied using optical light, however, with x-rays the analysis of dynamics on a much smaller length scale is possible. Recently, this experimental technique has been extended to analyze the angular correlations [32, 33, 34] within the measured speckle pattern. This technique has the potential to recover the local structure of individual constituents in disordered matter.

1.1 Synchrotron sources

Storage rings are nowadays the principle sources of high-brilliance x-ray beams. Here we shortly outline the development of these sources. In particular, we point out the main features of the radiation generated at third generation synchrotron sources, which combine many attractive techniques. They provide high brilliance x-ray beams, which are highly stable in photon energy, beam intensity, size and position. The photon energy is easily tunable over a wide spectrum ranging from infrared to hard x-ray and beams at storage ring sources are typically linearly polarized in the plane of the ring. Finally, storage rings serve many experiments simultaneously and are comparably cost effective.

First synchrotron radiation was observed in the storage rings build to conceive particle physics experiments and was classified as parasitic radiation. To hold the particles in the ring bending magnets are necessary, which change the trajectory of the particles. Due to this sideway acceleration the particles loose energy and emit electromagnetic radiation [35]. Because the relativistic particles move with a speed close to the speed of light, in the laboratory frame the wavelength of the emitted radiation is significantly reduced due to the Lorentz contraction and lies within x-ray range. Additionally, the radiation is confined to a narrow cone of angles $\theta = 1/2\gamma$, where $\gamma = 1/\sqrt{1 + (v/c)^2}$ is

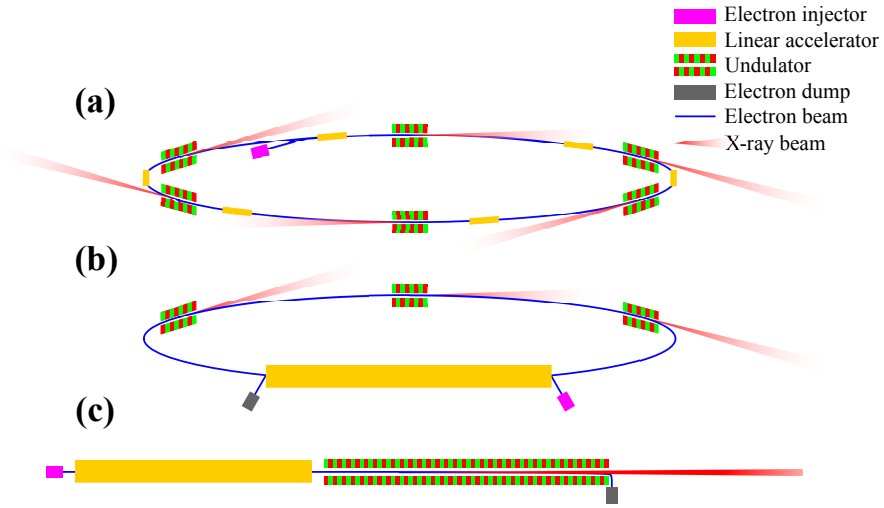

Figure 1.3: A schematic view of a synchrotron radiation source (a), an ERL (b, adapted from [9]), and a FEL (c).

the Lorentz factor, v is the speed of the particles and c is the speed of light in vacuum[3]. The angle θ is often referred to as the natural opening angle of synchrotron radiation.

To enhance the amount of emitted radiation an arrangement of several alternating bending magnets, called wiggler, was developed. In a wiggler the particles are forced to oscillate or wiggle many times while propagation through the magnetic structure. Compared with a single bending magnet the brilliance is enhanced by a factor of N, which is the number of the bending magnets in the wiggler. It was realized then that if the angular excursions of the particle are much smaller than the natural opening angle θ, the electromagnetic wave emitted by a single particle in one turn of the magnetic structure interferes constructively for a given photon energy and its harmonics n with the field of the same particle emitted in another turn. As a consequence, the radiation has an even smaller angular divergence and a smaller bandwidth. The opening angle in this case may be approximated by $\theta/\sqrt{N}$ and the brilliance roughly scales with N^2. An insertion device operated with this scheme is called the *undulator*. Provided the electromagnetic field generated in the undulator is weak and does not influence the motion of the electron, the wavelength of the emitted radiation can be expressed as [36]

$$\lambda = \frac{\lambda_\mathrm{u}}{2\gamma^2}\left(1 + \frac{K^2}{2} + \gamma^2\theta^2\right), \tag{1.4}$$

where λ_u is the undulator period, $K = eB_0\lambda_u/2\pi m_\mathrm{e}c$ is the undulator parameter, θ is the off axis angle, B_0 is the magnetic field of the undulator, e is the elementary charge, and m_e is the rest mass of the electron. Due to the Doppler shift the wavelength depends on the off axis angle θ and the shortest wavelength is observed on axis.

[3] For example, at the third generation synchrotron source PETRA III electrons have an energy of 6 GeV.

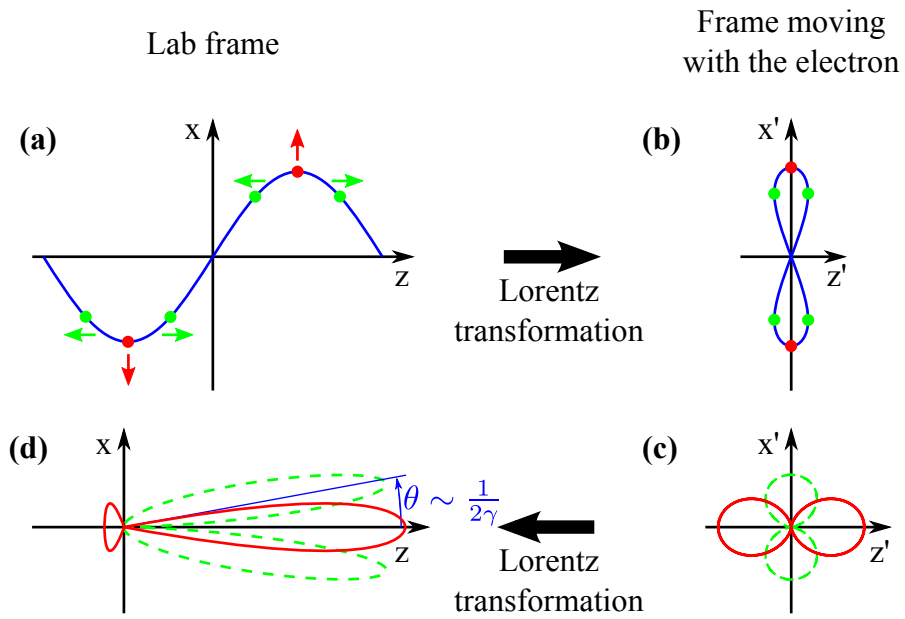

Figure 1.4: Generation of even and odd harmonics in an undulator. (a) The electron (or positron) lateral position x as function of propagation distance z in the lab frame. (b) Lorentz transformation yields the same movement in the frame moving with the electron. Positions with maximum deviation from the center of origin in z (green) and x (red) direction, respectively, are shown. Same positions are indicated in (a). During one oscillation in x the electron oscillates twice in z. (c) The radiation intensity as a function of radiation angle in the frame moving with the electron. Both are represented by dipole radiation. (d) After a Lorentz transformation to the lab frame odd harmonics are observed on axis (red solid line) and even harmonics off axis (greed dashed line). (Figure reproduced from [36])

The spectrum of the radiation generated in a linear undulator consists not only of the wavelength described by equation (1.4) but also contains harmonics with wavelengths $\lambda_n = \lambda/n$, where $n = 1, 2, 3, 4, \ldots$. The origin of the harmonics is the sine like trajectory of the electron through the undulator and its approximately constant total velocity $v = \sqrt{v_x^2 + v_z^2}$, with v_z being the velocity in the propagation direction and v_x perpendicular to v_z. Figure 1.4 (a) shows schematically the lateral position x of the electron as a function of propagation distance z in the lab frame. The electron propagates from left to right. In figure 1.4 (b) the same movement is shown in the frame moving with the electron. During one oscillation period in x the electron executes two oscillations in z. These oscillations give rise to dipole radiation intensity characteristics (see Figure 1.4 (c)). The frequency of emitted radiation in the frame moving with the electron is given by the frequency of oscillation. The radiation distribution in the lab frame can be

This yields $\gamma \approx 10^4$ and $\theta \approx 50$ µrad.

Table 1.1: Overview of the typical electron beam emittance $\varepsilon_{ex,ey}$, photon source size $\sigma_{x,y}$, and divergence $\sigma'_{x,y}$ at different operating third generation synchrotron sources [3] and at the proposed ERL source in Cornell [9]. The photon beam parameters for the third generation sources were calculated for a photon energy of 12 keV [3] and the same parameters for the ERL source are given for an energy of 8 keV [9].

	PETRA III high -β	ESRF high -β	SPring-8	APS	ERL high flux	ERL high coherence
ε_{ex} [nmrad]	1	3.9	3.4	3	0.03	0.008
ε_{ey} [nmrad]	0.005	0.03	0.007	0.03	0.03	0.008
σ_x [µm]	141	402	277	217	13.0	9.0
σ_y [µm]	5.5	7.9	6.4	12.6	13.0	9.0
σ'_x [µrad]	7.7	10.7	13	15.3	3.3	2.3
σ'_y [µrad]	3.8	3.2	5	5.7	3.3	2.3
ζ [%]	0.3	0.06	0.06	0.03	8.5	36

obtained through a Lorentz transformation (see Figure 1.4 (d)). Apparently, only odd harmonics are present on axis and even harmonics are observed off axis.

The transition from the undulator radiation to the wiggler radiation can be described by the undulator parameter K in equation (1.4). If $K \leq 1$, undulator radiation with distinct harmonics is generated. In a magnetic structure with larger values of K wiggler radiation is produces. The harmonics spectrum merges into a continuum in the wiggler limit $K \gg 1$. It extends to higher photon energies, therefore wigglers are used to generate x-ray photons in the range of a few tens of keV to hundreds of keV at synchrotron sources. At PETRA III the undulator parameter is $K \approx 2.2$ for undulator radiation and $K \approx 7$ for wiggler radiation [3].

To generate a beam which can be effectively used in experiments a large number of radiating particles is required. Most of the synchrotron sources are storage rings, where the particles circulate repetitively and generate x-rays each time they pass the straight sections with the undulators (see Figure 1.3 (a)). Several different experimental stations are positioned along the synchrotron ring and utilize the same electron bunches. The separation between consecutive electron bunches is set by the radio frequency (RF), used in the accelerators, which restores the power of the electrons lost to synchrotron radiation. The radio frequency is typically given by about 1 GHz, hence, the separation between consecutive x-ray pulses can be as short as 1 ns and up to 10^9 x-ray pulses per second at each experimental station can be made available.

A complicated magnetic structure is required to hold the electron bunches in the storage ring and to refocus these bunches, which tend to blow up due to Coulomb forces. A short time after the electron bunches are filled into the ring they reach an equilibrium state with its characteristics being determined by the ring characteristics. Typically, the radiation properties, including the brilliance and the degree of transverse

coherence, are determined by the electron bunch properties and are thus limited by the ring characteristics. These are characterized by the electron beam emittance $\varepsilon_e = \sigma_e \sigma'_e$, where σ_e and σ'_e is the size of the electron bunch and its divergence, respectively. A low emittance ε_e of the electron bunch implies a low emittance ε of the photon beam and therefore a higher brilliance (1.1) and a higher coherent photon flux (1.2) of the source. A common feature of all storage ring sources is the comparably poor emittance in the horizontal direction. As a consequence the photon beam has a small degree of transverse coherence in the same direction. Typical electron bunch characteristics and photon beam properties of third generation photon sources are summarized in Table 1.1. The pulse duration is also influenced by the ring and is typically about 100 ps FWHM at third generation x-ray sources.

1.2 Next generation synchrotron sources

The electron and consecutively the photon beam properties could be significantly better, if the electrons with an extremely small beam emittance would pass the ring and its RF system just once or a few times. It is anticipated [37, 9] that the energy of the electron bunch can be recovered and used for the acceleration of the next bunches. Sources based on this principle are called Energy Recovery Linacs (ERL) and have the potential to be superb coherent x-ray sources. The main component of an ERL is a linac (see Figure 1.3 (b)). It accelerates electrons and generates bunches with extremely low emittance and a high total charge. These bunches travel along the ring equipped with undulators and produce highly brilliant x-ray beams. Importantly, since the electron bunches propagate just a few times through the ring, the emittance is not deteriorated significantly. Finally, the electrons enter the linac, which transforms the energy of the electrons into radio frequency energy. This energy is used to accelerate the next electron bunch. Clearly, not all the energy of the electrons can be recovered and an electron beam dump is required to stop the remaining low energy electrons (see Figure 1.3 (b)).

The radiation generated by ERLs is spontaneous undulator radiation, similar to that generated by synchrotron sources. However, due to the fact that the electrons are not forced to circulate for a long time, the electron bunch emittance in horizontal direction can be as small as the emittance in vertical direction [9]. Theoretically the electron bunch emittance can be about 10 pmrad in both directions (see Table 1.1). Due to this lower total emittance of the electron bunches a higher brilliance and a higher degree of coherence are expected at these sources. The parameters of the proposed ERL source at Cornell University are presented in Table 1.1. Other important properties of ERLs are the short x-ray pulses – on the order of 1 ps – and a higher repetition rate of the x-ray pulses, as compared with third generation sources. Due to the higher repetition rate the average brilliance at an ERL source can be significantly larger than at third generation x-ray sources (see Figure 1.1).

1.3 Free-electron lasers

The next milestone in producing x-ray radiation was proposed by A. Kondratenko and E. Saldin [38] and independently by R. Bonifacio, C. Pellegrini and L. M. Narducci [39]. It was realized that if the electromagnetic field produced in the undulator has a significant impact on the properties of the electron bunch an exponential growth of the energy emitted by the particles is possible. That process was called Self Amplification of Spontaneous Emission (SASE). A free-electron laser (FEL) based on SASE principle consists of an injector, a linear accelerator and an undulator (see Figure 1.3 (c)). The FEL requirements on the electron beam quality in terms of small emittance, low energy spread, and a large critical current are quite demanding, therefore, linear accelerators are used to generate the electron beam [40]. Additionally, comparably long undulators – on the order of 100 m – are necessary to generate SASE radiation in the x-ray range.

Several SASE FELs are operating, being constructed or planned [8]. The parameters of the first extreme ultraviolet (XUV) FEL FLASH at DESY, of the first hard x-ray FEL LCLS at SLAC and of the European XFEL, presently under construction at DESY, are presented in Table 1.2 (see also Figure 1.1 for a comparison of the average brilliance of XFELs with other x-ray sources). Most important features of a SASE FEL is the extremely short pulse duration – on the order of 100 fs and below –, the high energy per pulse – on the order of mJ – and its high coherent fraction of the radiation – on the order of 1. Due to these characteristics the peak brilliance at FELs (see Table 1.2) exceeds the peak brilliance at synchrotron sources by several orders of magnitude.

The SASE process is a result of the interaction between the electrons and the radiation field generated by the electrons. To describe quantitatively the radiation of a FEL one has to solve self consistently a set of coupled differential equations. These equations describe the emitted radiation, the motion of the electrons and the coupling between the electromagnetic field and the electrons [44, 40]. Although analytical solution of these equations may be found in some simplified cases, such as the one dimensional high gain-FEL, generally these equations have to be solved numerically. Here we restrict our attention to the physical processes [45] behind the SASE generation.

Table 1.2: Typical parameters of FLASH [41], LCLS [42], and European XFEL [43]. The fundamental wavelength, λ, the average energy per photon pulse, E, the pulse duration T, the bandwidth, bw, and the peak brilliance are shown. *The peak brilliance is given in photons/s $\cdot$ mm^2 $\cdot$ mrad^2 $\cdot$ 0 1%bandwidth.

	FLASH	LCLS (soft x-rays)	LCLS (hard x-rays)	European XFEL SASE 1
λ [nm]	4.1-45	0.6-2.2	0.15	0.1
E [mJ]	0.01-0.1	1-2.5	1.5-3.0	2.0
T (FWHM) [fs]	50-200	70-500	70-100	100
bw (FWHM) [%]	1.0	0.2-1.0	0.2-0.5	0.08
peak brilliance*	$10^{29} - 10^{31}$	$3 \cdot 10^{31}$	$2 \cdot 10^{33}$	$5 \cdot 10^{33}$

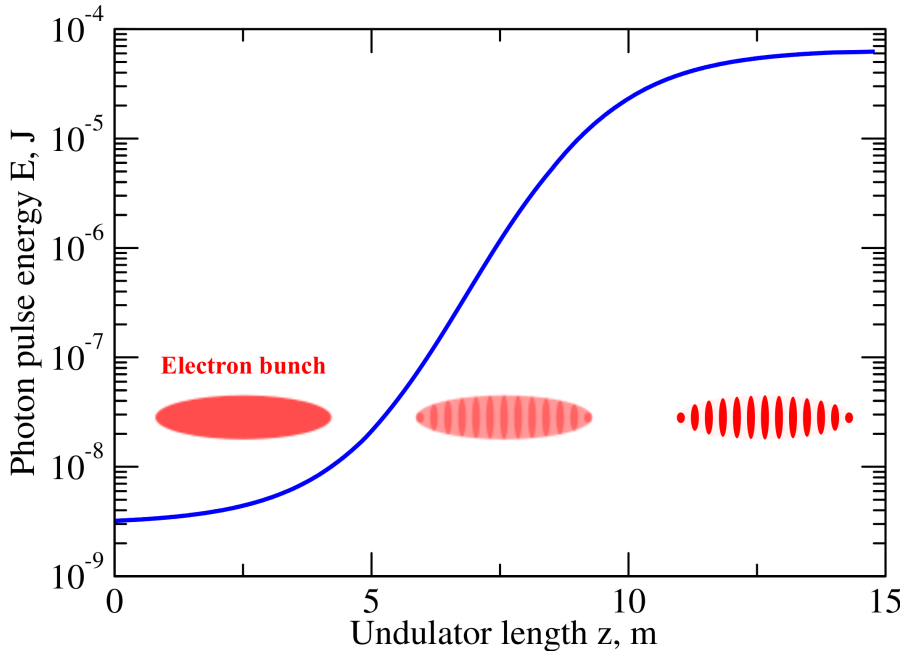

Figure 1.5: A schematic view of the generation of light in a SASE FEL. The average pulse energy as a function of the active undulator length at the TTF FEL, Phase 1 is shown (reproduced from [43]). The behaviour of the electron bunch for different regimes of operation is schematically shown by the red cloud.

The starting point of the SASE process is the spontaneous undulator radiation described in the previous chapter. As this radiation and the electron beam co-propagate along the undulator, the electromagnetic field produced by the electrons gets intense enough and is able to modulate the electron distribution in the electron bunch. Microbunches separated by a single radiation wavelength appear (see Figure 1.5) and the radiation power increases exponentially, because the electrons in the microbunch radiate almost coherently. According to electrodynamics all electrons confined within a space with its extend being smaller than the wavelength can be considered as a single macroparticle with the corresponding charge n_e. The radiated energy is proportional to n_e^2, where n_e is the number of the electrons in a single micro-bunch. The amplification of the radiation field enhances the microbunching process even further. Therefore, the radiation power increases exponentially with the undulator length. This regime of operation is referred to as linear regime. In the linear regime the amplified electromagnetic field is proportional to the stimulation i.e. spontaneous undulator radiation. Therefore, the statistical properties of a SASE FEL in the linear regime are similar to the properties of the spontaneous undulator radiation and obey Gaussian statistics [44, 46].

When all electrons are distributed in microbunches, with their extend being much smaller than the radiation wavelength, no significant amplification can be obtained.

The radiated power saturates and the FEL is said to operate in the saturation regime. Above saturation an FEL operates in the deep nonlinear regime. The latter conditions of operation belong to the nonlinear regime, where the statistical properties of the radiation differ from the spontaneous undulator radiation.

The key quantity in the realization of a SASE FEL is the gain length L_g, which describes how fast the pulse energy is growing with the propagation distance in the undulator. In particular, in the linear regime the radiation power P increases exponentially according to [40, 44]

$$P(z) \sim \exp\left(\frac{z}{L_g}\right).$$

The gain length can also be used to estimate the degree of correlation between individual micro-bunches, described by the cooperation length L_c. It is estimated as [47] $L_c = \lambda N_g$, where $N_g = L_g/\lambda_u$ is the number of undulator periods within a gain length. The light is faster than the relativistic electrons on a sinusoidal trajectory and passes them by one radiation wavelength each period of the undulator. As a consequence, after propagating the distance L_g through the undulator the electrons within the corresponding slippage L_c get correlated. The micro-bunches within the cooperation length interfere with each other and as a result a smaller angular divergence is observed.

A rough estimate of the coherence properties of an FEL can be readily obtained. The coherence time can be estimated from the cooperation length $\tau_c = L_c/c$ [47]. The degree of transverse coherence can be estimated from the ratio between the gain length L_g and the Rayleigh length of emitted radiation [48]. The latter describes how fast the generated wave fields expand in space due to diffraction. If the Rayleigh length is much smaller than the gain length a fully transversely coherent beam is expected. In the opposite limit many transverse modes within the beam can coexist and the degree of coherence is lowered. However, this estimate of the degree of transverse coherence is rather qualitative.

Although SASE FELs are called lasers, there is a significant difference between optical lasers and SASE FELs. Contrary to the optical laser, where a resonator typically permits the growth of a single mode, in a SASE FEL a variety of modes can be amplified. The SASE process starts from shot noise in the electron bunch, which means that the signal at the end of the undulator depends on the instabilities in the electron bunch entering the undulator. Therefore, the radiation properties, including the mean frequency of radiation, bandwidth, and total pulse energy, change from shot to shot. For instance, the intensity as a function of time consists of spikes with the width being the coherence time τ_c. The positions of the spikes and their relative phases change from pulse to pulse. The small coherence time limits the resolution in single particle diffraction imaging experiments at FELs [49]. These and other experiments require a higher stability of the FEL pulses.

Using a comparably weak temporally coherent and stable seed radiation, the temporal coherence and the reproducibility of the FEL pulses can be significantly improved. Different techniques for seeding are considered. In soft x-ray regime high harmonic generation [50], which is a technique to generate soft x-ray light with optical lasers, can

be used. This design is planned for FLASH2 at DESY, which is currently under construction. For hard x-ray FELs a self seeding technique has been proposed [51, 52]. A monochromator on the early stage of the SASE amplification process is used to generate monochromatic light. This monochromatic light is then further amplified. The first experimental realization has been achieved recently at LCLS [53]. In these experiments the coherence time increased by a factor of about 50, whereas the total pulse energy has not been reduced significantly. Ultimately, these seed techniques will possibly provide transverse and temporally fully coherent x-ray pulses, very similar to the light pulses generated by optical lasers.

2 Theory of optical coherence

2.1 Propagation of electromagnetic waves

In our discussion of the statistical characteristics of light we will require elements of the electromagnetic theory. In particular, the propagation of light waves in vacuum will be used in the discussion of coherence properties of the radiation. A rigorous description of the electromagnetic theory can be found in [35, 54]. Here we restrict our attention to the scalar theory of light waves, which considers only one polarization component of the radiation field. A brief summary of the formulas utilized throughout the thesis is presented in this chapter.

The propagation of the electromagnetic field $E(\mathbf{r}, t)$[1] in vacuum is governed by the wave equation

$$\nabla^2 E(\mathbf{r}, t) + \frac{1}{c^2}\frac{\partial^2}{\partial t^2} E(\mathbf{r}, t) = 0, \tag{2.1}$$

where $c \approx 3 \cdot 10^8$ m/s is the velocity of light in vacuum. The wave equation is a partial differential equation, which has to be solved subject to the initial and boundary conditions [56]. A boundary condition might be, for example, the known field at the source of the radiation. Fourier transformation of (2.1) yields the Helmholtz equation

$$\nabla^2 E(\mathbf{r}, \omega) + k^2 E(\mathbf{r}, \omega) = 0, \tag{2.2}$$

for each frequency component $E(\mathbf{r}, \omega) = \int E(\mathbf{r}, t) e^{-i\omega t} \mathrm{d}t$. Here ω is the frequency of the radiation and $k = \omega/c$ is the modulus of the wave vector $\mathbf{k}$.

Often the solution of the Helmholtz equation is simpler than the solution of the wave equation, since the derivative of $E(\mathbf{r}, t)$ with respect to t is replaced by a multiplication with k. After the propagation of each frequency component, the electromagnetic field as a function of position and time can be readily determined from the inverse Fourier transform $E(\mathbf{r}', t) = \int E(\mathbf{r}', \omega) e^{i\omega t} \mathrm{d}\omega/(2\pi)$.

For us it will be particularly important to propagate the field in free space from one plane positioned at z_0 over a distance z to another plane at z_1 (see Figure 2.1). The transverse coordinates in the plane at z_0 are denoted by $\mathbf{s} = (s_x, s_y)$, in the plane at z_1 by $\mathbf{u} = (u_x, u_y)$ and z is the coordinate along the optical axis. Here we assume that the propagation distance z is much larger than the wavelength λ of the radiation. In this geometry the solution of the Helmholtz equation can be found in the form of the

[1] We will use the complex analytic signal representation of the wave-fields [55] throughout the thesis.

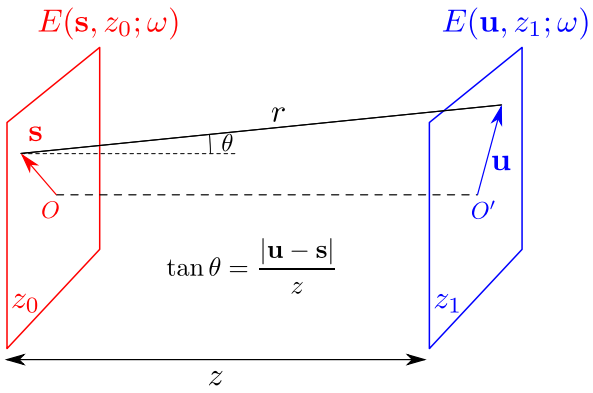

Figure 2.1: A sketch to illustrate the Fresnel approximation. The propagation of the field from a plane at z_0 to a plane at z_1 is considered. Optical axis is joining the origins of the two planes and is indicated by the dashed black line. The field is confined within small angles θ.

Huygens-Fresnel principle [54]

$$E(\mathbf{u}, z_1; \omega) = \int E(\mathbf{s}, z_0; \omega) P_z(\mathbf{u}, \mathbf{s}; \omega) \mathrm{d}\mathbf{s}, \tag{2.3}$$

where $E(\mathbf{s}, z_0; \omega)$ is the field in the plane at z_0, $E(\mathbf{u}, z_1; \omega)$ is the field in the plane at z_1 and the integration is made over all $\mathbf{s}$ in the plane at z_0. The propagator is given by

$$P_z(\mathbf{u}, \mathbf{s}; \omega) = \frac{k}{2\pi i} \frac{e^{ikr}}{r} \chi(\theta), \tag{2.4}$$

where r is the distance between the points $(\mathbf{s}, z_0)$ and $(\mathbf{u}, z_1)$, and θ is the angle between the line joining $(\mathbf{s}, z_0)$ to $(\mathbf{u}, z_1)$ and the optical axis. The angle θ is defined through $\tan\theta = |\mathbf{u} - \mathbf{s}|/z$ and $\chi(\theta)$ is the obliquity factor with $\chi(0) = 1$ and $0 \leq \chi(\theta) \leq 1$.

When only small angles θ are of importance in equation (2.3), it is sufficient to work in the frame of the Fresnel approximation. In this case we expand the term kr in the propagator (2.4) into a Taylor series

$$kr \approx kz \left(1 + \frac{|\mathbf{u} - \mathbf{s}|^2}{2z^2} - \frac{|\mathbf{u} - \mathbf{s}|^4}{8z^4} + \cdots\right), \tag{2.5}$$

and take only the first two terms in (2.5) into account. The Fresnel propagator can be written as

$$P_z(\mathbf{u}, \mathbf{s}; \omega) = \frac{k}{2\pi i} \frac{e^{ikz}}{z} \exp\left(ik \frac{|\mathbf{u} - \mathbf{s}|^2}{2z}\right) = \frac{k}{2\pi i} \frac{e^{ikz}}{z} \exp\left(ik \frac{|\mathbf{u}|^2 + |\mathbf{s}|^2 - 2\mathbf{u} \cdot \mathbf{s}}{2z}\right). \tag{2.6}$$

where $r \approx z$ is used in the denominator. A more accurate approximation of r is used in the phase since there the sensitivity to errors is greater than in the denominator. The

Fresnel approximation is valid if the third and all higher terms in (2.5) vanish, i.e. if [57]

$$\frac{kz}{8}\left(\frac{|\mathbf{u}-\mathbf{s}|}{z}\right)^4 \ll \pi. \tag{2.7}$$

Since the Huygens-Fresnel principle is valid for $kz \gg 1$ and we want to neglect terms of order higher than $kz\tan^4\theta$, only small angles with $\tan^4\theta \ll 1$ are considered. In this limit the approximation $\tan\theta \approx \theta$ can be used and the obliquity factor is well approximated by $\chi(\theta) \approx 1$ due to small angles θ. The Fresnel approximation condition for all angles θ for the radiation to propagate is given by

$$\theta \ll \sqrt[4]{\frac{8\pi}{kz}}. \tag{2.8}$$

Let us shortly discuss the applicability of the Fresnel approximation to the case of coherent x-ray diffraction. As an example we consider a typical x-ray diffractive imaging experiment [28]. The wavelength of the radiation is 1.5 Å and the propagation distance is 5 m. The Fresnel approximation is then valid for angles θ smaller than approximately 10 mrad or for transverse dimensions smaller than 50 mm. These conditions were easily satisfied in such experiments.

In the Fraunhofer (or far-field) approximation the propagator is further simplified

$$P_z(\mathbf{u},\mathbf{s};\omega) = \frac{k}{2\pi i}\frac{e^{ikz}}{z}\exp\left(ik\frac{|\mathbf{u}|^2 - 2\mathbf{u}\cdot\mathbf{s}}{2z}\right). \tag{2.9}$$

The Fraunhofer propagator can be applied if the Fresnel number $N_F = d^2/(\lambda z)$ satisfies $N_F \ll 1$, where d is the spatial extend of the field in the plane at z_0[2]. The propagation of wave fields through free space is considered frequently throughout the thesis. The numerical implementation of propagation laws in Fresnel and Fraunhofer approximation is presented in Appendix A.1.

When propagation of radiation fields is considered, thin optical elements are often involved, such as apertures or thin lenses. The transmission through a thin optical element can be performed by multiplication with a transmission function $T(\mathbf{u},\omega)$

$$E^{\text{out}}(\mathbf{u}, z_1;\omega) = T(\mathbf{u};\omega)\cdot E^{\text{in}}(\mathbf{u}, z_1;\omega), \tag{2.10}$$

where $E^{\text{in}}(\mathbf{u}, z_1;\omega)$ is the field incident on and $E^{\text{out}}(\mathbf{u}, z_1;\omega)$ is the field behind the aperture. The transmission function of a circular aperture, for example, can be written as

$$T(\mathbf{u},\omega) = \begin{cases} 1 & \text{for} \quad |\mathbf{u}| < D/2 \\ 0 & \text{elsewhere} \end{cases} \tag{2.11}$$

[2]The extend of the field in the source plane can be defined through the condition $|E(\mathbf{s}, z_0)| = 0$ for all $|\mathbf{s}| > d$.

where D is the diameter of the aperture. The transmission function of a slit is given by

$$T(\mathbf{u},\omega) = \begin{cases} 1 & \text{for} \quad |u_x| < a_x/2 \text{ and } |u_y| < a_y/2 \\ 0 & \text{elsewhere} \end{cases}, \tag{2.12}$$

where u_x, u_y are the horizontal and vertical components of $\mathbf{u}$ and a_x and a_y are the slit width and height, respectively. A thin lens with an infinite aperture may be described by [57]

$$T(\mathbf{u},\omega) = \exp\left(-\frac{ik|\mathbf{u}|^2}{2f(\omega)}\right), \tag{2.13}$$

where $f(\omega)$ is the focal distance of the lens.

2.2 Coherence: Basic Equations

The description of radiation properties within the classical electromagnetic theory, outlined in the previous chapter, may fail in many realistic cases due to the statistical nature of light. To illustrate this fact we consider a source that consists of a number of independent point sources distributed over the source volume (see Figure 2.2). Let us assume that each point source radiates for some period of time but it cannot be precisely known for each point source, when it radiates and when it does not. The latter condition is the Heisenberg's uncertainty principle in the quantum mechanics [58]. As a consequence, the total radiation field, which due to the superposition principle is the sum of all fields from individual point sources, fluctuates as a function of time. These fluctuations are extremely fast[3] and can not be detected, therefore only statistical properties of these fluctuations can be determined. In the beginning of the 20th century it was recognized (see [59] for a historical introduction) that the radiation field from such a source can be treated with a correlation function of the complex wave fields. These developments led to the theory of statistical optics and optical coherence. For a rigorous description of optical coherence see references [46, 60].

The concept of optical coherence has long been associated with interference phenomena, where the Mutual Coherence Function (MCF)

$$\Gamma(\mathbf{r}_1,\mathbf{r}_2;t_1,t_2) = \langle E^*(\mathbf{r}_1,t_1)E(\mathbf{r}_2,t_2)\rangle, \tag{2.14}$$

plays the main role. It describes the correlations between two complex values of the electric field $E^*(\mathbf{r}_1,t_1)$ and $E(\mathbf{r}_2,t_2)$ a different points $\mathbf{r}_1$ and $\mathbf{r}_2$ and different times t_1 and t_2. The brackets denote the ensemble average [46]

$$\langle f(\mathbf{r},t)\rangle = \lim_{N\to\infty}\frac{1}{N}\sum_{r=1}^{N} f^{(r)}(\mathbf{r},t), \tag{2.15}$$

[3] The fluctuation time coincides with the coherence time τ_c, which can be estimated from $\tau_c = 1/\Omega$, where Ω is the bandwidth of the radiation. For example, using approximate bandwidth of the radiation from the sun ($\lambda \approx 250 - 1000$ nm) we estimate $\tau_c < 1$ fs.

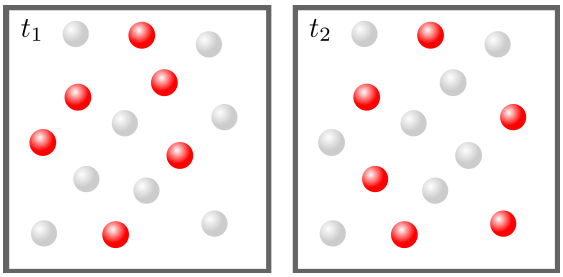

Figure 2.2: Illustration of a fluctuating source of light. The source consists of a number of radiators. At a certain time t_1 (left side) some sources (red circles) radiate and others (grey circles) do not. At another time t_2 (right side) other radiators radiate. The source undergoes fluctuations.

where $f^{(r)}(\mathbf{r},t)$ is one possible realization from the ensemble of all possible realizations of the statistical function $f(\mathbf{r},t)$.

From the definition (2.14) it follows that when two points and times coincide the MCF yields the average intensity

$$\langle I(\mathbf{r},t)\rangle = \Gamma(\mathbf{r},\mathbf{r};t,t) = \left\langle |E(\mathbf{r},t)|^2 \right\rangle . \tag{2.16}$$

It is convenient to normalize the MCF as

$$\gamma(\mathbf{r}_1,\mathbf{r}_2;t_1,t_2) = \frac{\Gamma(\mathbf{r}_1,\mathbf{r}_2;t_1,t_2)}{\sqrt{\langle I(\mathbf{r}_1,t_1)\rangle}\sqrt{\langle I(\mathbf{r}_2,t_2)\rangle}}, \tag{2.17}$$

which is known as the complex degree of coherence (CDC). For all values of $\mathbf{r}_1,\mathbf{r}_2$ and t_1,t_2 the CDC satisfies $|\gamma(\mathbf{r}_1,\mathbf{r}_2;t_1,t_2)| \leq 1$. The modulus of the CDC is often measured in interference experiments as the contrast of the interference fringes. If $|\gamma(\mathbf{r}_1,\mathbf{r}_2;t_1,t_2)| = 1$ the field is said to be coherent, if $|\gamma(\mathbf{r}_1,\mathbf{r}_2;t_1,t_2)| = 0$ it is completely incoherent and if $0 < |\gamma(\mathbf{r}_1,\mathbf{r}_2;t_1,t_2)| < 1$ it is partially coherent.

Substituting $\mathbf{r}_1 = \mathbf{r}_2$ and $t_1 = t_2$ in the definition of the CDC (2.17) one finds $\gamma(\mathbf{r},\mathbf{r};t,t) = 1$. This means that the field is always coherent with itself in a single point. In the most cases the CDC drops to lower values as the separation between the points in space $\mathbf{r}_2 - \mathbf{r}_1$ and time $t_2 - t_1$ increases. A characteristic width[4] of the CDC $|\gamma(\mathbf{r}_1,\mathbf{r}_2;t_1,t_2)|$ in the spatial domain and in the temporal domain is often called the transverse and the temporal coherence length. The product of these values, called coherence volume, can be considered as the region throughout the space within which the electromagnetic field is highly correlated.

After the invention of the maser [61, 62], laser [1] and the experiments of Hanbury Brown and Twiss [63], the concept of the MCF, which is a first order correlation function, was found to be inadequate for the interpretation of the experimental results. To

[4] In this thesis the coherence length is the separation $\mathbf{r}_2 - \mathbf{r}_2$ or time difference $t_2 - t_1$ at which the modulus of the CDC drops to a value of 0.6. For a Gaussian function this value corresponds to the rms width.

provide a more rigorous description of coherence, higher order correlation functions were introduced. The $n-$th order correlation function expresses the correlation of values of the fields at $2n$ different points of space and time [46]

$$\begin{aligned}\Gamma^{(n)}&(\mathbf{r}_1,\ldots,\mathbf{r}_{2n};t_1,\ldots,t_{2n})\\ &=\langle E^*(\mathbf{r}_1,t_1)\cdots E^*(\mathbf{r}_n,t_n)E(\mathbf{r}_{n+1},t_{n+1})\cdots E(\mathbf{r}_{2n},t_{2n})\rangle\,.\end{aligned} \tag{2.18}$$

A fully coherent field was defined by Glauber [64] "as one whose correlation functions satisfy an infinite succession of stated conditions"[5]. In particular, the electromagnetic field possesses $n-$th order coherence, if the normalized coherence function

$$\gamma^{(m)}(\mathbf{r}_1,\ldots,\mathbf{r}_{2m};t_1,\ldots,t_{2m})=\Gamma^{(m)}(\mathbf{r}_1,\ldots,\mathbf{r}_{2m};t_1,\ldots,t_{2m})\Big/\prod_{j=1}^{2m}\sqrt{\Gamma^{(1)}(\mathbf{r}_j,t_j,\mathbf{r}_j,t_j)} \tag{2.19}$$

is equal to 1 for all $m\leq n$. Such coherent fields can be generated by a maser and a laser. Higher order coherence of matter waves has recently been observed in a Bose-Einstein condensate [65].

In the measurements of the higher order correlation functions, as for example in the photon correlation experiments of Hanbury Brown and Twiss [63], the degeneracy parameter δ plays an important role [66]. According to Heisenberg's uncertainty relation for the conjugate pairs $\Delta p_x\Delta x$, $\Delta p_y\Delta y$ and $\Delta E\Delta t$ the phase space volume V satisfies [46]

$$V=\Delta p_x\Delta x\Delta p_y\Delta y\Delta E\Delta t\geq\left(\frac{\hbar}{2}\right)^3. \tag{2.20}$$

It is therefore natural to consider the phase space to be divided in to cells of phase space volume $V_c=(\hbar/2)^3$. The degeneracy parameter is defined as [46]

$$\delta=\frac{N_{\mathrm{ph}}V_c}{V}, \tag{2.21}$$

where N_{ph} is the total number of photons in the beam. The degeneracy parameter δ is the average number of photons in the same cell of phase space or the same quantum mechanical state. The degeneracy parameter differs drastically for thermal and laser light. In the former case it is typically $\delta\ll 1$, whereas for laser light it can be several orders of magnitude higher $\delta\approx 10^9$ [46]. Clearly, fully coherent beam can be described by the relation $N_{\mathrm{ph}}=\delta$.

In x-ray physics, no fully coherent sources have been available up to now and the first-order correlation function was sufficient to predict the outcome of most experiments. However, it has to be investigated whether x-ray FELs generate beams with higher order coherence in the x-ray regime. If this would be the case, techniques utilizing the higher order coherence may either be adapted from the optical wavelength range or

[5] Glauber developed a quantum mechanical treatment of the correlation functions and introduced fully coherent photon states, which today are known as Glauber states.

completely new approaches could be proposed at FELs. We will address this question later in the thesis (see chapter 5.5) and will for the moment restrict ourselves to the first-order correlation function, i.e. the MCF.

It is worth noting that the theory of optical coherence is not limited to photon beams. Electron beams with a comparably high first order coherence can also be produced and be used in imaging experiments such as coherent diffractive imaging [67]. The theory of first order correlation functions can be applied to describe these beams.

2.3 Correlation functions of stationary wave-fields

For stationary and ergodic wave-fields [46] the MCF is invariant under time translation and can be written as

$$\Gamma(\mathbf{r}_1, \mathbf{r}_2; \tau) = \langle E^*(\mathbf{r}_1, t) E(\mathbf{r}_2, t+\tau) \rangle_T \,, \tag{2.22}$$

where $\tau = t_2 - t_1$ is the time difference and the ensemble average (2.15) is replaced by the time average

$$\langle f(\mathbf{r}, t) \rangle_T = \lim_{T\to\infty} \int_{-T/2}^{T/2} f(\mathbf{r}, t) \mathrm{d}t. \tag{2.23}$$

This average is often observed in a real measurement, where typically a detector accumulates the signal over time. At most x-ray sources, including x-ray tubes and synchrotron sources, the radiation is stationary and ergodic in good approximation.

Another simplification in the theory of coherence can be used if the radiation has a narrow bandwidth, i.e. $\Omega/\omega_0 \ll 1$, where Ω is the bandwidth of radiation and ω_0 is the mean frequency. As most of the x-ray sources have a narrow bandwidth, we will use the narrow bandwidth approximation throughout this thesis.

2.3.1 Propagation of the wave-field correlation functions

In general, the propagation of the MCF in free space is governed by two wave equations [46]

$$\nabla_i^2 \Gamma(\mathbf{r}_1, \mathbf{r}_2; t_1, t_2) + \frac{1}{c^2} \frac{\partial^2}{\partial t_i^2} \Gamma(\mathbf{r}_1, \mathbf{r}_2; t_1, t_2) = 0, \tag{2.24}$$

for $i = 1, 2$. For stationary conditions these wave equations simplify to

$$\nabla_i^2 \Gamma(\mathbf{r}_1, \mathbf{r}_2; \tau) \pm \frac{1}{c^2} \frac{\partial^2}{\partial \tau^2} \Gamma(\mathbf{r}_1, \mathbf{r}_2; \tau) = 0, \tag{2.25}$$

where $+$ is used for $i = 1$ and $-$ for $i = 2$.

When we consider the propagation of the correlation function of the field in free space, it is convenient to introduce the cross-spectral density function (CSD), $W(\mathbf{r}_1, \mathbf{r}_2; \omega)$,

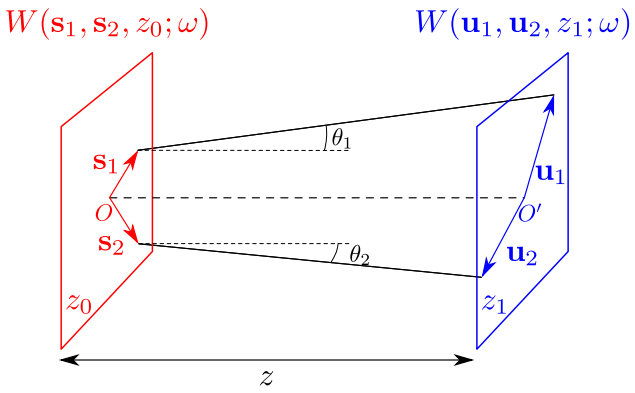

Figure 2.3: The propagation geometry considered here: The source is positioned in the plane at z_0 and is described by the CSD $W(\mathbf{s}_1, \mathbf{s}_2, z_0; \omega)$. The CSD, $W(\mathbf{u}_1, \mathbf{u}_2, z_1; \omega)$ of the radiation field in the observation plane positioned at a distance z from the source is calculated.

which is defined as the Fourier transform of the MCF [46]

$$W(\mathbf{r}_1, \mathbf{r}_2; \omega) = \int \Gamma(\mathbf{r}_1, \mathbf{r}_2; \tau) e^{-i\omega\tau} \mathrm{d}\tau, \tag{2.26}$$

where ω is the angular frequency of the radiation. The wave-equations (2.25) for the MCF simplify to a set of two Helmholtz equations for the CSD [46]

$$\nabla_i^2 W(\mathbf{r}_1, \mathbf{r}_2; \omega) \pm k^2 W(\mathbf{r}_1, \mathbf{r}_2; \omega) = 0. \tag{2.27}$$

Before we proceed, let us summarize some basic properties of the CSD function $W(\mathbf{r}_1, \mathbf{r}_2; \omega)$. Equation (2.26) together with its Fourier inverse

$$\Gamma(\mathbf{r}_1, \mathbf{r}_2; \tau) = \frac{1}{2\pi} \int W(\mathbf{r}_1, \mathbf{r}_2; \omega) e^{i\omega\tau} \mathrm{d}\omega, \tag{2.28}$$

are known as the generalized Wiener-Khintchine theorem [46]. By definition, when the two points $\mathbf{r}_1$ and $\mathbf{r}_2$ coincide, the CSD represents the spectral density of the radiation field,

$$S(\mathbf{r}; \omega) = W(\mathbf{r}, \mathbf{r}; \omega) \tag{2.29}$$

and (2.28) simplifies to

$$\Gamma(\mathbf{r}, \mathbf{r}; \tau) = \frac{1}{2\pi} \int S(\mathbf{r}; \omega) e^{i\omega\tau} \mathrm{d}\omega,$$

which is the original Wiener-Khintchine theorem. The normalized CSD is known as the

spectral degree of coherence (SDC)

$$\mu(\mathbf{r}_1, \mathbf{r}_2; \omega) = \frac{W(\mathbf{r}_1, \mathbf{r}_2; \omega)}{\sqrt{S(\mathbf{r}_1; \omega) S(\mathbf{r}_2; \omega)}}, \qquad |\mu_{12}(\omega)| \leq 1. \tag{2.30}$$

To characterize the transverse coherence properties of a wave field by a single number, the degree of transverse coherence can be introduced as [68, 69]

$$\zeta(\omega) = \frac{\int |W(\mathbf{r}_1, \mathbf{r}_2; \omega)|^2 \, \mathrm{d}\mathbf{r}_1 \mathrm{d}\mathbf{r}_2}{\left(\int S(\mathbf{r}; \omega) \mathrm{d}\mathbf{r} \right)^2}. \tag{2.31}$$

According to its definition the values of the parameter $\zeta(\omega)$ lie in the range $0 \leq \zeta(\omega) \leq 1$, where $\zeta(\omega) = 1$ and $\zeta(\omega) = 0$ characterizes fully coherent and incoherent radiation, respectively. It will be shown later (Equation (2.64)) that the degree of transverse coherence, $\zeta(\omega)$, in many cases has the same meaning as the coherent fraction of the beam in Equation (1.3).

In the following we will apply the concept of correlation functions to planar secondary sources [46], where the CSD of the radiation field is given in the source plane at z_0 with the transverse coordinates $\mathbf{s}$, $W(\mathbf{r}_1, \mathbf{r}_2; \omega) = W(\mathbf{s}_1, \mathbf{s}_2, z_0; \omega)$ (see Figure 2.3). The propagation of the CSD from the source plane at z_0 to the plane at a distance z from the source is governed by the following expression [46]

$$W(\mathbf{u}_1, \mathbf{u}_2, z_1; \omega) = \iint W(\mathbf{s}_1, \mathbf{s}_2, z_0; \omega) P_z^*(\mathbf{u}_1, \mathbf{s}_1; \omega) P_z(\mathbf{u}_2, \mathbf{s}_2; \omega) \mathrm{d}\mathbf{s}_1 \mathrm{d}\mathbf{s}_2, \tag{2.32}$$

where $W(\mathbf{s}_1, \mathbf{s}_2, z_0; \omega)$ is the CSD in the source plane z_0, $P_z(\mathbf{u}, \mathbf{s}; \omega)$ is the propagator. The integration is performed in the source plane. Formula (2.32) is a solution of the set of Helmholtz equations (2.27). Depending on the propagation geometry the Huygens-Fresnel (2.4), Fresnel (2.6) or Fraunhofer (2.9) propagator can be used. The propagation of the CSD through a thin optical element can be described by a transmission function $T(\mathbf{u}, \omega)$ (2.10) [70]

$$W(\mathbf{u}_1, \mathbf{u}_2, z, \omega) = W(\mathbf{u}_1, \mathbf{u}_2, z, \omega) T^*(\mathbf{u}_1, \omega) T(\mathbf{u}_2, \omega). \tag{2.33}$$

2.3.2 Coherent mode representation of correlation functions

Due to the fact that second order correlation functions (2.14,2.26) are defined at two positions $\mathbf{r}_1$ and $\mathbf{r}_2$, it is clear that a numerical implementation of these functions may be difficult due to the high dimensionality of the problem. For fully coherent radiation, however, an analysis in the frame of statistical optics is not required. The correlation functions may be replaced by the product of the electromagnetic field at positions $\mathbf{r}_1$ and $\mathbf{r}_2$ [46]. This field depends on one spatial component $\mathbf{r}$ only and the dimensionality is reduced in this case. One might ask the question, whether a similar treatment can be applied to partially coherent fields. An affirmative answer to this question was given by Wolf [71].

It has been shown, that under very general conditions, one can represent the CSD of a partially coherent, statistically stationary field of any state of coherence as a sum of independent coherent modes[6]

$$W(\mathbf{r}_1, \mathbf{r}_2; \omega) = \sum_j \beta_j(\omega) E_j^*(\mathbf{r}_1, \omega) E_j(\mathbf{r}_2, \omega), \tag{2.34}$$

where $\beta_j(\omega)$ and $E_j(\mathbf{r}, \omega)$ are the eigenvalues and eigenfunctions from the Fredholm integral equation of the second kind

$$\int W(\mathbf{r}_1, \mathbf{r}_2; \omega) E_j(\mathbf{r}_1, \omega) \mathrm{d}\mathbf{r}_1 = \beta_j(\omega) E_j(\mathbf{r}_2, \omega). \tag{2.35}$$

According to Equation (2.29) we find the spectral density

$$S(\mathbf{r}, \omega) = \sum_j \beta_j(\omega) |E_j(\mathbf{r}, \omega)|^2. \tag{2.36}$$

and the degree of transverse coherence (2.31)

$$\zeta(\omega) = \frac{\sum \beta_j^2(\omega)}{\left(\sum \beta_j(\omega)\right)^2}.$$

The so-called modes[7], $E_j(\mathbf{r}, \omega)$, can be chosen to be statistically independent and to form an orthonormal set $\int E_i^*(\mathbf{r}, \omega) E_j(\mathbf{r}, \omega) \mathrm{d}\mathbf{r} = \delta_{ij}$, where δ_{ij} is the Kronecker delta. Importantly, the mode decomposition of the CSD describing a fully coherent field consists of a single mode [46]

$$W(\mathbf{r}_1, \mathbf{r}_2; \omega) = E^*(\mathbf{r}_1, \omega) E(\mathbf{r}_2, \omega). \tag{2.37}$$

The mode decomposition can be used to propagate partially coherent radiation from the plane at z_0 to a plane at z_1. Substituting Equation (2.34) in the propagation formula (2.32) yields

$$\begin{aligned} W(\mathbf{u}_1, \mathbf{u}_2, z; \omega) = \iint \sum_j \beta_j(\omega) E_j^*(\mathbf{s}_1, z_0; \omega) E_j(\mathbf{s}_2, z_0; \omega) \\ P_z^*(\mathbf{u}_1, \mathbf{s}_1; \omega) P_z(\mathbf{u}_2, \mathbf{s}_2; \omega) \mathrm{d}\mathbf{s}_1 \mathrm{d}\mathbf{s}_2 \end{aligned} \tag{2.38}$$

We interchange the order of summation and integration and find

$$W(\mathbf{u}_1, \mathbf{u}_2, z_1; \omega) = \sum_j \beta_j(\omega) E_j^*(\mathbf{u}_1, z_1; \omega) E_j(\mathbf{u}_2, z_1; \omega), \tag{2.39}$$

where $E_j(\mathbf{u}, z_1; \omega) = \int E_j(\mathbf{s}, z_0; \omega) P_z(\mathbf{u}, \mathbf{s}; \omega) \mathrm{d}\mathbf{s}$ according to (2.3) describes the propa-

[6] The mode decomposition is very similar to the diagonalization of a matrix in the linear algebra.
[7] The term mode is also used for $W_j(\mathbf{r}_1, \mathbf{r}_2; \omega) = \beta_j E_j^*(\mathbf{r}_1, \omega) E_j(\mathbf{r}_2, \omega)$ [46].

gation of a single mode from the plane at z_0 to the observation plane at z_1. This means that each mode can be treated as a classical electromagnetic field and can be propagated using Equation (2.3). According to Equation (2.38) the weights of the modes $\beta_j(\omega)$ remain constant during propagation in free space. The mode decomposition is especially convenient when we propagate highly coherent beams with a small number of modes.

2.3.3 Gaussian Schell-model sources

A useful model to describe the radiation properties of partially coherent sources is the Gaussian Schell-model (GSM) [46]. This model has been applied for the analysis of the radiation field generated by optical lasers [72], third generation synchrotron sources [73, 74, 75, 76, 69] and x-ray free-electron lasers [77, 78, 79].

The CSD of a GSM source positioned in the plane at z_0 is expressed as [46][8]

$$W(\mathbf{s}_1, \mathbf{s}_2; z_0) = \sqrt{S(\mathbf{s}_1)}\sqrt{S(\mathbf{s}_2)}\mu(\mathbf{s}_2 - \mathbf{s}_1), \tag{2.40}$$

where the spectral density and the SDC in the source plane are Gaussian functions

$$\begin{aligned} S(\mathbf{s}) &= S_0 \exp\left(-\frac{s_x^2}{2\sigma_x^2} - \frac{s_y^2}{2\sigma_y^2}\right) \\ \mu(\mathbf{s}_2 - \mathbf{s}_1) &= \exp\left(-\frac{(s_{2x} - s_{1x})^2}{2\xi_x^2} - \frac{(s_{2y} - s_{1y})^2}{2\xi_y^2}\right). \end{aligned} \tag{2.41}$$

Here S_0 is a normalization constant, and the parameters $\sigma_{x,y}$ and $\xi_{x,y}$ define the rms source size and transverse coherence length in the source plane in x- and y- directions, respectively.

The expression of the CSD function in the form of (2.40), is based on the definition of the SDC (2.30). In the GSM the main approximations are

- the source is modeled as a plane two-dimensional source
- the source is spatially uniform, i.e. the SDC $\mu(\mathbf{s}_1, \mathbf{s}_2) = \mu(\mathbf{s}_2 - \mathbf{s}_1)$ depends on $\mathbf{s}_1$ and $\mathbf{s}_2$ only through the difference $\mathbf{s}_2 - \mathbf{s}_1$. Sources characterized by this property are known as Schell-model sources.
- the spectral density, $S(\mathbf{s})$, and the SDC, $\mu(\mathbf{s}_2 - \mathbf{s}_1)$, are Gaussian functions.

It is readily seen from (2.40,2.41) that the CSD of a GSM source can be factorized into two transverse components

$$W(\mathbf{s}_1, \mathbf{s}_2) = W(s_{1x}, s_{2x})W(s_{1y}, s_{2y}), \tag{2.42}$$

[8] In this equation and below we omit the frequency dependence ω for brevity. The GSM will be applied to narrowband radiation, where ω will be the average frequency ω_0.

where

$$W(s_{1x}, s_{2x}) = \sqrt{S_0} \exp\left(-\frac{s_{1x}^2 + s_{2x}^2}{4\sigma_x^2} - \frac{(s_{2x} - s_{1x})^2}{2\xi_x^2}\right) \tag{2.43}$$

and a similar expression for $W(s_{1y}, s_{2y})$.

In the frame of the GSM, the degree of transverse coherence (2.31), also factorizes into x and y components $\zeta = \zeta_x \zeta_y$. For each transverse direction an analytical expression for ζ_x can be found (see Appendix A.2)

$$\zeta_x = \frac{\iint |W(s_{1x}, s_{2x})|^2 \, \mathrm{d}s_{1x} \mathrm{d}_{2x}}{\left(\int W(s_x, s_x) \mathrm{d}s_x\right)^2} = \frac{q_x}{\sqrt{q_x^2 + 4}}, \tag{2.44}$$

where the ratio of the coherence length to the source size

$$q_x = \frac{\xi_x}{\sigma_x} \tag{2.45}$$

is introduced. The value of q_x is also considered as a measure of the degree of transverse coherence of the source [46].

We will see later (2.48,2.50) that other important quantities of a GSM source are the effective distance [69]

$$z_{\mathrm{eff},x,y} = k\sigma_{x,y}\delta_x = 2k\sigma_{x,y}^2 \zeta_{x,y}. \tag{2.46}$$

and the parameter δ defined through [46]

$$\frac{1}{\delta_{x,y}^2} = \frac{1}{4\sigma_{x,y}^2} + \frac{1}{\xi_{x,y}^2}. \tag{2.47}$$

2.3.4 Propagation of Gaussian Schell-model beams in free space

Here we will use the propagation formula (2.32) in Fresnel approximation and calculate the CSD at a distance z from the GSM source described by Equations (2.40,2.41). According to Equation (2.42) the integration in Equation (2.32) can be done for each dimension independently. We will present calculations for one transverse direction, say x, and will drop the subscript x for brevity.

Let us first consider the validity of the Fresnel approximation for GSM sources. The radiation generated by the GSM source should irradiate into a cone of narrow angles. The Fresnel approximation can be applied if these angles satisfy Equation (2.8). We will see later that the angular divergence of a GSM source is given by $\theta = 1/(\delta k)$. Substituting this angle into the Fresnel approximation condition (2.8) we find lower limits for the parameter δ

$$\delta \gg \frac{1}{k}. \tag{2.48}$$

Equation (2.48) may be referred to as the beam condition [46]. Substituting Equation

(2.48) in (2.46) a similar condition for the degree of transverse coherence ζ can be found

$$\zeta \gg \frac{1}{k\sigma}.$$

The last expression shows that only partially coherent source can generate a beam.

There are two important limits of an incoherent and a coherent source. The source is called *incoherent* if its coherence length ξ is much smaller than the source size $\xi \ll \sigma$. From the beam condition (2.48) we find for such a source

$$\delta \approx \xi \gg \frac{\lambda}{2\pi}$$

To satisfy the beam conditions for a spatially incoherent source, the coherence length has to be much larger than the wavelength, i.e. $\sigma \gg \xi \gg \lambda/2\pi$. Otherwise the coherence is too poor to generate beams with small divergence.

In the opposite limit of a spatially *coherent* source $\xi \gg \sigma$ we find from the beam condition (2.48)

$$\delta \approx 2\sigma \gg \frac{\lambda}{2\pi}.$$

To satisfy the beam condition for a spatially coherent source, the source size should be larger than the wavelength, i.e. $\xi \gg \sigma \gg \lambda/2\pi$. Otherwise the divergence is too large due to the diffraction limit.

Assuming the GSM source parameters satisfy the Fresnel conditions, the integration in Equation (2.32) yields the CSD $W(u_1, u_2; z)$ at distance z from the source [80, 81, 46])

$$W(u_1, u_2, z) = \frac{\sqrt{S_0}}{\Delta(z)} \exp\left(-\frac{u_1^2 + u_2^2}{4\Sigma^2(z)} - \frac{(u_2 - u_1)^2}{2\Xi^2(z)} + \frac{ik(u_2^2 - u_1^2)}{2R(z)}\right), \tag{2.49}$$

where $\Sigma(z) = \sigma\Delta(z)$, $\Xi(z) = \xi\Delta(z)$,

$$\Delta(z) = \sqrt{1 + \left(\frac{z}{z_{\text{eff}}}\right)^2} \tag{2.50}$$

is called the expansion coefficient and

$$R(z) = z\left[1 + \left(\frac{z_{\text{eff}}}{z}\right)^2\right] \tag{2.51}$$

is the radius of the curvature of the GSM beam. In Equations (2.50, 2.51) the effective distance z_{eff} defined in Equation (2.46) was used. At that distance the expansion coefficient gives $\Delta(z_{\text{eff}}) = \sqrt{2}$. In the limit of a spatially coherent source, $\zeta = 1$, the effective distance z_{eff} coincides with the Rayleigh length $z_R = 2k\sigma^2$, which is often introduced in the theory of optical Gaussian beams [57]. According to (2.50) the effective distance z_{eff} is a measure of the distance, where near field or Fresnel effects in the propagation

of the radiation are still strong. Distances, which satisfy the condition $z \gg z_{\text{eff}}$, can be considered as the far-field limit[9], where the expansion parameter $\Delta(z) \to z/z_{\text{eff}}$ and the radius $R(z) \to z$ change linearly with the distance z.

Substituting $u_1 = u_2 = u$ in Equation (2.49) we find the spectral density at the distance z

$$S(u,z) = \frac{\sqrt{S_0}}{\Delta(z)} \exp\left(-\frac{u^2}{2\Sigma^2(z)}\right), \tag{2.52}$$

where

$$\Sigma(z) = \sigma\Delta(z) = \left(\sigma^2 + \theta_\Sigma^2 z^2\right)^{1/2} \tag{2.53}$$

is the size (rms) of the x-ray beam at a distance z from the source. In Equation (2.53) θ_Σ is the angular divergence of the beam, which can be written as

$$\theta_\Sigma = \frac{\sigma}{z_{\text{eff}}} = \frac{1}{k\xi}(1 + q^2/4)^{1/2}. \tag{2.54}$$

According to its definition (2.30) and (2.49, 2.52), the SDC at a distance z from the source is given by

$$\mu(u_1, u_2, z) = \exp\left(-\frac{(u_2 - u_1)^2}{2\Xi(z)^2} + \frac{ik(u_2^2 - u_1^2)}{2R(z)}\right), \tag{2.55}$$

where

$$\Xi(z) = \xi\Delta(z) = \left(\xi^2 + \theta_\Xi^2 z^2\right)^{1/2} \tag{2.56}$$

is the coherence length of the beam at the same distance. In Equation (2.56) θ_Ξ is the angular width of the coherent part of the beam and can be written as

$$\theta_\Xi = \frac{\xi}{z_{\text{eff}}} = \frac{1}{k\sigma}(1 + q^2/4)^{1/2}. \tag{2.57}$$

The transverse coherence length $\Xi(z)$ and the beam size $\Sigma(z)$ for different propagation distances z are shown in Figure 2.4. A radiation wavelength of 1 Å and a source size of 50 µm were simulated. Calculations for different values of the degree of transverse coherence between a coherent source $\zeta = 1$ and a rather incoherent source $\zeta = 0.1$ are presented. It is well seen that for a larger degree of transverse coherence ζ the beam is more collimated and the transverse coherence length is larger. The effective distance z_{eff} is smaller for less coherent beams with the same source size, which means that for less coherent beams the linear z dependence of the parameters starts earlier (compare with numerical results in [82]).

One important property of the beams generated by the GSM sources is that at any

[9] The term z_{eff}/z is similar to the Fresnel number introduced in chapter 2.1.

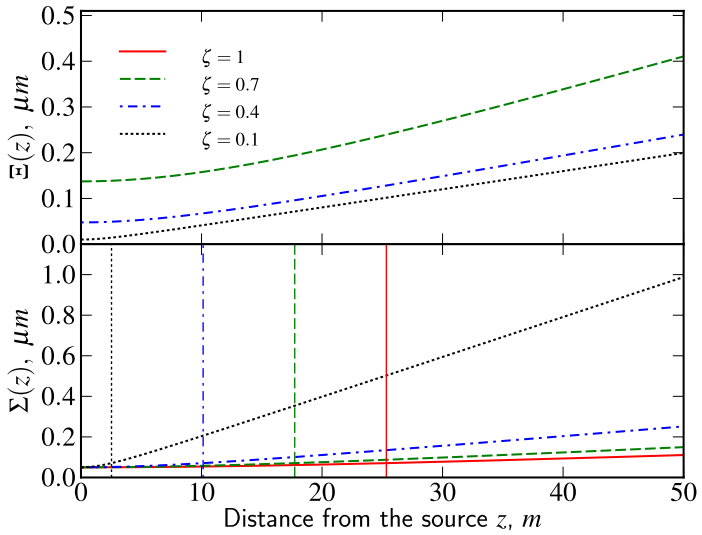

Figure 2.4: The transverse coherence length, $\Xi(z)$, (top) and the beam size, $\Sigma(z)$ (bottom) of the radiation generated by a Gaussian Schell-model source at different distances downstream of the source. A source size of 50 µm and a wavelength of 1 Å were assumed for all curves. The degree of coherence was varied between $\zeta = 1$ and $\zeta = 0.1$. The transverse coherence length for $\zeta = 1$ is $\Xi(z) = \infty$ and is not visible on the plot. The effective distance z_{eff} for different cases is indicated by the vertical lines on the bottom.

distance from the source, the ratio of the coherence length $\Xi(z)$ to the beam size $\Sigma(z)$ has a constant value and is equal to its value at the source

$$q = \frac{\xi}{\sigma} = \frac{\Xi(z)}{\Sigma(z)}. \tag{2.58}$$

As a consequence, the degree of transverse coherence ζ is also constant along the optical axis.

In the limit of a *coherent* source ($q \gg 1$ or $\zeta \approx 1$), we find from Equations (2.54, 2.57)

$$\theta_\Sigma = \frac{1}{2k\sigma}, \quad \theta_\Xi = \frac{1}{2k\sigma} q.$$

In this coherent limit the angular width of the coherent part of the beam exceeds the angular divergence of the beam, which is determined now only by the size of the source, and we are approaching here the limit of a so-called diffraction limited source.

For an *incoherent* source ($q \ll 1$ or $\zeta \ll 1$) we find from Equations (2.54,2.57)

$$\theta_\Sigma = \frac{1}{k\xi}, \quad \theta_\Xi = \frac{1}{k\sigma}. \tag{2.59}$$

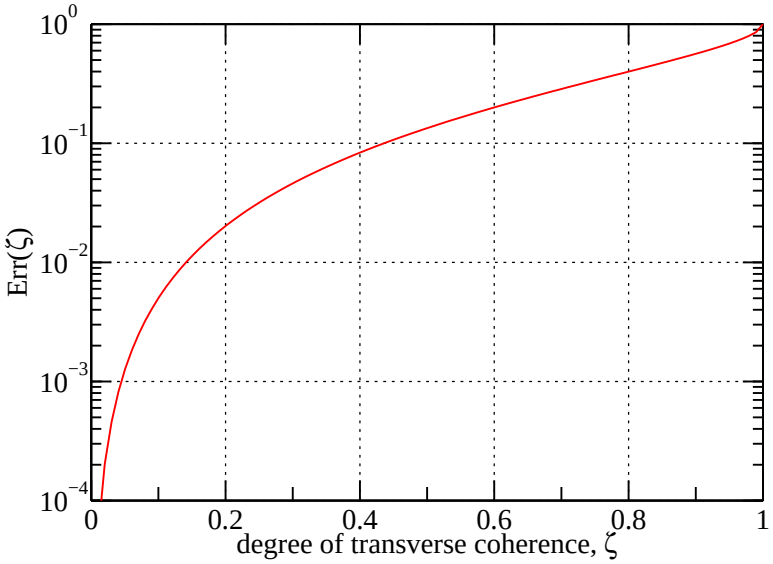

Figure 2.5: The relative error $\mathrm{Err}(\zeta) = [\Xi(z) - \Xi_{\mathrm{inc}}(z)]/\Xi(z)$ between the transverse coherence length determined by the van Cittert- Zernike theorem $\Xi_{\mathrm{inc}}(z)$ and within the GSM $\Xi(z)$ as a function of the degree of transverse coherence ζ.

In this limit Equation (2.56) predicts the same values for the coherence length $\Xi(z)$ at large distances z from the source as the van Cittert-Zernike theorem [83, 84, 46]

$$\Xi_{\mathrm{inc}}(z) = \frac{z}{k\sigma}. \tag{2.60}$$

In the same limit the expression (2.59) gives an estimate for the divergence of an incoherent source, which is determined by the coherence length ξ of the source. So, the coherence length of the source is readily estimated from Equation (2.59)

$$\xi = \frac{\lambda}{2\pi\theta_{\Sigma}}.$$

The van Cittert-Zernike theorem is, in principle, valid only for incoherent sources. However, it gives a reasonable estimate of the transverse coherence length also for partially coherent sources. The relative error $\mathrm{Err} = (\Xi(z) - \Xi_{\mathrm{inc}}(z))/\Xi(z)$ between the value of the transverse coherence length estimated by the van Cittert-Zernike theorem $\Xi_{\mathrm{inc}}(z)$ (2.60) and by the GSM $\Xi(z)$ (2.56) is less than 1 %, unless the degree of transverse coherence is higher than $\zeta = 0.1$ (see Figure 2.5). Even at a value of $\zeta = 0.4$, which can be considered as quite coherent, the van Cittert-Zernike estimation (2.60) concords with the full expression (2.54) within an error of 10 %. A comparison between Equations (2.60) and (2.56) also shows, that the van Cittert-Zernike gives a lower limit for the

transverse coherence length

$$\Xi(z) \geq \Xi_{\mathrm{inc}}(z).$$

In the frame of the GSM, the coherence length of a source of any state of coherence can be expressed conveniently through its emittance

$$\varepsilon = \sigma\theta_{\Sigma}. \tag{2.61}$$

It can be determined by inverting the full expression of the angular divergence of the beam (2.54)

$$\xi = \frac{2\sigma}{\sqrt{4k^2\varepsilon^2 - 1}}. \tag{2.62}$$

The emittance of a GSM source ε can be expressed as well through the degree of the transverse coherence ζ. From Equations (2.54,2.46) we find the emittance of a GSM source in the form

$$\varepsilon = \frac{1}{2k\zeta}. \tag{2.63}$$

Taking into account that for a source of any degree of transverse coherence the values of ζ lie in the range $0 < \zeta \leq 1$ the values of the emittance satisfy $\varepsilon \geq 1/2k = \lambda/4\pi$. For a fully coherent source $\zeta = 1$ and the emittance $\varepsilon_{\mathrm{coh}} = \lambda/4\pi$. This value is the emittance of the diffraction limited Gaussian beam. For an incoherent source $\zeta \to 0$ we find from (2.63) $\varepsilon \gg \lambda/4\pi$. Eventually, writing

$$\varepsilon_{\mathrm{coh}} = \varepsilon \cdot \zeta \tag{2.64}$$

we note, that in the GSM the degree of transverse coherence, ζ, defined as a normalized integral over $|W(u_1, u_2)|^2$ (2.31) is identical to the coherent fraction of the beam noted in Equation (1.3) [69].

2.3.5 Coherent mode representation of a Gaussian Schell-model source

Coherent modes of a GSM source are well known [46]. Due to the fact that the CSD of the source factorizes into two transverse components (2.42), the coherent modes can be determined separately for each direction. The modes E_j and the corresponding occupancies β_j can be found for each direction separately

$$W(s_{1x}, s_{2x}, z_0) = \sum_j \beta_j^x E_j^*(s_{1x}, z_0) E_j(s_{2x}, z_0) \tag{2.65}$$

by solving the Fredholm integral equation of the second kind

$$\int W(s_{1x}, s_{2x}, z_0) E_j(s_{2x}, z_0) \mathrm{d}x_2 = \beta_j^x E_j(s_{1x}, z_0). \tag{2.66}$$

Similar expressions are valid for the y direction. The total CSD is expressed as [85]

$$W(\mathbf{s}_1, \mathbf{s}_2, z_0) = \sum_{j,j'} \beta_{jj'} E^*_{jj'}(\mathbf{s}_1, z_0) E_{jj'}(\mathbf{s}_2, z_0), \tag{2.67}$$

where $E_{jj'}(\mathbf{s}, z_0) = E_j(s_x, z_0) \cdot E_{j'}(s_y, z_0)$ and $\beta_{jj'} = \beta^x_j \beta^y_{j'}$.

Below we again consider one transverse direction and drop the subscript. The solution of the Fredholm integral Equation (2.66) for a GSM source (2.43) can be obtained analytically in the form of the Gaussian Hermite-modes [72, 86]

$$E_j(s) = A_{0j} \cdot H_j\left(\frac{s}{\sigma\sqrt{2\zeta}}\right) \exp\left(-\frac{s^2}{4\sigma^2\zeta}\right), \tag{2.68}$$

where $A_{0j} = (\pi\sigma^2\zeta)^{-1/4}(2^j j!)^{-1/2}$ and $H_j(x)$ are the Hermite polynomials of order j. The intensity of each mode is normalized to unity, i.e. $\int |E_j(s)|^2 \mathrm{d}s = 1$, for all j. Four first modes in the source plane are shown in Figure 2.6 (a).

Within the GSM the eigenvalues are given by a power law

$$\frac{\beta_j}{\beta_0} = \kappa^j, \tag{2.69}$$

where $\kappa = (1-\zeta)/(1+\zeta)$ and $\beta_0 = \sqrt{2\pi\sigma^2 S_0} \cdot (2\zeta)/(1+\zeta)$. The parameter S_0 has the same meaning as in (2.41). The eigenvalues (2.69) of the Fredholm integral equation are, in fact, the relative weights with which different modes contribute to the CSD of the GSM source. The normalized eigenvalues β_j/β_0 for different values of the degree of coherence are shown in Figure 2.6 (b). A logarithmic scale is used to illustrate the exponential decay of the eigenvalues. It is well seen in this figure that for a high degree of coherence $\zeta = 0.7$ a small number of modes contribute to the total radiation field. For lower values of ζ more modes have to be included in the calculations to reproduce correctly the coherence properties. For a fully coherent beam or $\zeta = 1$ only one mode contributes to radiation field ($\kappa = 0$ in Equation (2.69)).

Correlation properties of the radiation field at any distance z from the source can be calculated with the help of expression (2.3) by propagating individual modes $E_j(x, z)$. In case of a GSM source the propagated modes $E_j(x, z)$ at a distance z from the source are described by the following expression [85]

$$\begin{aligned} E_j(x, z) =& A_j \cdot H_j\left(\frac{x}{\Sigma(z)\sqrt{2\zeta}}\right) \exp\left(-\frac{x^2}{4\Sigma(z)^2\zeta}\right) \times \\ & \times \exp\left\{\mathrm{i}[kz - (j+1)\phi_x(z)] + \frac{\mathrm{i}kx^2}{2R(z)}\right\} \end{aligned} \tag{2.70}$$

where $A_j = (\pi\Sigma(z)^2\zeta)^{-1/4}(2^j j!)^{-1/2}$, $\Sigma(z) = \sigma\Delta(z)$ is the beam size at the distance z from the source and $\phi_x(z) = \arctan(z/z_{\mathrm{eff}})$ is the so called Gouy phase [57]. Parameters $\Delta(z)$ and $R(z)$ have the same meaning as in Equations (2.50, 2.51). For $j = 0$ these modes coincide with the expression for a monochromatic Gaussian beam propagating

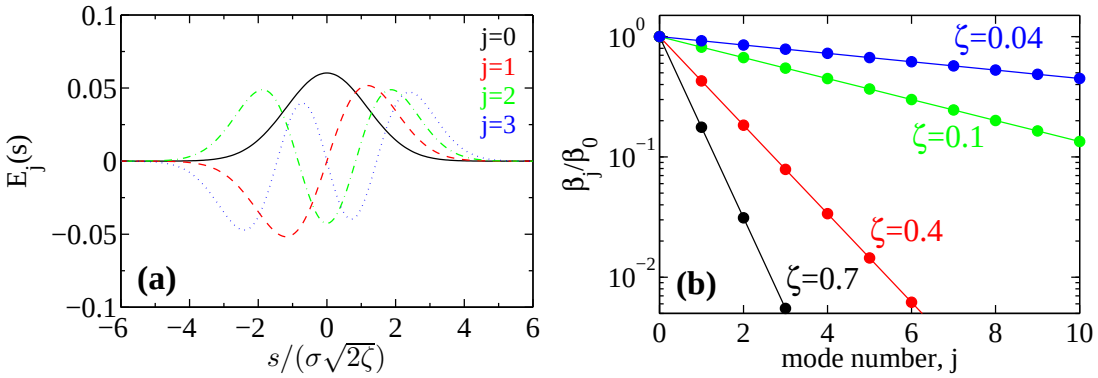

Figure 2.6: (a) First four modes $E_j(s)$ shown as function of the position $s/(\sigma\sqrt{2\zeta})$ normalized to the rms width $\sigma\sqrt{2\zeta}$ of $|E_0(s)|^2$. (b) The ratio of the eigenvalue β_j to the lowest order eigenvalue β_0 as a function of mode number j. Calculations for different values of the degree of coherence ζ are shown.

from a Gaussian source.

As mentioned in the introduction to this chapter the mode decomposition approach becomes most powerful if the number of contributing modes is small. To estimate the number of significantly contributing modes for a spatially coherent source ($\zeta \to 1$) we obtain from Equation (2.69)

$$\frac{\beta_j}{\beta_0} \approx \left(\frac{1-\zeta}{2}\right)^j, \qquad \beta_0 \approx \sqrt{2\pi\sigma^2 S_0}$$

and $\beta_j \ll \beta_0$ for all $j \neq 0$. In the fully coherent limit the source is well characterized by its lowest mode, which is a fully coherent Gaussian beam.

In the opposite limit of an incoherent source ($\zeta \to 0$) we have from (2.69)

$$\frac{\beta_j}{\beta_0} \approx (1-\zeta)^{2j} \approx e^{-2j\zeta} \tag{2.71}$$

and a large number of modes is required for a sufficient description of the source. All modes with a number higher than

$$j = \frac{\ln(100)}{2\zeta} \approx \frac{2.3}{\zeta} \tag{2.72}$$

contribute by less than 1% of the fundamental mode.

Before we proceed we summarize a few important points about the coherent mode decomposition. First of all, we show in Appendix A.6 that the mode decomposition can be performed numerically for a properly sampled representation of a CSD function. In appendix the numerical mode decomposition of the CSD of a Gaussian Schell-model source is compared with the analytical expressions (2.68). The modes determined numerically

coincide with the analytical expressions.

It is also important to note that although the modes are statistically independent upstream from the optical element, they can become statistically dependent behind the optical element. For instance, this may occure when the optical element is a circular aperture. However, the statistical independence of the modes is not necessary for separate propagation of individual modes. In general, one can write

$$W(\mathbf{s}_1, \mathbf{s}_2, z_0; \omega) = \sum_{jl} \beta_{jl}(\omega) E_j^*(\mathbf{s}_1, \omega) E_l(\mathbf{s}_2, \omega), \tag{2.73}$$

where the modes are statistically dependent and cross terms with contributions β_{jl} appear. Substituting this expression in (2.32) we find through a calculation similar to (2.38,2.39)

$$W(\mathbf{u}_1, \mathbf{u}_2, z_1; \omega) = \sum_{jl} \beta_{jl}(\omega) E_j^*(\mathbf{u}_1; \omega) E_l(\mathbf{u}_2; \omega).$$

This means that any mode decomposition of the type of (2.73) can be utilized to propagate the CSD in free space. However, the mode decomposition found by solving the Fredholm integral equation has the convenient property that the spectral density has the form of (2.36). Additionally, due to the work by Wolf [71] it is known that there is at least one coherent mode representation of the CSD function.

It is further worth noticing that due to the degeneracy[10] of some eigenvalues the solution of the eigenvalue problem is not unique. Only the eigenvectors with different eigenvalues are orthogonal. The modes corresponding to the same eigenvalue span a subspace, which is orthogonal to every mode corresponding to a different eigenvalue, and any orthonormal basis of this subspace can be used in the mode decomposition. This degree of freedom is especially apparent in the rather incoherent case. There a large number of modes contribute significantly to the CSD. In the limit of an incoherent source the contribution of all modes is the same, which means that there is only one eigenvalue, at least approximately. In this case any orthonormal basis of the whole space can be used in the mode decomposition. For a discretized CSD the standard basis $\vec{E}_0 = (1, 0, \ldots, 0), \vec{E}_1 = (0, 1, 0, \ldots, 0) \ldots \vec{E}_{N^2} = (0, 0, \ldots, 0, 1)$ leads us to the limit of geometrical optics, where the source is decomposed into a set of incoherent point sources.

The degeneracy occurs also in the GSM if the source size and the transverse coherence length have the same magnitudes in both directions. In this case $\beta_1 = \beta_2$, $\beta_3 = \beta_4 = \beta_5$ etc. and different mode decompositions, including the Gaussian-Hermite modes (2.68) and the Gaussian-Laguerre modes [87], are possible. If no precautions are made in the mode decomposition, a mixture of these two sets appears in the result. In the Appendix A.6 we choose different sampling in the x and y direction, to suppress the circular symmetry, so that the Gaussian-Hermite modes appear in Figure A.1.

[10] If an eigenvalue appears more than once in the mode decomposition the modes corresponding to this eigenvalue are said to be degenerate.

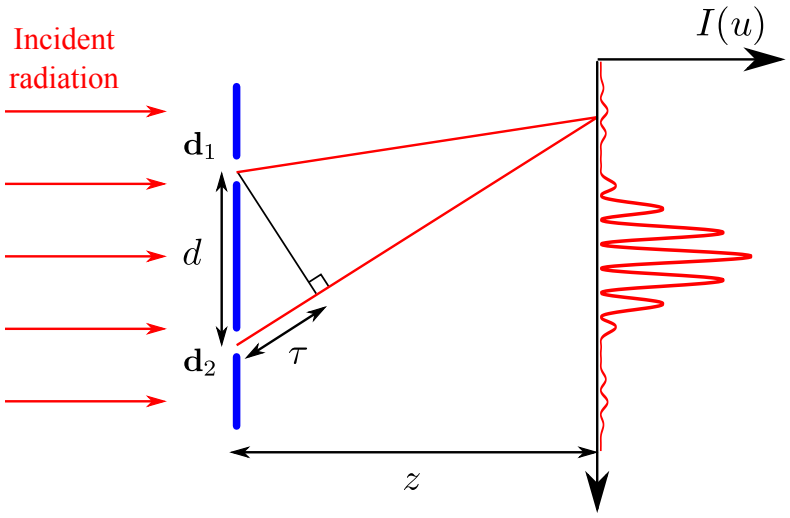

Figure 2.7: A sketch of a double pinhole experiment. Partially coherent radiation is incident on a double pinhole (or double slit). In the observation plane the intensity distribution $I(\mathbf{u})$ is recorded. Interference fringes are observed if the radiation incident on the double pinhole has a non vanishing degree of coherence at the pinhole separation.

2.3.6 Young's double pinhole experiment

As mentioned earlier, the concept of first order correlation functions is associated with interference phenomena. Young's double pinhole experiment [60] is probably the most prominent experiment demonstrating the interference effect and is well suited to illustrate the concept of partial coherence. It is also the most widely used method for characterization of coherence and has been successfully employed with light beams [88], pulsed sources in the XUV energy range [89, 90, 91, 77, 92, 93] and with soft x-rays at synchrotron sources [94] and FELs [79].

In a Young's double pinhole experiment a partially coherent wave-field is incident on an opaque screen with two separated pinholes (see Figure 2.7). If the field transmitted by different pinholes is correlated, then due to the superposition principle the total radiation field in the observation plane will have interference fringes. If these fields are uncorrelated, then the intensities from the individual pinholes sum up and no interference is observed.

To calculate the intensity distribution measured in a double pinhole experiment we start with the field incident on the aperture, which can be described by the CSD $W(\mathbf{s}_1, \mathbf{s}_2; \omega)$. The CSD behind the double pinhole can be found by using Equation (2.33) and the transmission function of a double pinhole[11]

$$T(\mathbf{s}) = T_1(\mathbf{s}) + T_2(\mathbf{s}). \tag{2.74}$$

[11] The aperture transmission function of a pinhole does not depend on the frequency ω, hence we omit ω in $T(\mathbf{s})$ for brevity.

Here $T_{1,2}(\mathbf{s}) = T_D(\mathbf{s}-\mathbf{d}_{1,2})$ is the transmission function of a single pinhole of diameter D (2.11), the pinholes are positioned at $\mathbf{d}_1$ and $\mathbf{d}_2$, and the pinhole separation d is assumed to be larger than the diameter D of the pinholes. Typically, it can furter be assumed that the pinholes are sufficiently small, so that the CSD is constant over their spatial extend. Using this approximation we readily find the CSD behind the double pinhole inserting Equation (2.74) in Equation (2.33)

$$W_{\text{out}}(\mathbf{s}_1,\mathbf{s}_2,\omega) = T_1(\mathbf{s}_1)T_1(\mathbf{s}_2)W(\mathbf{d}_1,\mathbf{d}_1,\omega) + T_2(\mathbf{s}_1)T_2(\mathbf{s}_2)W(\mathbf{d}_2,\mathbf{d}_2,\omega) \\ +2\text{Re}\left(T_1(\mathbf{s}_1)T_2(\mathbf{s}_2)W(\mathbf{d}_1,\mathbf{d}_2,\omega)\right).$$

According to Equation (2.32) the spectral density in the observation plane is given by

$$S(\mathbf{u},\omega) = |E_1(\mathbf{u},\omega)|^2 W(\mathbf{d}_1,\mathbf{d}_1;\omega) + |E_2(\mathbf{u},\omega)|^2 W(\mathbf{d}_2,\mathbf{d}_2;\omega) \\ + 2\text{Re}\left[E_1^*(\mathbf{u},\omega)E_2(\mathbf{u},\omega)W(\mathbf{d}_1,\mathbf{d}_2;\omega)\right], \tag{2.75}$$

where $E_j(\mathbf{u},\omega) = \int T_j(\mathbf{s})P_z(\mathbf{u},\mathbf{s};\omega)\text{d}\mathbf{s}$ for $j = 1,2$ can be considered as the scattered field from an individual pinhole (see Equation (2.3)). For our purposes it is sufficient to calculate these fields in Frauenhofer approximation (2.9), i.e. for pinhole sizes satisfying $D^2/(\lambda z) \ll 1$. Then the field from pinhole one ($j = 1$) and two ($j = 2$) can be expressed as

$$E_j(\mathbf{u},\omega) = \exp\left(ikz + ik\frac{|\mathbf{u}-\mathbf{d}_j|^2}{2z}\right) A_j(\mathbf{u},\omega), \tag{2.76}$$

where [54]

$$A_j(\mathbf{u},\omega) = \left(\frac{kD^2}{2z}\right)\frac{J_1\left(Dq_j/2\right)}{(Dq_j/2)}, \tag{2.77}$$

$q_j = k|\mathbf{u}-\mathbf{d}_j|/z$, and $J_1(u)$ is the Bessel function of the first kind. Substituting Equation (2.76) in Equation (2.75) we find

$$S(\mathbf{u},\omega) = |A_1(\mathbf{u},\omega)|^2 S(\mathbf{d}_1;\omega) + |A_2(\mathbf{u},\omega)|^2 S(\mathbf{d}_2;\omega) \\ + 2A_1(\mathbf{u},\omega)A_2(\mathbf{u},\omega)\text{Re}\left[W(\mathbf{d}_1,\mathbf{d}_2;\omega)e^{i\omega\tau}\right], \tag{2.78}$$

where $\omega\tau$ is the phase of $E_1^*(\mathbf{u},\omega)E_2(\mathbf{u},\omega)$ and

$$\tau = \frac{1}{c}\left(\frac{|\mathbf{u}-\mathbf{d}_2|^2 - |\mathbf{u}-\mathbf{d}_1|^2}{2z}\right) \tag{2.79}$$

is the time delay between the field to reach point $\mathbf{u}$ from pinhole one and two for small angles θ. Equation (2.78) is valid if all angles within the propagation geometry satisfy the Fresnel approximation condition (2.8).

For narrowband radiation considered throughout the thesis the average intensity $I(\mathbf{u}) = \int S(\mathbf{u},\omega)\text{d}\omega$ (see Equation (2.28)) measured during a double pinhole experiment

can be expressed as

$$\begin{aligned} I(\mathbf{u}) &= I_1|A_1(\mathbf{u})|^2 + I_2|A_2(\mathbf{u})|^2 \\ &\quad + 2\sqrt{I_1 I_2}A_1(\mathbf{u})A_2(\mathbf{u})\mathrm{Re}\left[\gamma(\mathbf{d}_1,\mathbf{d}_2;\tau)\right], \end{aligned} \tag{2.80}$$

where $I_j = I(\mathbf{d}_j)$ for $j = 1, 2$. Because the CSD was assumed to be constant across each pinhole, the intensity is also constant across each pinhole. For narrowband radiation the weak ω dependence of the fields $A(\mathbf{u}, \omega)$ can be neglected. In this case it is convenient to rewrite the complex valued CDC $\gamma(\mathbf{d}_1, \mathbf{d}_2; \tau) = |\gamma_{12}(\tau)|e^{i\omega_0\tau+\alpha_{12}(\tau)}$, where $|\gamma_{12}(\tau)|$ and $\alpha_{12}(\tau)$ vary slowly with τ and ω_0 is the average frequency. Finally, the diffraction pattern can be written as (compare with [60, 46])

$$\begin{aligned} I(\mathbf{u}) &= I_1|A_1(\mathbf{u})|^2 + I_2|A_2(\mathbf{u})|^2 \\ &\quad + 2A_1(\mathbf{u})A_2(\mathbf{u})\sqrt{I_1 I_2}\left\{|\gamma_{12}(\tau)|\cos\left[\omega_0\tau + \alpha(\tau)\right]\right\}. \end{aligned} \tag{2.81}$$

The first and the second term in Equation (2.81) are the intensity distributions from pinhole one and two, respectively. The interference phenomena arise from the last term: they are strong if the magnitude of the third term is comparable with the first two terms (see Figure 2.8 (b)). For larger pinhole separations interference is typically weaker (see Figure 2.8 (c,d)) and no interference is observed if the third term vanishes. To determine the functional form of the CDC completely it is necessary to perform double pinhole measurements at different pinhole separations (see Figure 2.8 (a)). The transverse coherence length of the radiation field is defined as a typical width of $|\gamma_{12}(\tau)|$ as a function of the pinhole separation d.

The periodicity of the fringes in the double pinhole experiment is determined by the phase factor $\omega_0\tau$ of the cosine in the third term. In the Fresnel approximation this phase factor is given by (see equation (2.79) and [60])

$$\omega_0\tau = \frac{k\left(|\mathbf{d}_2|^2 - |\mathbf{d}_1|^2\right)}{2z} - \mathbf{d}\cdot\mathbf{q}, \tag{2.82}$$

where the momentum transfer $\mathbf{q}$ is defined as

$$\mathbf{q} = k\frac{\mathbf{u}}{z}.$$

It is important to note, that in Fresnel approximation the time delay τ is constant for all $\mathbf{q}_\perp$ perpendicular to the pinhole separation $\mathbf{d}$, $\mathbf{q}_\perp \cdot \mathbf{d} = 0$.

If the fields from individual pinholes overlap on the detector $A_1(\mathbf{u}) = A_2(\mathbf{u}) =: A(\mathbf{u})$ then

$$\begin{aligned} I(\mathbf{u}) &= (I_1 + I_2)I_D(\mathbf{u}) \\ &\quad \left(1 + 2\frac{\sqrt{I_1 I_2}}{I_1 + I_2}|\gamma_{12}(\tau)|\cos(\omega_0\tau + \alpha(\tau)\right). \end{aligned} \tag{2.83}$$

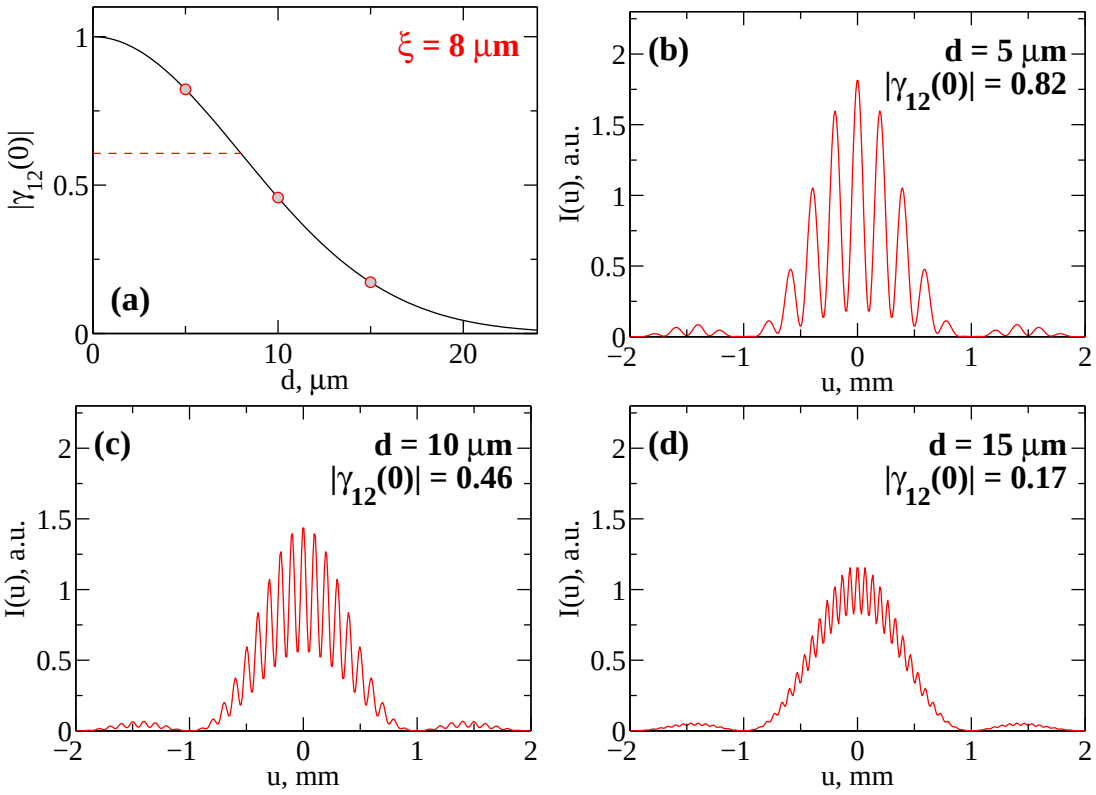

Figure 2.8: Simulated intensity distribution from a double slit experiment for transverse partially coherent radiation. Following parameters were used $\lambda = 1$ nm, slit width $a = 1$ μm, and double slit to detector distance $z = 1$ m. (a) The simulated complex degree of coherence $|\gamma_{12}(0)|$. (b-d) The intensity distribution on the detector for a slit separation d of 5 μm (b), 10 μm (c), and 15 μm (d). The transverse coherence length is defined by the rms width of $|\gamma_{12}(0)|$ (red dashed line in (a)). Temporally coherent radiation has been assumed in this simulation.

where $I_D(\mathbf{u}) = |A(\mathbf{u})|^2$ is the Airy distribution due to diffraction through a round pinhole of diameter D. In this case it is convenient to analyze the visibility [60]

$$\mathcal{V}(\tau) = \frac{I_{\max} - I_{\min}}{I_{\max} + I_{\min}} = \frac{2\sqrt{I_1 I_2}}{I_1 + I_2}\gamma_{12}(\tau). \tag{2.84}$$

A Young's double pinhole experiment can also provide a measurement of the temporal coherence [90, 92, 79]. The CDC $|\gamma_{12}(\tau)|$ as a function of time delay τ (see Figure 2.7) can be analyzed and the coherence time can be defined as a typical width of the CDC $|\gamma_{12}(\tau)|$. According to the Wiener-Khintchine theorem (2.26) the coherence time is inversely proportional to the bandwidth. This is evident in the double pinhole experiment, as the period of the interference fringes varies for different wavelengths present in the

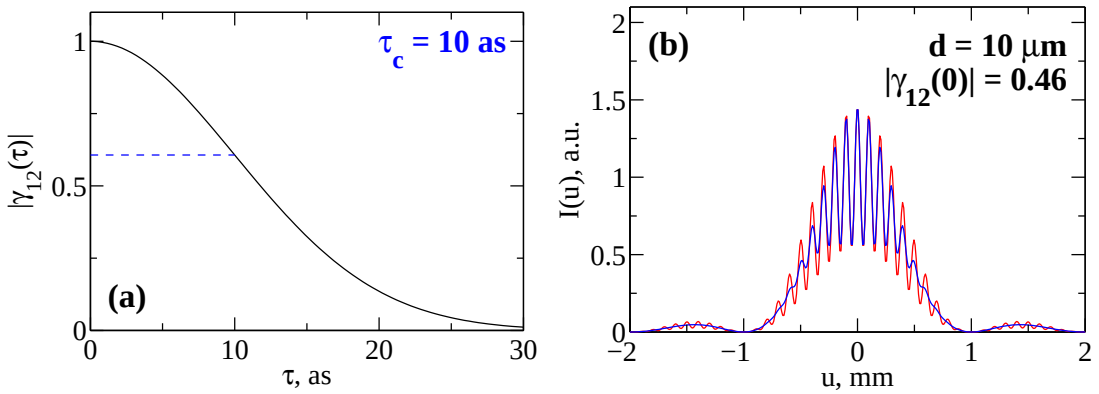

Figure 2.9: Simulated intensity distribution from a double slit experiment. (a) The modulus of the complex degree of coherence $|\gamma_{12}(\tau)|$ as a function of the time delay τ. The coherence time τ_c is shown by the blue dashed line. (b) The intensity distribution in the observation plane calculated with a coherence time of 15 as (blue line). The red line shows the same calculation with full temporal coherence and is identical the plot (c) in Figure 2.8.

spectrum (see Equation (2.82)). In the center of the diffraction pattern fringes from all spectral components are in phase, for large offsets from the optical axis they run out of phase and the interference fringes are smeared at higher off axis angles (blue line in Figure 2.9).

We can estimate time delays, which can be observed in a double pinhole measurement. We take into account interference fringes within the first Airy ring, which have the strongest signal and can be easily analyzed. The maximum momentum transfer $\mathbf{q}$ within this region is given by $|\mathbf{q}_{\max}| = 2\pi/D$, where D is the pinhole diameter. The maximum time delay can be estimated by Equation (2.82) : $\tau_{\max} = \mathbf{q}_{\max} \cdot \mathbf{d}/\omega_0$. In the direction perpendicular to interference fringes it is given by $\tau_{\max} = 2\pi d/(D\omega_0)$ and is proportional to the ratio d/D between the pinhole separation and the pinhole size. Taking into account that the coherence time is on the order of the inverse width of the spectrum Ω we conclude, that in Young's double pinhole experiments time delays larger than the coherence time are accessible if the ratio d/D is larger than the inverse bandwidth ω_0/Ω.

2.4 Correlation functions of non-stationary wave-fields

Up to now we have assumed stationary conditions, which is questionable in many real-world situations. We might think of synchrotron, FEL, and ERL sources, which are pulsed sources and are strictly speaking not stationary. However, at synchrotron sources the pulse duration is much larger than the temporal coherence time of the source, i.e. the source undergoes a large number of fluctuations during a single pulse of synchrotron radiation and all possible realizations of the field are contained within each pulse. As a consequence, the statistical properties of the synchrotron radiation are well described

within the stationary theory. At FEL and ERL sources the pulses are significantly shorter than at synchrotron sources, and a careful investigation is required whether the stationarity condition can be applied also for these sources.

The theory of non-stationary statistical light sources has not found much attention until recently [95]. The two extreme cases of fully coherent and stationary wave fields proved to be sufficient in the description of the radiation up to now. The former approximation is widely used in the theory of optical pulses, where the temporal shape of the pulses is exactly the same for each pulse and the spectral components are said to be completely correlated. In the other extreme of stationary fields, the spectral components are known to be completely uncorrelated [46]. The latter approximation is applied to chaotic sources, including synchrotron sources in the x-ray range. In the intermediate region one speaks of partially coherent pulses [95].

In a series of papers ([95] and references therein) H. Lajunen and colleagues investigated non-stationary fields, in particular, the propagation of these fields in free space. They apply the GSM in the spatial domain as well as in the spectral domain to describe partial coherence between individual spectral components of the field. The propagation of non-stationary fields in free space was also studied in refs. [96, 97]. The authors in [95, 96, 97] considered optical light pulses. We will outline the formalism developed in these works and apply these results to x-ray radiation sources.

2.4.1 Propagation of the wave-field correlation functions in free space

In the description of non-stationary statistical wave-fields the assumption, that the MCF $\Gamma(\mathbf{r}_1, \mathbf{r}_2, \tau)$ depends only on the time difference τ has to be dropped and the full expression for the MCF (2.14) $\Gamma(\mathbf{r}_1, \mathbf{r}_2, t_1, t_2)$ has to be considered. As a consequence the ensemble average (2.15) cannot be replaced by the time average. Furthermore, the average intensity (2.16) becomes a function of time. The CDC (2.17) also depends on the times t_1 and t_2, rather than on the time difference τ. As a consequence, the propagation rules developed for stationary fields have to be revised with respect to non-stationary statistics.

The propagation of the general MCF $\Gamma(\mathbf{r}_1, \mathbf{r}_2; t_1, t_2)$ in free space is governed by the set of wave equations (2.24). To solve this set of equations it is is convenient to introduce a generalized CSD function [95] as a double Fourier transform (similar to Equation (2.26))

$$W(\mathbf{r}_1, \mathbf{r}_2; \omega_1, \omega_2) = \iint \Gamma(\mathbf{r}_1, \mathbf{r}_2; t_1, t_2) e^{i\omega_1 t_1 - \omega_2 t_2} \mathrm{d}t_1 \mathrm{d}t_2. \tag{2.85}$$

Then the wave equations for $\Gamma(\mathbf{r}_1, \mathbf{r}_2; t_1, t_2)$ simplify to a set of two Helmholtz equations for $W(\mathbf{r}_1, \mathbf{r}_2; \omega_1, \omega_2)$ [95]

$$\nabla_i^2 W(\mathbf{r}_1, \mathbf{r}_2; \omega_1, \omega_2) \pm k_i^2 W(\mathbf{r}_1, \mathbf{r}_2; \omega_1, \omega_2) = 0, \tag{2.86}$$

where " $+$ " is used for $i = 1$ and " $-$ " for $i = 2$.

Again we are interested in propagation of the correlation functions from a source positioned at z_0 to the observation plane at a distance z from the source (see Figure

2.3). The propagation formula for the CSD function is expressed as

$$W(\mathbf{u}_1, \mathbf{u}_2, z_1; \omega_1, \omega_2) = \iint W(\mathbf{s}_1, \mathbf{s}_2, z_0; \omega_1, \omega_2) P_z^*(\mathbf{u}_1, \mathbf{s}_1; \omega_1) P_z(\mathbf{u}_2, \mathbf{s}_2; \omega_2) \mathrm{d}\mathbf{s}_1 \mathrm{d}\mathbf{s}_2, \tag{2.87}$$

where the Huygens-Fresnel (2.4), the Fresnel (2.6) or the Fraunhofer (2.9) propagator can be used depending on the geometry. This expression is similar to Equation (2.32), however, here two frequencies ω_1, ω_2 are used in $W(\mathbf{s}_1, \mathbf{s}_2, z_0; \omega_1, \omega_2)$ and the propagators $P_z(\mathbf{u}, \mathbf{s}; \omega)$.

The CSD forms a Fourier transform pair with the MCF

$$\Gamma(\mathbf{r}_1, \mathbf{r}_2; t_1, t_2) = \frac{1}{(2\pi)^2} \iint W(\mathbf{r}_1, \mathbf{r}_2; \omega_1, \omega_2) e^{-i(\omega_1 t_1 - \omega_2 t_2)} \mathrm{d}\omega_1 \mathrm{d}\omega_2. \tag{2.88}$$

The spectral density and the SDC are defined as

$$S(\mathbf{r}, \omega) = W(\mathbf{r}, \mathbf{r}; \omega, \omega)$$

$$\text{and} \qquad \mu(\mathbf{r}_1, \mathbf{r}_2; \omega_1, \omega_2) = \frac{W(\mathbf{r}_1, \mathbf{r}_2; \omega_1, \omega_2)}{\sqrt{S(\mathbf{r}_1, \omega_1) S(\mathbf{r}_2, \omega_2)}}.$$

Possibly the most remarkable difference between propagation of stationary and non-stationary fields is the following. For stationary fields there are no correlations between different frequency components and it is sufficient to consider them separately. In the frame of non-stationary statistics different spectral components might be partially or completely correlated, depending on positions and frequencies [95].

2.4.2 Statistical properties of pulsed sources

In this thesis we are especially interested in a certain type of non-stationary fields, which appear when the source consecutively emits pulses with a finite pulse duration. In this case the MCF can be described as an ensemble average (2.14) [95]

$$\Gamma(\mathbf{r}_1, \mathbf{r}_2; t_1, t_2) = \lim_{N \to \infty} \frac{1}{N} \sum_{n=1}^{N} E_n^*(\mathbf{r}_1, t_1 - t_{0n}) E_n(\mathbf{r}_2, t_2 - t_{0n}), \tag{2.89}$$

where $E_n(\mathbf{r}, t - t_{0n})$ is the field distribution of the nth pulse and t_{0n} is the center of the nth pulse. Each pulse is considered as a single realization of the radiation field and the ensemble average is performed over different pulses. Importantly, different pulses do not overlap in time [97]. Using the Fourier transform of the field[12] $E_n(\mathbf{r}, \omega) =$

[12] Since the pulse duration is finite the field of each pulse as a function of time is integrable $\int |E_n(\mathbf{r}, t)| \mathrm{d}t < \infty$, thus the Fourier transform of $E_n(\mathbf{r}, t)$ exists.

$\int E_n(\mathbf{r},t)e^{-i\omega t}\mathrm{d}t$ we write

$$W(\mathbf{r}_1,\mathbf{r}_2;\omega_1,\omega_2) = \lim_{N\to\infty}\frac{1}{N}\sum_{n=1}^{N} e^{-it_{0n}(w_2-w_1)}E_n^*(\mathbf{r}_1,\omega_1-\omega_0)E_n(\mathbf{r}_2,\omega_2-\omega_0), \quad (2.90)$$

where ω_0 is the average frequency of the radiation.

The average intensity can be expressed as

$$\langle I(\mathbf{r},t)\rangle = \lim_{N\to\infty}\frac{1}{N}\sum_{n=1}^{N}|E_n(\mathbf{r},t-t_{0n})|^2,$$

and describes the spatial and temporal distribution of an averaged pulse. The average spectrum

$$S(\mathbf{r},\omega) = \lim_{N\to\infty}\frac{1}{N}\sum_{n=1}^{N}|E_n(\mathbf{r},\omega-\omega_0)|^2$$

is the spectrum of an averaged pulse.

Statistical properties of non-stationary fields may be quite complicated to characterize. However, the analysis can be significantly simplified using the following approximation

$$\gamma(\mathbf{r}_1,\mathbf{r}_2;t,t+\tau) = \gamma(\mathbf{r}_1,\mathbf{r}_2;\tau). \quad (2.91)$$

Note that this assumption is less restrictive than stationarity, described by

$$\Gamma(\mathbf{r}_1,\mathbf{r}_2;t,t+\tau) = \Gamma(\mathbf{r}_1,\mathbf{r}_2;\tau), \quad (2.92)$$

because Equation (2.91) can be a good approximation for pulsed sources and Equation (2.92) fails in this case due to the pulsed structure of the field intensity. We will use Equation (2.91) in the next chapter to estimate the radiation characteristics of non-stationary x-ray sources.

2.4.2.1 Spectrally Gaussian Schell-model pulses

Similar to the GSM sources described earlier, it is convenient to work with GSM pulsed beams [95]. This model has to be used with caution, as it might be inappropriate to describe in detail the radiation properties of x-ray sources considered in this thesis. However, it can be used for order of magnitude estimations and for predictions whether non-stationary effects play a role at pulsed x-ray sources.

The MCF of a GSM pulsed beam in the source plane at z_0 can be defined as [95, 96][13]

$$\begin{aligned}\Gamma(s_1, s_2, z_0; t_1, t_2) = &\exp\left(-\frac{s_1^2 + s_2^2}{4\sigma^2} - \frac{(s_2 - s_1)^2}{2\xi^2}\right) \\ &\exp\left(-\frac{t_1^2 + t_2^2}{4T^2} - \frac{(t_1 - t_2)^2}{2\tau_c^2} + i\omega_0[t_2 - t_1]\right)\end{aligned} \tag{2.93}$$

where σ is the source size, ξ is the transverse coherence length at the source, T is the pulse duration and τ_c is the coherence time. The expression (2.93) reduces to the stationary case if the pulse duration is very large $T \to \infty$.

The CSD at the source is the double Fourier transform (2.85) of the MCF at the source. The CSD in the far field can be calculated using Equations (2.87,2.9) and the substitution $\Delta\omega = \omega_2 - \omega_1$, $\bar{\omega} = (\omega_1 + \omega_2)/2$

$$\begin{aligned}W(u_1, u_2, z_1; \omega_1, \omega_2) = &\exp\left(i\frac{z}{c}\Delta\omega + i\frac{zc}{2}(q_2^2/\omega_2 - q_1^2/\omega_1)\right) \\ &\exp\left(-\frac{\bar{q}^2}{2}\delta^2 - \frac{\Delta q^2}{2}\sigma^2 - \frac{(\bar{\omega} - \omega_0)^2}{2\Omega^2} - \frac{\Delta\omega^2}{2}T^2\right),\end{aligned}$$

where $q_j = \omega_j u_j/(zc)$ for $j = 1, 2$ and $\bar{q} = (q_1 + q_2)/2$, $\Delta q = q_2 - q_1$. Here δ is defined in Equation (2.47) and Ω is the width of the spectrum, which can be defined through [95]

$$\Omega^2 = \frac{1}{4T^2} + \frac{1}{\tau_c^2}. \tag{2.94}$$

For narrowband light we can approximate using $\omega_{1,2} = \omega_0 + (\bar{\omega} - \omega_0) \mp \Delta\omega/2$

$$\frac{1}{\omega_{1,2}} \approx \frac{1}{\omega_0} - \frac{\bar{\omega} - \omega_0}{\omega_0^2} \pm \frac{\Delta\omega}{2\omega_0^2}. \tag{2.95}$$

In this approximation ω_0 is constant and both $\bar{\omega} - \omega_0$ and $\Delta\omega$ are very small compared with ω_0. This yields for the propagated CSD

$$\begin{aligned}W(u_1, u_2, z_1; \omega_1, \omega_2) = &\exp\left(i\frac{z}{c}\Delta\omega + i\frac{zc}{2\omega_0}(q_2^2 - q_1^2)\right) \\ &\exp\left(-i\frac{(\bar{\omega} - \omega_0)zc}{2\omega_0^2}(q_2^2 - q_1^2) - i\frac{\Delta\omega zc}{4\omega_0^2}(q_2^2 + q_1^2)\right) \\ &\exp\left(-\frac{\bar{q}^2}{2}\delta^2 - \frac{\Delta q^2}{2}\sigma^2 - \frac{(\bar{\omega} - \omega_0)^2}{2\Omega^2} - \frac{\Delta\omega^2}{2}T^2\right),\end{aligned} \tag{2.96}$$

We do not expect coupling between the spectral and spatial components in the real part of equation (2.96). The changes in the q vectors for different frequencies are small, because we use narrowband light. Strong coupling between the spectral and spatial

[13] We define $t_{0n} = 0$ for all pulses. Here, we again use one transverse direction because of the symmetry of the problem.

	Ω/ω_0	wavelength, nm	source size, μm	z, m
Opt. laser	0.13	500	100	0.05
FLASH	0.005	10	160	125
XFEL	10^{-3}	0.1	70	$16 \cdot 10^3$
PETRA III (V, Mono)	10^{-4}	0.1	5	500

Table 2.1: For distances smaller than z no coupling between spectral and spatial part of the correlation functions is expected.

components is expected in the frequency and spatially dependent phase factors. These phase factors increase with propagation distance and are negligible if

$$\frac{(\bar{\omega}-\omega_0)zc}{2\omega_0^2}(q_2^2-q_1^2) \ll 1, \qquad \frac{\Delta\omega zc}{4\omega_0^2}(q_2^2+q_1^2) \ll 1.$$

To estimate the distances for which this factor can be neglected we use the fact that only the frequencies $(\bar{\omega}-\omega_0) \leq \Omega$ and $\Delta\omega \leq 1/T$ are important due to the real part of $W(u_1,u_2,z_1;\omega_1,\omega_2)$. The maximum reasonable momentum transfer can be estimated by $q = 2\pi/d$, where d is the source size. With these asumptions we obtain

$$z \ll 2k_0\frac{\omega_0}{\Omega}\left(\frac{d}{2\pi}\right)^2, \qquad z \ll 4k_0\omega_0 T\left(\frac{d}{2\pi}\right)^2 \tag{2.97}$$

where $k_0 = \omega_0/c$. According to equation (2.94) the following inequality is valid $\Omega T \geq 1/2$, i.e. $2T \geq 1/\Omega$. This means that the first condition in (2.97) is always stronger than the second.

We have not considered the first two phase terms in equation (2.96). The first term is not spatially dependent and can be neglected in the discussion of the coupling between spatial and spectral components. The second term $zc/(2\omega_0)\cdot(q_2^2-q_1^2)$ can be quite large, as it represents the quadratic curvature of the GSM beam. However, the frequency dependent variation of this term is of the order of $(\Omega/\omega_0)^2$ smaller than the term itself and is in particular by a factor of Ω/ω_0 smaller than the limit in equation (2.97). This means this term can also be neglected.

We have evaluated Equation (2.97) for different x-ray sources and summarized the results in table 2.1. It can be readily seen from this table that for present designs of x-ray radiation sources no coupling between spatial and spectral components due to propagation in free space can be expected. Our results also suggest strong coupling for optical lasers, as demonstrated earlier [96].

3 Coherence properties of third and fourth generation x-ray sources the frame of statistical optics

3.1 Synchrotron sources

Synchrotron sources are generally considered as incoherent sources, since different electrons in the electron bunch radiate independently. In the laboratory frame the radiation is confined to a narrow cone of angles $\theta \leq 1/2\gamma$ due to the Lorentz transformation. This confinement implies a finite degree of transverse coherence, as totally incoherent sources radiate into all directions [60] (see also Figure 2.4).

The coherence area $\Delta x \Delta y$ of a synchrotron source can be estimated from Heisenberg's uncertainty principle (2.20) [46]

$$\Delta x \Delta y \geq \frac{\hbar^2}{4 \Delta p_x \Delta p_y}. \tag{3.1}$$

Due to the Einstein - de Broglie relation [54] $p = \hbar k$ the uncertainty in the momentum $\Delta p_{x,y}$ is associated with the source divergence $\theta_{x,y}$ (see Figure 3.1),

$$\Delta p_{x,y} = \hbar k \theta_{x,y}.$$

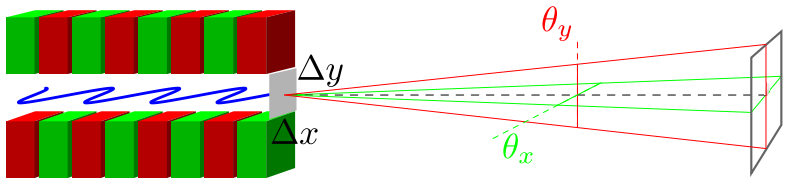

Figure 3.1: Coherence area of a synchrotron radiation source in the source plane. Due to the Heisenberg's uncertainty principle the finite beam divergence implies a non-vanishing coherence area $\Delta x \Delta y$ in the source plane.

According to Equation (3.1) the coherence area in the source plane is given by [1]

$$\Delta x \Delta y = \left(\frac{\lambda}{4\pi}\right)^2 \frac{1}{\theta_x \theta_y}. \tag{3.2}$$

Substituting typical values of the divergence of the source at the third generation synchrotron source PETRA III (see Table 1.1, high-β) in Equation (3.2) we find the minimum transverse coherence length $\Delta y \approx 2$ µm in the vertical $\Delta x \approx 1$ µm in the horizontal direction.

To get a more detailed description of the synchrotron radiation, correlation functions, such as the CSD, have to be considered. Generally, the CSD of the undulator source can be expressed as [82, 98]

$$W(\mathbf{u}_1, \mathbf{u}_2, z) = \langle E^*_{\eta,\mathbf{s}}(\mathbf{u}_1, z) E_{\eta,\mathbf{s}}(\mathbf{u}_2, z) \rangle, \tag{3.3}$$

where $E_{\eta,\mathbf{s}}(\mathbf{u}, z)$ is the field generated by an electron traversing the undulator with an offset $\mathbf{s}$ and a deflection angle η, and z is the distance from the center of the undulator to the observation plane. The disregard of the cross terms of the type $E^*_{\eta_1,\mathbf{s}_1}(\mathbf{u}_1, z) E_{\eta_2,\mathbf{s}_2}(\mathbf{u}_2, z)$ reflects the fact that the fields generated by different electrons are completely uncorrelated. The brackets $\langle \cdots \rangle$ denote the average over the phase space, momentum η and position $\mathbf{s}$, of the electron bunch [98]

$$\langle h_{\eta,\mathbf{s}} \rangle = \int h_{\eta,\mathbf{s}} f(\eta, \mathbf{s}) \mathrm{d}\eta \mathrm{d}\mathbf{s},$$

where $f(\eta, \mathbf{s})$ is the phase space distribution of the electron bunch in the center of the undulator. It is usually considered to have a Gaussian form [98]

$$f(\mathbf{s}, \eta) = \exp\left(-\frac{s_x^2}{2{\sigma_{ex}}^2} - \frac{s_y^2}{2{\sigma_{ey}}^2} - \frac{\eta_x^2}{2{\sigma'_{ex}}^2} - \frac{\eta_y^2}{2{\sigma'_{ey}}^2}\right),$$

where $\sigma_{ex,ey}, \sigma'_{ex,ey}$ is the electron bunch size and the electron bunch divergence in the center of the undulator. The electron bunch size $\sigma_{ex,ey}$ and divergence $\sigma'_{ex,ey}$ can be calculated from the values of the electron bunch emittance $\varepsilon_{ex,y}$ and known β-function of the synchrotron source according to [73]

$$\begin{aligned} \sigma_{ex,ey} &= \sqrt{\varepsilon_{ex,y} \beta_{x,y}} \\ \sigma'_{ex,ey} &= \sqrt{\varepsilon_{ex,y} / \beta_{x,y}}. \end{aligned} \tag{3.4}$$

Below we will consider the situation, when the resonance condition for the undulator radiation (1.4) is satisfied. In this case the normalized electromagnetic field $E_{\eta,\mathbf{s}}(\mathbf{u}, z)$

[1] This formula depends on the definition of the widths and is correct if both uncertainties Δx and θ_x are given as rms widths.

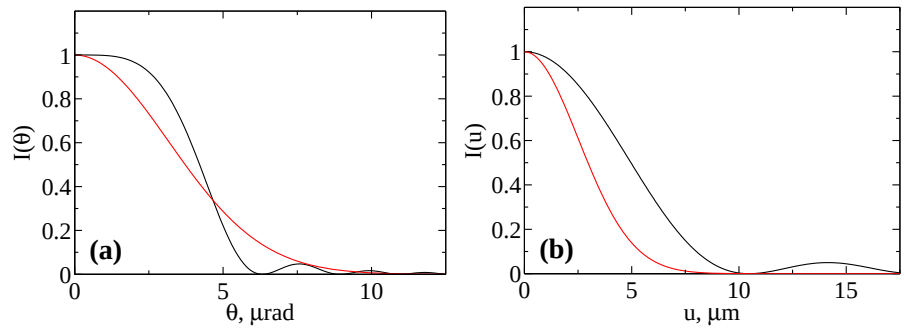

Figure 3.2: The intensity distribution of a single electron traversing the undulator (a) in the far field and (b) in the source plane. The intensity determined through expressions (3.5,3.6) (black lines) and the approximation with Gaussian functions (red line) are shown.

far from the source can be expressed as [98]

$$E_{\eta,\mathbf{s}}(\mathbf{u},z) = \exp\left(ik\frac{|\mathbf{u}-\mathbf{s}|^2}{2z}\right)\mathrm{sinc}\left(\frac{|\mathbf{u}-\mathbf{s}-\eta z|^2 k L_\mathrm{u}}{4z^2}\right), \tag{3.5}$$

where L_u is the undulator length and $\mathrm{sinc}(x) = \sin(\pi x)/(\pi x)$. This field can be considered to be generated at a planar source with the normalized field distribution [98]

$$E_{\eta,\mathbf{s}}(\mathbf{u},0) = -\frac{i}{\pi}\exp\left(i\eta\cdot[\mathbf{u}-\mathbf{s}]\right)\left[\pi - 2\mathrm{Si}\left(\frac{k|\mathbf{u}-\mathbf{s}|^2}{L_\mathrm{u}}\right)\right]. \tag{3.6}$$

The source in this case is positioned in the center of the undulator. In Figure 3.2 the intensity distribution generated by a single electron without an angular and spatial offset ($\eta = 0, \mathbf{s} = 0$) in the far field $|E_{0,0}(\mathbf{u},z)|^2$ (a) and in the source plane $|E_{0,0}(\mathbf{u},0)|^2$ (b) is shown. Often, in describing synchrotron radiation it is sufficient to approximate the intensity distribution with a Gaussian. Then the angular divergence σ_r' and the source size σ_r of the single electron field are the same in the horizontal and vertical direction and may be expressed as [73]

$$\sigma_r = \sqrt{2\lambda L_u}/4\pi, \sigma_r' = \sqrt{\lambda/2L_u} \tag{3.7}$$

The Gaussian curves with the respective widths are shown in Figure 3.2 by red lines.

Equation (3.3) can be considered as the averaging of the radiation characteristics of the single electron $E_{\eta,\mathbf{s}}(\mathbf{u},z)$ by the properties of the electron bunch $f(\eta,\mathbf{s})$. At third generation synchrotron sources typically the following parameter configurations occur

1. If $\sigma_{ex,ey}/\sigma_r \approx 1$ and $\sigma'_{ex,ey}/\sigma'_r \approx 1$, the GSM can be used [69], and the photon source size and divergence are determined from the convolution of the size and divergence of the electron bunch (σ_e, σ'_e) with the intrinsic radiation characteristics of a single

electron (σ_r, σ'_r)

$$\begin{aligned} \sigma_{x,y} &= \sqrt{\sigma_{ex,ey}^2 + \sigma_r^2} \\ \sigma'_{x,y} &= \sqrt{{\sigma'_{ex,ey}}^2 + {\sigma'_r}^2}. \end{aligned} \tag{3.8}$$

2. If the ratio $\sigma_{ex,ey}/\sigma_r \gg 1$ and $\sigma'_{ex,ey}/\sigma'_r \gg 1$, the total beam source size and divergence are Gaussian and the GSM can be applied [98]. The total photon source size and divergence are determined by $\sigma = \sigma_{ex,ey}$, $\sigma' = \sigma'_{ex,ey}$ and the radiation is rather incoherent. This approximation may be utilized to describe the transverse coherence properties of the synchrotron radiation in the horizontal direction, especially for high x-ray energies , as σ_r, σ'_r are proportional to $\sqrt{\lambda}$.

3. On the opposite, if the ratio $\sigma_{ex,ey}/\sigma_r \ll 1$ and $\sigma'_{ex,ey}/\sigma'_r \ll 1$ the radiation characteristics of the total photon beam are dominated by the radiation of a single electron, $\sigma = \sigma_r$, $\sigma' = \sigma'_r$ and the radiation is coherent. As a consequence, the GSM cannot be applied. This description is applicable for the vertical direction of the synchrotron radiation, especially at low x-ray energies.

The GSM has been successfully used to describe the coherence properties of radiation generated at storage rings. In an early paper [99] Kim proposed to describe the brightness (or the Wigner function[2]) of the synchrotron beam as a convolution of the single electron radiation characteristics with the electron bunch properties. He approximated the radiation characteristics of the single electron radiation by Gaussian functions and described the propagation of the brightness in free space. Howells and Kincaid [73] then used the GSM to calculate the CSD of the undulator radiation at the source and at a certain distance downstream of the source. Similar results were reported in [74, 75]. These authors also discussed the limits of the van Cittert-Zernike theorem, which is typically utilized to estimate the transverse coherence properties of the synchrotron radiation. The applicability of the GSM to synchrotron beams was investigated in [82]. It was found that the GSM has its limitations in the description of the undulator radiation in the XUV regime (the calculations were performed for a photon energy of 140 eV).

3.1.1 Transverse coherence properties of the PETRA III source [69]

Here we want to use the results presented in chapter 2.3.3 to estimate the coherence properties of the hard x-ray radiation produced by 3-rd generation synchrotron sources, provided the source parameters (source size and divergence) are known. As an example, we made [69] this calculation for the high brilliance synchrotron source PETRA III, which recently started user operation at DESY. The storage ring is operated at 6 GeV with an emittance as small as $\varepsilon_{ex} = 1$ nmrad [3] in the horizontal direction. Due to 1% coupling, the emittance in the vertical direction is two orders of magnitude lower, $\varepsilon_{ey} = 10$ pmrad.

[2] The Wigner function $B(\mathbf{u}, \mathbf{k})$ is defined as $B(\mathbf{u}, \mathbf{k}) = \int W(\mathbf{u} - \Delta\mathbf{u}/2, \mathbf{u} - \Delta\mathbf{u}/2) e^{i\mathbf{k}\Delta\mathbf{u}} \mathrm{d}\Delta\mathbf{u}$, where W is the CSD.

Before we proceed, let us verify that Fresnel approximation (2.8) used in chapter 2.3.3 is valid for the description of x-ray beams generated by third generation synchrotron sources. The typical wavelength is 1 Å and the propagation distances are about 100 m. The Fresnel approximation (2.8) is well satisfied if the angles θ are much smaller than $\theta_{\max} = 1.5$ mrad. Typically, the angular divergence of the x-ray beam is less than 50 µrad [3, 69]. From these estimates we conclude that the Fresnel approximation is well satisfied for x-ray beams at third generation synchrotron sources. This gives us confidence in using the results presented in chapter 2.3.3 to describe the properties of x-ray radiation from these sources.

The parameters of a 5 m long undulator source at a photon energy of 12 keV are summarized in Table 3.1. Two cases for high-β and low-β operation [3] are considered. The values of the coherence length of the source calculated according to Equations (2.62,3.4,3.7,3.8) vary from 0.6 µm to 2 µm in the horizontal direction and are about 5 µm in the vertical. We can estimate the values of the parameter q (2.45) and the degree of transverse coherence ζ (2.44) of that source. Using tabulated values of the source size we find for the horizontal direction $q_x \approx 0.02$ and for the vertical $q_y \approx 0.8$. For the degree of transverse coherence ζ we obtain $\zeta_x \approx 0.01$ in horizontal and $\zeta_y \approx 0.4$ in vertical direction. These estimates immediately show that in horizontal direction the PETRA III source is rather incoherent with a degree of transverse coherence of about 1 %. In vertical direction the transverse coherence length of the source is comparable with the size of the source and the radiation is highly coherent with a degree of transverse coherence of about 40%. Substituting these numbers into Equations (2.53, 2.56) we find the values of the beam size and transverse coherence length at any distance downstream of the source. These values are listed in Table 3.1 for a distance of $z = 90$ m, that is a

Table 3.1: Parameters of the high brilliance synchrotron radiation source PETRA III for a 5 m undulator [3] (energy E=12 keV, distance from the source $z = 90$ m). The values for the total photon source size and divergence were found using Equation (3.8).

	High-β		**Low-β**	
	x	y	x	y
Source size σ, [µm]	141	5.5	36	6
Source divergence σ', [µrad]	7.7	3.8	28	3.7
Transverse coherence length at the source ξ, [µm]	2.1	4.5	0.57	4.8
Degree of coherence q	0.015	0.82	0.016	0.77
Degree of transverse coherence ζ	0.008	0.38	0.008	0.36
Effective length z_{eff}, [m]	18.3	1.5	1.3	1.6
Beam size at distance z, $\Sigma(z)$, [mm]	0.71	0.34	2.5	0.33
Transverse coherence length at distance z, $\Xi(z)$, [µm]	10	280	40	260

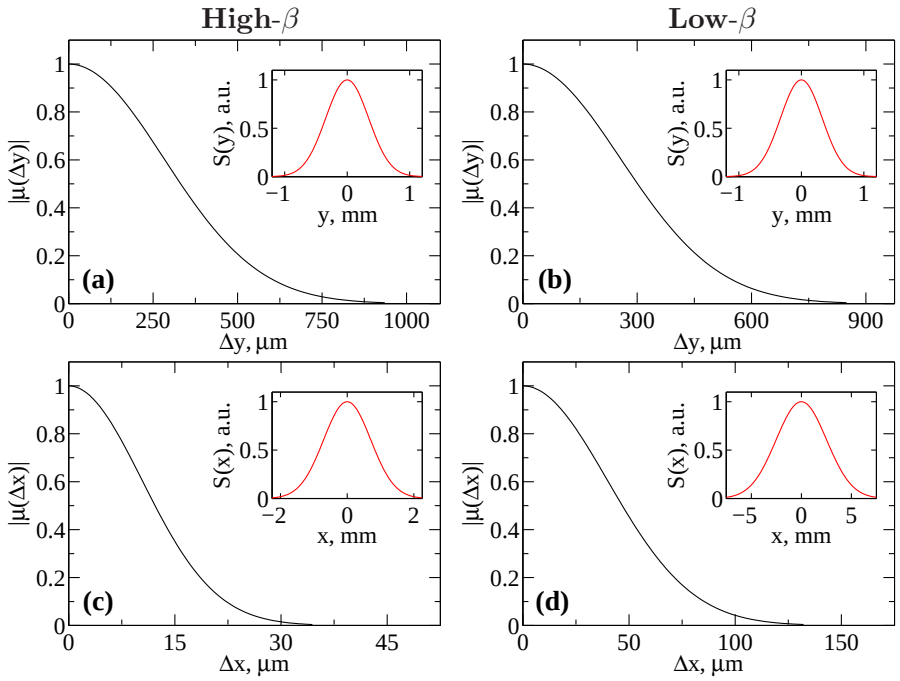

Figure 3.3: The absolute value of the SDC $|\mu(\Delta x)|$ as a function of separation of two points across the beam at a distance of 90 m downstream of the source for high-β (a,c) and low-β (b,d) operation of PETRA III. The spectral density $S(x)$ as a function of the position across the beam calculated at the same distance from the source is shown in the insets. The rms values of the beam size $\Sigma_{x,y}(z)$ and transverse coherence length $\Xi_{x,y}(z)$ at that distance were taken from Table 3.1.

typical distance from the undulator source to experimental stations. We see that at this distance the coherence length varies from 10 μm to 40 μm in horizontal direction and from 260 μm to 280 μm in vertical direction. The product of these values defines the coherence area across the beam within which one can plan experiments with coherent beams. The absolute value of the SDC, $|\mu(\Delta x)|$, (2.55) and the spectral density, $S(x)$, (2.52) at a distance 90 m downstream of the source are presented in Figure 3.3 for high-β and low-β sections of the PETRA III storage ring.

The beam size, $\Sigma_{x,y}(z)$, and the transverse coherence length, $\Xi_{x,y}(z)$, at different distances z from the source were calculated according to Equations (2.53, 2.56) and are presented in Figure 3.4 for high-β operation. These calculations show that in vertical direction the rms values of the coherence length, $\Xi_y(z)$, (black, solid line) are slightly smaller than the rms values of the beam size, $\Sigma_y(z)$, (red, dash line) along the beamline. The effective distance is $z^y_{\text{eff}} = 1.5$ m in vertical direction and for all practical cases all parameters scale linearly with the distance z. As expected, in horizontal direction the transverse coherence length is significantly smaller than the beam size. Due to a large source size the linear z-dependence of the beam parameters in the horizontal direction

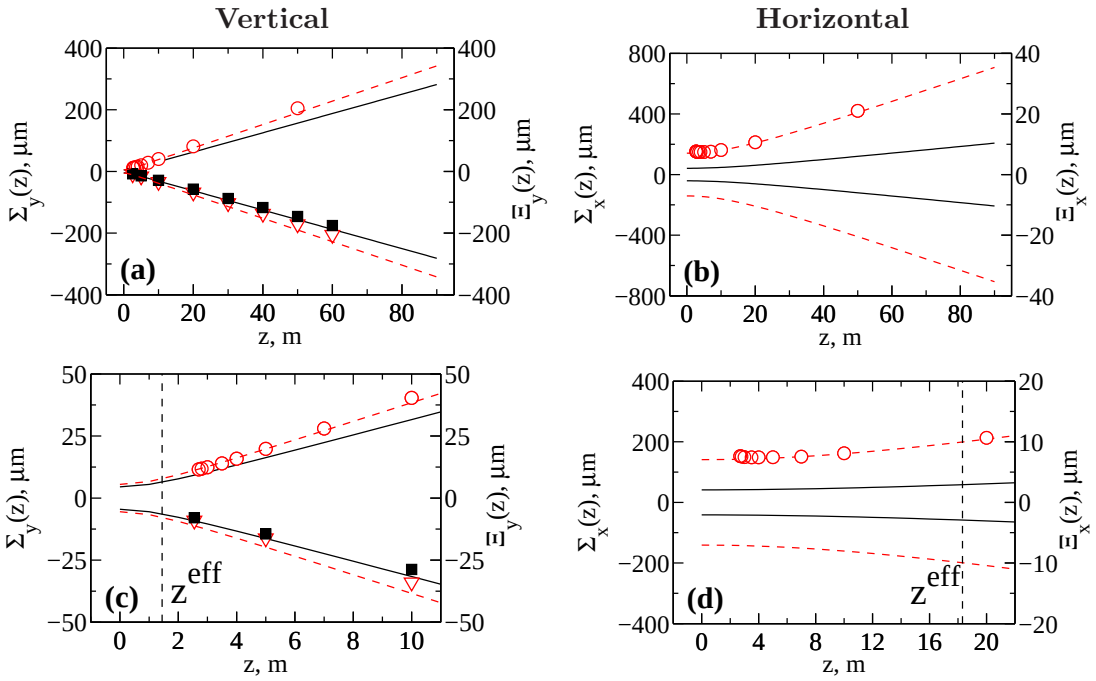

Figure 3.4: The beam size $\Sigma_{x,y}(z)$ (red dashed line) and the transverse coherence length $\Xi_{x,y}(z)$ (black solid line) at different distances z from the source for a high-β section of the PETRA III storage ring. Parameters of the source are taken from Table 3.1. Open circles correspond to calculations performed by the ESRF simulation code SRW [100], open triangles are the beam size and squares are the transverse coherence length obtained from the analytical results of [98]. (a, c) Vertical direction of the beam. (b, d) Horizontal direction of the beam. The vertical dashed line in (c) and (d) correspond to an effective distance z_{eff}. Note, different range for the coherence length comparing to that of the beam size in (b,d).

starts from distances further away from the source. The effective distance z^y_{eff} is about 20 m in this case. Similar results for the low-β operation of the PETRA III source were determined using parameters listed in Table 3.1 and are shown in Figure 3.5.

3.1.1.1 Comparison of the Gaussian Schell-model with other models

We compared our results for the PETRA III five meter undulator source with the calculations performed with the simulation code SRW[3] [100]. The divergence of the beam both in vertical and in horizontal directions is well described by the GSM as compared with the SRW calculations (see Figures 3.4, 3.5).

[3]The SRW calculations were performed by M. Tischer. The code explicitly propagates the electrons through the magnetic structure and calculates the final intensity distribution of the x-ray beam as a sum of the intensities from different electrons.

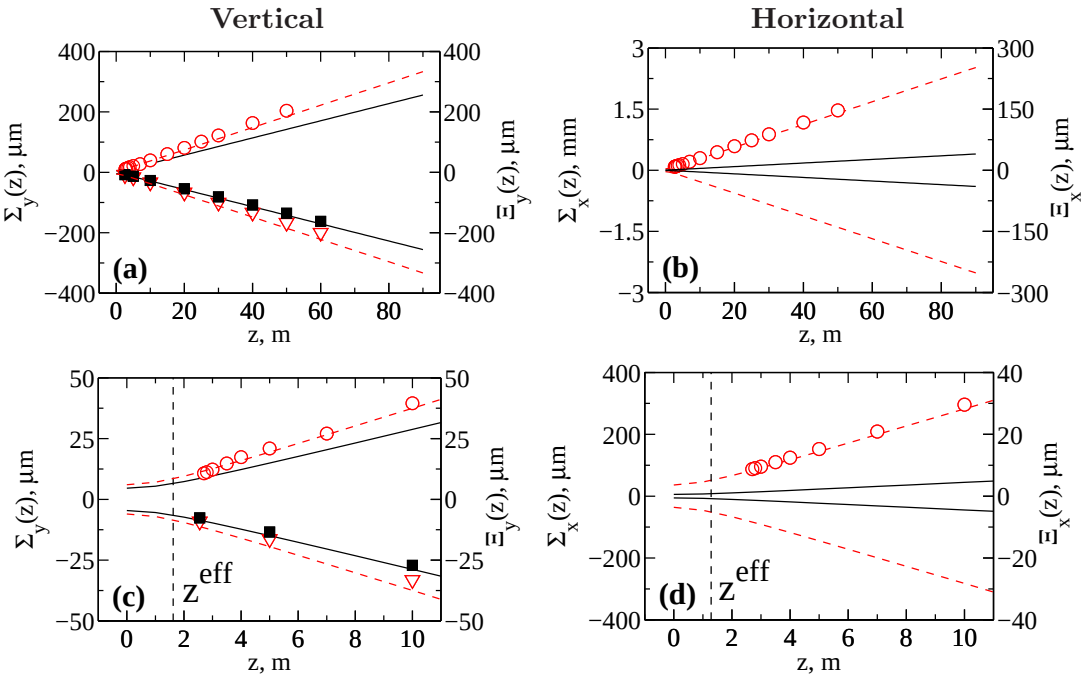

Figure 3.5: The same as in Figure 3.4 for low-β section of the PETRA III storage ring.

We have also compared our simulation results with the analytical formulas [98], where the average $\langle \cdots \rangle$ in Equation (3.3) is explicitly calculated using the known expression for the field (3.5) from a single electron in the undulator resonance condition (1.4). There are two critical dimensionless parameters of the theory [98]

$$D_{x,y} = k\sigma'^2_{ex,ey} L_u \text{ and } N_{x,y} = \frac{k\sigma^2_{ex,ey}}{L_u}. \tag{3.9}$$

For large parameters D, N the electron bunch dominates the radiation properties and the GSM sufficiently reproduces the coherence properties of the x-ray beam. If D, N are small, the effects of single electron radiation dominate and the GSM gives rather poor estimates.

For the five meter undulator at PETRA III, a photon energy of $E = 12$ keV and high-β operation[4] we find $D_x = 15$, $D_y = 1.3$ and $N_x = 243$, $N_y = 0.3$. Because in the horizontal direction these parameters are $D_x \gg 1, N_x \gg 1$ (see Table 3.2) we conclude, that the GSM can be safely used in the horizontal direction. In this limit the analytical results of [98] completely coincide with the description of the source in the frame of the GSM. However, in the vertical direction we find for the same photon energy $D_y \sim 1$, $N_y \sim 1$, and a more careful analysis has to be applied.

To perform a comparison between these two approaches we used the far-field expressions for the CSD function $W(\bar{y}, \Delta y)$ (Equation (65) in [98]) and spectral density $S(y)$

[4]Similar values are found for the low-β operation.

Table 3.2: Parameters of the synchrotron radiation source PETRA III for a 5 m undulator, high-β operation, and different photon energies. Parameters $N_{x,y}$, $D_{x,y}$ are defined in (3.9), $\sigma_{Tx,y}$ and $\sigma'_{Tx,y}$ are the total photon source sizes and divergences, σ_r and σ'_r are the intrinsic radiation characteristics of a single electron. The following electron beam sizes $\sigma_x = 141$ μm, $\sigma_y = 4.9$ μm and divergences $\sigma'_x = 7.1$ μrad, $\sigma'_y = 2.0$ μrad were used in these calculations.

	20 keV	12 keV	6 keV	3 keV
N_x	405	243	122	61
D_x	25	15	7.6	3.8
N_y	0.5	0.30	0.15	0.07
D_y	2.0	1.3	0.63	0.32
σ_{Tx}, [µm]	141	141	141	142
σ'_{Tx}, [µrad]	7.5	7.7	8.4	9.6
σ_{Ty}, [µm]	5.3	5.5	6.1	7.1
σ'_{Ty}, [µrad]	3.2	3.8	5.0	6.7
σ_r, [µm]	2.0	2.6	3.6	5.1
σ'_r, [µrad]	2.5	3.2	4.5	6.4

(Equation (71) in [98]) valid in the limit $D_x \gg 1$ and $N_x \gg 1$. We calculated the SDC $\mu(\bar{y}, \Delta y)$ according to Equation (2.30)

$$\mu(\bar{y}, \Delta y) = \frac{W(\bar{y}, \Delta y)}{\sqrt{S(\bar{y} + \Delta y/2)}\sqrt{S(\bar{y} - \Delta y/2)}}, \tag{3.10}$$

where $\bar{y} = (y_1 + y_2)/2, \Delta y = y_2 - y_1$ and y_1, y_2 are two positions in the vertical direction. Applying these equations to the parameters of the PETRA III source we determined the rms values of the source size $\Sigma_y(z)$ and the coherence length $\Xi_y(z)$ at different distances from the source and compared them with the results from the GSM presented above (see Figures 3.4 (a,c)). This comparison shows very good agreement between two approaches for these energies. As all three approaches (SRW, analytical results [98] and the GSM) yield similar results, we conclude that the approach based on the GSM gives a sufficient description of the PETRA III source at a photon energy of 12 keV.

To determine, for which photon energies the GSM can be applied at PETRA III we compared results from the GSM with the results of [98] for different photon energies. Both calculations were performed for a five meter undulator of the PETRA III source, high-β operation, 90 m downstream of the source at the central position of the beam ($\bar{y} = 0$). As a result the SDC and spectral density for the energy range from 3 keV up to 24 keV are presented in Figure 3.6. As we can see from Figure 3.6, although the parameters satisfy $D_y \leq 1$, $N_y \leq 1$ (see Table 3.2), the difference between two approaches is negligible down to an energy of 6 keV. It becomes more pronounced only at energies of about 3 keV for large separation distances Δy. It is also interesting to note that the transverse coherence length is the same in both approaches down to the lowest

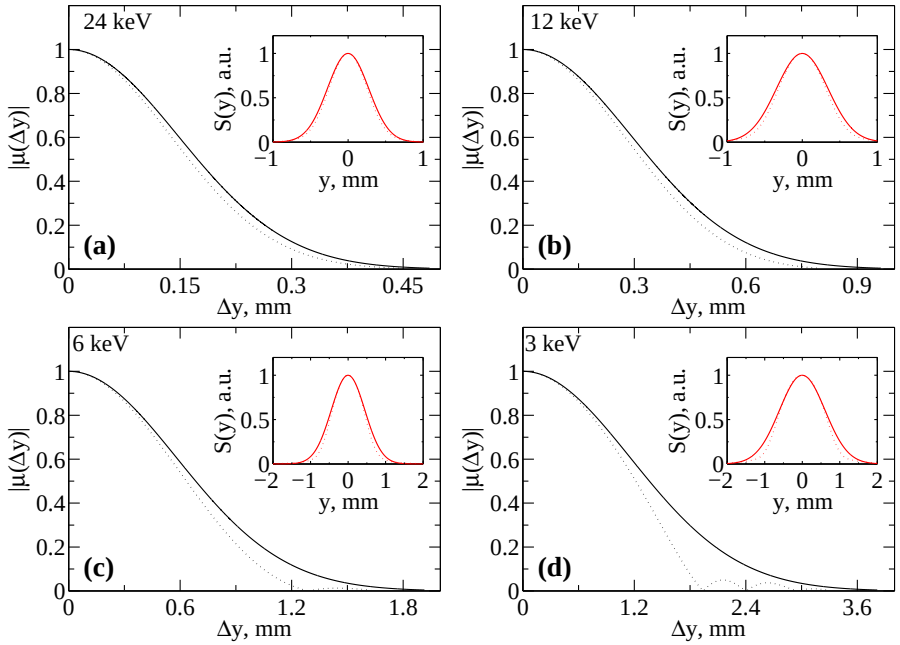

Figure 3.6: The absolute value of the SDC $|\mu(\Delta y)|$ in the vertical direction at the distance 90 m downstream of the source for a high-β operation calculated for different photon energies ((a) 24 keV, (b) 12 keV, (c) 6 keV, (d) 3 keV) using results of [98] (dotted line). The spectral density $S(y)$ (dotted line) calculated in the same conditions is shown in the insets. For comparison, calculations performed in the frame of the GSM are also shown in this figure (solid lines).

energy of 3 keV. At the same time, for this very low energy the effects of the single electron radiation (at photon energy $E = 3$ keV $\sigma_r \geq \sigma_y$ and $\sigma'_r \geq \sigma'_y$) are becoming more pronounced and reveal themselves in the form of oscillations at large separations Δy. A close inspection of Figure 3.6 shows that the GSM slightly overestimates the values of the SDC compared to the results of [98]. We relate this to the fact that at low energies, at the source position, the intensity distribution obtained in the frame of the model [98] contains long tails that effectively produce a larger source size in comparison to a source size obtained by the GSM approach.

In conclusion, our analysis shows that for the high brilliance source PETRA III the GSM can be safely used for the five meter undulator at x-ray energies higher than 6 keV. It will also give a reasonable upper limit estimate of the coherence length for the energies as low as 3 keV. Similar analysis for a shorter undulator of 2 m length, which is also used at PETRA III, shows that both approaches give similar results even for lower energies.

We note here as well that according to the Table 3.2 the approximation $D_x \gg 1$ and $N_x \gg 1$ is no longer valid at energies below 3 keV. Consequently, at these low energies the Equations (65, 71) from [98] cannot be applied for the calculation of the coherence

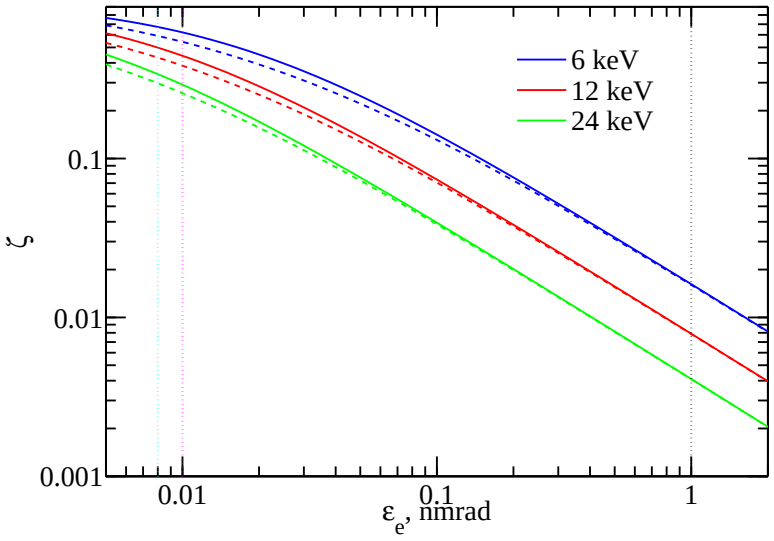

Figure 3.7: The degree of transverse coherence ζ as a function of the electron bunch emittance ε_e in one direction. Calculations with the parameter $a = L_\mathrm{u}/2\pi\beta = 1$ (solid lines) and $a = 0.33$ (dashed lines), typical at PETRA III. The electron bunch emittance at PETRA III in vertical (magenta dotted line), horizontal (black dotted line) direction and (cyan dotted line) at Cornell ERL source (see Table 1.1) are shown.

properties of the five meter undulator source at PETRA III. A more careful treatment using general expressions for the correlation functions should be used in this case (see Appendix A.4). Figure 3.6 (d) was calculated with the formulas derived in this appendix.

3.2 Next generation synchrotron sources

Currently proposed ERLs promise to be superb coherent light sources with a brilliance or coherent flux, which is two orders of magnitude higher than at the state of the art third generation source PETRA III (see Figure 1.1). In this chapter we will analyze coherence properties of ERL sources and compare them with the radiation properties of the existing third generation sources.

To estimate the degree of transverse coherence at ERL sources a similar analysis as was performed for third generation sources can be applied. The main difference between third generation synchrotron sources and ERLs is the electron beam emittance $\varepsilon_{e,x}$ in the horizontal direction. At third generation sources $\varepsilon_{e,x}$ is about two orders of magnitude smaller than the emittance $\varepsilon_{e,y}$ in the vertical direction and at ERLs these quantities are of the same order $\varepsilon_{e,x} \approx \varepsilon_{e,y}$. The electron beam emittance on the order of 10 pm in both directions is planned in the ERL design [9] being studied at Cornell University. This value is similar to the vertical electron beam emittance at PETRA III (see Table 1.1). During the discussion of the coherence properties of the PETRA III source we have

shown, that for such a small electron beam emittance the GSM adequately describes the coherence properties of the undulator radiation for x-ray photon energies larger than 6 keV. For lower energies a more careful treatment is necessary.

We employed the GSM to estimate the degree of transverse coherence for an undulator source as a function of the x-ray photon energy and electron beam emittance. In the frame of this model the emittance of the total photon beam is expressed as (see Equation (2.61))[5]

$$\varepsilon = \sigma\sigma',$$

where σ and σ' are the photon source size and divergence. Substituting Equations (3.4,3.7,3.8) in the last expression we find

$$\varepsilon = (\varepsilon_{\mathrm{coh}} + \varepsilon_e)\sqrt{1 + \frac{b}{a}\cdot\frac{(1-a)^2}{(1+b)^2}}, \tag{3.11}$$

where

$$\varepsilon_{\mathrm{coh}} = \frac{\lambda}{4\pi}, \quad a = \frac{L_{\mathrm{u}}}{2\pi\beta}, \qquad \text{and} \qquad b = \frac{\varepsilon_{\mathrm{coh}}}{\varepsilon_e}.$$

Substituting Equation (3.11) in Equation (2.64) the degree of transverse coherence can be expressed as

$$\zeta = \frac{\varepsilon_{\mathrm{coh}}}{\varepsilon} = \frac{1}{(1+b)}\left(1 + \frac{b}{a}\cdot\frac{(1-a)^2}{(1+b)^2}\right)^{-1/2},$$

For fixed photon energy and emittance of the electron bunch the total photon beam emittance has its minimum value

$$\varepsilon_{\mathrm{min}} = \varepsilon_{\mathrm{coh}} + \varepsilon_e, \tag{3.12}$$

when $a = 1$. At these conditions the degree of transverse coherence takes its maximum value at

$$\zeta_{\mathrm{max}} = \frac{1}{1 + \varepsilon_e/\varepsilon_{\mathrm{coh}}}.$$

For $\varepsilon_e \ll \varepsilon_{\mathrm{coh}}$ the photon beam is fully coherent $\zeta \to 1$. On the opposite, the incoherent limit is described by $\varepsilon_e \gg \varepsilon_{\mathrm{coh}}$ or equivalently by $\zeta \ll 1$. Importantly, the photon beam is transversely not fully coherent even if the electron beam emittance is on the order of the diffraction limit $\varepsilon_{\mathrm{coh}}$. For $\varepsilon_e = \varepsilon_{\mathrm{coh}}$ the degree of transverse coherence is $\zeta = 0.5$.

The degree of transverse coherence ζ_{max} as a function of the electron beam emittance ε_e for x-ray photon energies of 6 keV, 12 keV, and 24 keV is shown in Figure 3.7. In Figure 3.7 we also present the values corresponding to a 5 m undulator source at PETRA III (high-β, vertical). The latter values were calculated according to (3.11) with the corresponding value of parameter $a = L_{\mathrm{u}}/2\pi\beta = 0.33$. We readily see in Figure 3.7, that the transverse coherence for the ideal and realistic value of the parameter a is

[5] As the beam properties are the same in both the horizontal and vertical direction we calculate all values only for one direction and drop the subscript for brevity.

very similar. From our results we conclude, that with the anticipated electron beam parameters x-ray beams with a high degree of coherence can be expected in the hard x-ray regime in both directions. However, the beams at ERL sources will not be fully coherent but will have a total degree of coherence of about 50% at 12 keV.

3.3 Free-electron lasers

Contrary to synchrotron sources the radiation at FELs is intrinsically highly coherent. Different approaches may be used to analyse the coherence properties of FELs. One of them is based on a detailed modelling of the SASE process by performing calculations of non-linear electromagnetic equations at different conditions of operation (linear regime, saturation, *etc.*) [68]. Another possible approach is based on the results of statistical optics (see chapter 2), when the statistics of radiation fields is analysed with very general assumptions about the origin of the radiators. We use the second approach and substitute a real FEL source by an equivalent model planar source, in particular a GSM source. In the same way as optical lasers, FELs based on the SASE principle can be described as sources with a finite number of transverse and longitudinal modes [44, 40]. As we are interested in the coherence properties of FEL beams in the transverse direction, we use a decomposition of the statistical field into a sum of independently propagating transverse modes and show that for a source as coherent as an FEL only a few modes contribute substantially to the total radiation field.

3.3.1 Transverse coherence properties of the European XFEL source [69]

We used this approach to make a realistic and simple estimate of the coherence properties of the radiation at the European XFEL. In particular we analyzed the SASE1 undulator source [43, 68] with the parameters summarized in Table 3.3. We simulated a GSM source using Equations (2.40, 2.41) with a source size of $\sigma = 29.7$ μm and a transverse coherence length of $\xi = 48.3$ μm. The latter parameter was obtained from (2.62) using the values of the source size and angular divergence listed in Table 3.3. With these parameters the CSD, $W(x_1, x_2; z)$, was calculated at a distance of 500 m from the source using the coherent mode decomposition. The eigenvalues β_j and eigenfunctions $E_j(x, z)$ were evaluated from Equations (2.68,2.69). The same CSD may be obtained using Equation (2.49). A distance of 500 m was considered because at that distance first optical elements of the European XFEL are planned [43]. In Figure 3.8 the results of these calculations are presented. An analysis of these results shows that for the parameters of the SASE1 undulator at the European XFEL a small number of transverse modes contribute to the total field (Figure 3.8 (c)). The parameter κ defined in Equation (2.69) has a value of $\kappa = 0.22$ in these conditions, hence the contribution of the first mode is about 20% of the fundamental and the contribution of the fourth mode is below one percent of the fundamental $\beta_4/\beta_0 = \kappa^4 = 2.3 \times 10^{-3}$. Five modes were used in Equation (2.65) for calculations of the CSD $W(x_1, x_2; z)$ (Figure 3.8 (a)). The modulus of the SDC, $|\mu(x_1, x_2, z)|$, and the spectral density, $S(x)$, at that distance are shown in Figure 3.8

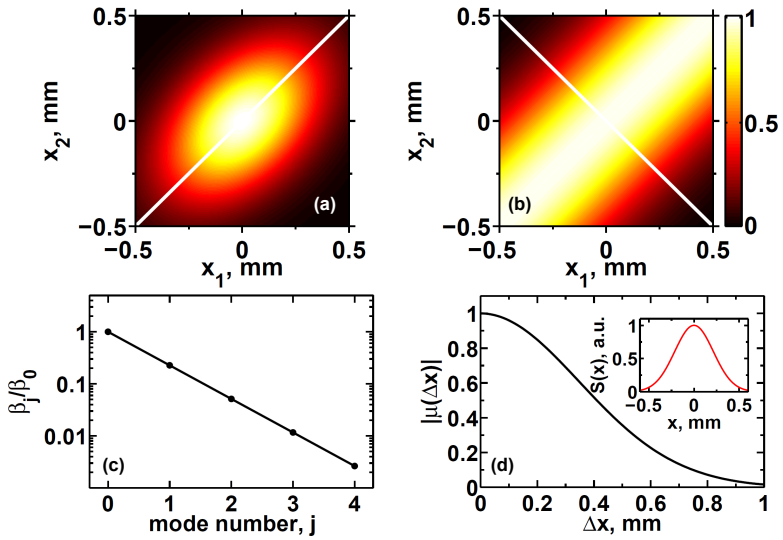

Figure 3.8: Calculations of the coherence properties of the SASE1 undulator at the European XFEL (see Table 3.3) 500 m downstream of the source in the frame of a GSM source. (a) The absolute value of the CSD $|W(x_1, x_2)|$. (b) The absolute value of the SDC $|\mu(x_1, x_2)|$. (c) The ratio β_j/β_0 of the eigenvalue β_j to the lowest order eigenvalue β_0 as a function of mode number j. (d) The absolute value of the SDC $|\mu(\Delta x)|$ taken along the white line in (b). In the inset the spectral density $S(x)$ is shown that is taken along the white line in (a).

(b,d). At a distance of $z = 500$ m downstream of the source we find a coherence length of $\Xi(z) = 348$ µm and a beam size of $\Sigma(z) = 214$ µm.

An analysis of Figure 3.8 (d) shows that our model source, though being highly coherent, cannot be described as a fully coherent source due to contributions of higher modes. This is illustrated in more detail in Figure 3.9, where the SDC, $|\mu(\Delta x)|$, is calculated with a different number of contributing modes. The separations Δx higher than 1 mm were not considered, as the spectral density $S(x)$ significantly reduces at higher separations (see inset in Figure 3.8 (d)). It is readily seen from this figure that only in the case of a single mode contribution will an XFEL beam be fully coherent (Figure 3.9 (a)). As soon as the first transverse mode contributes to the fundamental mode, the SDC, $|\mu(\Delta x)|$, drops to zero at a separation distance of $\Delta x \approx 700$ µm (Figure 3.9 (b)). It again increases up for higher separation distances and reaches the value $|\mu(\Delta x)| = 0.3$ at $\Delta x \approx 1$ mm. This increase in the correlation function is due to the fact that at these distances the contribution of the lowest mode (fundamental in this particular case) is negligible and the correlation properties are determined again by a single mode (the first in this case) (see Figure 2.6 (a)). We note that the spectral density can be described well by three modes (see Figure 3.9 (c)).

The values of the beam size $\Sigma(z)$ and transverse coherence length $\Xi(z)$ at different

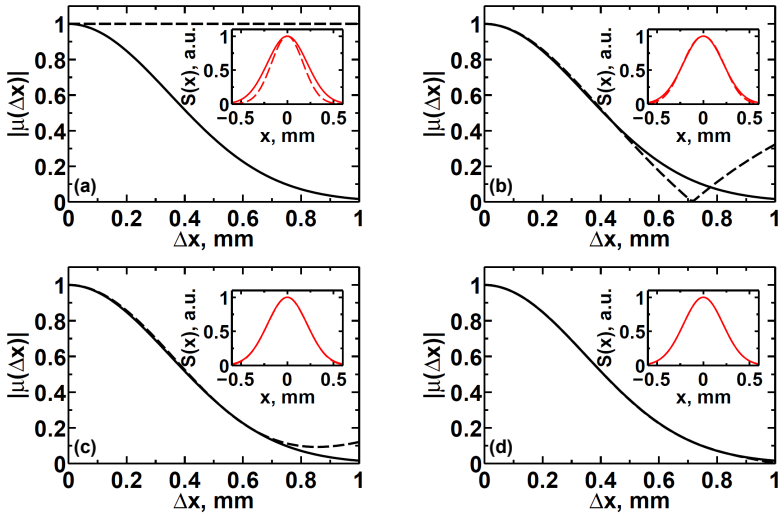

Figure 3.9: Contribution of the higher transverse modes to the radiation field. The absolute value of the SDC $|\mu(\Delta x)|$ and the spectral density $S(x)$ (insets) calculated with one lowest mode (a), two lowest modes (b), three lowest modes (c), and four lowest modes (d) are shown by dashed lines. Solid lines correspond to a full calculation with five modes, which is equivalent to (2.52,2.55) in this case. Calculations were made for the same parameters as in Figure 3.8.

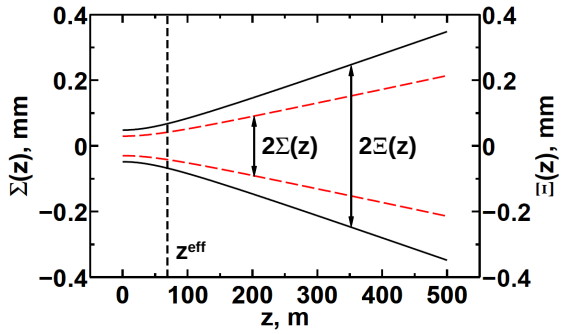

Figure 3.10: The beam size $\Sigma(z)$ (dashed line) and the transverse coherence length $\Xi(z)$ (solid line) at different distances z from the SASE1 undulator of the European XFEL source. Parameters of the source are the same as in Figure 3.8. The vertical dashed line correspond to an effective distance z_{eff}.

distances z from the simulated GSM source are presented in Figure 3.10. Calculations were performed using a coherent mode decomposition (2.65) of the CSD $W(x_1, x_2; z)$ and mode propagation (2.70) at different distances from the GSM source. It can be seen from Figure 3.10 that contrary to the analysis performed for a synchrotron source, here, in the case of the European XFEL, the values of the transverse coherence length $\Xi(z)$

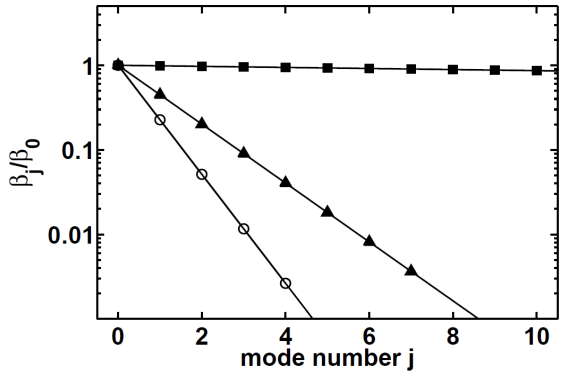

Figure 3.11: The ratio β_j/β_0 of the eigenvalue β_j to the lowest order eigenvalue β_0 as a function of mode number j. Results of the calculations for the parameters of the SASE1 undulator of the European XFEL (open circles), high-β section of the five meter undulator of the PETRA III source in the vertical direction (triangles) and in the horizontal direction (squares) (see Table 3.1).

are higher than the values of the beam size $\Sigma(z)$. The effective distance z_{eff} (2.46) is about 70 m in this case. In other words, for distances $z \gg 70$ m all z-dependencies of parameters, such as the coherence length and the beam size, are linear.

Using the parameter of the SASE1 undulator source (see Table 3.3) we find the degree of transverse coherence (see Equation (2.44)) to be $\zeta_x = 0.63$ in each direction. We estimate a total degree of transverse coherence to be $\zeta = 0.41$ at the European XFEL. This number is smaller than the value $\zeta = 0.65$ obtained by the ensemble average of the wave-fields generated by the code FAST for the parameters of the SASE1 undulator of the European XFEL [68]. We attribute this disagreement to the quality factor [57]. If the beam intensity at the source or in the far field is not Gaussian our estimated value

Table 3.3: Parameters of the SASE1 undulator source at the European XFEL [43, 68] and the FLASH source [47].

	XFEL SASE1 undulator	**FLASH**
Wavelength, fundamental λ, [nm]	0.1	13.7
Source size σ, [μm]	30	68
Source divergence σ', [μrad]	0.43	38
Transverse coherence length at the source ξ, [μm]	48	62
Degree of coherence q	1.6	0.9
Degree of transverse coherence $\zeta_{x,y}$	0.63	0.41
Total degree of transverse coherence ζ	0.41	0.18
Effective length z_{eff}, [m]	70	1.8

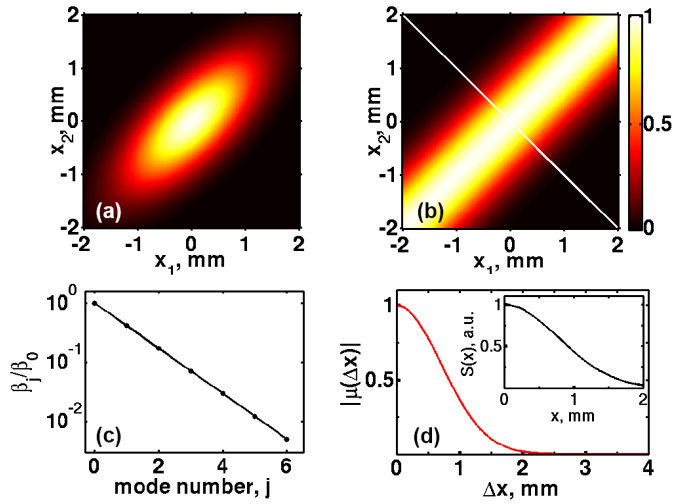

Figure 3.12: The same as in figure 3.8 for the FLASH parameters. Calculations are made in the frame of a GSM source 20 m downstream of the source for a wavelength of $\lambda = 13.7$ nm, when the FEL operates at its saturation.

gives a lower estimate of ζ than calculated with the correct CSD function.

Here, for the description of the transverse coherence properties of FELs, we used the coherent mode decomposition approach. In principle, the same approach may be used for the description of the third generation synchrotron sources. However, being mostly incoherent sources, especially in the horizontal direction, they would require a large number of modes for a sufficient description. This is illustrated in Figure 3.11 where the ratio β_j/β_0 of the eigenvalue β_j to the lowest order eigenvalue β_0 as a function of a mode number j for the PETRA III synchrotron source is presented. For comparison, results of the calculations for the SASE1 undulator of the European XFEL are also shown in the same figure. Our results demonstrate that in the vertical direction correlation functions can be properly described by the contribution of eight modes and in the horizontal direction a large number of modes (about 300, compare with Equation (2.72)) is necessary to describe the coherence properties of the undulator source.

3.3.2 Transverse coherence properties of the FLASH source [77]

We used the same method to estimate coherence properties of the FLASH source. For the calculations we took parameters of FLASH as reported in [47] at a fundamental wavelength of 13.7 nm, which are summarized in Table 3.3. Simulations were made for a GSM source with a source size of $\sigma = 68$ µm, which corresponds to the FWHM of 160 µm reported in [47]. The transverse coherence length $\xi = 62$ µm corresponding to the FWHM angular divergence of 90 µm [47] was determined by Equation (2.62). The CSD at a distance of 20 m downstream of the source was calculated using Equation (2.65) and is presented in Figure 3.12. Similar to European XFEL, at FLASH a small number of transverse modes is sufficient to describe the total field (Figure 3.12 (c)). As

the parameter $\kappa = 0.41$ (see Equation (2.69)), the contribution of the second mode is about 40% of the fundamental, and the contribution of the sixth mode is more than two orders of magnitude smaller than the fundamental $\beta_6/\beta_0 = \kappa^6 \approx 5 \cdot 10^{-3}$. Using the determined CSD we also calculated the values of the spectral density $S(x)$ and the modulus of the SDC $|\mu(\Delta x)|$ (Figure 3.12 (d)). A beam size of $\Sigma(z) = 764$ µm and a transverse coherence length of $\Xi(z) = 715$ µm were found at a distance of $z = 20$ m downstream of the source. The total degree of transverse coherence of the source was determined to be $\zeta = 0.18$.

4 Thin optical elements at third and fourth generation x-ray photon sources

As presented in the preceding chapters, third and fourth generation x-ray sources produce highly brilliant and coherent beams. These sorces are large typically scale facilities with source to experimental station distances of tens to hundreds of meters. Due to the large propagation distances the size of the unfocused beam at the experimental station is in the range of a millimeter. To effectively utilize these coherent beams a large fraction of the photons have to be focused on the sample. Special optical elements are needed to focus x-ray radiation.

Röntgen predicted, that x-rays could not be focused. However, in the end of the last century different sophisticated focusing schemes for x-rays have been developed. Nowadays typically four different techniques at third and fourth generation sources are used.

1. Kirkpatrick-Baez (KB) mirrors utilize the total reflection of x-rays on surfaces. Total reflection appears when the incident angle is below the critical angle, which is in the range of a tenth of a degree for hard x-rays. Due to the curvature of the mirror surface a focus can be achieved. This method has been used to obtain an extremely tight focus $7 \times 20\,\mathrm{nm}^2$ at SPring-8 [102][1]. The KB mirrors are achromatic and can be used for a wide spectrum of photon energies.

2. In the soft x-ray regime Fresnel zone plates [103] can be effectively used. Due to the fact that the index of refraction approaches unity for hard x-rays it is challenging to achieve small foci with Fresnel zone plates in the hard x-ray regime. However, at PETRA III C. David and colleagues recently succeeded in generating a focus with a FWHM of 21 nm in both directions at a photon energy of 10 keV [104].

3. For hard x-rays bent crystals in Bragg geometry can be used as focusing elements as well as spectrometers [105].

4. Refractive lenses similar to conventional lenses for optical light can also be effectively used to focus x-ray radiation, especially in the hard x-ray regime. Because the real part of the refractive index $n(\omega)$ is smaller than unity for x-rays, these lenses are produced by manufacturing holes in material (see Figure 4.1). Lenses of this type are known as compound refractive lenses (CRL) [106, 107].

[1] In situ wavefront correction approach was used to take account of the imperfections of the mirror surface, which is the main difficulty in achieving a small focus size.

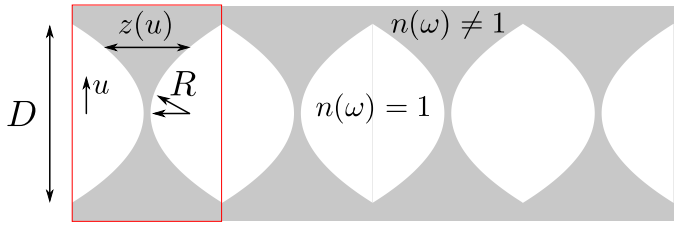

Figure 4.1: Schematic of a CRL. A single lens is marked by the red square. Typically several identical lenses (four in this sketch) are stacked together to improve the focusing properties of the lens. (Adapted [101]).

As an example we will consider here a parabolic CRL [106] in a somewhat greater detail. The complex valued transmission function $T(u,\omega)$ of such a lens can be written in the form [57, 101]

$$T(u,\omega) = B(u,\omega)\exp\left(-i\frac{ku^2}{2f(\omega)}\right). \tag{4.1}$$

The function $B(u,\omega)$ defines the opening aperture of the lens and $f(\omega)$ is the focal distance. Lens imperfections or aberrations, if present, can be taken into account by introducing additional phase factors in $B(u,\omega)$. We restrict ourselves to the aberration free optics and assume that for a thin parabolic lens the opening aperture function can be described by a Gaussian function

$$B(u,\omega) = B_0\exp\left(-\frac{u^2}{4\Omega_0^2(\omega)}\right), \tag{4.2}$$

where $\Omega_0(\omega)$ is the effective opening aperture of the lens and $0 < B_0 \leq 1$. The parameter B_0 describes the transmission of the lens in its center. The focal distance and the opening aperture of a parabolic lens in the x-ray regime can be estimated from the refractive index [54] $n(\omega) = 1-\delta(\omega)+i\beta(\omega)$. Because $\delta(\omega)$ is positive for x-rays, the lenses are produced by manufacturing holes in low absorbing material (see Figure 4.1). For a double concave parabolic lens the propagation distance of the radiation through the lens is given by $z(u) = u^2/R$, where u is the distance from the center of the lens and R is the radius of curvature of the lens. Comparing the phase accumulated during propagation through the material of the lens with the phase of the exponential in Equations (4.1,4.2)

$$\exp\left(-i\frac{ku^2}{2f(\omega)} - \frac{u^2}{4\Omega_0^2(\omega)}\right) = \exp\left(ikn(\omega)z(u)\right)$$

we find [101]

$$f(\omega) = \frac{R}{2\delta(\omega)}, \qquad \Omega_0(\omega) = \sqrt{\frac{R}{4k\beta(\omega)}}.$$

Low atomic-weight materials are used to reduce the absorption, as $\beta(\omega)$ is small for these materials. Because $\delta(\omega)$ is extremely small for x-ray energies ($\delta(\omega) = 2.3\cdot 10^{-6}$ for

Beryllium at a photon energy of 12 keV) the focal distance $f(\omega)$ of a single lens is quite large. Typically several lenses are stacked together (see Figure 4.1) to reduce the focal distance For N lenses stacked together the focal distance and the opening aperture are given by [106]

$$f(\omega) = \frac{R}{2N\delta(\omega)}, \qquad \Omega_0(\omega) = \sqrt{\frac{R}{4Nk\beta(\omega)}}.$$

The above expressions hold if the total arrangement of lenses fulfils the thin lens approximation.

It is important to note that often the opening aperture of the lens is determined not by $\Omega_0(\omega)$ but rather by the size of the aperture in front of the lens or the size of the lens itself D (see Figure 4.1). As an approximation we introduce the opening aperture as

$$\frac{1}{\Omega^2(\omega)} = \frac{1}{\Omega_0^2(\omega)} + \frac{8\ln(2)}{D^2},$$

where the slit transmission function has been approximated as a Gaussian with the FWHM being the slit width D. This simplification is used to obtain analytic expressions for the propagated coherence functions. Analytic solutions can then easily be used to estimate the performance of optical systems.

4.1 Focusing of partially coherent Gaussian Schell-model beams

The GSM beams have been extensively studied in the optics community. In particular, the propagation of these beams through free space and thin optical elements has been investigated in the Fresnel approximation. The ABCD matrix approach [108] widely used to calculate the propagation of fully coherent Gaussian beams has been extended to the case of the GSM beams [109]. Turunen and Friberg [109] did not consider finite apertures, which are especially important for x-rays. Finite apertures have been introduced later for Gaussian beams [110], however, the incorporation of finite apertures into the ABCD matrix approach for partially coherent radiation has not yet been done yet and seems to be difficult.

Here we will use general results from chapter 2.4.1 to calculate the coherence properties of partially coherent beams at different distances from the focusing lens including the region near the focal plane. In particular, lenses with a finite aperture, which are typically used in the x-ray range, are investigated. We will consider the simple geometry (see Figure 4.2) with the source positioned at z_0 and a single lens at z_1. We aim for the calculation of the transverse coherence properties of the focused beam in the plane at z_2. The focal plane is positioned at z_f.

In general, the propagation of partially coherent radiation through a beamline with a thin optical element can be performed in the following steps.

- The CSD $W(\mathbf{s}_1, \mathbf{s}_2, z_0)$ at the source is defined.

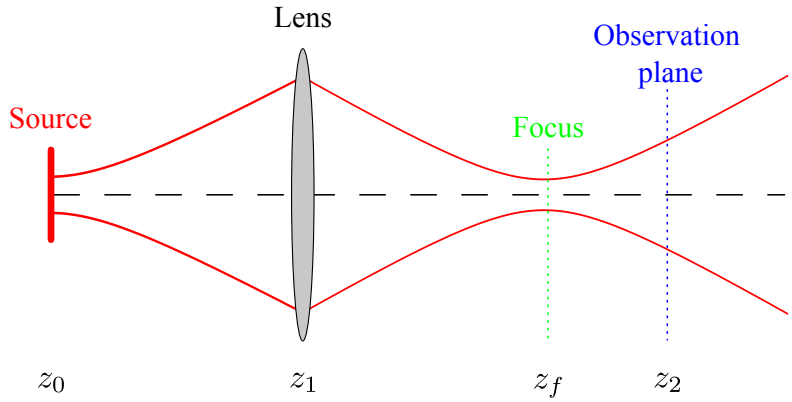

Figure 4.2: The propagation geometry. The source is positioned at z_0, the lens is at z_1 and the observation plane is at z_2.

- The propagation of the CSD $W(s_1, s_2, z_0)$ from the source to the lens can be described by Equation (2.32).
- The propagation of the CSD $W(u_1, u_2, z_1)$ through the focusing element in the thin lens approximation can be described by (2.33).
- The coherence properties at z_2 are obtained using Equation (2.32).

In principle, this procedure can be applied to simulate the propagation of partially coherent radiation through a beamline containing several optical elements, provided all optical elements can be well described in the frame of the thin lens approximation.

We will describe the source at z_0 in the frame of the Gaussian Schell-model with the CSD $W(s_1, s_2, z_0)$ defined in Equations (2.40,2.41) [2] . The CSD function incident on the lens at z_1 is found from Equation (2.49). Substituting the lens transmission function $T(u)$ (4.1,4.2) in Equation (2.33) we find the CSD behind the lens[3]

$$W_{\text{out}}(u_1, u_2, z_1) = \frac{\sqrt{S_0}B_0}{\Delta_1(z_{10})} \exp\left(-\frac{u_1^2 + u_2^2}{4\tilde{\Sigma}_1^2(z_{10})} - \frac{(u_2 - u_1)^2}{2\tilde{\Xi}_1^2(z_{10})} + ik\frac{u_2^2 - u_1^2}{2\tilde{R}_1(z_{10})} \right), \tag{4.3}$$

where

$$\frac{1}{\tilde{\Sigma}_1^2(z_{10})} = \frac{1}{\Sigma_1^2(z_{10})} + \frac{1}{\Omega^2}, \qquad \tilde{\Xi}_1(z_{10}) = \Xi_1(z_{10}), \qquad \frac{1}{\tilde{R}_1(z_{10})} = \frac{1}{R_1(z_{10})} - \frac{1}{f}. \tag{4.4}$$

The distance between the source and the lens is denoted by $z_{10} = z_1 - z_0$ and the parameters $\Sigma_1(z_{10})$, $\Xi_1(z_{10})$, $\Delta_1(z_{10})$ and $R_1(z_{10})$ are the beam size (2.53), transverse

[2] We consider only one transverse direction and drop the subscript for brevity. One transverse direction is sufficient since both transmission function and the CSD are separable in our simulation.

[3] Here narrowband radiation is assumed and the calculations are performed for the average frequency ω_0.

coherence length (2.56), expansion coefficient (2.50), and radius of curvature (2.51) incident on the lens, respectively. The quantities $\tilde{\Sigma}_1(z_{10})$, $\tilde{\Xi}_1(z_{10})$, and $\tilde{R}_1(z_{10})$ describe the same parameters behind the lens. It is worth noting that a thin optical element reduces the beam size $\tilde{\Sigma}_1 \leq \Sigma$, but it does not change the transverse coherence length $\tilde{\Xi}_1 = \Xi_1$. However, the degree of transverse coherence behind the lens (and due to Equation (2.58) in the focus)

$$\zeta_f = \frac{1}{\sqrt{1 + \left(2\tilde{\Sigma}_1/\tilde{\Xi}_1\right)^2}} \tag{4.5}$$

increases due to a smaller beam size, as compared with ζ of the incident beam. In fact, the lens cuts out the coherent part of the beam. Importantly, the change in the curvature $\tilde{R}_1 \neq R_1$ is responsible for the focusing.

By applying the general propagation formula (2.32) the CSD in the focus can be obtained. However, it is more convenient to invert the problem and to use the reciprocity relation in optics [54]. In particular, we think of the CSD behind the lens being generated by a source positioned in the focus at a distance $z_{f1} = z_f - z_1$ from the lens. In other words, we want to determine the parameters of the partially coherent GSM beam knowing its size $\tilde{\Sigma}_1$, transverse coherence length $\tilde{\Xi}_1$ and curvature $\tilde{R}_1$ at a given point, which is the position behind the aperture in our case. Using the result stated in Equation (2.49) we find the distance z_{f1} from the lens to the focus (see Appendix A.5)

$$z_{f1} = -\frac{\tilde{R}_1}{1 + \left(\tilde{R}_1/Z_1\right)^2}, \tag{4.6}$$

where $Z_1 = 2k\tilde{\Sigma}_1^2\zeta_f$ is the parameter which determines the focusing properties of the lens in a certain geometry. It depends on the degree of transverse coherence ζ_f and the beam size $\tilde{\Sigma}_1$ (4.4) behind the lens. From Equation (4.6) it is readily seen, that the distance from the lens to the focus coincides with the focal distance f if a plane wave is incident on the lens and the lens aperture is large.

The CSD in the focus is identical to the CSD of a Gaussian Schell-model source, with the source size σ and transverse coherence length ξ are replaced with the values in the focus, σ_f, ξ_f. These values can be expressed as (see Appendix A.5)

$$\sigma_f = \frac{\tilde{\Sigma}_1}{\sqrt{1 + (Z_1/\tilde{R}_1)^2}} \tag{4.7}$$

$$\xi_f = \frac{\tilde{\Xi}_1}{\sqrt{1 + (Z_1/\tilde{R}_1)^2}}. \tag{4.8}$$

It is possible to calculate the CSD at an arbitrary position z_2 behind the lens, after the position of the focus and the transverse coherence properties in the focus have been obtained. Using the fact that the radiation in the focus can be considered as a planar

GSM source, the CSD at z_2 can be expressed as (see Equation (2.49))

$$W(u_1,u_2,z_2)=\frac{\sqrt{S_0}B_0\Delta_2(z_{2f})}{\Delta_1}\exp\left(-\frac{u_1^2+u_2^2}{4\Sigma_2^2(z_{2f})}-\frac{(u_2-u_1)^2}{2\Xi_2^2(z_{2f})}+ik\frac{u_2^2-u_1^2}{2R_2(z_{2f})}\right), \quad (4.9)$$

where $\Sigma_2(z_{2f})$ is the beam size, $\Xi_2(z_{2f})$ is the transverse coherence length, $R_2(z_{2f})$ is the beam curvature and $z_{2f}=z_2-z_f$ is the distance between the observation plane at z_2 and the focus at z_f. Using the beam parameters in the focus (4.7,4.8) we find

$$\begin{aligned}\Sigma_2(z_{2f}) =&\sigma_f\Delta_2(z_{2f}),\\ \Xi_2(z_{2f}) =&\xi_f\Delta_2(z_{2f}),\\ R_2 =&z_{2f}\left[1+\left(\frac{2k\sigma_f^2\zeta_f}{z_{2f}}\right)^2\right],\\ \Delta_2(z_{2f}) =&\left[1+\left(\frac{z_{2f}}{2k\sigma_f^2\zeta_f}\right)^2\right]^{1/2}.\end{aligned} \quad (4.10)$$

The spectral density and the SDC at any position behind the lens are expressed as

$$\begin{aligned}S(u)&=\frac{\sqrt{S_0}B_0\Delta_2(z_{2f})}{\Delta_1}\exp\left(-\frac{u^2}{2\Sigma_2^2}\right)\\ \mu(u_1,u_2)&=\exp\left(-\frac{(u_2-u_1)^2}{2\Xi_2^2(z_{2f})}+ik\frac{u_2^2-u_1^2}{2R_2(z_{2f})}\right).\end{aligned}$$

In particular setting $z_{2f}=0$ we obtain $S(u)$ and $\mu(u_1,u_2)$ in the focus.

Below we discuss general features as well as limiting cases. It is important to note that only for $f>0$ is a lens able to focus the radiation. Depending on the geometry, three different cases may occur

1. For $f<R_1$ we find from Equations (4.4,4.6) $z_{f1}>0$: The beam is focused by the lens, which means that the focus lies behind the lens. It is readily seen from Equations (4.7,4.8) that the focus is smaller for a higher degree of transverse coherence ζ_f and for a smaller value of $\tilde{R}_1$. The latter corresponds to a smaller focal distance. In the fully coherent limit, $\zeta_f=1$ the results (4.6,4.7) are identical to the formulas known for Gaussian beams [57].

2. For $f=R_1$ we find $z_{f1}=\tilde{R}_1=0$: In this case the wavefront behind the lens is flat and the radiation field behind the lens can be considered as a planar GSM source with size $\tilde{\Sigma}_1$ and transverse coherence length $\tilde{\Xi}_1$.

3. For $f>R_1$ we find $z_{f1}<0$: The divergence of the beam is decreased, however, the beam is not focused. A virtual source is present at the distance $|z_{f1}|$ in front of the lens.

In the following we consider only the first case, as we are interested in the focusing properties of the lens. We briefly outline the limits which may occur. In particular, we analyze the beam size, the transverse coherence length, and the degree of transverse coherence in the focus as a function of the opening aperture of the lens.

A lens with a large aperture

If the aperture of the lens is large compared with the beam size incident on the lens $\Omega \gg \Sigma_1$, the beam size behind the aperture is $\tilde{\Sigma}_1 \approx \Sigma_1$ and we find in the focus (see Appendix A.5 for a detailed derivation. This case was also analyzed in [109].)

$$\sigma_f = M\sigma, \qquad \xi_f = M\xi, \tag{4.11}$$

where

$$M = \left|\frac{f}{z_{10} - f}\right| \left(1 + \frac{z_{\text{eff}}^2}{(z_{10} - f)^2}\right)^{-1/2} \tag{4.12}$$

is the magnification factor. This means that the CSD in the focus is identical to the CSD at the source scaled by the magnification factor M. The ratio $q_f = \xi_f/\sigma_f$ between the transverse coherence length and the beam size is constant everywhere along the optical axis and is determined by the source parameters $q = \xi/\sigma$. The same holds for the degree of transverse coherence ζ. As an important result we note that in the frame of the GSM the focus generated by a thin optical element of infinite aperture is just a magnified $M > 1$ or demagnified $M \leq 1$ image of the source.

If the distance from the source to the lens z_{10} is much larger than the focal distance f and the effective distance z_{eff}, the magnification factor simplifies to

$$M = \left|\frac{f}{z_{10} - f}\right|, \tag{4.13}$$

which can be considered as the geometrical optics limit. The same expression for the magnification factor M is found even for smaller distances z_{10} if the beam is incoherent, $\zeta \to 0$.

A strongly focusing lens with a moderate aperture

Here we consider an especially interesting case for practical purposes : strongly focusing lenses with the size of the focus being much smaller than the size of the beam behind the aperture, $\sigma_f \ll \tilde{\Sigma}_1$. In this limit one may approximate

$$\sqrt{1 + (Z_1/\tilde{R}_1)^2} \gg 1 \quad \text{or equivalently} \quad Z_1 = 2k\tilde{\Sigma}_1^2\zeta_f \gg R_f,$$

Table 4.1: Propagation of partially coherent radiation through a thin lens.

The aperture is much larger than the beam size $\Omega \gg \Sigma_1$

Focus size	$\sigma_f = M\sigma$
Transverse coherence length	$\xi_f = M\xi$
Focus position	$z_{f1} = f + M^2(z_{10} - f)$
Depth of focus	$z^f_{\text{eff}} = M^2 z_{\text{eff}}$
Magnification	$M = \left\lvert \frac{f}{f - z_{10}} \right\rvert \left(1 + \frac{z^2_{\text{eff}}}{(f - z_{10})^2}\right)^{-1/2}$
Effective distance	$z_{\text{eff}} = 2k\sigma^2\zeta$

The aperture is comparable with the beam size $\Omega \leq \Sigma_1$ and $\sigma_f \ll \Omega$

Focus size	$\sigma_f = \sigma_{\text{dl}} \left[1 + \left(\frac{\Omega}{\tilde{\Sigma}_1}\right)^2 + 4\left(\frac{\Omega}{\tilde{\Xi}_1}\right)^2\right]^{1/2}$
Diffraction limit	$\sigma_{\text{dl}} = \frac{z_{f1}}{2k\Omega}$
Transverse coherence length	$\xi_f = \sigma_f q \left[1 + \left(\frac{\Sigma_1}{\Omega}\right)^2\right]$

and find the distance $z_{f1} = -R_f$ from the lens to the focus. The focus size is given by Equation (4.7)

$$\sigma_f = \frac{z_{f1}}{2k\tilde{\Sigma}_1\zeta_f} = \sigma_{\text{dl}} \left[1 + \left(\frac{\Omega}{\Sigma_1}\right)^2 + 4\left(\frac{\Omega}{\Xi_1}\right)^2\right]^{1/2}, \tag{4.14}$$

where we have introduced

$$\sigma_{\text{dl}} = \frac{z_{f1}}{2k\Omega}$$

which is often referred to as the diffraction limited (rms) size of the focus. It can also be written as $\lambda/(4\pi\text{NA})$, where NA is the numerical aperture of the lens.

The coherence length in the focus can be calculated using the ratio $\xi_f/\sigma_f = \tilde{\Xi}_f/\tilde{\Sigma}_1$ from Equations (4.7,4.8)

$$\xi_f = \sigma_f q \left[1 + \left(\frac{\Sigma_1}{\Omega}\right)^2\right], \tag{4.15}$$

where $q = \xi/\sigma$ is the value at the source.

Typically at third generation x-ray sources the beam size of the radiation incident on the lens is much larger than the opening aperture of the lens. This is especially valid for the horizontal direction of synchrotron sources. Assuming $\Omega \ll \Sigma_1$, three limits can be considered.

1. The radiation incident on the lens is highly coherent $\Xi_1 \sim \Sigma_1$ and consequently $\Sigma_1 \gg \Omega$, $\Xi_1 \gg \Omega$. In this limit the focus size is diffraction limited $\sigma_f = \sigma_{\text{dl}}$, as follows from Equation (4.14). From $\Xi_1 \gg \tilde{\Sigma}_1 \approx \Omega$ we conclude $\xi_f \gg \sigma_f$. The beam in the focus is fully coherent.

2. The radiation incident on the lens is rather incoherent $\Xi_1 \ll \Sigma_1$, but its transverse coherence length is larger than the aperture $\Xi_1 \gg \Omega$. In this case, a diffraction limited focus is achieved $\sigma_f = \sigma_{\mathrm{dl}}$. Here, however, the aperture is smaller than in the first case and the amount of transmitted photon flux is reduced. Similar to the first case $\Xi_1 \gg \Omega$ and $\xi_f \gg \sigma_f$, meaning the beam is fully coherent in the focus.

3. The radiation is rather incoherent $\Xi_1 \ll \Sigma_1$ and the coherence length of the incoming radiation is smaller than the aperture $\tilde{\Xi}_1 \ll \Omega$. In this limit we find $\sigma_f = z_{f1}/(k\tilde{\Xi}_1)$. The focus size is no longer determined by the aperture, neither by the size of the beam incident on the lens, it is only determined by the transverse coherence length of the beam incident on the lens. Rewriting $\tilde{\Xi}_1 = z_{f1}/(k\sigma_f)$ it can readily be seen that this case is very similar to the van Cittert-Zernike theorem (2.60). The focus can be considered as a planar incoherent GSM source and the transverse coherence length at a distance z_{f1} from this source is given by $\tilde{\Xi}_1$. In fact, the coherence length is demagnified in the focus by the lens.

We summarize the main results discussed in this section in Table 4.1 (a similar table for fully coherent light can be found in [57]).

4.2 Focusing of x-ray beams at PETRA III beamline P10

We applied the results of the previous section to calculate the coherence properties of the focused beam at PETRA III. In particular the P10 beamline was considered. This beamline is dedicated for coherence applications and a transfocator can be used with different sets of CRLs [111], optimized to meet different user requirements. Additionally, β-function parameters can be varied to even further optimize the beamline conditions.

The layout of the optical system is depicted in Figure 4.3. Three parabolic CRLs manufactured from Beryllium were used. The first CRLs with a radius of 200 µm in both directions was positioned 90 m downstream of the undulator source. Additional two CRLs with a radius of 48 µm in both directions followed at a distance of 74 mm further downstream. The distance between these two CRLs is on the order of a few millimeters and can be neglected. A slit system with a width of 300 µm in vertical and

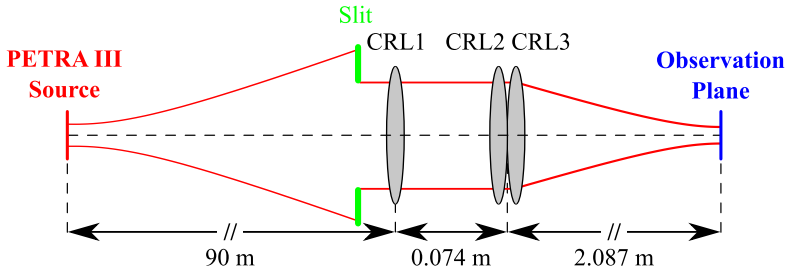

Figure 4.3: The schematic of the CRL arrangement used in the simulation.

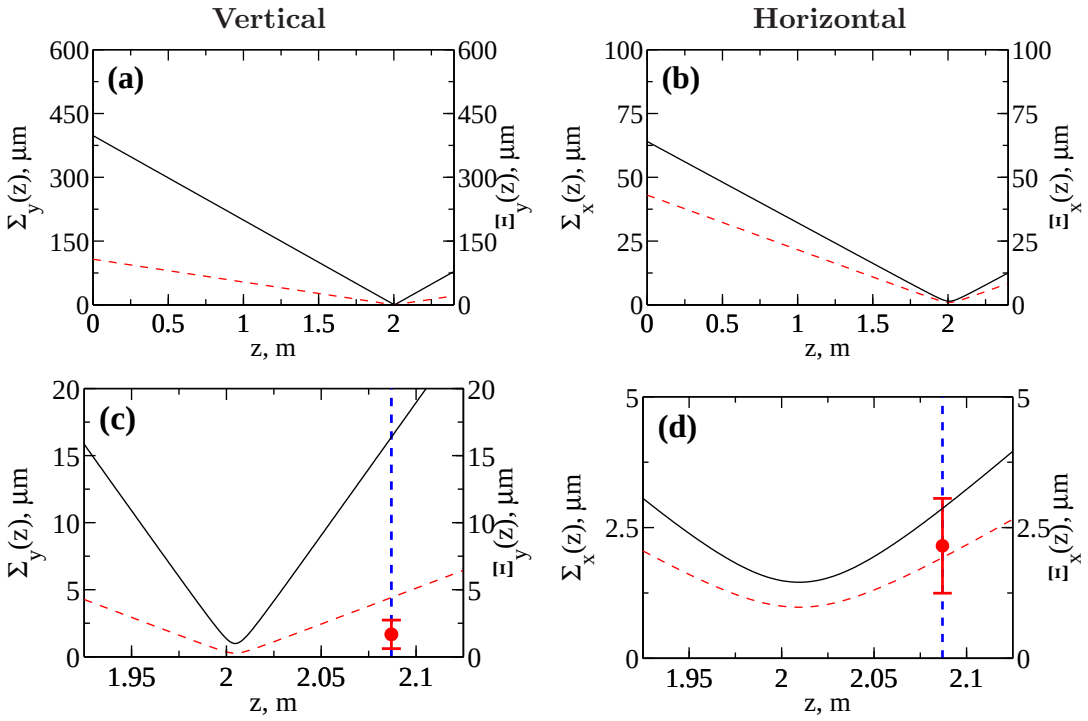

Figure 4.4: Focusing properties of the transfocator with three beryllium lenses at P10 beamline (PETRA III) at an energy of 7.9 keV. The beam size $\Sigma(z)$ (red dashed line) and the transverse coherence length $\Xi(z)$ (black line) are presented. The focusing in the vertical direction (a) and in the horizontal direction (b) are shown. The magnified region near the focal position is presented in (c) and (d). The results from the beam size measurements at the position indicated by the blue dashed line are shown by red dots.

100 μm in horizontal direction was used to cut out the coherent part of the beam (see Figure 4.3).

We described the source in the frame of the Gaussian Schell-model. The beam size and the transverse coherence length in the source plane were obtained from Equations (3.4,3.7,3.8,2.62) for a 5 m undulator and low-β operation of the machine [3]. The photon energy was set to 7.9 keV. Equation (4.9) was used to propagate the radiation through CRL1 and to determine the coherence properties at the position of CRL2/CRL3. The same equation was applied to obtain coherence properties in the observation plane. The beam size $\Sigma(z)$ and the transverse coherence length $\Xi(z)$ are presented in Figure 4.4 as a function of the distance z from the last lens. A focus size of $\sigma_f^y = 0.3$ μm in the vertical and $\sigma_f^x = 1.0$ μm in the horizontal direction were determined. The transverse coherence length $\xi_f^y = 1.0$ μm in the vertical direction and $\xi_f^x = 1.5$ μm in the horizontal direction were found. The transverse coherence length is larger in the horizontal direction, which is a consequence of a smaller slit opening in the same direction. The degree of coherence in

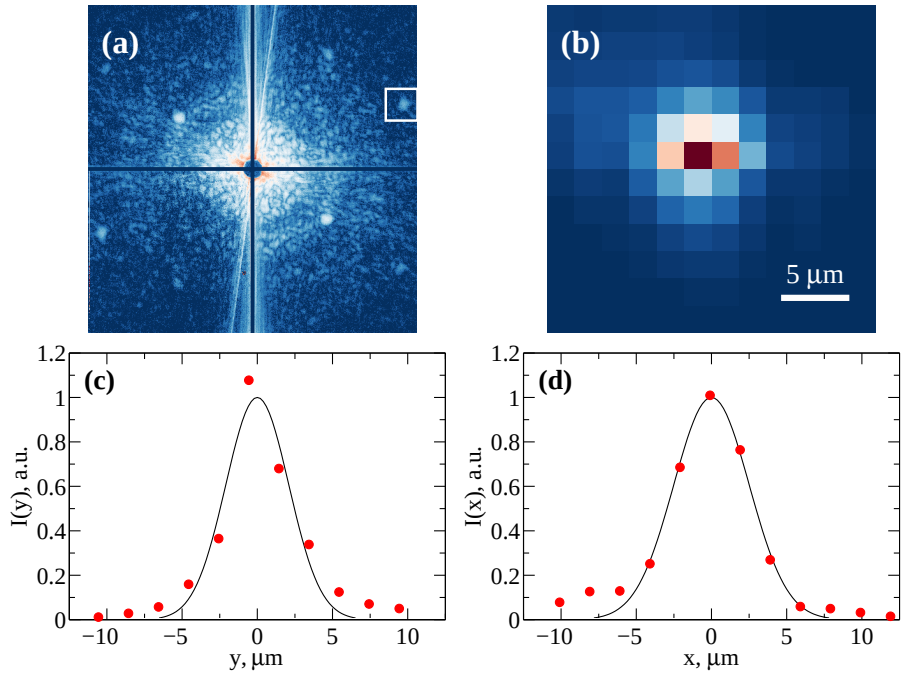

Figure 4.5: Intensity profile measurements using a micrometer size colloidal crystal. (a) A diffraction pattern measured at the central position of the beam. (b) The integrated signal of a Bragg peak (marked by a white box in the top right corner) as a function of the position of the crystal in the beam. The projected intensity profile in the vertical (c) and horizontal (d) direction is shown by red dots. Gaussian fits with widths (rms) of 2.1 ± 0.4 µm (c) in the vertical and 2.5 ± 0.3 µm (d) in horizontal direction are shown by black lines.

the focus was determined to be $\zeta_f^y = 0.88$ in the vertical and $\zeta_f^x = 0.60$ in the horizontal direction. The total degree of coherence is $\zeta_f^x \cdot \zeta_f^y = 0.53$. The transmission of this optical system is about 0.5%, which means that the total intensity in the focus is about two orders of magnitude smaller than the total intensity emitted from the source. However, the flux density in the focus is increased by four orders of magnitude as compared with the unfocused beam.

We compared our simulations with the beam profile measurements, which were performed at P10 using the same optical system as shown in Figure 4.3. The intensity profile was determined by scanning the beam in transverse direction with a colloidal crystal at a distance of 2.09 m downstream of the last lens. For each position the scattered signal was recorded (see Figure 4.5 (a)). The integrated signal of a single Bragg peak (the area marked with a white box in the top right corner of Figure 4.5 (a)) was considered as the beam intensity at the position of the crystal. The beam profile obtained by these measurements is shown in Figure 4.5 (b). The projected beam profiles in the vertical and horizontal directions are also shown in Figure 4.5 (c) and (d), respectively. The pro-

jections are well reproduced by Gaussian functions with widths (rms) of 2.1 ± 0.4 µm in the vertical and 2.5 ± 0.3 µm in horizontal direction. The size of the colloidal crystal used in this measurement was estimated by optical microscopy to be 3 ± 2 µm in all directions[4]. Assuming that the measured beam size is the convolution of the real beam size and the particle size we estimate the real beam size to be $\Sigma_y(z) = 1.7 \pm 1.1$ µm in vertical and $\Sigma_x(z) = 2.2 \pm 0.9$ µm in horizontal direction.

For comparison, the measured beam sizes in the vertical and horizontal directions are shown by red circles in Figure 4.4 (c,d). Whereas the experimental and the theoretical values concord well for the horizontal direction, they are different for the vertical direction. A possible explanation for this discrepancy is the fact that the radii of the CRLs are not precisely known. Small deviations of these radii affect dramatically the focus position and therefore the beam size in the sample plane. For instance, the radius of the last two lenses expected from the manufacturing process is 50 µm. However, several measurements have shown [111, 112] that this number has to be corrected to a value of about 48 µm. This change in the curvature moves the focus position by about 80 mm.

4.3 Modelling of partially coherent radiation based on the coherent mode decomposition [113]

Here, we present a general approach, which can be applied to partially coherent wave fields, and which is capable of calculating both, the intensity (spectral density) profile of the beam as well as the transverse coherence properties of the radiation at any position in a beamline. It is based on the coherent mode decomposition of the CSD (see Equation (2.34)) and can be effectively used to propagate partially coherent radiation. First application of this approach to FEL radiation was performed in [77]. A similar technique was used in the frame of geometrical optics [114] and for advanced phase retrieval methods in coherent imaging [10].

In general, the propagation of the partially coherent radiation through an arbitrary arrangement of the optical elements in a beamline can be performed in the following steps

1. Decomposition of the CSD, $W(\mathbf{u}_1, \mathbf{u}_2; z_0)$, in the source plane into coherent modes $E_j(\mathbf{u}, z_0)$ according to Equation (2.34).

2. Propagation of all modes $E_j(\mathbf{u}, z_0)$ from the source plane through the optical elements to the observation plane using a wave propagation technique. For example, Equation (2.3) can be used to propagate all modes in vacuum between optical elements. For thin optical elements the transmitted modes can be obtained by Equation (2.10).

3. Finally, after performing the previous step for all optical elements present in the beam line each mode is calculated in the plane of observation, and the CSD,

[4] The size of the crystal was characterized by Johannes Gulden at DESY. Here we assume, that this size corresponds to the size of the crystal, which gives rise to Bragg peaks.

$W(\mathbf{u}_1, \mathbf{u}_2; z)$, is determined by Equation (2.34).

As the number of contributing modes at an FEL is small, this method may be more effective than a straightforward propagation of the CSD (2.32), which deals with a four-dimensional function $W(x_1, y_1, x_2, y_2)$.

Often an analytical description of the propagation is not possible and numerical methods have to be applied to estimate, for example, the beam properties at different positions along the beamline. Although many computational methods have been developed to calculate the beam profile at the sample position, most of them do not provide the coherence properties of the beam in the plane of observation. In addition, the majority of these calculations are either ray tracing, or wave propagation approaches. Strictly saying, these methods are valid either in the limit of incoherent or fully coherent radiation. The partially coherent beams generated at third and fourth generation x-ray sources is not correctly covered by these methods.

As an example we applied the coherent mode decomposition method to propagate partially coherent radiation generated by a GSM source (2.40,2.41) through a beamline including a circular aperture (see Figure 4.6). As source parameters we used values reported for FLASH operating at a wavelength of 13.7 nm (see section 3.3.2): a source size of $\sigma_x = \sigma_y = 68$ µm and a transverse coherence length $\xi_x = \xi_y = 62$ µm. For these parameters the contribution of each mode at the source position is given by Equation (2.69) $\beta_{nm} = 0.41^{n+m}$. Modes with a contribution of less than 1 % were neglected in our simulations. In total, 21 modes with $n+m \leq 5$, where $n = 0, 1, \ldots 5,\ m = 0, 1, \ldots 5$, were used in the calculations presented here. The spectral density distribution of the total field and nine lowest modes at the source position are shown in Figure 4.7.

We considered the following geometry in our simulations: the pinhole is positioned 25 m downstream of the source and the radiation properties are analyzed 70 m downstream of the source (see Figure 4.6). Such an arrangement is typical for experiments performed using the unfocused beam at FLASH. We applied the general scheme of propagation of partially coherent radiation described earlier to this experimental geometry. The propagation in free space was performed in Fresnel approximation. For numerical implementation Equation (A.1) from Appendix A.1 was used. Different pinholes with the diameter from 5 mm to 1 mm were analyzed. The pinhole transmission function,

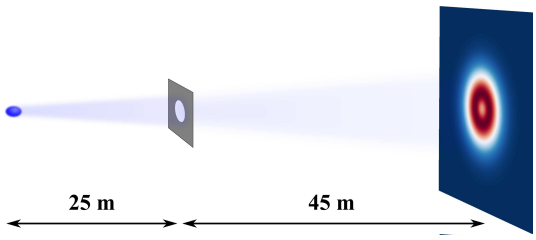

Figure 4.6: Partially coherent radiation is generated at the source. The circular aperture is positioned 25 m downstream of the source. The coherence properties of the radiation are analyzed 45 m downstream of the aperture.

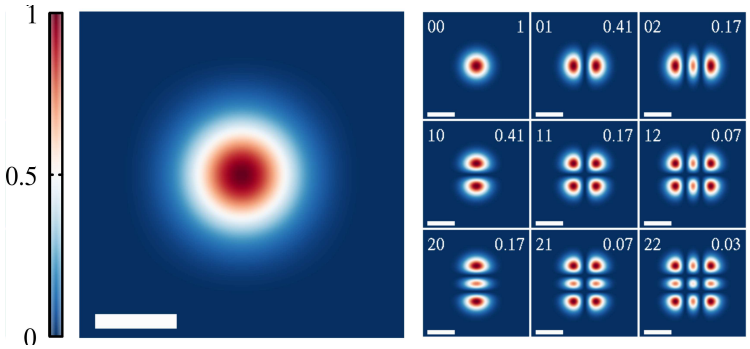

Figure 4.7: (left) The total spectral density distribution at the source position. (right) The spectral density distribution of the nine lowest modes at the source position. The relative contribution of each mode is indicated (top right). The length of the white scale bar is 150 µm.

$T(\mathbf{u})$, was described by Equation (2.11). It was convolved with a 200 µm wide (FWHM) Gaussian function to account for imperfections of the pinhole edges. The spectral density distribution of the total beam and the lowest modes behind 3 mm and 1 mm pinholes are presented in Figure 4.8. Figure 4.9 shows the same in the plane of observation.

One readily sees in Figure 4.8 (a) that in the case of the 3 mm pinhole the lowest modes, which dominate the radiation field, are just slightly affected by the aperture. The 1 mm pinhole, however, substantially cuts all modes, including the dominant ones (see Figure 4.8 (b)). The spectral density distribution of each mode in the plane of observation is similar to the spectral density distribution behind the pinhole. Additional spectral density modulations due to the scattering from the edges of the aperture are observed in Figure 4.9 (a). This can be attributed to the Fresnel diffraction effects, which are stronger for sharper pinhole boundaries. The Fresnel number, $d^2/(\lambda L)$, where d is the diameter of the pinhole and L is the distance from the pinhole to the detector, is 15 for the 3 mm pinhole and 1.6 for the 1 mm pinhole in this experimental geometry. We want to note here that due to Fresnel diffraction, small variations in the propagation distances might change these spectral density modulations significantly.

Finally, the CSD, $W(\mathbf{u}_1, \mathbf{u}_2; z)$, was determined in the plane of observation. In the horizontal direction it can be given by the following expression

$$W(x_1, x_2; z) = \sum_{nm} \beta_{nm} E^*_{nm}(x_1, y_1 = 0; z) E_{nm}(x_2, y_2 = 0; z). \tag{4.16}$$

Due to the symmetry of our scattering geometry, the same result is obtained in the vertical direction. The modulus of the CSD, $|W(x_1, x_2; z)|$, as a function of the transverse positions, x_1 and x_2, is shown in Figure 4.10 (a-d) for different apertures. The modulus of the SDC $|\mu(\Delta x)| = |\mu(-\Delta x/2, \Delta x/2)|$ as a function of the separation Δx for the same apertures is presented in Figure 4.10 (e-h) (red solid line). This calculation corresponds to the measurements of the contrast in a double pinhole experiment with varying pinhole

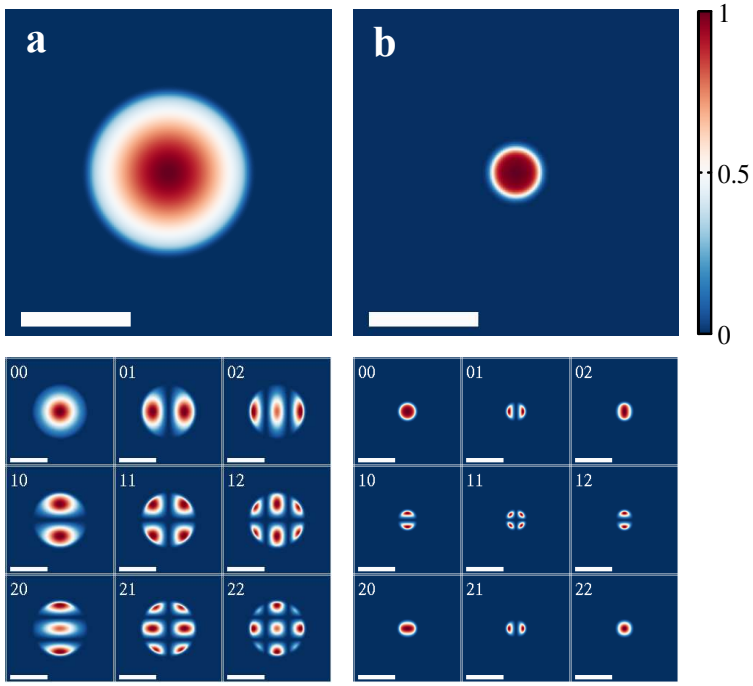

Figure 4.8: (top) The total spectral density distribution behind a circular aperture with (a) 3 mm and (b) 1 mm diameter. (bottom) The spectral density of the lowest nine modes behind the aperture. The length of the scale bar is 2 mm.

separation Δx and the center of the double pinhole positioned on the optical axis of the beam. For comparison, the SDC, $|\mu(\Delta x)|$, for the same geometry and source parameters, but without the pinhole is shown by the blue dashed line. The spectral density profiles, $S(x)$, for the same aperture sizes are shown in the insets of Figure 4.10 (e-h).

As a result of our simulations, we notice that the 5 mm pinhole does not affect the transmitted radiation. The spectral density profile $S(x)$ as well as the modulus of the SDC $|\mu(\Delta x)|$ in the observation plane calculated with and without the pinhole are the same. For the smaller pinhole diameters of 3 mm and 2 mm the size of the beam decreases, but the modulus of the SDC is not significantly altered. Our simulations suggest, that in the present geometry down to pinhole sizes of 2 mm no significant changes in the coherence length of the beam in the observation plane are expected. Only for the smallest pinhole size of 1 mm are the values of $|\mu(\Delta x)|$ significantly enhanced at large separations (see Figure 4.10 (h)). In this case the SDC cannot be described by a single Gaussian function (compare to results in [115]). However, we should note here that these separations are much larger than the beam size and will be difficult to access in a real experiment.

We analyzed as well the degree of transverse coherence ζ (2.31) and the available photon flux P_T behind each pinhole (see Table 4.2). The transmitted photon flux was calculated by the equation $P_T = \int S_{\text{out}}(\mathbf{u})\mathrm{d}\mathbf{u} / \int S_{\text{in}}(\mathbf{u})\mathrm{d}\mathbf{u}$, where $S_{\text{in}}(\mathbf{u})$ and $S_{\text{out}}(\mathbf{u})$ is

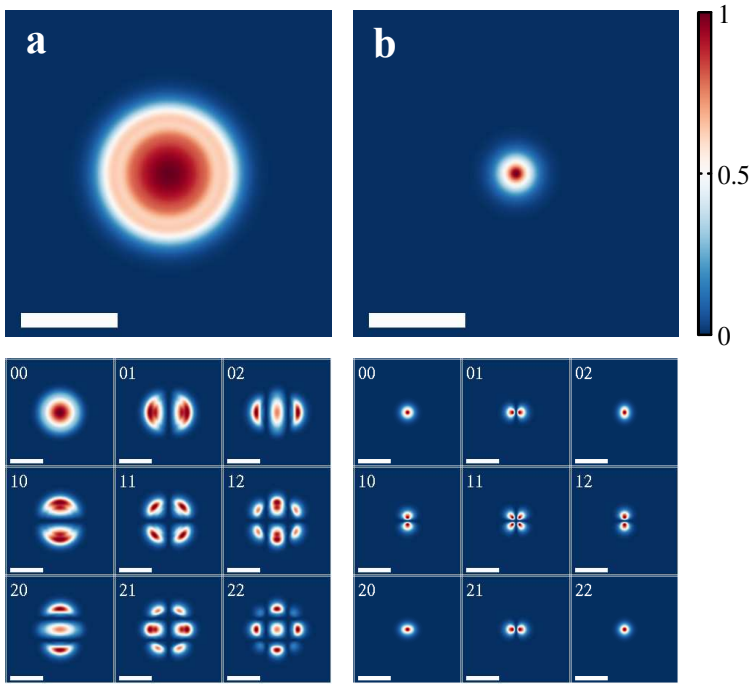

Figure 4.9: (top) The total spectral density distribution in the plane of observation calculated for a circular aperture, (a) 3 mm and (b) 1 mm in diameter. (bottom) The spectral density distribution of the lowest nine modes in the plane of observation. The length of the scale bar is 5 mm.

the spectral density distribution (2.36) incident on and behind the aperture. If no pinhole is present in the beamline, then obviously the transmitted photon flux is $P_T = 100\%$ and the degree of transverse coherence has the value determined by the source parameters $\zeta = 0.18$. Results from the Table 4.2 show that the degree of transverse coherence, ζ, is significantly increased for the smaller pinholes. However, this happens at a loss of the transmitted photon flux P_T. It is interesting to note that the product $P_T \cdot \zeta$, which may be considered as the amount of the coherent photon flux, is about 20 % after transmission through the larger pinholes. It drops down to a value of about 10 % for the 1 mm pinhole. However, in the latter case almost a fully coherent beam , $\zeta = 0.78$, is achieved with 10% of the transmitted radiation.

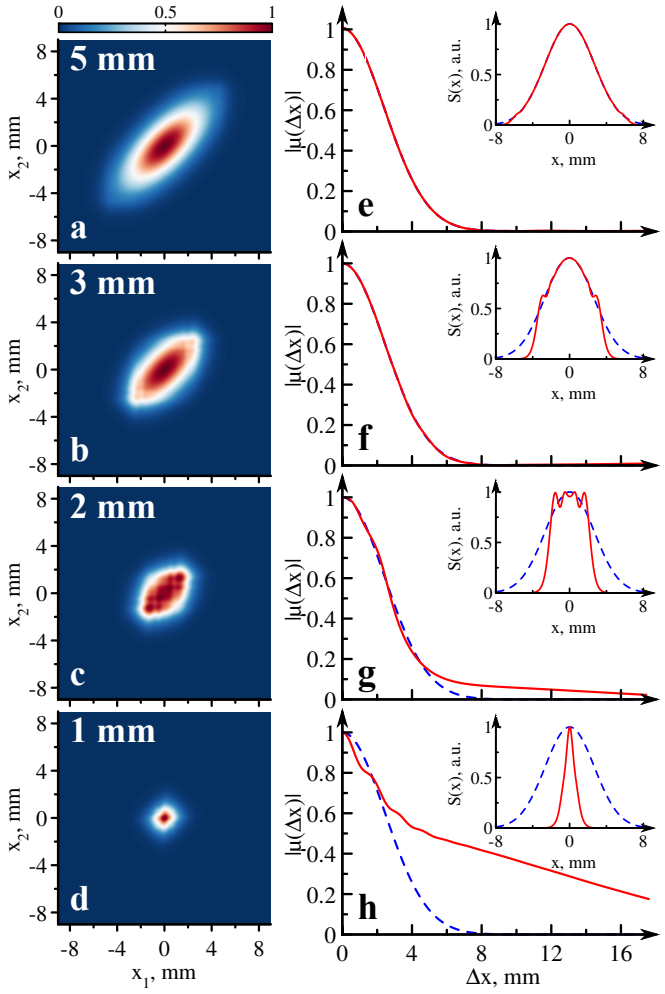

Figure 4.10: Transverse coherence properties of the radiation in the observation plane. (a-d) The modulus of the CSD $|W(x_1, x_2; z)|$. (e-h) The modulus of SDC $|\mu(\Delta x)|$ as a function of the separation Δx. The insets in (e-h) show the spectral density distribution $S(x)$ in the horizontal direction. The red solid lines show the simulations with the presence of the circular aperture. The blue dashed lines show the same functions obtained without a pinhole. Simulations were performed with pinhole diameters of (a,e) 5 mm, (b,f) 3 mm, (c,g) 2 mm, and (d,h) 1 mm.

Table 4.2: The transmitted photon flux, P_T, and the degree of transverse coherence, ζ, behind the aperture. Four different pinhole diameters are analyzed.

no pinhole	$P_T = 100\%$	$\zeta = 18\%$
5 mm	$P_T = 97\%$	$\zeta = 19\%$
3 mm	$P_T = 69\%$	$\zeta = 29\%$
2 mm	$P_T = 39\%$	$\zeta = 46\%$
1 mm	$P_T = 10\%$	$\zeta = 78\%$

5 Transverse coherence measurements at free-electron lasers

A variety of techniques to measure the transverse coherence properties of radiation has been developed. These techniques can be divided into two classes: amplitude correlation and intensity correlation measurements. The methods belonging to the former class are based on the superposition principle. The interference of waves is observed and the visibility of the interference fringes is analyzed. Most prominent representatives of such measurements are the Young's double slit experiment (see chapter 2.3.6) and the Michelson experiment [60].

Interestingly, in their pioneering experiments Hanbury Brown and Twiss have shown [63, 2], that correlation measurements can be performed even if no interference pattern is observable. They systematically studied intensity fluctuations of thermal light, in particular the degree of intensity correlation in a coincidence measurement. They showed, that for thermal light these measurements provide the same information about the degree of transverse coherence as the amplitude measurements.

5.1 Young's double pinhole measurements at LCLS [79]

LCLS is the first free-electron laser in the x-ray regime and started its operation in 2009 [42]. In this chapter we present the first coherence measurements at LCLS. These measurements are of vital importance for understanding the FEL operation and for planing coherence based experiments at x-ray FELs.

Conventionally, Young's experiment is performed with the apertures being positioned in a relatively weak photon beam, allowing multiple measurements with the same aperture. The objective of the present experiment was to characterize the coherence properties of a strongly focused FEL beam, as it is used by most users. These single shot measurements were performed in the so-called "diffract-and-destroy" mode [116], meaning that due to the extremely high power density in the focus, each aperture was destroyed during the interaction with a single FEL pulse. However, the FEL pulses are so short, that the pulse passes the aperture before the destruction occures. Several identical apertures (about 10) for each pinhole separation were manufactured to increase the number of measurements.

The experiment was conducted at the soft x-ray research (SXR) instrument of the LCLS. A sketch of the experiment is shown in Figure 5.1. The LCLS was operated with an electron bunch charge of 250 pC and with 13 undulator segments tuned to deliver 780 eV ($\lambda = 1.6$ nm) x-ray photons. Under these conditions, LCLS is expected to reach its saturation regime [42, 117, 118]. The duration of a single pulse of about

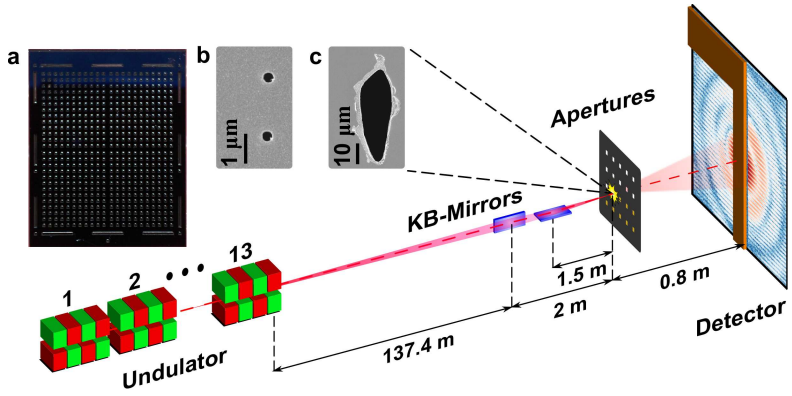

Figure 5.1: A sketch of the experiment showing thirteen undulator modules, a set of KB-mirrors focusing the beam on a sample frame and the detector, protected from the direct beam by a beamstop. The inset shows (a) a photograph of the silicon wafer containing the apertures, and SEM images of different apertures (b) before and (c) after the exposure to a single LCLS pulse.

300 fs was determined from electron bunch measurements. The average energy was about 1 mJ per pulse, which corresponds to $0.8 \cdot 10^{13}$ photons per pulse. The beam was delivered to the end-station through a beam transport system that includes three plane distribution mirrors and a monochromator comprised of a spherical mirror followed by a plane grating [119]. The measurements presented here were performed with the monochromator grating replaced by a plane mirror. The spherical mirror was operated in grazing incidence geometry (incidence angle of 89.2°) and focused the beam at the exit slit of the monochromator (focal length 7.8 m). At the sample position, the beam was focused to a size (FWHM) of 5.7 ± 0.4 µm in the horizontal and 17.3 ± 2.4 µm in the vertical direction (see Appendix A.9). Focusing was achieved by a pair of bendable Kirkpatrick-Baez (KB) mirrors consisting of a silicon substrate coated with a 37.4 nm thick boron carbide reflective coating [120, 121, 122], with focal lengths of 1.5 m (V) and 2 m (H). The limiting vertical aperture of the beam delivery system was twice the FWHM of the beam size at the grating position for 800 eV x-ray photons. Therefore, we assume that in the vertical direction the degree of coherence measured in the focus corresponds to the degree of coherence of the source.

A multiple aperture array with varying pinhole separations in the range from 2 µm to 15 µm was manufacured. The apertures were fabricated[1] by electroplating a 1.3 µm thick gold layer on top of a 100 nm silicon nitride substrate supported by windows etched in a 200 nm thick silicon wafer (see Figure 5.1 (a)). The 1.3 µm gold film attenuates the beam by eight orders of magnitude at the photon energies of 780 eV used here. The sample was 20×25 mm^2 in size and consisted of 4 arrays of 11 x 13 windows, for a total of 572 windows. Each window, 50×50 µm^2 in size, contained one pair of

[1]The apertures were manufactured by A. Sakdinawat, Y. Liu, W. Bang, and D. Attwood from the University of California in Berkley.

pinholes. The distance between individual windows was 768 μm in both directions. The pinhole diameter varied from 340 nm for the smallest separation to 500 nm for the largest separation to account for the reduction in intensity due to the larger separations probing the less intense regions of the beam.

These apertures were positioned in the focus of the beam inside the Resonant Coherent Imaging (RCI) end-station[2] (Figure 5.1). After each shot on the sample, the array was moved to an unexposed sample position. To accumulate statistics, each pinhole configuration was measured several times giving 110 patterns in total. Interference patterns were recorded by a Princeton Instruments PI-MTE 2048B direct illumination Charge Coupled Device (CCD) with 2048×2048 pixels, each 13.5×13.5 μm^2 in size, positioned 80 cm downstream of the apertures (Figure 5.1). A 3 mm wide rectangular beamstop manufactured from B_4C was positioned in front of the CCD to protect it from the exposure to the direct FEL beam.

5.1.1 Determination of the spatial coherence properties

Figure 5.2 shows typical single-shot diffraction patterns measured with different pinhole separations. For small separations between the pinholes a high contrast diffraction pattern was observed implying a high degree of coherence on that length scale. For larger separations the visibility of the fringes is slightly reduced due to the partial coherence of the incoming beam.

The diffraction data were analyzed by fitting expression (2.83)

$$I(\mathbf{q}) = (I_1 + I_2) \cdot I_D(\mathbf{q}) \cdot \left[1 + \left|\gamma_{12}^{\text{eff}}(\tau)\right| \cos(\mathbf{q}\cdot\mathbf{d} + \alpha_{12}(0))\right], \tag{5.1}$$

to each measured diffraction pattern in the 2D area shown in Figure 5.2 (a,d,g) by black dashed rectangles. Here $I_{1,2}$ are the intensities incident on pinhole one and two, $I_D(\mathbf{q}) = |A(\mathbf{q})|^2$ is the Airy distribution (2.77) due to diffraction through a round pinhole of diameter D, and effective complex degree of coherence (CDC) is given by

$$\gamma_{12}^{\text{eff}} = 2\frac{\sqrt{I_1 I_2}}{I_1 + I_2}\gamma_{12}. \tag{5.2}$$

In this analysis (see Appendix A.8 for details), we considered a region of the diffraction pattern shown in Figure 5.2 where $|\gamma_{12}^{\text{eff}}(\tau)| \approx |\gamma_{12}^{\text{eff}}(0)|$ and $\alpha_{12}(\tau) \approx \alpha_{12}(0)$ are good approximations as the time delay associated with the path-length difference[3] is much shorter than the coherence time τ_c, $\tau \ll \tau_c = 0.55$ fs (see below).

The analysis of all diffraction patterns has shown that some of them contain a contribution from an incoherent background, mostly to one side of the diffraction pattern, which leads to a reduced visibility of fringes (see Figure A.3 in Appendix). A possible origin of the apparent background is the presence of the higher harmonics in the FEL

[2]The RCI chamber was constructed and operated by the group of A. Scherz.

[3]The maximum time delay in the analyzed region is 0.2 fs for the maximum aperture separation of 15 μm.

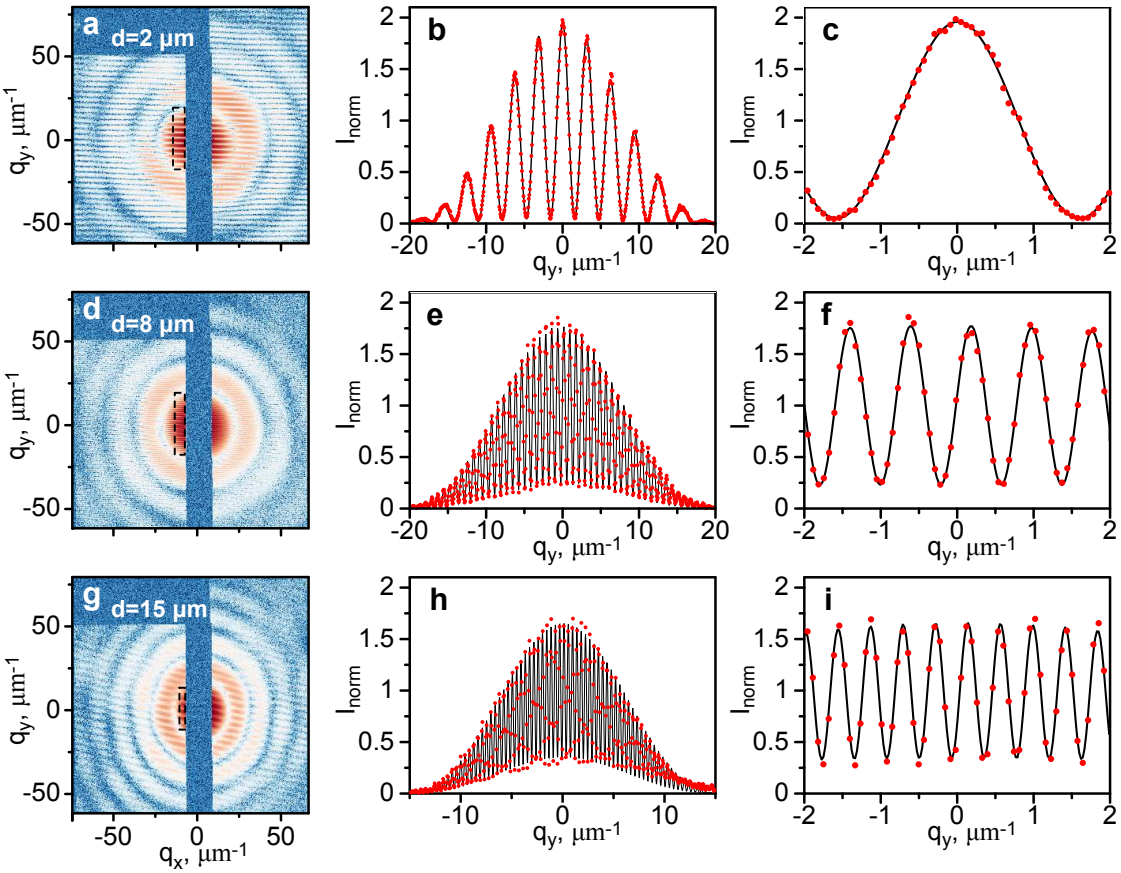

Figure 5.2: Measured diffraction patterns. Left column: Interference fringes from pinholes separated by (a) 2 µm, (d) 8 µm and (g) 15 µm each exposed to a single shot of the LCLS beam as a function of the transverse momentum transfer q_x, q_y. The area used for the analysis of the transverse coherence is shown by the dashed black rectangle close to the center of the patterns. Middle column: Line scans of the interference fringes on the right edge of the marked region, experimental data (red dots) and results of the theoretical fit (black lines). Right column: enlarged regions of the line scans shown in the middle column.

beam, which are transmitted by the material. For the analysis considered here, regions with sufficient signal on the opposite side of the beamstop (marked with the dashed rectangle in Figure 5.2 (a,d,g)) were considered.

The following parameters were determined while fitting Equation (5.1) to the experimental data: the incident intensity $I_1 + I_2$, the modulus of the effective CDC $|\gamma_{12}^{\text{eff}}|$, the relative phase $\alpha_{12}(0)$ of the wave-field between the pinholes, the pinhole separation d, the pinhole diameter D, and the position of the beam centre $q_{x,y}^0$. The small inclination angle of about 30 mrad in the vertical alignment of the double pinholes was taken

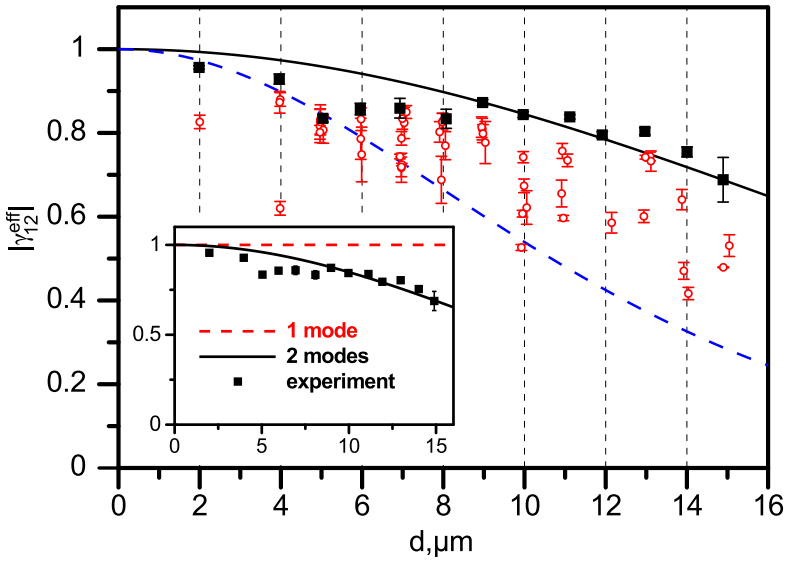

Figure 5.3: The modulus of the effective CDC, $|\gamma_{12}^{\text{eff}}|$, as a function of pinhole separation. The experimental values determined from the fitting procedure are shown by red circles. The error bars show the standard deviation of these values. A Gaussian function (black line) has been fit to the best shot values (black squares), which gives a coherence length of 16.8 ± 1.7 μm. The blue dashed line shows the decrease in the value of $|\gamma_{12}^{\text{eff}}|$ due to the maximum measured offset between the position of the apertures and the incident beam. (inset) The contribution of higher order modes to the modulus of the CDC. The fully coherent case (single mode) is shown by the red dashed line. The two mode contribution is shown by the black line.

into account during the data analysis. Measured values of $|\gamma_{12}^{\text{eff}}|$ were corrected for the finite width of the modulation transfer function (MTF) of the detector [123]. The detector MTF was measured[4] at the SSRL synchrotron source by observing the variation of the contrast produced by two pinholes at a fixed pinhole separation as a function of the sample to detector distance. A Gaussian MTF function with a width (rms) of 25 fringes/mm was found for our detector. Finally, the modulus of the effective CDC $|\gamma_{12}^{\text{eff}}|$ at a particular pinhole separation was determined for each shot (Figure 5.3). A Gaussian fit, $\exp\left(-d^2/2{\xi_y}^2\right)$, through the 'best' shots (those that provided the highest degree of coherence and which are shown as black squares in Figure 5.3) gives an upper estimate for the transverse coherence length, $\xi_y = 16.8 \pm 1.7$ μm, of the focused LCLS beam in vertical direction.

Our analysis shows a significant variation of the effective degree of coherence between different pulses for the same pinhole separation (see Figure 5.3). While this variation could be explained by shot-to-shot fluctuations of the coherence properties of the XFEL

[4]The measurements of the MTF were carried out by D. Zhou from the group of J. Stör and A. Scherz at the SSRL.

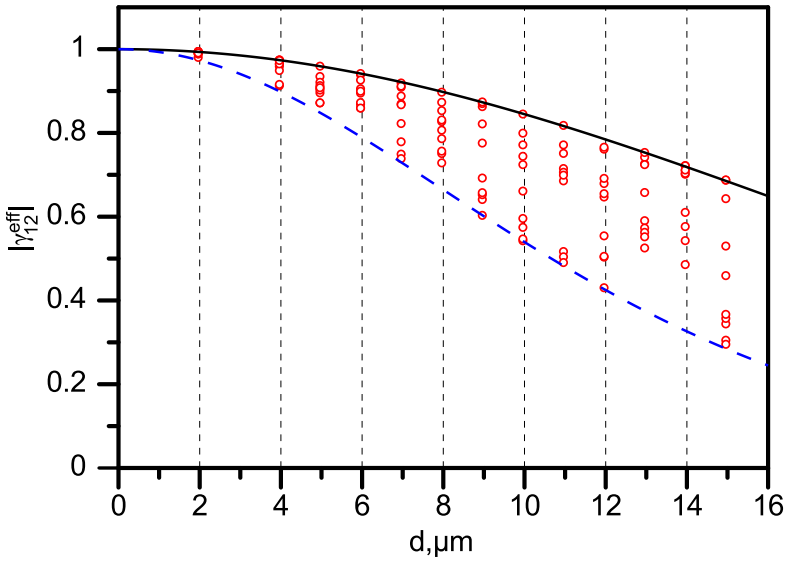

Figure 5.4: The modulus of the effective degree of coherence $|\gamma_{12}^{\text{eff}}|$as a function of the pinhole separation d. Each red circle corresponds to a single value of $|\gamma_{12}^{\text{eff}}|$ determined in the simulation with a random shift of the center of the incoming beam. The black solid and the blue dashed line are the same as in Figure 5.3.

beam, it may also arise from uncertainty in the position of the incoming beam with respect to the center of the pinhole pair, which leads to a difference in intensity at each pinhole. According to Equation (5.2) the value of the effective CDC, $|\gamma_{12}^{\text{eff}}|$, can be significantly lower than the intrinsic CDC, $|\gamma_{12}|$, if these incident intensities are not equal. We observed that some pulses were not centered on the apertures and did not destroy the pinholes (see Figure A.4 (a) in Appendix A.9). To determine the possible maximum deviation of the incident pulses with respect to the center of the pinhole pair we analyzed SEM images of these apertures. A maximum deviation of 11 µm in vertical direction was found. The impact of this positional uncertainty on the contrast, deduced from the beam size and the Gaussian fit through the 'best' shots, is described by the blue dashed line in Figure 5.3. Most of the experimentally determined values lie in the range between the two lines corresponding to the 'best' and the maximum offset shots. From this we conclude that this positional uncertainty is the dominant cause of the apparent shot-to-shot variation of the CDC.

To support this conclusion we performed additional simulations. We assumed that the modulus of the CDC, $|\gamma_{12}^{\text{eff}}|$, for a centered FEL beam is described by the black curve in Figure 5.4, which corresponds to a coherence length of $\xi_y = 16.8$ µm determined from our analysis of exerimental data (see Figure 5.3). The effect of the positional uncertainty on $|\gamma_{12}^{\text{eff}}|$ was simulated for a Gaussian incident intensity with a beam size of 17.3 µm (FWHM) and randomly distributed offsets of the beam in vertical direction. A uniformly distributed random number within a range of ±11 µm, that corresponds

to the maximum offset observed from SEM images, was generated for each offset and the corresponding values I_1 and I_2 of the intensities incident on individual pinholes were calculated. The effective degree of coherence, $|\gamma_{12}^{\text{eff}}|$, was calculated for each specific position of the incoming beam according to equation $|\gamma_{12}^{\text{eff}}| = 2\sqrt{I_1 I_2}/(I_1+I_2)|\gamma_{12}|$. These values are shown in Figure 5.4 by red circles. Ten shots were considered for each pinhole separation. Comparison of the simulations shown in Figure 5.4 with the results of the experimental data presented in Figure 5.3 confirms our conclusion, that the positional uncertainty is the dominant cause for the apparent shot-to-shot variation of the effective CDC.

The analysis of the highly offset shots in the horizontal direction also allowed us to estimate how uniform the coherence properties of the pulses are as a function of the transverse position within the pulse. We compared the values of the CDC for strongly horizontally offset and vertically centered pulses with the remainder of the pulses. These offset pulses also displayed high coherence, which implies that the coherence properties of the LCLS pulses appear to be spatially uniform.

The knowledge of the transverse coherence length of the LCLS beam in the vertical direction and an estimate of its vertical focus size is sufficient to determine the degree of transverse coherence, ζ_y (2.44), in vertical direction. For the focused LCLS beam we found $\zeta_y = 0.75 \pm 0.08$. A similar value, ζ_x, is expected in the horizontal direction as the source size and the beam divergence at LCLS have comparable magnitudes in both directions (see chapters 3.3.2,5.3 and [42, 117]). Thus the total degree of transverse coherence for the full beam is $\zeta = 0.56 \pm 0.12$, which agrees well with the value $\zeta \approx 0.65$ obtained in simulations [118] for similar LCLS parameters.

Using the Gaussian Schell-model (GSM), the photon beam emittance (2.61) ε_y in vertical direction can be expressed as (2.64) $\varepsilon_y = \lambda/(4\pi\zeta_y)$, where σ_y is the size (rms) and σ'_y is the divergence (rms) of the source. Substituting into this expression the measured value of the degree of transverse coherence, ζ_y, we find that the emittance of the LCLS beam is $\varepsilon_y = 0.17 \pm 0.02$ nmrad. This agrees well with typical values reported for the LCLS photon beam at 800 eV with a source size of $\sigma_y = 20$ µm and a divergence of $\sigma'_y = 8.5$ µrad [117]. For a diffraction limited beam with $\zeta_y = 1$, the same source size and x-ray photon energy would have a smaller divergence of about 6.4 µrad (see Figure 5.5).

To estimate the number of independent coherent modes contributing to the total radiation field we apply the GSM to the 'best' shots in vertical direction. This yields $\beta_1/\beta_0 = 0.14 \pm 0.05$ and $\beta_2/\beta_0 = 0.02 \pm 0.01$ for the first and for the second mode, respectively. This indicates that for separations of up to 15 µm, which corresponds to the FWHM of the beam, two modes are sufficient to describe the coherence properties of the beam in vertical direction (see inset in Figure 5.3).

The total power of the wave-field

$$P = \int S(\mathbf{u}) \mathrm{d}\mathbf{u}$$

can be determined in this case by integrating the total spectral density, which is a

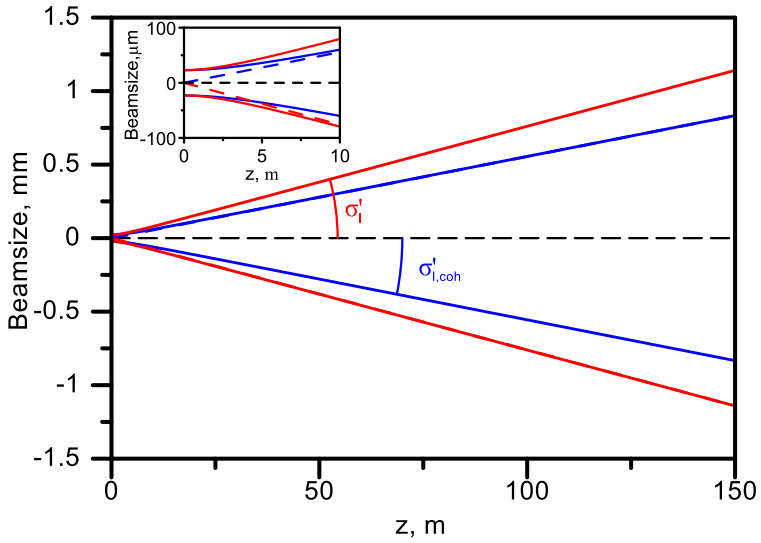

Figure 5.5: Divergence of the LCLS beam. Simulations for the partially coherent LCLS beam with a degree of transverse coherence of 75 % (red line) (source size $\sigma = 20$ µm and divergence $\sigma' = 8.5$ µrad. Compared to a fully coherent (diffraction limited) source with the same source size and divergence $\sigma'_{coh} = 6.4$ µrad (blue line) as function of the propagation distance from the source. The inset shows an enlarged region.

product of the horizontal and vertical contributions, each described by Equation (2.36). This leads to the following result

$$P = P_0 + P_{0,1} + P_{1,0} + \cdots = \sum_j \beta_j^x \sum_i \beta_i^y = \beta_0^x \beta_0^y + \beta_0^x \beta_1^y + \beta_1^x \beta_0^y + \cdots ,$$

where we have neglected the contribution of modes higher than two. From this expression, the relative power of the dominant mode is

$$P_0/P = [1 + \beta_1^y/\beta_0^y + \beta_1^x/\beta_0^x + \cdots]^{-1} . \tag{5.3}$$

We have measured the degree of coherence in the vertical direction only. Extrapolating our results to the horizontal direction and using Equation (5.3) we estimate that 78 ± 8 % of the total FEL beam power is concentrated in the dominant transverse "TEM_{00}" mode. This value is substantially higher than at any existing x-ray source at that wavelength (it is about 1% for synchrotron sources). From these results we conclude, that at FEL sources like LCLS almost the full photon flux can be used in coherence based experiments, contrary to the synchrotron sources, where only a small fraction of the beam is available for such applications.

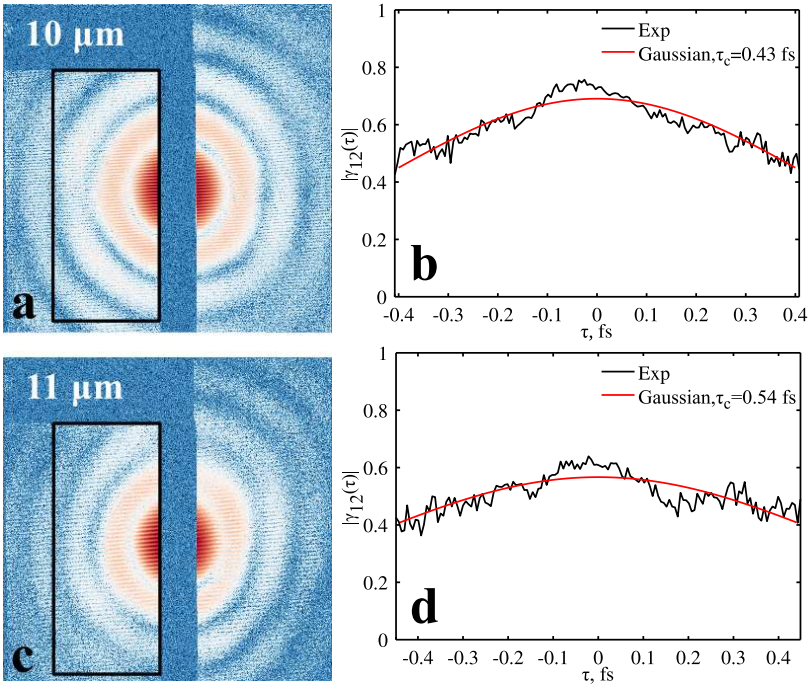

Figure 5.6: Temporal coherence characterization. (a,c) Interference patterns, the analyzed region is shown by a black square. (b,d) The visibility (black line) as a function of the time delay τ associated with the path-length difference. (b,d) show results determined from (a,c). Gaussian fits are also shown (red lines).

5.1.2 Determination of the temporal coherence properties

Some of the pulses (six in total) that illuminated apertures with larger pinhole separations (greater than 10 µm) produced extremely bright interference patterns. This allows the determination of the fringe visibility up to the edge of the detector, which corresponds to time delays of $\tau \approx 0.6$ fs for a pinhole separation of 15 µm. In these conditions the time dependence in (5.1) was taken into account explicitly, providing a measurement of the temporal coherence for individual femtosecond pulses. We have seen in chapter 2 that in Fresnel approximation, which can be assumed here, the time delay is constant along the lines perpendicular to the pinhole separation. We averaged the visibility in the analyzed region (red square in Figure 5.6 (a,c)) along the fringes for each selected pulse (black line in Figure 5.6 (b,d)) and fitted this visibility $|\gamma_{12}^{\text{eff}}(\tau)|$ by a Gaussian, $\exp\left(-\tau^2/2\tau_c^2\right)$ (red line in Figure 5.6 (b,d)). An average over six pulses, $\bar{\tau}_c$, of the determined single pulse values of τ_c yields a temporal coherence time, $\bar{\tau}_c \approx 0.55 \pm 0.12$ fs. For a beam with a Gaussian spectrum this value is in good agreement with the estimate [60] $\tau_c \sim 1/\sigma_\omega = 0.4$ fs, where $\sigma_\omega = 2.5$ fs^{-1} is the rms bandwidth of the LCLS beam at that energy [117].

Combining the results from the transverse and temporal coherence measurements we can estimate the degeneracy parameter δ_{LCLS} of the LCLS beam. It is given by (see

Appendix A.7)

$$\delta_{\mathrm{LCLS}} = N_{\mathrm{ph}} \cdot \zeta_x \cdot \zeta_y \cdot \frac{\tau_c}{2\sigma_t}, \tag{5.4}$$

where N_{ph} is the number of photons in a single pulse, $\zeta_{x,y}$ is the degree of transverse coherence in the horizontal and vertical directions, σ_t is the rms pulse duration and τ_c is the coherence time. Substituting $N_{\mathrm{ph}} = 10^{12} - 10^{13}$ photons per pulse, $\zeta_x \cdot \zeta_y = 0.56$, $T = 300$ fs, and $\tau_c = 0.55$ fs in Equation (5.4) we estimate the degeneracy parameter of the LCLS beam to be

$$\delta_{\mathrm{LCLS}} = 10^9 - 10^{10}.$$

The x-ray radiation from the LCLS is therefore highly degenerate and about 10^{10} photons are contained in the coherence volume or equivalently [59] in the phase space volume occupied by a single photon. This number is slightly lower than $\delta = 10^{10} - 10^{14}$ predicted by E. Saldin and colleagues [44] based on SASE simulations. However, this number is significantly higher than degeneracy parameter at synchrotron sources. For instance, at high brilliance synchrotron source PETRA III we estimate from Equation (5.4) $\delta \approx 1$ for the same photon energy.

5.2 Young's double pinhole measurements at FLASH [124]

We employed the single pulse methodology developed in [79] to measure the transverse coherence properties of individual pulses at FLASH. The measurements were carried out at the BL2 beamline. The machine was operated at a wavelength of 7.9 nm delivering photon pulses with 180 μJ per pulse on average. The beam delivery system consisted of two flat distribution mirrors and an elliptical mirror, which focuses the beam to a size of about $(10 \pm 2) \times (10 \pm 2)$ μm^2 FWHM (see Appendix A.9.2) 70 m downstream of the undulator exit. The acceptance of the mirrors was sufficiently large in both directions [125], therefore we assume that the beam was not cut by the mirrors. Double pinhole apertures, identical to those used at LCLS (see chapter 5.1), were positioned in the focus of the beam inside a dedicated vacuum chamber HORST[5] [126]. The double pinhole diffraction patterns were recorded with an in-vacuum CCD (LOT/Andor DODX436-BN) with 2048×2048 pixels, each 13.5×13.5 μm^2 in size. A 3 mm linear beam stop manufactured out of B_4C was oriented perpendicular to the interference fringes and protected the CCD from the direct FEL beam. A 200 nm thick Pd foil was mounted few centimeters upstream from the camera to absorb the visible light generated during the damage process of the apertures. A sample to detector distance of 0.34 m provided a sufficient sampling of the fringes and the observation of the first zero of the Airy distribution on the detector.

Typical recorded and dark field corrected single shot diffraction patterns are shown in Figures 5.7 and 5.8 as a function of the momentum transfer $\mathbf{q}$ for a pinhole separation of 4 μm (a) and 11 μm (d). In Figure 5.7 the double pinholes were oriented horizontally and vertical fringes originate from the interference between the field scattered at different

[5] The HORST chamber was constructed and operated by the group of A. Rosenhahn.

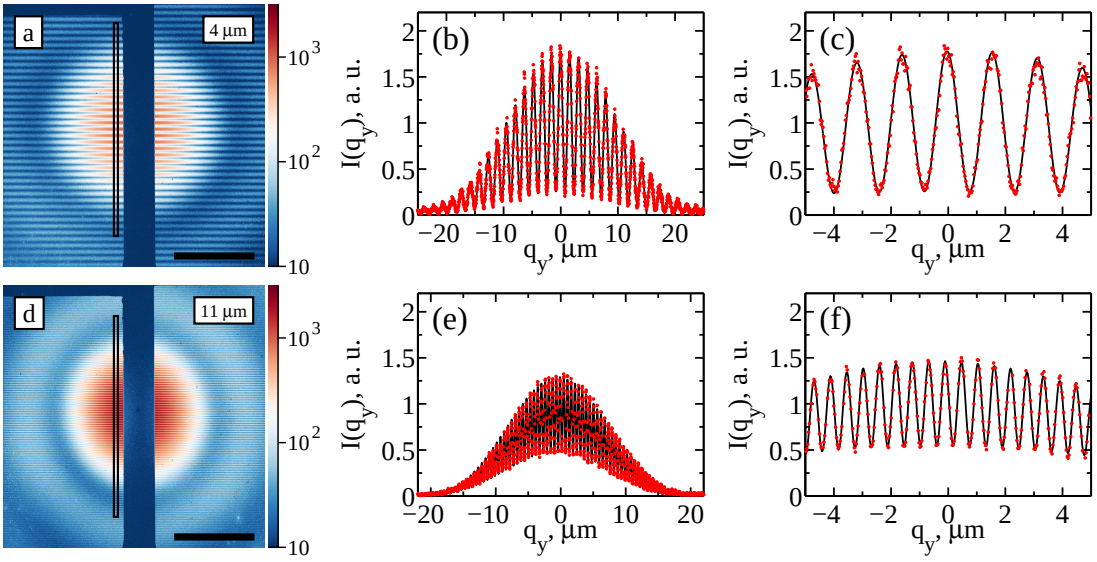

Figure 5.7: Left column: Single shot interference patterns from pinholes separated by 4 µm (a) and 11 µm (d) oriented vertically. The scale bar is 20 μm^{-1} wide. The area used for the analysis is marked by the black rectangle close to the center of the patterns. Middle column: Line scans of the interference fringes on the edge of the marked region close to the center of the diffraction pattern, experimental data (red dots), and results of the theoretical fit (black lines). Right column: Enlarged regions of the line scans shown in the middle column.

pinholes. In Figure 5.8 a similar diffraction pattern measured with vertically oriented double pinholes are presented. The first minimum of the Airy distribution is visible at $|\mathbf{q}| \approx 25\ \mu m^{-1}$ in all figures. The line scans through the measured diffraction patterns (Figures 5.7 (b) and 5.8 (b)) show a high contrast level for the small pinhole separation for both the horizontal and vertical directions. The contrast decreases for larger separations (see Figures 5.7(e) and 5.8(e)), which indicates a smaller magnitude of the complex degree of coherence at these length scales.

On most of the diffraction patterns a noise was observed. It consisted of a constant background and a few hot pixels randomly distributed over the whole diffraction pattern ('salt and pepper noise'). We attribute the appearance of this noise to the light generated during the damage process of the pinholes. Since the Pd foil was not attached to the detector but was positioned a few centimeters upstream, light could leak between the foil and detector and be a source of this noise.

To determine the modulus of the effective complex degree of coherence $|\gamma_{12}^{\text{eff}}|$ for each measured single shot interference pattern, Equation (5.1) was fit to the data. We added a constant A to Equation (5.1) to accommodate for the presence of the constant background noise. The hot pixels were removed from the diffraction patterns and were not considered in the analysis procedure. In particular, the two-dimensional area marked

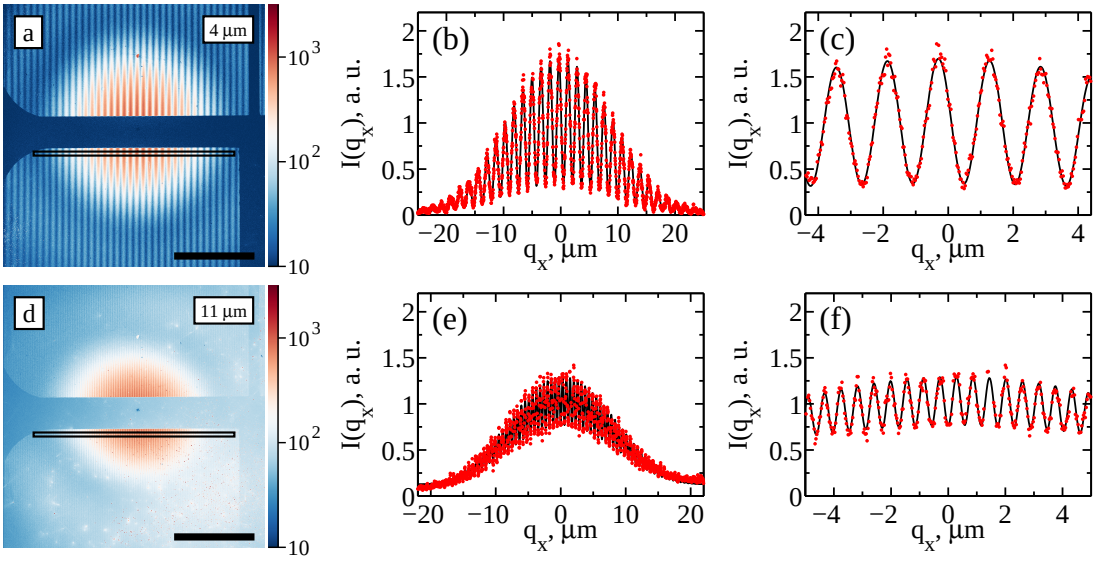

Figure 5.8: The same as in Figure 5.7 for horizontally oriented double pinholes.

with a black rectangle in Figures 5.7(a,d) and 5.8(a,d) was analyzed. Eight fit parameters including $|\gamma_{12}^{\text{eff}}|$, $(I_1 + I_2)$, D, d, α_{12}, A and the position of the optical axis in the horizontal and vertical directions were found. The quality of fit was characterized by an R-factor $R = \sum_i (I_i^{\text{th}} - I_i^{\text{exp}})^2 / \sum_i (I_i^{\text{exp}})^2$, where I^{exp} is the background corrected measured data, I^{th} is the fit and summation is made over all points in the fitted area. All fits with $R > 0.01$ were excluded from the further analysis (less than 50% from the total number of the diffraction patterns in each direction). For each shot a confidence interval of $|\gamma_{12}^{\text{eff}}|$ was determined as a value for which R was twice as large as the minimum value, while all other fit parameters were fixed. Typical fit results are shown in Figures 5.7(b,d), 5.8(b,d).

As a result of the data analysis, the modulus of the effective CDC $|\gamma_{12}^{\text{eff}}|$ as a function of the pinhole separation is shown in Figures 5.9 (a) and (b) for the horizontal and vertical directions. We approximated the highest values of $|\gamma_{12}^{\text{eff}}|$ for each pinhole separation (shown by black squares) with the Gaussian function $\exp[-d^2/(2l_c^2)]$ shown by black line in Figures 5.9 (a) and (b). This yields an upper bound estimate of the transverse coherence length in each direction. In this way we determined the transverse coherence length (rms) to be $l_c^H = 6.2 \pm 0.9$ μm in the horizontal and $l_c^V = 8.7 \pm 1.0$ μm in the vertical direction. During this fitting procedure we fixed the value of $|\gamma_{11}^{\text{eff}}|$ at zero pinhole separation to one according to its definition in Equation (5.2). An unconstrained fit yields a value of $|\gamma_{11}^{\text{eff}}| \approx 0.8$ in both directions and provides slightly larger values for the transverse coherence length. We attribute this to inhomogenities in the transmission through the pinholes.

To measure the beam profile in the plane of the apertures we analyzed polymethylmethacrylate (PMMA) imprints produced by single FEL pulses with a varying degree of attenuation of the beam (see Appendix A.9.2). Three sets of PMMA imprints with

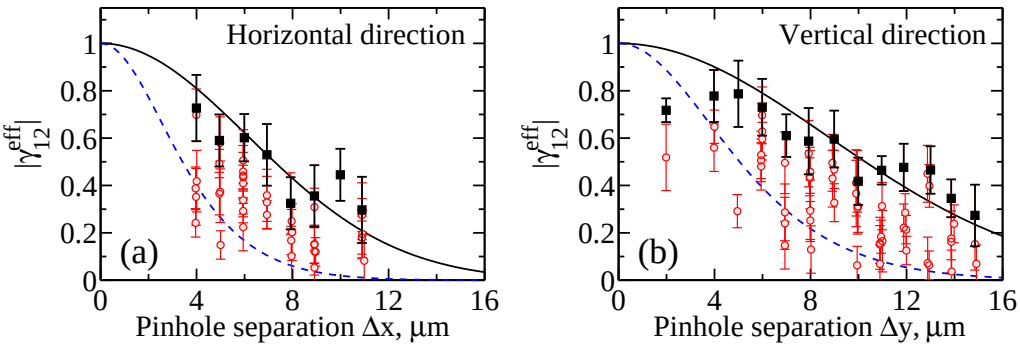

Figure 5.9: The modulus of the CDC in horizontal (a) and vertical (c) direction. The red circles show the measured values. Each point corresponds to a single FEL shot. Gaussian fits through he highest values are shown by black lines. Blue dashed lines show the reduction of contrast due to beam positioning instabilities.

one order of magnitude difference in attenuation of the incoming beam were analyzed. Using a Gaussian beam approximation a beam size of $(10 \pm 2) \times (10 \pm 2)$ μm^2 FWHM was determined. In the horizontal direction additional features on the sides of the beam were observed. For the strongly attenuated beam, however, round craters, 15 μm in diameter, indicate that the central part of the beam is round.

As follows from our analysis (see Figure 5.9) the values of $|\gamma_{12}^{\mathrm{eff}}|$ vary significantly from shot to shot for the same pinhole separation. We attribute this variation mainly to the beam position instabilities in the plane of the sample (see section 5.1). We estimated the deviation of the beam center relative to the sample by analysing the PMMA imprints measurements. The positions of thirty two craters in the PMMA were found and compared with the nominal positions expected from the sample stage movement. A maximum offset between the position of the apertures and the incident beam was determined to be ± 12 μm in the horizontal and ± 8 μm in the vertical direction. We attribute this positional uncertainty to both, instabilities of the sample stages and beam positional jitter. Using these values as the offset of a Gaussian beam with a size of 10×10 μm^2, we can calculate the difference of the intensity incident on pinhole one and two. The error imposed by this uncertainty in position compared to the Gaussian fit through the highest values of $|\gamma_{12}^{\mathrm{eff}}|$ (black solid line in Figures 5.9 (a) and (b)) is shown by the blue dashed line in Figures 5.9 (a) and (b). Most of the measured values lie between the black and the blue line, which indicates that the positional uncertainty is the dominant cause for the apparent variations in $|\gamma_{12}^{\mathrm{eff}}|$. However, as this error is quite significant, we cannot definitively exclude shot to shot variations in the degree of coherence $|\gamma_{12}|$. Moreover, simulations of the FLASH beam with the code GENESIS for a similar wavelength 13.5 nm indicate slight shot to shot variations in the CDC [127].

We have also characterized the temporal coherence of the FLASH beam for the same operation conditions of FLASH [124]. The temporal coherence measurements were carried out at the PG2 beamline immediately after the transverse coherence measurements

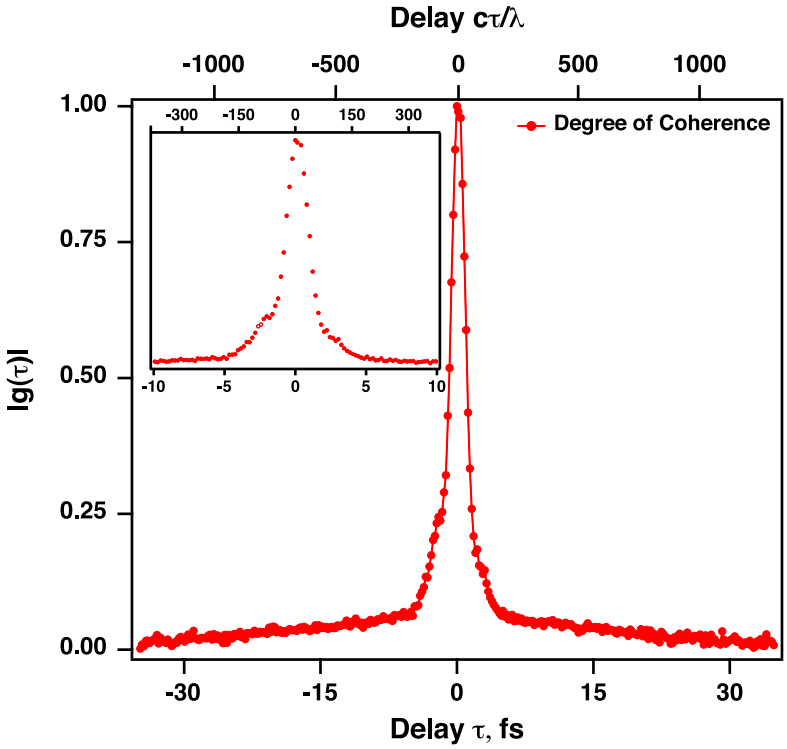

Figure 5.10: The modulus of the complex coherence function $g(\tau)$ as a function of the time delay. The top and bottom axes show the delay in wavecycles and femtoseconds, respectively. In the inset an enlarged region of ± 10 fs, which corresponds to about ± 375 wavecycles, is shown. This Figure was made by F. Sorgenfrei from the group of W. Wurth.

using an autocorrelator [128, 78]. The coherence time was found to be $\tau_c = 2$ fs (see Figure 5.10). The pulse duration was estimated to be in the order of 100 fs.

The statistical properties of the radiation at FLASH are described by the full mutual coherence function $\Gamma(\mathbf{r}_1, \mathbf{r}_2; \tau)$. We have characterized the MCF as a function of the space coordinates and as a function of the time delay. Combining the results from these measurements we determined the magnitude of the complete MCF of the radiation at FLASH, assuming the radiation is cross spectrally pure [60]. According to its definition in Equation (2.22) the MCF is a function of two coordinates in space and one coordinate in time. For visualization purposes we show a 3D representation of the MCF $|\Gamma^V(y_1, y_2; \tau)|$ in the vertical direction in Figure 5.11. A similar result is obtained for the MCF $|\Gamma^H(x_1, x_2; \tau)|$ in the horizontal direction.

A similar analysis as in chapter 5.1 yields a degree of coherence of $\zeta_y = 0.72 \pm 0.08$ in the vertical and $\zeta_x = 0.59 \pm 0.10$ in the horizontal direction for the best shots. The total degree of transverse coherence $\zeta = \zeta_x \zeta_y = 0.42 \pm 0.09$ is slightly smaller than the value 0.56 ± 0.12 found for the LCLS beam. From mode decomposition in the frame of the Gaussian Schell-model we estimate that 62 ± 11 % of the total radiation

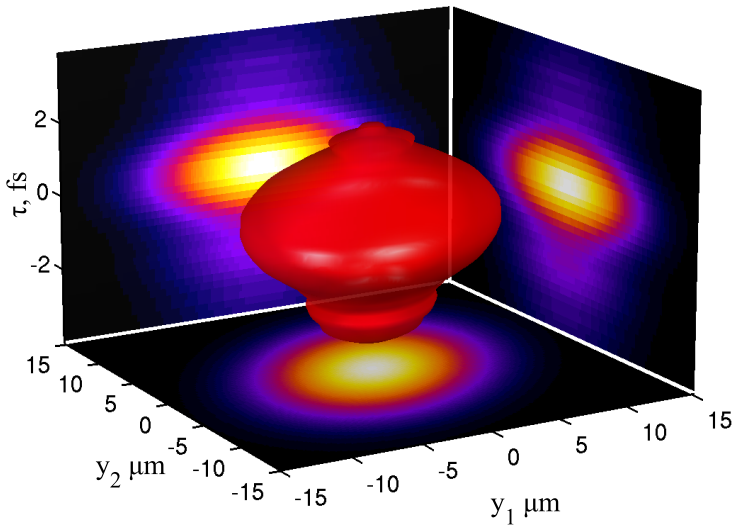

Figure 5.11: A representation of the MCF $|\Gamma^V(y_1, y_2; \tau)|$ determined from the measurements of the transverse (Gaussian fit to the maximum values) and temporal coherence properties. The MCF was normalized according to $|\Gamma^V(0, 0; 0)| = 1$ and the isosurface with $|\Gamma^V(y_1, y_2; \tau)| = 0.15$ (red), is shown. The projections of $|\Gamma^V(y_1, y_2; \tau)|$ in τ, y_1, y_2 directions are also presented.

power is contained in the dominant transverse mode. According to Equation (A.24) the degeneracy parameter is given by

$$\delta_{\mathrm{FLASH}} \approx 10^{10} - 10^{11},$$

where we used $N_{\mathrm{ph}} = 7 \cdot 10^{12}$ as the total number of photons in a single pulse. This value is comparable with the degeneracy parameter found for the LCLS beam.

The coherence measurements presented here indicate a significantly higher degree of transverse coherence of the FLASH beam than previously reported values (see sections 3.3.2, 5.3 and [77]). We attribute this to the higher performance of the FLASH accelerator complex after its upgrade [129]. A comparison with values reported for the LCLS [79] shows, that both machines, though operating at significantly different wavelengths and different pulse energies, provide similar values of the degree of coherence.

5.3 Young's double slit measurements at FLASH [77]

In an experiment before the major upgrade of FLASH in 2009 the transverse coherence was measured using a double-slit experiment. This measurement was conducted at the fundamental undulator harmonic at a wavelength of 13.7 nm during the commissioning phase of FLASH. The average energy per pulse was about 10 µJ, which is well below the

saturation that was reached at 40 μJ in an earlier experiment [47] at the same wavelength. At these average energies about 10^{12} photons are produced per pulse. FLASH was operated at 1 MHz repetition rate with 10 bunches per train and a 5 Hz repetition rate of the bunch trains.

The experiment was performed with a set of horizontal and vertical slits laser cut into an 80 μm thick stainless steel foil that was positioned at a distance $z_1 = 20$ m downstream of the last operating undulator module in the FEL tunnel. The distance d between the slit centers was 150, 300 and 600 μm for both vertical and horizontal pairs. The individual slit width was $a = 30$ μm for the first two pairs and $a = 50$ μm for the last pair. The detection system consisted of a fluorescent screen (Ce doped YAG crystal) converting the XUV radiation into the visible range. The resulting fluorescent radiation was imaged with a standard objective lens with a focal length of $f = 50$ mm onto a Basler A311f CCD camera. In this geometry of the experiment the effective detector pixel size was 29.4 μm in the vertical direction and 20.8 μm in the horizontal one. The detector was located at a distance $z_2 = 4.438 \pm 0.005$ m downstream of the slit mask. Each interference pattern measured in this experiment was a result of the accumulation of ten bunches of a single train of FEL radiation. Each measurement for a given slit separation was repeated ten times.

A typical interference pattern measured on the detector with a vertical slit separation of 150 μm is shown in Figure 5.12 (a). From these 2D data sets 1D interference patterns were obtained by choosing an area on the detector centered at the maximum intensity and averaging over three pixels (shown in Figure 5.12 (a)) in the direction perpendicular to fringes. The averaging procedure was necessary to improve the statistics of the measured signal.

The experimental data was analyzed using fitting. Here, the diffraction patterns from individual slits did not overlap on the detector and the full expression (2.81) was used for the analysis. The diffraction pattern from a single slit was described by [54]

$$I_{1,2}(\mathbf{q}) = \left(\frac{a_x a_y}{4z}\right)^2 \left(\frac{\sin\left(q_x a_x/2\right)}{q_x a_x/2}\right)^2 \left(\frac{\sin\left(q_y a_y/2\right)}{q_y a_y/2}\right)^2, \tag{5.5}$$

where a_x and a_y are the slit width and height, respectively. Typical results of the fit for different slit separations are shown in Figure 5.12 (b-d). As a result of the fitting procedure the absolute value of the complex coherence factor $|\gamma_{12}|$ was obtained for each slit separation for both the horizontal and vertical directions (see Figure 5.13). During this analysis we found, that the values of $|\gamma_{12}|$ do not vary significantly between different diffraction patterns, measured with the same slit separation. Contrary to the measurements presented in chapters 5.1 and 5.2 this experiment was conducted in nondestructive regime that allowed to carefully align the slits for each measurement. An average over several pulse trains produces a single diffraction pattern. To compare the obtained values of the complex coherence factor with the intensity distribution we plotted on the same figure the intensity distribution. It was obtained by rescaling the experimental results reported in reference [47] to a 20 m distance from the source.

The obtained values of the degree of coherence were approximated by a Lorentzian

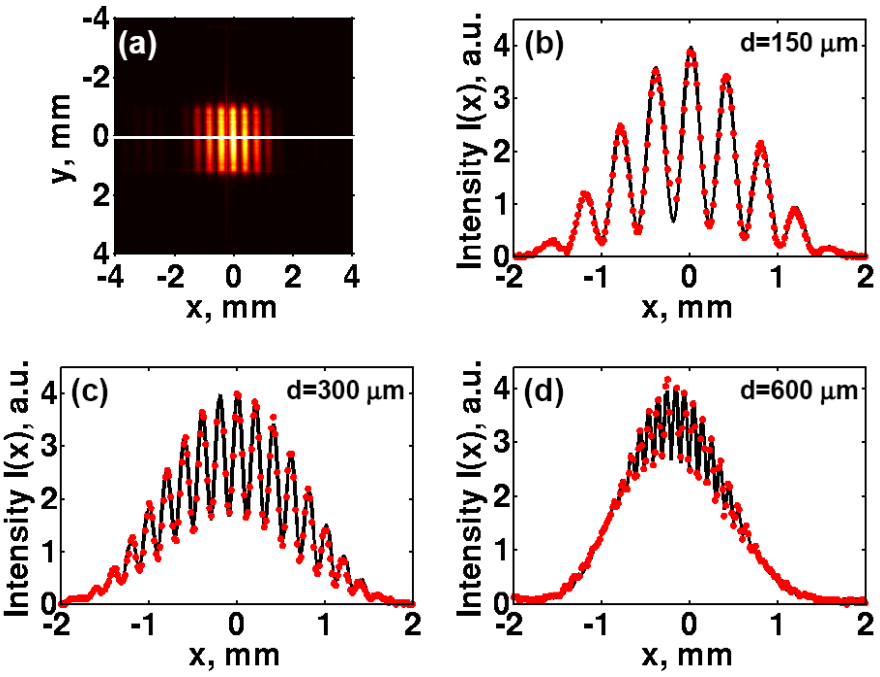

Figure 5.12: Results of a double-slit experiment. (a) A typical data set measured on the detector with vertical slits of 150 µm separation. Each image is a result of an accumulation of ten pulses. The framed region in the image of three pixels wide was used for further analysis. (b-d) Results of the fit (solid lines) to experimental data (points) for different slit separations d=150 µm (b), d=300 µm (c), d=600 µm (d) in the horizontal direction. The error bars of the data are less than 3 % and are smaller than the symbols used to represent the data. The error metric defined as $E = \sum_{i=1}^{N} \left(I_i^{\text{exp}} - I_i^{\text{fit}}\right)^2 / \sum_{i=1}^{N} \left(I_i^{\text{fit}}\right)^2$ was less than 0.002 for all fits.

function

$$L(x) = \frac{1}{1 + \left(\frac{x}{\xi}\right)^2}$$

with parameters $\xi_H = 300 \pm 15$ µm and $\xi_V = 250 \pm 13$ µm, which can be considered as an estimate of the coherence length at that distance from the source. These estimates show that the coherence properties of the FEL are of the same order of magnitude in both vertical and horizontal directions, though slightly higher in the horizontal direction. However, a comparison with our GSM simulations in chapter 3.3.2 shows that the measured values of the degree of coherence for different slit separations are considerably lower than ultimately predicted by the model (see Figure 3.12 (d)). The apparent source size corresponding to the experimentally found values for the coherence lengths can be calculated using the GSM. The analysis gives a value of $\sigma = 180$ µm, which is about 2.5 times larger than considered in our theoretical modelling. This size is in good agreement

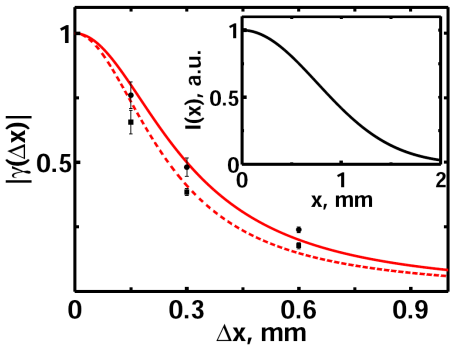

Figure 5.13: Modulus of the CDC as function of slit separation in the horizontal (circles) and vertical (squares) directions obtained as a result of the fit to experimental data. A Lorentzian fit to the obtained values of $|\gamma(\Delta x)|$ is shown by solid (vertical direction) and dash (horizontal direction) lines. The intensity distribution scaled from the results of the reference [47] is shown in the inset.

with the source size observed with the wavefront sensor at similar operating conditions of FLASH [130].

5.4 Coherence measuremens at FLASH using a uniformly redundant array [93]

A single double pinhole (or slit) coherence measurement yields the complex coherence factor at a certain separation, the pinhole separation. A full characterization of the CDC requires a number of double pinhole measurements with varying pinhole separations. The complete coherence function can also be measured using other techniques, including x-ray grating interferometry [131], phase space tomography [132, 133] and methods, which employ statistical (Brownian) motion of scattering objects [134]. However, similar to the Young's double pinhole experiments, these techniques require a number of measurements.

There is considerable interest to fully characterize the transverse coherence properties of the radiation from a single diffraction pattern. Such a technique can be applied to measure the coherence of single FEL pulses or provide a fast and effective coherence measurement at synchrotron sources. To probe the degree of coherence at different separations in a single interferogram, a scattering structure with more slits or scatterers can be utilized. The diffraction pattern of an arbitrary aperture illuminated by partially coherent, narrow bandwidth light can be written as a convolution of the Fourier transform of the CDC, $\gamma(\mathbf{q})$, and the diffraction pattern produced by fully coherent radiation $I_{\mathrm{coh}}(\mathbf{q})$ [135, 136, 70]

$$I(\mathbf{q}) = \gamma(\mathbf{q}) \otimes I_{\mathrm{coh}}(\mathbf{q}), \tag{5.6}$$

where $\otimes$ denotes the convolution operation. The inverse Fourier transform of this expression gives the values of the complex degree of coherence $\gamma(\Delta\mathbf{r})$ for different separations

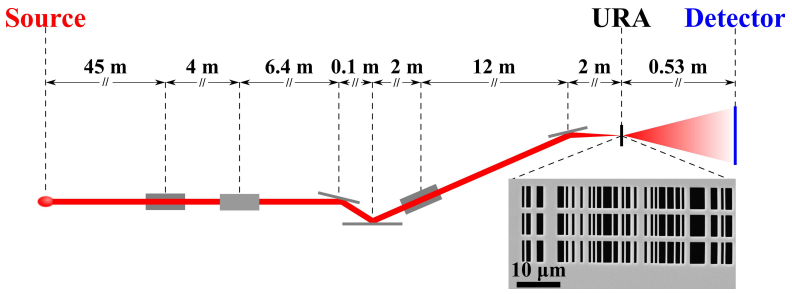

Figure 5.14: The layout of the PG2 beamline (Reproduced from [139]) and the SEM image of the URA aperture used during the coherence measurements.

of points $\Delta\mathbf{r} = \mathbf{r}_2 - \mathbf{r}_1$,

$$\gamma(\Delta\mathbf{r}) = I(\Delta\mathbf{r})/I_{\mathrm{coh}}(\Delta\mathbf{r}) \tag{5.7}$$

where $I_{\mathrm{coh}}(\Delta\mathbf{r})$ is the inverse Fourier transform of $I_{\mathrm{coh}}(\mathbf{q})$.

According to Equation (5.7), the knowledge of $I_{\mathrm{coh}}(\Delta\mathbf{r})$ and the measurement of the diffraction pattern produced by a partially coherent beam provides a way to obtain the CDC $\gamma(\Delta\mathbf{r})$ of the radiation incident on the aperture. To optimize this measurement, the aperture can be refined to find the best functional form of $I_{\mathrm{coh}}(\Delta\mathbf{r})$. It can be shown [137, 115] that in the far field, given a known incident wavefront and beam intensity profile, a measurement with a uniformly redundant array (URA) [138] as the aperture is an exemplary tool for diffraction-based coherence measurements. A URA consists of slits, which are arranged such, that on a finite grid every slit separation is present an equal number of times. It follows directly from Equation (5.7) that the CDC can be determined for all relative distances from the smallest separation within the URA up to the size of the URA aperture in a single measurement.

A drawback of a URA measurement is the fact, that the analysis requires a precise knowledge of the function $I_{\mathrm{coh}}(\mathbf{q})$. This function, however, depends on the properties of the incident radiation, such as intensity profile and the wavefront curvature. Different methods can be applied to determine $I_{\mathrm{coh}}(\mathbf{q})$. One can simulate the properties of the incident beam and find $I_{\mathrm{coh}}(\mathbf{q})$ by propagating the incident field through the URA structure and through free space to the detector using for example Equations (2.3,2.10). Another possibility is to use an aperture and to filter out the coherent part of the beam further upstream and to measure $I_{\mathrm{coh}}(\mathbf{q})$ on the detector using the same experimental apparatus.

The incident wave field has to be known, because each slit separation appears an equal number of times, but not only once. The double slit interference patterns from different positions within the whole aperture interfere in the plane of observation and a straightforward analysis without the knowledge of the wavefront is not possible. Instead of URAs non redundant arrays (NRA) [140, 141] can be used. There each slit separation is used only once and the wavefront curvature can be reconstructed from the interference pattern. However, also in an NRA measurement the intensity profile has to be known [140, 141].

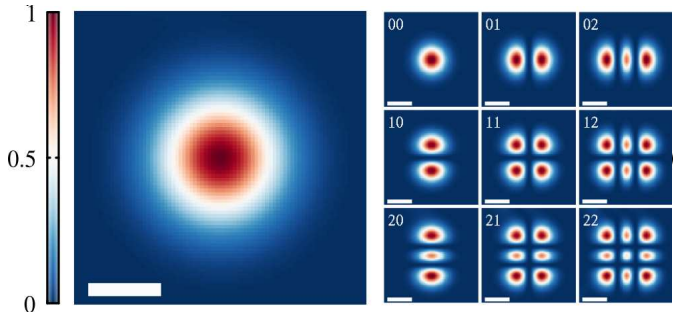

Figure 5.15: The total intensity distribution (left) and the intensity distribution of the lowest nine contributing modes (right) calculated in the focus of the PG2 beamline. The length of the scale bar is 20 µm. The contribution of the modes is the same as at the source shown in Figure 4.7.

We have used a URA to completely characterize the transverse coherence properties of individual FLASH pulses. The experiment was conducted at the plane grating monochromator beamline PG2 [139] at FLASH, where we measured the transverse coherence of the third harmonic (wavelength 2.7 nm) of the fundamental harmonic at a wavelength of 8 nm [93]. The beamline consists of 1 distribution mirror and a monochromator comprised of a collimating mirror, plane mirror ,plane grating, focusing mirror and an exit slit. The monochromatic beam is focused by a spherical mirror on the sample position 71.6 m downstream of the source. A schematic sketch of the beamline is shown in Figure 5.14 and an overview of the optical elements present in the beamline is shown in Table 5.1. To measure the coherence properties of the third harmonic the plane grating was set to its first order.

A one dimensional URA pattern was generated using the algorithm described in [138] [6]. The sample was a combination of three copies of the URA shifted in the vertical direction. The horizontal size of the URA was 50.5 µm, the smallest slit width and the smallest slit separation were both 0.5 µm. The vertical size was 18 µm, a slit width of 4.8 µm and a slit separation of 6.5 µm (see inset in Figure 5.14). The URA structure was manufactured[7] on a 100 nm thick silicon nitride membrane coated with 600 nm of gold and 200 nm of palladium by focused ion beam (FIB) milling. An SEM image of the complete structure is shown in Figure 5.14. The aperture was positioned in the focus of the beam, and the diffracted radiation was detected using a CCD camera 0.53 m downstream of the sample (see Figure 5.14).

For quantitative analysis of the URA measurements, the beam properties in the focus of the PG2 beamline were simulated for a wavelength of 2.7 nm. We considered the same source parameters as described in Section 3.3.2, i.e. a source size of 68 µm and a transverse coherence length at the source of 62 µm. This choice of source parameters is motivated by GENESIS simulations, which show that the source size of the fundamental

[6] The dimension parameter $r = 103$ was used.

[7] The structure was manufactured by D. Stickler in the group of H-P. Oepen at the University of Hamburg.

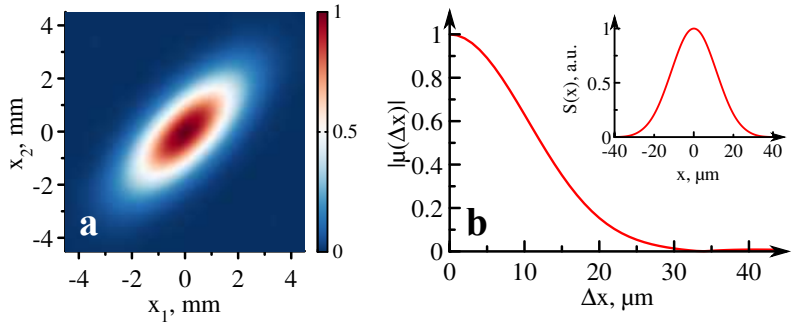

Figure 5.16: The transverse coherence properties of the radiation in the focus of the PG2 beamline for horizontal direction. The modulus of the CSD, $|W(x_1, x_2)|$ (a) the modulus of the SDC $|\mu(-\Delta x/2, \Delta x/2)|$ as a function of separation Δx (b). The inset in (b) shows the respective spectral density profile. The coherence properties in vertical direction are identical.

and the third harmonic are similar [127]. We applied the general scheme of propagation presented in Section 4.3 to calculate the coherence properties in the focus of the PG2 beamline. The propagation of individual modes $E^s_{jj'}(x, y)$ from the source to the observation plane was carried out using a conventional wave propagation code PHASE [143]. Perfect optics were assumed in our simulations.

As a result of these calculations the total spectral density distribution (or intensity profile in case of a monochromatic beam) and the lowest nine modes in the focus of the PG2 beamline are shown in Figure 5.15. The structure of the modes looks similar to the modes calculated at the source (see Figure 4.7), which is reasonable, since perfect optics have been assumed in our simulations. The simulated transverse coherence properties in the focus of the beam are presented in Figure 5.16. The CSD in the horizontal direction was calculated according to (4.16). The absolute values of this function are shown in Figure 5.16 (a). The corresponding modulus of the SDC, $|\mu(\Delta x)|$, is shown in Figure

Table 5.1: The layout of the PG2 beamline. The parameters for the monochromator [142] used in the calculations are shown in brackets.

element	distance from the source	incidence angle (surface)	Radius
plane mirror	45 m	2 deg	
toroidal mirror	49 m	2 deg	718.8 m/ 3.63 m
plane mirror	55.4 m	1.039 deg	
plane grating	55.5 m	2.75 deg	
sagittal mirror	57.5 m	2 deg	0.698 m
toroidal mirror	69.5 m	2 deg	57.3 m / 0.093 m
focus	71.5 m		

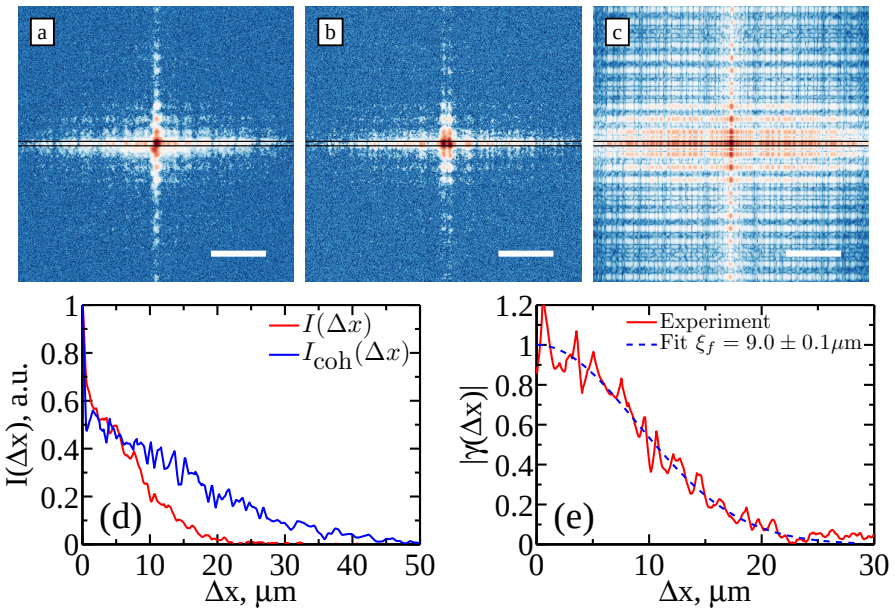

Figure 5.17: (a,b) URA diffraction patterns measured with different single pulses shown in logarithmic intensity scale. (c) The diffraction pattern $I_{\mathrm{coh}}(\mathbf{q})$ calculated in Fresnel approximation for the URA shown in Figure 5.14. (d) The inverse Fourier transforms $I(\Delta x)$ and $I_{\mathrm{coh}}(\Delta x)$ of $I(q_x)$ and $I_{\mathrm{coh}}(q_x)$ shown in (a,c). The analyzed region is shown by black rectangles. (e) The modulus of the CDC, $\gamma(\Delta x)$ as a function of separation Δx determined from the single pulse diffraction pattern (a) using Equation (5.7) (red solid line). A Gaussian fit is shown by blue dashed line. The scale bar in (a-c) is 1 mm wide.

5.16 (b). The SDC is perfectly fit by a Gaussian with a transverse coherence length of 10 μm in the horizontal direction. The inset of Figure 5.16 (b) shows the spectral density profile in the horizontal direction. The rms width of the beam is 11 μm. A wavefront curvature of $R = 4.8$ m in the horizontal direction for the most dominant TEM_{00} mode was found. The coherence properties in horizontal and vertical direction are identical, therefore only horizontal direction is presented.

For the URA analysis the coherent diffraction pattern $I_{\mathrm{coh}}(\mathbf{q})$ was calculated in Fresnel approximation using Equations (2.10,2.3). The aperture transmission function $T(\mathbf{r})$ with a value of $T(\mathbf{r}) = 1$ for the transmission region and a value of $T(\mathbf{r}) = 0$ for the opaque region was obtained from the SEM image of the URA shown in Figure 5.14. The incident beam properties determined through simulations in the horizontal direction were used: a beam size of $\sigma_f = 12$ μm and a wavefront curvature of $R = 4.8$ m. To calculate I_{coh} the CDC was set to 1 everywhere $\gamma(\Delta\mathbf{r}) = 1$, i.e. $\xi \gg \sigma$. According to Equation (5.7) the intehsity profile of the partially coherent and coherent beam are the same.

Fifty single shot diffraction patterns in each direction were recorded and analyzed using Equation (5.7). The analysis of a typical single shot interferogram is shown in

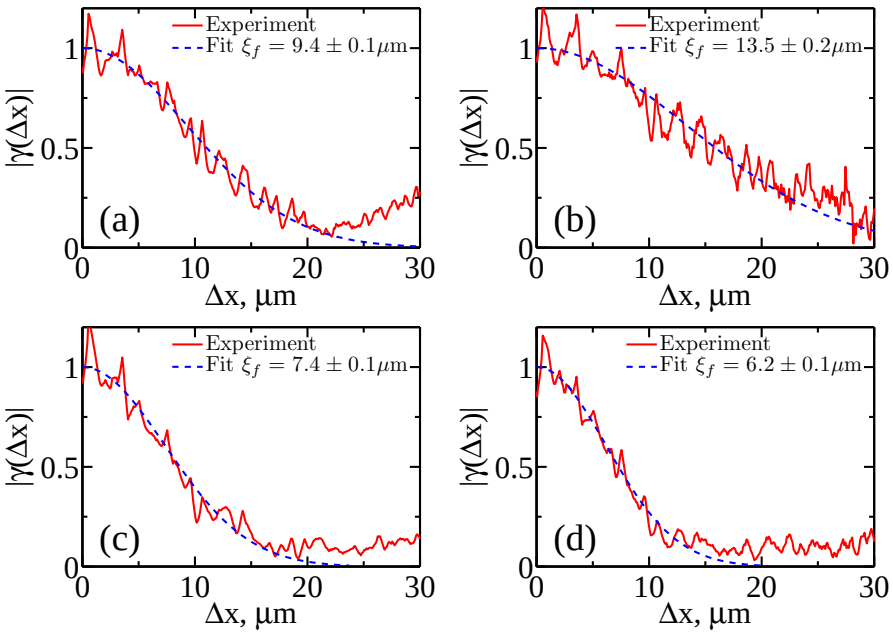

Figure 5.18: The analysis of URA diffraction patterns for different individual FLASH pulses.

Figure 5.17. The measured $I(\mathbf{q})$ and the calculated $I_{\mathrm{coh}}(\mathbf{q})$ diffraction patterns are shown in Figure 5.17 (a,b) and (c), respectively. The rectangular region (indicated by a black box) in the image (seven pixels high) was averaged to determine $I(q_x)$ and $I_{\mathrm{coh}}(q_x)$. The inverse Fourier transforms $I(\Delta x)$ and $I_{\mathrm{coh}}(\Delta x)$ of the intensities $I(q_x)$ and $I_{\mathrm{coh}}(q_x)$ are shown in Figure 5.17 (d). The modulus of the CDC $|\gamma(\Delta x)|$ as a function of the separation Δx in the horizontal direction was determined for this individual FLASH pulse by applying Equation (5.7) and is shown in Figure 5.17 (e) by the red line. The experimentally found $|\gamma(\Delta x)|$ is well reproduced by a Gaussian $N \cdot \exp(-\Delta x^2/[2\xi_f^2])$ (blue dashed line in Figure 5.17 (e)). The fit parameter N was introduced to normalize $|\gamma(\Delta x)|$ to unity at $\Delta x = 0$. A transverse coherence length of $\xi_f = 9.0 \pm 0.1$ µm was found for this particular pulse.

The same analysis was performed for all measured data. In a large number (27 out of 50) of single shot measurements two superimposed diffraction patterns shifted by a small distance with respect to each other were observed (see Figures 5.17 (b)). The direction and magnitude of this shift in different recorded diffraction patterns appears to be uncorrelated. The analysis of these diffraction patterns yields an oscillatory behaviour of $|\gamma(\Delta x)|$. The possibility that unintentionally two FLASH pulses were measured in one diffraction pattern was excluded during the measurement by reducing the fast shutter opening time to a value, which was significantly smaller than the time between two consecutive pulses from FLASH. A possible explanation for the appearance of the superposition of two diffraction patterns could be the presence of two spatially separated sources in the FLASH undulator which both contribute to a single FEL pulse. An indi-

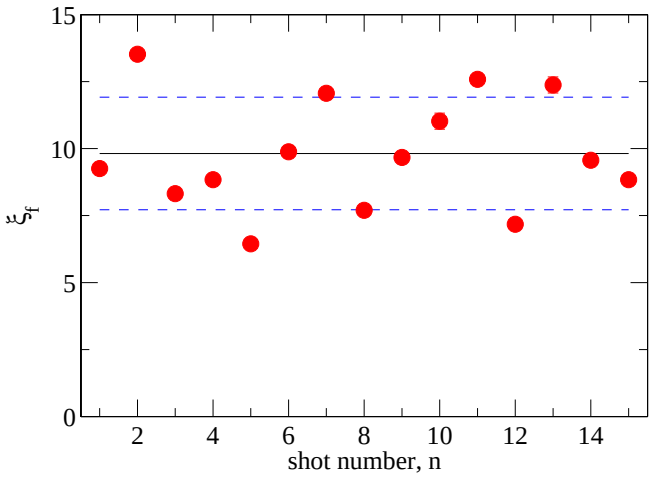

Figure 5.19: The analysis of the URA diffraction patterns for different individual FLASH pulses. Each circle represents a transverse coherence length determined from the Gaussian fit to the modulus of the CDC $|\gamma(\Delta x)|$ (see Figure 5.18). The mean value (black solid line) and the rms deviation (blue dashed lines) of all values are shown. The error bars are smaller than the symbols used to represent the results.

cation of two sources at FLASH was also observed during beam position measurements in the far field [142].

In total 15 out of 50 pulses produced clean diffraction patterns with a high signal[8]. In Figure 5.18 we present the modulus of the complex coherence factor in the horizontal direction for some of these FEL pulses. It can be seen in Figure 5.18 that $|\gamma(\Delta x)|$ is well approximated by a Gaussian function for each FEL pulse. The transverse coherence length ξ_f was obtained for each analyzed pulse and is shown in Figure 5.19. The values vary from shot to shot between $\xi_f = 6.2 \pm 0.1$ µm (Figure 5.18 (d)) and $\xi_f = 13.5 \pm 0.2$ µm (Figure 5.18 (b)). The average over 15 single shot values of the transverse coherence length is $\bar{\xi}_f = 9.8 \pm 2$ µm. For the majority of these (10 out of 15) the transverse coherence length lies within the error bar of the average value (see Figure 5.19).

We compared the experimentally determined values with our simulations performed using the coherent mode decomposition. Both the measured and the simulated modulus of the CDC $|\gamma(\Delta x)|$ are well reproduced by Gaussian functions. The measured transverse coherence length $\bar{\xi}_f = 9.4 \pm 2$ µm and the calculated value $\xi_f = 10$ µm are in good agreement. The simulated rms beam width of $\sigma_f = 12$ µm concords with beam size measurements at a distance of 0.37 m downstream of the source (see Appendix A.9). The experimental data, however, indicate a slightly larger focus size. The agreement between

[8]The remaining 8 diffraction patterns were neglected in the analysis due to poor statistics in the diffracted signal.

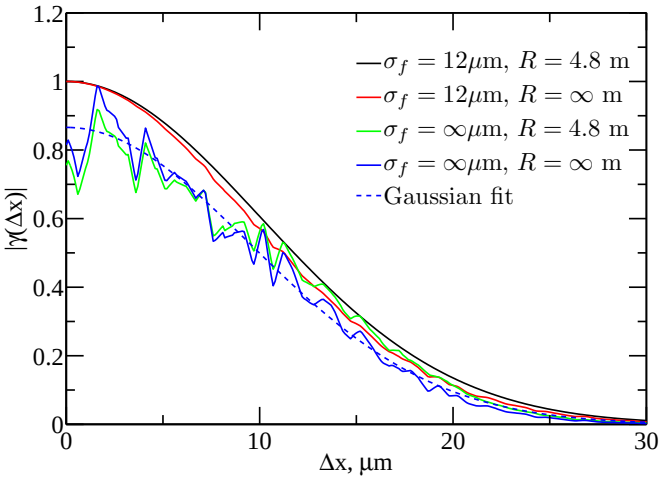

Figure 5.20: The impact of the wavefront curvature on the analysis of the URA diffraction patterns. The "experimental" diffraction pattern $I(\mathbf{q})$ in (5.7) is calculated using a Gaussian Schell-model beam with $\xi_f = 10$ µm, $\sigma_f = 12$ µm, and $R = 4.8$ m. The coherent ($\xi_f = \infty$) diffraction pattern $I_{\text{coh}}(\mathbf{q})$ was simulated with $\sigma_f = 12$ µm and $R = 4.8$ m (black solid line), $\sigma_f = 12$ µm and $R = \infty$ m (red solid line), $\sigma_f = \infty$ µm and $R = 4.8$ m (green solid line), and $\sigma_f = \infty$ µm and $R = \infty$ m (blue solid line). A Gaussian fit to the blue circles is shown by the blue dashed line.

the measured and the simulated values is surprising, as we used source parameters in the simulations, which were determined at a different wavelength. It is very likely that during the measurement the source parameters were different. Nevertheless, the agreement between the experimental and theoretical results shows that the assumption made for the theoretical simulations were not too far off from the real situation.

The impact of the intensity profile and the wavefront of the incident beam on the CDC determined in a URA measurement was analyzed. In particular, we replaced the experimental diffraction pattern $I(\mathbf{q})$ with a simulated pattern. A beam size, transverse coherence length, and wavefront curvature of $\sigma = 12$ µm, $\xi = 10$ µm and $kx^2/(2R)$ with $R = 4.8$ m, respectively, were used to calculate $I(\mathbf{q})$. These values were determined through the mode decomposition method (see Figure 5.16). This "experimental" diffraction pattern was analyzed exactly in the same way as the measured data, i.e. using Equation (5.7). The analysis was performed four times with varying conditions to calculate I_{coh} (see Figure 5.20).

1. $\sigma = 12$ µm, $\xi = 10$ µm, $R = 4.8$ m (input values)
2. $\sigma = 12$ µm, $\xi = 10$ µm, $R = \infty$ m (incorrect wavefront)
3. $\sigma = \infty$ µm, $\xi = 10$ µm, $R = 4.8$ m (incorrect beam size)
4. $\sigma = \infty$ µm, $\xi = 10$ µm, $R = \infty$ m (incorrect beam size and wavefront).

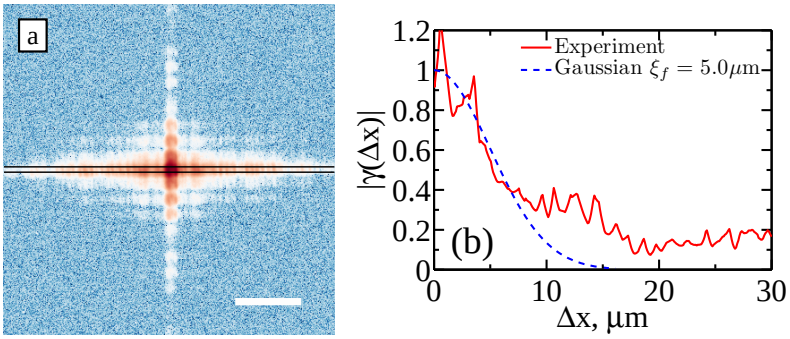

Figure 5.21: (a) Sum of all measured diffraction patterns. The rectangular area in the center is 7 pixel high and shows the analyzed region. (b) The average modulus of the CDC $|\gamma(\Delta x)|$ (red line) determined from the diffraction pattern in (a). A Gaussian function with $\xi_f = 5$ µm (blue dashed line) is also shown. The scale bar in (a) is 1 mm wide.

It is readily seen in Figure 5.20 that the determined CDC depends on both the intensity and the wavefront curvature of the parameters of the incident radiation, used in the analysis. The analysis with the correct beam parameters yields the CDC, which was used as the input of the simulation (black line). We also see in Figure 5.20 that the wavefront is not significant in our case. The red curve obtained with an incorrect wavefront in the analysis deviates just slightly from the input CDC shown by the black line. In our simulation the intensity distribution has a larger impact on the URA analysis (blue and green curves in Figure 5.20). Both curves show strong modulations, which appear as a result of inhomogeneous illumination of the slits within the URA structure. The Gaussian fit (blue dashed line in Figure 5.20) to $|\gamma(\Delta x)|$ obtained in the worst case, when both beam size and wavefront curvature are wrong (blue line in Figure 5.20), yields a transverse coherence length of 9.5 ± 0.1 µm. This number is about 5% smaller than the simulated transverse coherence length $\xi = 10$ µm. The analysis of all measured data with the plane wave approach provides slightly lower values for the transverse coherence length. However, the discrepancy of these values is less than 5% for all measured diffraction patterns.

We have also estimated the average transverse coherence length of all 50 measured pulses, including the pulses being generated by two sources. The average diffraction pattern (see Figure 5.21 (a)) was analyzed using the procedure, which was used for the analysis of single pulse diffraction patterns. The modulus of the CDC obtained from the average diffraction pattern is shown in Figure 5.21. We note that the functional form cannot be reproduced by a single Gaussian, however, the transverse coherence length can be estimated to be about 5 µm. The average transverse coherence length is reduced by a factor of two as compared with single shot diffraction patterns.

The decrease of the coherence length is possibly due to the mirror imperfections and small positional uncertainties of the FEL beam. Each shot 'sees' a different part of the mirror and an average over many shots smears out the features measured on the detector

and reduces the effective coherence length. Additionally to the surface imperfections of the optical elements, radiation at a wavelength of 2.7 nm is strongly absorbed by the carbon mirror coatings. This might introduce additional phases on each mirror. Another explanation is the presence of two sources in the FEL beam (see comment on page 102). In the single shot analysis we considered only clean diffraction patterns, where only one source was observed. During the averaging procedure we consider all measured pulses and obtain an average coherence length of two sources, which is smaller than the value determined from clean patterns.

5.5 Intensity correlations

More than half a century ago Hanbury Brown and Twiss have demonstrated [63, 2] that measurements of intensity fluctuations of light from a chaotic source at two separated spatial positions carry information on the coherence and hence the size of the source. These pioneering experiments initiated developments in the field of quantum optics [64]. Nowadays similar principles are used in the analysis of correlations in the systems of ultra-cold atoms forming Bose-Einstein condensates [65]. The core idea of the Hanbury Brown and Twiss experiment is to measure the second-order correlation function (2.18)[9]

$$\begin{aligned}\Gamma^{(2)}(\mathbf{r}_1,\mathbf{r}_2,;t_1,t_2) &= \langle E^*(\mathbf{r}_1,t_1)E^*(\mathbf{r}_2,t_2)E(\mathbf{r}_2,t_2)E(\mathbf{r}_1,t_1)\rangle = \\ &= \langle I(\mathbf{r}_1,t_1)I(\mathbf{r}_2,t_2)\rangle\,.\end{aligned} \tag{5.8}$$

They measured the intensity fluctuations at two detectors positioned at separated points $\mathbf{r}_1$ and $\mathbf{r}_2$ as a coincidence effect. The time resolution of the detectors was good enough to resolve the fluctuations of the radiation. With a not sufficient time resolution average intensities $\langle I(r,t)\rangle_T$ instead of the instantaneous intensities $I(r,t)$ appear in (5.8) and $\Gamma^{(2)}(\mathbf{r}_1,\mathbf{r}_2;t_1,t_2)$ approaches a constant value given by $\langle I(r_1,t_1)\rangle_T\langle I(r_2,t_2)\rangle_T$.

For chaotic light obeying Gaussian statistics Equation (5.8) reduces to [46, 144]

$$\Gamma^{(2)}(\mathbf{r}_1,\mathbf{r}_2;\tau) = \langle I(\mathbf{r}_1,t)\rangle\langle I(\mathbf{r}_1,t)\rangle\left(1+|\gamma(\mathbf{r}_1,\mathbf{r}_2;\tau)|^2\right) \tag{5.9}$$

where $\tau = t_2 - t_1$ and $\gamma(\mathbf{r}_1,\mathbf{r}_2;\tau)$ is the CDC defined in (2.17). Therefore, a measurement of the normalized second order correlation function (2.19)

$$\gamma^{(2)}(\mathbf{r}_1,\mathbf{r}_2;\tau) = \frac{\Gamma^{(2)}(\mathbf{r}_1,\mathbf{r}_2;\tau)}{\langle I(\mathbf{r}_1,t)\rangle\langle I(\mathbf{r}_1,t)\rangle} = 1+|\gamma(\mathbf{r}_1,\mathbf{r}_2;\tau)|^2$$

yields the absolute value of the first-order correlation function, $\gamma(\mathbf{r}_1,\mathbf{r}_2)$. Hanbury Brown and Twiss have measured the transverse coherence properties of the light from a star, and have used the van Cittert-Zernike theorem to determine the size of the star. The success of their method is based on the fact, that intensity measurements are not sensitive to phases, as they are simply not measured. The phase fluctuations introduced during

[9] For brevity we write $\Gamma^{(2)}(\mathbf{r}_1,\mathbf{r}_2;t_1,t_2)$ instead of $\Gamma^{(2)}(\mathbf{r}_1,\mathbf{r}_1,\mathbf{r}_2,\mathbf{r}_2;t_1,t_1,t_2,t_2)$.

the propagation through the atmosphere made amplitude based stellar interferometry extremely challenging.

Later it was suggested by Ikonen [145] that measurements of intensity correlations can be extended from stationary to pulsed sources. He pointed out that the pulse duration defines the time resolution of the measurement and has estimated the impact of a finite pulse duration on the outcome of the second-order correlation function [145]

$$\gamma^{(2)}(\mathbf{r}_1, \mathbf{r}_2) = 1 + \frac{\tau_c}{2T}|\gamma(\mathbf{r}_1, \mathbf{r}_2)|^2, \tag{5.10}$$

where τ_c is the coherence time of the radiation and T is the pulse duration[10]. It follows from (5.10) that the ratio between the coherence time τ_c and the pulse duration T has to be sufficiently high in order to determine the first order correlation function. In particular Ikonen proposed to measure intensity correlation at synchrotron sources, with their pulse durations of less than 100 ps and the ability to achieve a comparably high coherence time using monochromators.

This approach was demonstrated at synchrotron sources [146, 147], where an ultra high-resolution monochromator ($\Delta E = 120\,\mu\text{eV}$ at $E = 14\,\text{keV}$) was used to obtain a coherence time comparable with the 30 ps single pulse duration at the SPRING8 synchrotron source. Fast avalanche photo diode detectors were used in [146, 147] to discriminate different bunches from the synchrotron.

Both difficulties present at the synchrotron sources may be overcome at FEL sources:

- The pulse duration at FEL sources is about three orders of magnitude shorter than the pulse duration at synchrotron sources and intensity correlation measurements seem to be feasible. Typically, in the hard x-ray regime the ratio $\tau_c/2T$ is about 10^{-3}. However, a monochromator can be used to reduce the bandwidth and to increase the coherence time. For instance, with a pulse duration of about 100 fs and a bandwidth of $\Delta E/E = 10^{-4}$ at a photon energy of 12 keV, the ratio $\tau_c/2T$ will be about 0.01. As will be shown later this value should be sufficiently high to determine the correlation function from the intensity correlation measurement.

- Another important issue is that at FEL sources the time between consecutive pulses can be arbitrarily chosen. Then a pixelated detector with comparably poor time resolution can be used, and a coincidence measurement between all measured intensity positions (individual pixels) can be performed simultaneously. From the same dataset higher order correlation functions $\Gamma^{(n)}$ for $n > 2$ can be easily calculated.

According to FEL theory [44, 68] in the linear regime of operation FEL sources obey Gaussian statistics, and the second-order correlation function is expected to have the form of Equation (5.10). An ensemble of pulses in the frame of the Gaussian statistics, which mimics a FEL in linear regime, was simulated and analyzed. We utilized the

[10] In ref. [145] the pre factor τ_c/T appears in formula 5.10. It is, however, not specified which definition of the coherence function was used. We will see later in Figure 5.23 (a), that the ratio $\tau_c/2T$ provides the proper scaling in our simulations.

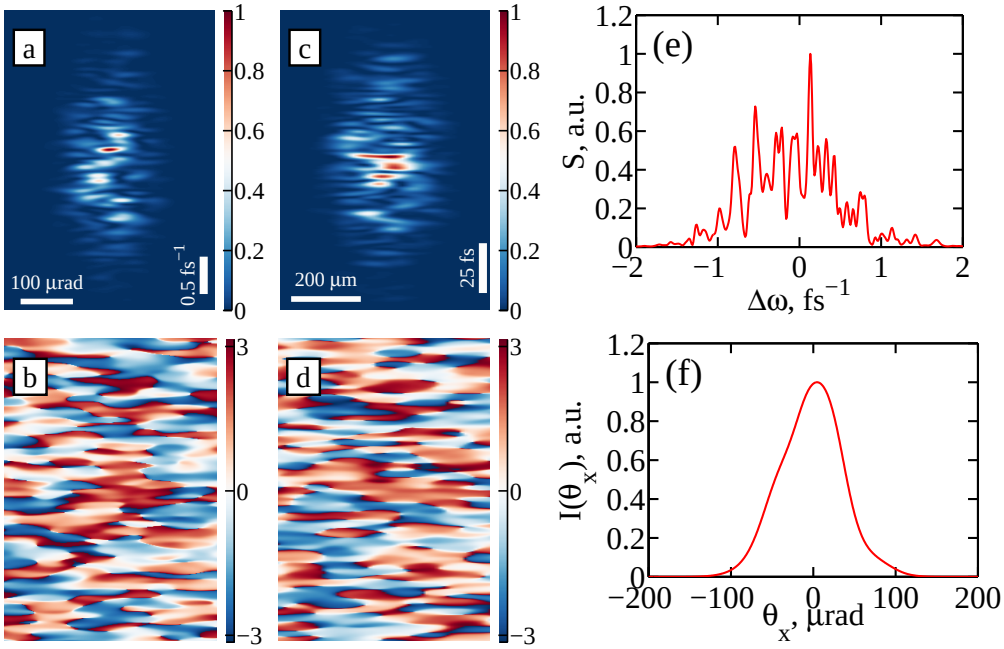

Figure 5.22: An individual radiation pulse generated with the method described in Appendix A.3. (a) The intensity and the (b) phase of the field $E(\theta_x, \Delta\omega)$ as a function of the angle $\theta_x = q_x/k$ and $\Delta\omega = \omega - \omega_0$. The same quantities for the field $E(x,t)$ (c,d). (e) The spectrum $S(\Delta\omega) = \int |E(\theta_x, \Delta\omega)|^2 \mathrm{d}\theta_x$ and (f) the intensity profile $I(\theta_x) = \int |E(\theta_x, \Delta\omega)|^2 \mathrm{d}\Delta\omega$ are also shown. The scale in (a,b) and (c,d) are identical.

approach described in the Appendix A.3 (see Equation (A.16)), to generate a large statistical ensemble of pulses. We then applied the intensity correlation analysis to this ensemble. We used parameters of FLASH (see chapter 3.3.2) with a wavelength of 13.5 nm, a source size of $\sigma = 68$ µm, and a transverse coherence length of $\xi = 62$ µm. We assumed a FWHM bandwidth of $\Delta\omega/\omega_0 = 1\%$, which is typical for FEL sources at this photon energy and $T = 21$ fs, which corresponds to a FWHM pulse duration of 50 fs. The field $E(\theta_x, \Delta\omega)$ as a function of the scattering angle $\theta_x = q_x/k$ in the far field and $\Delta\omega = \omega - \omega_0$ is shown in Figure 5.22(a,b). The field of the same pulse $E(x,t)$ as a function of the source position x and time t is shown in Figure 5.22 (c,d). It is readily seen from this figure that the field is partially coherent in space and time. From the structure of the 'speckles' in the intensity profile in x direction we estimate that the width of a single 'speckle' is about five times smaller than the width of the beam. This indicates that about five transverse modes are present in the beam, in agreement with the results in 3.3.2. The structure of the field in the spectral domain $\Delta\omega$ is slightly different. There are about twenty modes present. As such, the transverse coherence of the pulse is higher than its temporal coherence. It is worth noting that the area where the amplitude is approximately constant coincides with the size of the 'speckles' in the

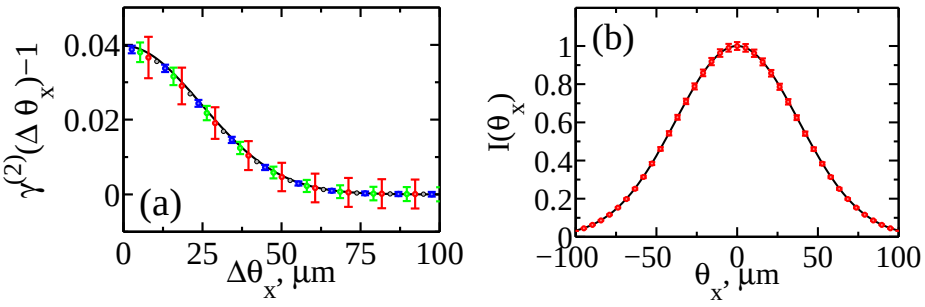

Figure 5.23: Intensity correlation analysis. The second order correlation function $\gamma^{(2)}(\Delta\theta_x) - 1$ determined from an average over 100 pulses (red circles), 500 pulses (green circles), 2500 pulses (blue circles), 25000 (black circles) pulses are shown. The black line shows the same function calculated according to (5.10). The intensity profile determined from the same number of pulses marked with the same colors as in (a) is shown in (b) for an average of 100 pulses.

intensity distribution. This is a characteristic of a chaotic ensemble, as mentioned above, and is the origin of the relation (5.9) [144].

The single pulse spectrum defined as $S(\Delta\omega) = \int |E(\theta_x, \Delta\omega)|^2 \mathrm{d}\theta_x$ and the intensity profile $I(\theta_x) = \int |E(\theta_x, \Delta\omega)|^2 \mathrm{d}\Delta\omega$ are presented in Figure 5.22 (e) and (f). The longitudinal mode structure is well visible in the spectrum. In the average intensity profile (Figure 5.22 (f)), however, the mode structure is suppressed. An average over a high number of longitudinal modes smears out the structure of the transverse modes. If the pulse would be longer and the bandwidth remained the same an even higher smearing would be observed in (Figure 5.22 (f)). In the limit $T \gg \tau_c$ the mode structure vanishes and an intensity correlation analysis is not possible, in agreement with (5.10).

The results from the intensity correlation analysis of the ensemble of the generated statistical pulses are shown in Figure 5.23. A total ensemble of 25000 pulses was generated and different portions of this ensemble were analyzed separately. The normalized second order correlation function calculated from 250 different ensembles of 100 pulses, 50 ensembles of 500 pulses, 10 ensembles of 2500 and from one ensemble of 25000 pulses is shown in Figure 5.23 (a). The standard deviations between values found during the analysis of different ensembles were considered as the errorbars. For comparison, $\gamma^{(2)}(\Delta\theta_x)$ calculated using Equation (5.10) is also shown. It can be seen that in our simulation about 500 pulses are sufficient to estimate the transverse coherence properties of the radiation and the errors are small. The values determined from the total ensemble of 25000 pulses reproduce well the analytical formula (5.10). The intensity distribution of the same ensemble of pulses is shown in Figure 5.23 (b). There 100 pulses give a sufficient estimate of the intensity distribution.

The same analysis was performed for a varying bandwidth of the radiation, which can be adjusted by a monochromator. Five different values of the bandwidth in the range between 1% and 0.1% were simulated, while the pulse duration was fixed. The

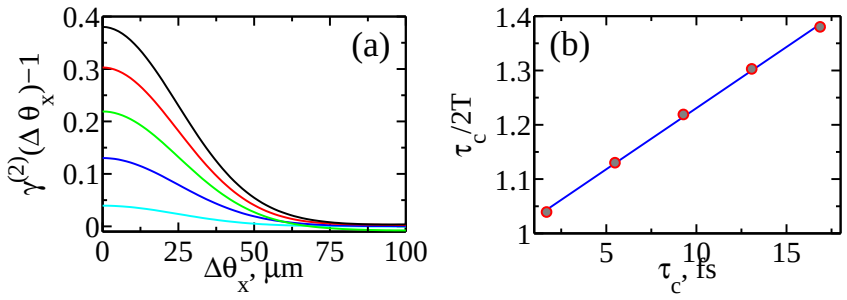

Figure 5.24: Intensity correlation analysis for a varying bandwidth. (a) The second order correlation function $\gamma^{(2)}(\Delta\theta_x) - 1$ determined from an average over 5000 pulses for a FWHM bandwidth σ_{FWHM} of 1% (black line), 0.31% (red line), 0.18% (green line), 0.13% (blue line), and 0.1% (cyan line). (b) The values $\gamma^{(2)}(0) - 1$ as a function of the coherence time $\tau_c = 1/\sigma_f$. From the linear fit (blue line) we determine a pulse duration of $T = 22.2 \pm 1.4$ fs.

second order correlation function determined from 5000 shots for each magnitude of the bandwidth is shown in Figure 5.24. All curves yield the same transverse coherence length, they have, however, a different value at $\Delta\theta_x$ as expected from Equation (5.10). We analyzed the ratio

$$\frac{\tau_c}{2T} = \gamma^{(2)}(0) - 1$$

for different values of the bandwidth, which correspond to different coherence times τ_c, and determined the pulse duration T (see Figure 5.24). A linear fit through the found values yields a pulse duration of $T = 22.2 \pm 1.4$ fs, which agrees well with the initial value of $T = 21$ fs. A similar approach was used in [147] to characterize the pulse duration of the synchrotron radiation.

Finally, the intensity correlation method can be effectively applied to measure the transverse coherence properties of beams generated at an FEL operating in the linear regime. These measurements for a varying bandwidth also provide the average pulse duration of the radiation. This method might be especially effective in characterizing the pulse durations of very short pulses, as shorter times increase the contrast in the measurement. Importantly, the experimental arrangement is simple and 5000 pulses can be accumulated in 10 minutes, provided the FEL operates with a repetition rate of 10 Hz.

Additionally, by a measurement of higher order correlation functions in the saturation or nonlinear regime one might investigate whether the FELs possess coherence of orders higher than one in the x-ray regime. Using the method outline above we can easily calculate the correlation function for order shigher than two, as the intensity in each detector pixel are available. This can be used to find out whether FELs obey Gaussian statistics or not. Second and higher order intensity correlation functions at FLASH were measured recently [148]. In these experiments we demonstrated the high transverse coherence properties of FEL beam that makes it similar to laser sources. At the same

time, we have seen that FEL radiation obeys Gaussian statistics in non-linear regime that makes it similar to chaotic sources.

6 Summary

Theoretical investigation

We have applied a general theoretical approach based on the results of statistical optics to describe the correlation properties of fields generated by third generation synchrotron, FEL and next generation synchrotron sources. Assuming stationary radiation, we have substituted a real source by an equivalent planar Gaussian Schell-model (GSM) source with the same size and divergence as a real source. This phenomenological approach characterizes the source with four parameters, the source size and its transverse coherence length in the horizontal and vertical direction. It can be used to propagate the correlation functions to different distances from the source, including the propagation through thin optical elements, with simple analytic functions. The size of an x-ray beam and its coherence length can be estimated at any distance from the source. As this approach is mostly suited for the description of synchrotron sources we have established limits of the applicability of the GSM for these sources. We found that at the state of the art third generation synchrotron source PETRA III the GSM can be applied to precisely calculate the coherence properties of wave fields at x-ray energies higher than 3 keV. At less brilliant sources the GSM yields realistic estimates at even lower photon energies. Additionally, an analytical description of focusing of partially coherent radiation has been developed. This method was used to calculate coherence properties near the focus of the P10 beamline at PETRA III, which concord well with experimental beam size measurements.

The GSM was also used to estimate the coherence properties of planned new generation x-ray sources. We found, that with the anticipated electron beam parameters highly coherent photon beams with a total degree of coherence of about 30% can be expected in the hard x-ray regime.

We have investigated whether the approximation of stationary radiation is applicable to pulsed sources, which is especially questionable at FEL sources with their ultrashort pulses. We have shown that the temporal coherence does not influence the spatial coherence (and vice versa) of x-ray wave fields during propagation in free space for all realistic sources available today and in near future. As such, in the x-ray regime the propagation laws for the coherence functions well known for stationary fields can be applied to propagate the wave fields generated at pulsed sources. This is in contrast to the radiation fields produced by optical lasers, where a coupling between temporal and spatial coherence may occur during propagation.

Theoretical investigations of highly coherent fields generated at FELs were performed using the mode decomposition of the correlation functions. We found, that sources as coherent as FELs can be described by a small number of contributing modes. We have

also presented a computational method, which is based on the mode decomposition and allows to calculate the transverse coherence properties as well as the beam intensity profile of partially coherent radiation at any position in a beamline. Our approach can be easily implemented, since it is based on wavefront propagation, for which several powerful computational methods are already developed. The important extension to the conventional wave propagation methods is the consideration of all contributing modes. We applied this method to calculate the propagation of the correlation properties for two realistic examples. We also demonstrated that the modes and their contributions can be readily found numerically, if the correlation function at the source is known. This means, that the mode decomposition approach can be used to simulate the characteristics of realistic FEL beams, determined for example in detailed SASE calculations.

Experimental characterization of coherence at FELs

We have conducted several experiments to characterize coherence properties of FEL sources. The coherence properties of the LCLS using the focused soft x-ray beam at a photon energy of 780 eV were measured. The beam at LCLS is highly coherent, however, not fully coherent. The total degree of transverse coherence was found to be 56%, from which we estimate that 78% of the total power is contained in the dominant mode. Furthermore, the temporal coherence of the LCLS beam was measured to be 0.55 fs, in good agreement with an averaged LCLS spectrum at these energies. We have also estimated the degeneracy parameter of the LCLS radiation to be in the range of 10^{10} to 10^{11}. This value is in good agreement with $10^{10} - 10^{14}$ predicted from detailed SASE simulations [44]. This number is significantly larger than at any other existing sources operating at this photon energy range and is comparable with the degeneracy parameter of conventional optical lasers.

We have also measured the transverse and longitudinal coherence properties of the XUV free-electron laser FLASH. We have experimentally verified that the transverse coherence length is similar in both directions. From our measurements we conclude that the focused FLASH beam is highly coherent with a total degree of transverse coherence of about 40%. A mode decomposition has shown that about 60% of the total power is concentrated in the fundamental mode. The temporal coherence was measured to be 1.8 fs. The degeneracy parameter of the FLASH was found to be in the range of 10^{10} to 10^{11}, similar to LCLS.

In 2009 FLASH went through a major upgrade, where, along with another electron energy upgrade yielding photon wavelengths down to about 4 nm, a 3rd harmonic accelerator module was installed, in order to improve the capabilities for longitudinal electron bunch compression and in this way enhance the machine stability. This led to a higher stability of the FEL operation at the expense of longer pulse durations, typically around 100 fs. Our measurements before and after the upgrade indicate, that the transverse coherence has been significantly improved through the upgrade.

We also measured the transverse coherence using uniformly redundant arrays (URA). This method allows to determine the coherence properties completely from one interference pattern. In particular, the transverse coherence properties of the third harmonic

radiation at a wavelength of 2.7 nm in the water window were analyzed. The results of these measurements concord well with the simulations performed in the frame of a mode decomposition analysis. The transverse coherence length of single pulses varies, however, about 70% of these values lie within the standard deviation of all values. Averaging over a number of pulses reduced the transverse coherence length by a factor of two. The apparent drop of the transverse coherence length is possibly due to the impact of optics imperfections and positional instabilities of the FEL beam.

As an alternative method, we proposed to conduct Hanbury Brown and Twiss experiments at FELs. Measuring the intensity correlations it is possible to determine the average transverse coherence properties and the average pulse duration of FEL radiation. Analyzing higher order correlation functions gives a deeper understanding of the quantum statistics of FEL radiation. Using simulations we confirmed, that such measurements are feasible at FEL sources.

Conclusions

In conclusion, we have presented several theoretical techniques, which can be used to predict the transverse coherence properties of synchrotron and FEL radiation. These methods can be effectively used to calculate radiation characteristics at the experimental stations and will hopefully help the beamline scientists and experimentalists to better utilize the partially coherent beams at third and fourth generation x-ray sources.

Finally, coherence measurements presented in this thesis lead to a better undestanding of the high degree of coherence at FEL sources and provide a solid foundation for future coherence-based experiments that exploit these bright, coherent x-ray beams. These coherence measurements at FEL sources indicate that almost the full transverse photon flux is coherent and can be used for coherence-based applications. The degeneracy parameter was found to be in the range of $10^{10} - 10^{11}$, which is similar to conventional laser sources and was never observed at these wavelengths at synchrotron sources. However, in the time domain FEL and conventional laser sources are fundamentally different. The former produce pulses with poor temporal coherence, whereas the latter generate fully coherent pulses. Theory also predicts that SASE FELs are similar to chaotic sources and therefore can be only coherent in the first order. An intriguing question is whether seeded FELs will be fully coherent sources in all orders according to Glauber and in this way be equivalent to conventional single mode lasers. Hanbury Brown and Twiss experiments may be a tool to answer this question.

Acknowledgements

First of all I thank my family for supporting me throughout my work. I would like to express gratitude for my advisors, Prof. Dr. Ivan Vartaniants and Prof. Dr. Edgar Weckert for their supervision and useful ideas concerning my work.

The measurements have been performed in large collaborations. The work at LCLS would not be possible without the groups of D. Attwood, K. Nugent, A. Scherz, H. Sinn, Y. Acremann, J. Lüning, W. Wurth, and the LCLS team. The double pinhole measurements at FLASH were performed together with the groups of W. Wurth, A. Rosenhahn, T. Salditt, D. Attwood and the FLASH team. The double slit measurements were performed by the FLASH team, including M. Kuhlmann, S. Duesterer and R. Treusch. The URA measurements were done together with the groups of H-P. Oepen, S. Eisebitt, G. Gruebel and the FLASH team. The measurements at PETRA III were performed together with the group of A. Petukhov and the P10 team. I also would like to thank J. Bahrdt for providing the wave propagation code PHASE and for his support in using this code.

I appreciate support from all my colleagues at DESY in Hamburg, in particular Adrian Mancuso, who was deeply involved in most of the measurements described in this thesis. I would also like to thank Johannes Gulden, Oleksandr Yefanov and Ulf Lorenz, who have been a great help during my work. I also would like to thank Ulf Lorenz for carefully reading of my thesis.

7 List of Abbreviations

CDC	Complex Degree of Coherence
CRL	Compound Refractive Lenses
CSD	Cross Spectral Density
ERL	Energy Recovery Linac
ESRF	European Synchrotron Radiation Facility
FEL	Free-Electron Laser
FLASH	Free-Electron LASer in Hamburg
FWHM	Full Width at Half Maximum
GSM	Gaussian Schell-Model
LCLS	Linac Coherent Light Source
MCF	Mutual Coherence Function
SASE	Self Amplification of Spontaneous Emission
SDC	Spectral Degree of Coherence
SEM	Scanning Electron Microscopy
XUV	Extreme Ultra Violet

8 List of Symbols

$\langle \cdots \rangle$	Ensemble average
$\langle \cdots \rangle_T$	Time average
a_x, a_y	Slit width and height
c	Speed of light
D	Pinhole diameter
Δ	Expansion coefficient
δ	Degeneracy parameter
ε	Emittance of the photon beam
$\varepsilon_{\mathrm{coh}}$	Emittance of the diffraction limited Gaussian photon beam
ε_{e}	Emittance of the electron beam
$\Gamma(\mathbf{r}_1, \mathbf{r}_2, \tau)$	Mutual coherence function
γ	Lorentz factor
$\gamma(\mathbf{r}_1, \mathbf{r}_2, \tau), \gamma_{12}(\tau)$	Complex degree of coherence
$\gamma_{12}^{\mathrm{eff}}(\tau)$	Effective complex degree of coherence
$\hbar$	Planck constant
$I(\mathbf{r})$	Intensity distribution
$\mathbf{k}$	Wave vector
λ	Wavelength
$\mu(\mathbf{r}_1, \mathbf{r}_2, \omega), \mu_{12}(\omega)$	spectral degree of coherence
NA	Numerical aperture
N_{ph}	Number of photons per pulse
L_{u}	Undulator length
P_z	Propagator over distance z
q	Degree of transverse coherence
$\mathbf{r}$	Spatial position
R	Radius of curvature
$S(\mathbf{r}, \omega)$	Spectral density
σ, Σ	Beam size
σ'	Divergence of the beam
t	Time
τ	Time delay
$W(\mathbf{r}_1, \mathbf{r}_2, \omega)$	Cross spectral density
ξ, Ξ	Transverse coherence length
ζ	Normalized degree of transverse coherence
z_{eff}	Effective distance, Rayleigh length for coherent radiation

9 Own publications

Publications directly related to the thesis

1. A. Singer, I. A. Vartanyants, M. Kuhlmann, S. Duesterer, R. Treusch, and J. Feldhaus. Transverse-coherence properties of the free-electron-laser FLASH at desy. *Phys. Rev. Lett.* **101**, 254801 (2008).

2. I. A. Vartanyants and A. Singer. Coherence properties of hard x-ray synchrotron sources and x-ray free-electron lasers. *New Journal of Physics* **12**, 035004 (2010).

3. I. A. Vartanyants, A. P. Mancuso, A. Singer, O. M. Yefanov, and J. Gulden. Coherence measurements and coherent diffractive imaging at FLASH. *Journal of Physics B: Atomic, Molecular and Optical Physics* **43**, 194016 (2010)

4. A. Singer and I. A. Vartanyants. Modelling of partially coherent radiation based on the coherent mode decomposition. *Proceedings SPIE* **8141**, 814106 (2011).

5. I. A. Vartanyants, A. Singer, A. P. Mancuso, O. M. Yefanov, A. Sakdinawat, Y. Liu, E. Bang, G. J. Williams, G. Cadenazzi, B. Abbey, H. Sinn, D. Attwood, K. A. Nugent, E. Weckert, T. Wang, D. Zhu, B. Wu, C. Graves, A. Scherz, J. J. Turner, W. F. Schlotter, M. Messerschmidt, J. Lüning, Y. Acremann, P. Heimann, D. C. Mancini, V. Joshi, J. Krzywinski, R. Soufli, M. Fernandez-Perea, S. Hau-Riege, A. G. Peele, Y. Feng, O. Krupin, S. Moeller, and W. Wurth. Coherence properties of individual femtosecond pulses of an x-ray free-electron laser. *Phys. Rev. Lett.* **107**,144801 (2011).

6. I. A. Vartanyants, A. Singer, A. P. Mancuso, *et al.* Coherence properties of an x-ray free-electron laser, *Photon science 2011 (DESY)*, page 54, (2011).

7. W.F. Schlotter, J.J. Turner, M. Rowen, P. Heimann, M. Holmes, O. Krupin, M. Messerschmidt, S. Moeller, J. Krzywinski, R. Soui, M. Fernandez-Perea, N. Kelez, S. Lee, R. Coee, G. Hays, M. Beye, N. Gerken, F. Sorgenfrei, S. Hau-Riege, L. Juha, J. Chalupsky, V. Hajkova, A.P. Mancuso, A. Singer, O. Yefanov, I. A. Vartanyants, G. Cadenazzi, B. Abbey, H. Sinn, J. Lüning, S. Schaert, S. Eisebitt, W.-S. Lee, A. Scherz, A.R. Nilsson, and W. Wurth. The Soft X-ray Instrument for Materials Studies at the Linac Coherent Light Source X-ray Free-Electron Laser. *Review of Scientific Instruments* **83**, 043107 (2012).

8. A. Singer, F. Sorgenfrei, A. Mancuso, N. Gerasimova, O. Yefanov, J. Gulden, T. Gorniak, T. Senkbeil, A. Sakdinawat, Y. Liu, D. Atwood, S. Dziarzhytski, A. Al-Shemmary, S. Duesterer, R. Treusch, E. Weckert, A. Rosenhahn, W. Wurth, and

I. Vartaniants. Spatial and temporal coherence properties of single free-electron laser pulses. *Optics Express* **20**, 17480 (2012).

9. A. Singer, U. Lorenz,F. Sorgenfrei, N. Gerasimova, J. Gulden, O. Yefanov, R. Kurta, A. Shabalin, R. Dronyak, R. Treusch, V. Kocharyan, E. Weckert, W. Wurth, and I. A. Vartanyants. Hanbury Brown and Twiss interferometry at a free-electron laser. *submitted (2013)*

10. A. Singer and I. A. Vartanyants. Coherence properties of focused x-ray beams at high brilliance synchrotron sources. *in preparation*

11. A. Singer and I. A. Vartanyants. Coherence properties of x-ray free-electron lasers. *invited Review paper, in preparation*

Publications not directly related to the thesis

1. A. P. Mancuso, A. Schropp, B. Reime, L.-M. Stadler, A. Singer, J. Gulden, S. Streit-Nierobisch, C. Gutt, G. Grübel, J. Feldhaus, F. Staier, R. Barth, A. Rosenhahn, M. Grunze, T. Nisius, T. Wilhein, D. Stickler, H. Stillrich, R. Frömter, H.-P. Oepen, M. Martins, B. Pfau, C. M. Günther, R. Könnecke, S. Eisebitt, B. Faatz, N. Guerassimova, K. Honkavaara, V. Kocharyan, R. Treusch, E. Saldin, S. Schreiber, E. A. Schneidmiller, M. V. Yurkov, E. Weckert, and I. A. Vartanyants. Coherent-pulse 2d crystallography using a free-electron laser x-ray source. *Phys. Rev. Lett.* **102**, 035502 (2009).

2. A. P. Mancuso, T. Gorniak, F. Staier, O. M. Yefanov, R. Barth, C. Christophis, B. Reime, J. Gulden, A. Singer, M. E. Pettit, T. Nisius, T. Wilhein, C. Gutt, G. Grübel, N. Guerassimova, R. Treusch, J. Feldhaus, S. Eisebitt, E. Weckert, M. Grunze, A. Rosenhahn, and I. A. Vartanyants. Coherent imaging of biological samples with femtosecond pulses at the free-electron laser flash. *New Journal of Physics* **12**, 035003 (2010).

3. S. Roling, B. Siemer, M. Wöstmann, H. Zacharias, R. Mitzner, A. Singer, K. Tiedtke, and I. A. Vartanyants. Temporal and spatial coherence properties of free-electron-laser pulses in the extreme ultraviolet regime. *Phys. Rev. ST Accel. Beams* **14**, 080701 (2011).

4. J. Gulden, O.M. Yefanov, A.P. Mancuso, R. Dronyak, A. Singer, V. Bernatova, A. Burkhardt, O. Polozhentsev, A. Soldatov, M. Sprung, and I.A. Vartanyants. Three-dimensional structure of a single colloidal crystal grain studied by coherent x-ray diffraction. *Optics Express* **20**, 4039 (2012).

5. Ch. Kraus, A. Singer, K. Valerius, and Ch. Weinheimer. Limit on sterile neutrino contribution from the Mainz Neutrino Mass Experiment. *European Physical Journal C (on the Cover), in press* (2013).

6. A. V. Zozulya, J.-M. Meijer, A. Shabalin, A. Ricci, F. Westermeier, R. P. Kurta, U. Lorenz, A. Singer, O. Yefanov, A. V. Petukhov , M. Sprung and I. A. Vartanyants. In situ X-ray crystallographic study of structural evolution of colloidal crystals upon heating. *accepted* (2012).

7. D.D. Mai, J. Hallmann, T. Reusch, M. Osterhoff, S. Düsterer, R. Treusch, A. Singer, M. Beckers, T. Gorniak, T. Senkbeil, R Dronyak, J. Gulden, O.M. Yefanov, A. Al-Shemmary, A. Rosenhahn, A.P. Mancuso, I.A. Vartanyants, and T. Salditt. Single pulse coherence measurements in the water window at the free electron laser FLASH. *submitted (2013)*

Bibliography

[1] T. H. Mainman. Stimulated Optical Radiation in Ruby. *Nature*, **187**, 493 (1960).

[2] R. H. Brown and R. Q. Twiss. A test of a new type of stellar interferometer on sirius. *Nature*, **178**, 1046 (1956).

[3] K. Balewski, W. Brefeld, W. Decking, *et al.* PETRA III: A Low Emittance Synchrotron Radiation Source. Technical report, DESY, Hamburg, Germany (2004).

[4] G. Grübel and F. Zontone. Correlation spectroscopy with coherent X-rays. *Journal of Alloys and Compounds*, **362**, 3 (2004).

[5] S. Eisebitt, J. Lüning, W. F. Schlotter, *et al.* Lensless imaging of magnetic nanostructures by X-ray spectro-holography. *Nature*, **432**, 885 (2004).

[6] H. N. Chapman and K. A. Nugent. Coherent lensless X-ray imaging. *Nature Photonics*, **4**, 833 (2010).

[7] J. R. Fienup. Phase retrieval algorithms: a comparison. *Appl. Opt.*, **21**, 2758 (1982).

[8] B. W. J. McNeil and N. R. Thompson. X-ray free-electron lasers. *Nature Photonics*, **4**, 814 (2010).

[9] D. H. Bilderback, J. D. Brock, D. S. Dale, *et al.* Energy recovery linac (ERL) coherent hard x-ray sources. *New Journal of Physics*, **12**, 035011 (2010).

[10] L. W. Whitehead, G. J. Williams, H. M. Quiney, *et al.* Diffractive Imaging Using Partially Coherent X Rays. *Phys. Rev. Lett.*, **103**, 243902 (2009).

[11] W. C. Röntgen. Eine neue Art von Strahlen. *Sitzungsberichte der Würzburger Physik.-medic. Gesellschaft* (1985).

[12] M. von Laue. *Röntgenstrahlinterferenzen.* Akad. Verl.-Ges. (1960).

[13] M. Laue, W. Friedrich, and K. P. Interferenzerscheinungen bei Röntgenstrahlen. *Annalen der Physik*, **41** (1913).

[14] M. Laue, W. Friedrich, and K. P. Eine quantitative Prüfung der Theorie für die Interferenzerscheinungen bei Röntgenstrahlen. *Annalen der Physik*, **41** (1913).

[15] W. H. Bragg and B. W. L. *Proc. Roy. Soc. Ser. A*, **88** (1913).

[16] W. H. Bragg and B. W. L. *Proc. Roy. Soc. Ser. A*, **89** (1913).

[17] W. H. Bragg and B. W. L. *Proc. Roy. Soc. Ser. A*, **88** (1913).

[18] W. H. Bragg and B. W. L. *Proc. Roy. Soc. Ser. A*, **88** (1913).

[19] Nobelprize.org. The Nobel Prize in Chemistry 2009 - Advanced Information (2009).

[20] A. C. Thompson and D. Vaughan, editors. *X-ray Data Booklet*. Lawrence Berkeley National Laboratory, University of California, second edition (2001).

[21] R. Neutze, R. Wouts, D. van der Spoel, E. Weckert, and J. Hajdu. Potential for biomolecular imaging with femtosecond X-ray pulses. *Nature*, **406**, 752 (2000).

[22] H. N. Chapman *et al.* Femtosecond X-ray protein nanocrystallography. *Nature*, **470**, 73 (2011).

[23] V. Elser. Phase retrieval by iterated projections. *J. Opt. Soc. Am. A*, **20**, 40 (2003).

[24] J. Miao, P. Charalambous, J. Kirz, and D. Sayre. Extending the methodology of X-ray crystallography to allow imaging of micrometre-sized non-crystalline specimens. *Nature*, **400**, 342 (1999).

[25] M. A. Pfeifer, G. J. Williams, I. A. Vartanyants, R. Harder, and I. K. Robinson. Three-dimensional mapping of a deformation field inside a nanocrystal. *Nature*, **442**, 63 (2006).

[26] O. M. Yefanov, A. V. Zozulya, I. A. Vartanyants, *et al.* Coherent diffraction tomography of nanoislands from grazing-incidence small-angle x-ray scattering. *Applied Physics Letters*, **94**, 123104 (2009).

[27] A. P. Mancuso, A. Schropp, B. Reime, *et al.* Coherent-Pulse 2D Crystallography Using a Free-Electron Laser X-Ray Source. *Phys. Rev. Lett.*, **102**, 035502 (2009).

[28] J. Gulden, O. M. Yefanov, A. P. Mancuso, *et al.* Coherent x-ray imaging of defects in colloidal crystals. *Phys. Rev. B*, **81**, 224105 (2010).

[29] J. Nelson, X. Huang, J. Steinbrener, *et al.* High-resolution x-ray diffraction microscopy of specifically labeled yeast cells. *Proceedings of the National Academy of Sciences*, **107**, 7235 (2010).

[30] A. P. Mancuso, T. Gorniak, F. Staier, *et al.* Coherent imaging of biological samples with femtosecond pulses at the free-electron laser FLASH. *New Journal of Physics*, **12**, 035003 (2010).

[31] M. M. Seibert *et al.* Single mimivirus particles intercepted and imaged with an X-ray laser. *Nature*, **470**, 78 (2011).

[32] P. Wochner, C. Gutt, T. Autenrieth, *et al.* X-ray cross correlation analysis uncovers hidden local symmetries in disordered matter. *Proc. Nat. Acad. Sci.*, **106**, 11511 (2009).

[33] M. Altarelli, R. P. Kurta, and I. A. Vartanyants. X-ray cross-correlation analysis and local symmetries of disordered systems: General theory. *Phys. Rev. B*, **82**, 104207 (2010).

[34] D. K. Saldin, H. C. Poon, M. J. Bogan, *et al.* New Light on Disordered Ensembles: Ab Initio Structure Determination of One Particle from Scattering Fluctuations of Many Copies. *Phys. Rev. Lett.*, **106** (2011).

[35] J. D. Jackson. *Classical Electrodynamics*. Wiley, 3rd edition (1999).

[36] D. Attwood. *Soft X-Rays and Extreme Ultraviolet Radiatio*. Cambridge University Press, 1st edition (1999).

[37] G. Kulipanov, A. Skrinsky, and N. Vinokurov. MARS - a project of the diffraction-limited fourth generation X-ray source based on supermicrotron. *Nuclear Instruments and Methods in Physics Research Section A: Accelerators, Spectrometers, Detectors and Associated Equipment*, **467-468, Part 1**, 16 (2001).

[38] A. M. Kondratenko and E. L. Saldin. Generation of coherent radiation by a relativistic electron beam in an undulator. *Part. Accelerators*, **10**, 207 (1980).

[39] R. Bonifacio, C. Pellegrini, and L. Narducci. Collective instabilities and high-gain regime in a free electron laser. *Optics Communications*, **50**, 373 (1984).

[40] P. Schmüser, M. Dohlus, and J. Rossbach. *Ultraviolet and Soft X-Ray Free-Electron Lasers:Introduction to Physical Principles, Experimental Results, Technological Challenges*. Springer, Berlin Heidelberg (2008).

[41] Free-electron laser FLASH, http://flash.desy.de (2012).

[42] P. Emma *et al.* First lasing and operation of an angstrom-wavelength free-electron laser. *Nature Photonics*, **4**, 641 (2010).

[43] M. Altarelli *et al.* The European X-Ray Free-Electron Laser Technical design report . Technical report, DESY, Hamburg, Germany (2007).

[44] E. L. Saldin, E. Schneidmiller, and M. Yurkov. *The Physics of Free Electron Lasers*. Springer, 2nd edition (2000).

[45] E. Saldin. Private communication.

[46] L. Mandel and E. Wolf. *Optical Coherence and Quantum Optics*. Cambridge University Pres, New York (1995).

[47] W. Ackermann *et al.* Operation of a free-electron laser from the extreme ultraviolet to the water windo. *Nature Photonics*, **1**, 336 (2007).

[48] A. Murokh *et al.* Properties of the ultrashort gain length, self-amplified spontaneous emission free-electron laser in the linear regime and saturation. *Phys. Rev. E*, **67**, 066501 (2003).

[49] S. P. Hau-Riege. Effect of the coherence properties of self-amplified-spontaneous-emissionx-ray free electron lasers on single-particle diffractive imaging. *Opt. Express*, **16**, 2840 (2008).

[50] T. Brabec and F. Krausz. Intense few-cycle laser fields: Frontiers of nonlinear optics. *Rev. Mod. Phys.*, **72**, 545 (2000).

[51] G. Geloni, V. Kocharyan, and E. Saldin. Cost-effective way to enhance the capabilities of the LCLS baseline. *arXiv*, 1008:3036v1 (2009).

[52] G. Geloni, V. Kocharyan, and E. Saldin. A novel self-seeding scheme for hard X-ray FELs. *Journal of Modern Optics*, **58**, 1391 (2011).

[53] AmannJ., BergW., BlankV., *et al.* Demonstration of self-seeding in a hard-X-ray free-electron laser. *Nature Photonics*, **advance online publication** (2012).

[54] M. Born and E. Wolf. *Principles of Optics: Electromagnetic Theory of Propagation, Interference and Diffraction of Light (7th Edition)*. Cambridge University Press (1999).

[55] L. Mandel. Complex Representation of Optical Fields in Coherence Theory. *J. Opt. Soc. Am.*, **57**, 613 (1967).

[56] L. C. Evans. *Partial Differential Equations (Graduate Studies in Mathematics, V. 19) GSM/19*. American Mathematical Society (1998).

[57] B. E. A. Saleh and M. C. Teich. *Fundamentals of photonics*. Wiley, New York (1991).

[58] C. Cohen-Tannoudji, B. Diu, and F. Laloe. *Quantenmechanik: Teil 1*. Walter de Gruyter (1999).

[59] L. Mandel and E. Wolf. Coherence Properties of Optical Fields. *Rev. Mod. Phys.*, **37**, 231 (1965).

[60] J. W. Goodman. *Statistical Optics*. Wiley, New York (1985).

[61] J. P. Gordon, H. J. Zeiger, and C. H. Townes. Molecular Microwave Oscillator and New Hyperfine Structure in the Microwave Spectrum of NH_3. *Phys. Rev.*, **95**, 282 (1954).

[62] N. G. Basov and A. M. Prokhorov. *Zh. Exsp. Teor. Fiz. USSR*, **27**, 431 (1954).

[63] R. H. Brown and R. Q. Twiss. Correlation between Photons in two Coherent Beams of Light. *Nature*, **177**, 27 (1956).

[64] R. J. Glauber. The Quantum Theory of Optical Coherence. *Phys. Rev.*, **130**, 2529 (1963).

[65] S. S. Hodgman, R. G. Dall, A. G. Manning, K. G. H. Baldwin, and A. G. Truscott. Direct Measurement of Long-Range Third-Order Coherence in Bose-Einstein Condensates. *Science*, **331**, 1046 (2011).

[66] L. Mandel. Photon Degeneracy in Light from Optical Maser and Other Sources. *J. Opt. Soc. Am.*, **51**, 797 (1961).

[67] J. M. Zuo, I. Vartanyants, M. Gao, R. Zhang, and L. A. Nagahara. Atomic Resolution Imaging of a Carbon Nanotube from Diffraction Intensities. *Science*, **300**, 1419 (2003).

[68] E. Saldin, E. Schneidmiller, and M. Yurkov. Coherence properties of the radiation from X-ray free electron laser. *Optics Communications*, **281**, 1179 (2008).

[69] I. A. Vartanyants and A. Singer. Coherence properties of hard x-ray synchrotron sources and x-ray free-electron lasers. *New Journal of Physics*, **12**, 035004 (2010).

[70] I. A. Vartanyants and I. K. Robinson. Origins of decoherence in coherent X-ray diffraction experiments. *Optics Communications*, **222**, 29 (2003).

[71] E. Wolf. New theory of partial coherence in the space-frequency domain. Part I: spectra and cross spectra of steady-state sources. *J. Opt. Soc. Am.*, **72**, 343 (1982).

[72] F. Gori. Collett-Wolf sources and multimode lasers. *Optics Communications*, **34**, 301 (1980).

[73] M. R. Howels and B. M. Kincaid. *The properties of undulator radiation.* Kluver Academic Publishers (1994).

[74] R. Coïsson. Spatial coherence of synchrotron radiation. *Appl. Opt.*, **34**, 904 (1995).

[75] R. Coïsson and S. Marchesini. Gauss–Schell Sources as Models for Synchrotron Radiation. *Journal of Synchrotron Radiation*, **4**, 263 (1997).

[76] Y. Takayama, N. Takaya, T. Miyahara, *et al.* Spatial coherence of undulator radiation beyond the van Cittert-Zernike theorem. *Nuclear Instruments and Methods in Physics Research Section A: Accelerators, Spectrometers, Detectors and Associated Equipment*, **441**, 565 (2000).

[77] A. Singer, I. A. Vartanyants, M. Kuhlmann, *et al.* Transverse-Coherence Properties of the Free-Electron-Laser FLASH at DESY. *Phys. Rev. Lett.*, **101**, 254801 (2008).

[78] S. Roling, B. Siemer, M. Wöstmann, *et al.* Temporal and spatial coherence properties of free-electron-laser pulses in the extreme ultraviolet regime. *Phys. Rev. ST Accel. Beams*, **14**, 080701 (2011).

[79] I. A. Vartanyants, A. Singer, A. P. Mancuso, *et al.* Coherence Properties of Individual Femtosecond Pulses of an X-Ray Free-Electron Laser. *Phys. Rev. Lett.*, **107**, 144801 (2011).

[80] A. T. Friberg and R. J. Sudol. Propagation parameters of Gaussian Schell-model beams. *Optics Communications*, **41**, 383 (1982).

[81] A. T. Friberg and R. J. Sudol. The spatial coherence properties of Gaussian Schell-model beams. *Opt. acta*, **30**, 1075 (1983).

[82] Y. Takayama, T. Hatano, T. Miyaharac, and W. Okamotod. Relationship Between Spatial Coherence of Synchrotron Radiation and Emittance. *Journal of Synchrotron Radiation*, **5**, 1187 (1998).

[83] P. van Cittert. Die wahrscheinliche Schwingungsverteilung in einer von einer Lichtquelle direkt oder mittels einer Linse beleuchteten Ebene. *Physica*, **1**, 201 (1934).

[84] F. Zernike. The concept of degree of coherence and its application to optical problems. *Physica*, **5**, 785 (1938).

[85] F. Gori. Mode propagation of the field generated by Collett-Wolf Schell-model sources. *Optics Communications*, **46**, 149 (1983).

[86] A. Starikov and E. Wolf. Coherent-mode representation of Gaussian Schell-model sources and of their radiation fields. *J. Opt. Soc. Am.*, **72**, 923 (1982).

[87] S. A. Ponomarenko. Twisted Gaussian Schell-model solitons. *Phys. Rev. E*, **64**, 036618 (2001).

[88] B. J. Thompson and E. Wolf. Two-beam interference with partially coherent light. *J. Opt. Soc. Am.*, **47**, 895 (1957).

[89] R. A. Bartels, A. Paul, H. Green, *et al.* Generation of Spatially Coherent Light at Extreme Ultraviolet Wavelengths. *Science*, **297**, 376 (2002).

[90] R. A. Bartels, A. Paul, M. M. Murnane, *et al.* Absolute determination of the wavelength and spectrum of an extreme-ultraviolet beam by a Young's double-slit measurement. *Opt. Lett.*, **27**, 707 (2002).

[91] R. Ischebeck. *Transverse Coherence of a VUV Free Electron Laser*. Ph.D. thesis, University of Hamburg (2003).

[92] R. A. Dilanian, B. Chen, S. Teichmann, *et al.* High-harmonic-generation spectrum reconstruction from Young's double-slits interference pattern using the maximum entropy method. *Opt. Lett.*, **33**, 2341 (2008).

[93] I. A. Vartanyants, A. P. Mancuso, A. Singer, O. M. Yefanov, and J. Gulden. Coherence measurements and coherent diffractive imaging at FLASH. *Journal of Physics B: Atomic, Molecular and Optical Physics*, **43**, 194016 (2010).

[94] D. Paterson, B. E. Allman, P. J. McMahon, *et al.* Spatial coherence measurement of X-ray undulator radiation. *Optics Communications*, **195**, 79 (2001).

[95] H. Lajunen, P. Vahimaa, and J. Tervo. Theory of spatially and spectrally partially coherent pulses. *J. Opt. Soc. Am. A*, **22**, 1536 (2005).

[96] I. P. Christov. Propagation of partially coherent light pulses. *Opt. Acta*, **33**, 63 (1986).

[97] R. W. Schoonover, B. J. Davis, R. A. Bartels, and P. S. Carney. Optical interferometry with pulsed fields. *Journal of Modern Optics*, **55**, 1541 (2008).

[98] G. Geloni, E. Saldin, E. Schneidmiller, and M. Yurkov. Transverse coherence properties of X-ray beams in third-generation synchrotron radiation sources. *Nuclear Instruments and Methods in Physics Research Section A: Accelerators, Spectrometers, Detectors and Associated Equipment*, **588**, 463 (2008).

[99] K.-J. Kim. Brightness, coherence and propagation characteristics of synchrotron radiation. *Nuclear Instruments and Methods in Physics Research Section A: Accelerators, Spectrometers, Detectors and Associated Equipment*, **246**, 71 (1986).

[100] O. Chubar and P. Elleaume. Accurate And Efficient Computation Of Synchrotron Radiation In The Near Field Region. *Proc. of the EPAC98 Conference*, 1177–1179 (1998).

[101] V. G. Kohn. Focusing femtosecond X-ray free-electron laser pulses by refractive lenses. *Journal of Synchrotron Radiation*, **19**, 84 (2012).

[102] H. Mimura, S. Handa, T. Kimura, *et al.* Breaking the 10[thinsp]nm barrier in hard-X-ray focusing. *Nature Physics*, **6**, 122 (2010).

[103] A. Sakdinawat and D. Attwood. Nanoscale X-ray imaging. *Nature Photonics*, **4**, 840 (2010).

[104] C. Schroer, G. Falkenberg, and C. David. Hard X-ray nanoprobe at PETRA III. *Photon science 2011 (DESY)*, 100 (2011).

[105] D. Zhu, M. Cammarata, J. M. Feldkamp, *et al.* A single-shot transmissive spectrometer for hard x-ray free electron lasers. *Applied Physics Letters*, **101**, 034103 (2012).

[106] A. Snigirev, V. Kohn, I. Snigireva, and B. Lengeler. A compound refractive lens for focusing high-energy X-rays. *Nature*, **384**, 49 (1996).

[107] C. G. Schroer, M. Kuhlmann, U. T. Hunger, *et al.* Nanofocusing parabolic refractive x-ray lenses. *Applied Physics Letters*, **82**, 1485 (2003).

[108] H. Kogelnik and T. Li. Laser Beams and Resonators. *Appl. Opt.*, **5**, 1550 (1966).

[109] J. Turunen and A. Friberg. Matrix representation of Gaussian Schell-model beams in optical systems. *Optics; Laser Technology*, **18**, 259 (1986).

[110] H. T. Yura and S. G. Hanson. Optical beam wave propagation through complex optical systems. *J. Opt. Soc. Am. A*, **4**, 1931 (1987).

[111] A. V. Zozulya, S. Bondarenko, A. Schavkan, *et al.* Microfocusing transfocator for 1D and 2D compound refractive lenses. *Opt. Express*, **20**, 18967 (2012).

[112] M. Sprung and A. Zozulya. Private communication.

[113] A. Singer and I. A. Vartanyants. Modelling of partially coherent radiation based on the coherent mode decomposition. *Proceedings SPIE*, **8141**, 814106 (2011).

[114] A. M. Zysk, P. S. Carney, and J. C. Schotland. Eikonal Method for Calculation of Coherence Functions. *Phys. Rev. Lett.*, **95**, 043904 (2005).

[115] J. J. A. Lin, D. Paterson, A. G. Peele, *et al.* Measurement of the Spatial Coherence Function of Undulator Radiation using a Phase Mask. *Phys. Rev. Lett.*, **90**, 074801 (2003).

[116] H. N. Chapman *et al.* Femtosecond diffractive imaging with a soft-X-ray free-electron laser. *Nature Physics*, **2**, 839 (2006).

[117] J. N. Galayda, J. Arthur, D. F. Ratner, and W. E. White. X-ray free-electron lasers—present and future capabilities. *J. Opt. Soc. Am. B*, **27**, B106 (2010).

[118] Y. Ding, Z. Huang, and S. Ocko. Transverse-coherence properties of the FEL at the LCLS. *Proc. of FEL2010 Conf. (Malmö, Sweden, 2010)*, 151 (2010).

[119] P. Heimann *et al.* Linac Coherent Light Source soft x-ray materials science instrument optical design and monochromator commissioning. *Review of Scientific Instruments*, **82**, 093104 (2011).

[120] R. Soufli, M. J. Pivovaroff, S. L. Baker, *et al.* Development, characterization and experimental performance of x-ray optics for the LCLS free-electron laser. *Proc. SPIE*, **7077** (2008).

[121] R. Soufli, A. L. Aquila, F. Salmassi, M. Fernández-Perea, and E. M. Gullikson. Optical constants of magnetron-sputtered boron carbide thin films from photoabsorption data in the range 30 to 770 eV. *Appl. Opt.*, **47**, 4633 (2008).

[122] A. Barty, R. Soufli, T. McCarville, *et al.* Predicting the coherent X-ray wavefront focal properties at the Linac Coherent Light Source (LCLS) X-ray free electron laser. *Opt. Express*, **17**, 15508 (2009).

[123] G. D. Boreman. *Modulation Transfer Function in Optical and Electro-Optical Systems*. SPIE Press Book (2001).

[124] A. Singer, F. Sorgenfrei, A. P. Mancuso, *et al.* Spatial and temporal coherence properties of single free-electron laser pulses. *Opt. Express*, **20**, 17480 (2012).

[125] R. Treusch. Private communication (2011).

[126] F. Staier. Entwicklung, Bau und Test einer UHV Röntgenstreukammer für die digitale In-Line Holographie (2009).

[127] U. Lorenz, A. Singer, I. A. Vartanyants, *et al.* In preparation.

[128] W. F. Schlotter, F. Sorgenfrei, T. Beeck, *et al.* Longitudinal coherence measurements of an extreme-ultraviolet free-electron laser. *Opt. Lett.*, **35**, 372 (2010).

[129] K. Honkavaara, B. Faatz, J. Feldhaus, *et al.* FLASH upgrade. *First International Particle Accelerator Conference, IPAC'10, Kyoyo, Japan* (2010).

[130] M. Kuhlmann, E. Plönjes, S. Toleikis, P. Zeitoun, and P.Mercère. HASYLAB Annual Report, Part I. *Eds.: W. Caliebe, W. Drube, J.R. Schneider*, 213 (2006).

[131] F. Pfeiffer, O. Bunk, C. Schulze-Briese, *et al.* Shearing Interferometer for Quantifying the Coherence of Hard X-Ray Beams. *Phys. Rev. Lett.*, **94**, 164801 (2005).

[132] M. G. Raymer, M. Beck, and D. McAlister. Complex wave-field reconstruction using phase-space tomography. *Phys. Rev. Lett.*, **72**, 1137 (1994).

[133] C. Q. Tran, G. J. Williams, A. Roberts, *et al.* Experimental Measurement of the Four-Dimensional Coherence Function for an Undulator X-Ray Source. *Phys. Rev. Lett.*, **98**, 224801 (2007).

[134] M. D. Alaimo, M. A. C. Potenza, M. Manfredda, *et al.* Probing the Transverse Coherence of an Undulator X-Ray Beam Using Brownian Particles. *Phys. Rev. Lett.*, **103**, 194805 (2009).

[135] K. A. Nugent. Partially coherent diffraction patterns and coherence measurement. *J. Opt. Soc. Am. A*, **8**, 1574 (1991).

[136] I. A. Vartanyants and I. K. Robinson. Partial coherence effects on the imaging of small crystals using coherent x-ray diffraction. *Journal of Physics: Condensed Matter*, **13**, 10593 (2001).

[137] K. A. Nugent and J. E. Trebes. Coherence measurement technique for short-wavelength light sources. *Review of Scientific Instruments*, **63**, 2146 (1992).

[138] E. E. Fenimore and T. M. Cannon. Coded aperture imaging with uniformly redundant arrays. *Appl. Opt.*, **17**, 337 (1978).

[139] M. Martins, M. Wellhöfer, J. T. Hoeft, *et al.* Monochromator beamline for FLASH. *Rev. Sci. Instrum.*, **77**, 115108 (2006).

[140] Y. Mejía and A. I. González. Measuring spatial coherence by using a mask with multiple apertures. *Optics Communications*, **273**, 428 (2007).

[141] A. I. González and Y. Mejía. Nonredundant array of apertures to measure the spatial coherence in two dimensions with only one interferogram. *J. Opt. Soc. Am. A*, **28**, 1107 (2011).

[142] N. Gerasimova. Private communication.

[143] J. Bahrdt. Wavefront tracking within the stationary phase approximation. *Phys. Rev. ST Accel. Beams*, **10**, 060701 (2007).

[144] H. Paul. Interference between independent photons. *Rev. Mod. Phys.*, **58**, 209 (1986).

[145] E. Ikonen. Interference effects between independent gamma rays. *Phys. Rev. Lett.*, **68**, 2759 (1992).

[146] M. Yabashi, K. Tamasaku, and T. Ishikawa. Characterization of the Transverse Coherence of Hard Synchrotron Radiation by Intensity Interferometry. *Phys. Rev. Lett.*, **87**, 140801 (2001).

[147] M. Yabashi, K. Tamasaku, and T. Ishikawa. Measurement of X-Ray Pulse Widths by Intensity Interferometry. *Phys. Rev. Lett.*, **88**, 244801 (2002).

[148] A. Singer, U. Lorenz, F. Sorgenfrei, *et al.* Hanbury Brown and Twiss interferometry at a free-electron laser. *(in preparation)* (2012).

[149] The MathWorks, Inc. *MATLAB Documentation* (2007).

[150] T. Pfeifer, Y. Jiang, S. Düsterer, R. Moshammer, and J. Ullrich. Partial-coherence method to model experimental free-electron laser pulse statistics. *Opt. Lett.*, **35**, 3441 (2010).

[151] G. Vannucci and M. C. Teich. Computer simulation of superposed coherent and chaotic radiation. *Appl. Opt.*, **19**, 548 (1980).

[152] R. B. Lehoucq, D. C. Sorensen, and C. Yang. *Arpack User's Guide: Solution of Large-Scale Eigenvalue Problems With Implicityly Restorted Arnoldi Methods (Software, Environments, Tools)*. Soc for Industrial & Applied Math (2009).

[153] J. M. Liu. Simple technique for measurements of pulsed Gaussian-beam spot sizes. *Opt. Lett.*, **7**, 196 (1982).

A Appendix

A.1 Numerical implementation of the wave propagation in free space

In this section the numerical realization of the Fresnel approximation is briefly outlined. For brevity we omit ω in this section and consider only one transverse direction $E(s, z_0) := E(s_x, s_y = 0, z_0; \omega)$ and $E(u, z_1) := E(u_x, u_y = 0, z_1; \omega)$. The extension of our discussion to two dimensions is straightforward.

To numerically calculate the field in the plane at z_1 (see Figure 2.1) we discretized Equations (2.3,2.6)

$$E_n^{z_1} = \frac{\Delta s k e^{ikz}}{2\pi i z} e^{ik\frac{(n\,\cdot\,\Delta u)^2}{2z}} \sum_{m=-M/2}^{M/2} \left(E_m^{z_0} e^{ik\frac{(m\,\cdot\,\Delta s)^2}{2z}} \right) e^{-ik\frac{(m\,\cdot\,\Delta s)(n\,\cdot\,\Delta u)}{z}} \Delta s, \tag{A.1}$$

where $s = m \cdot \Delta s$, $u = n \cdot \Delta u$, $E_m^{z_0} = E(m \cdot \Delta s, z_0)$ and $E_n^{z_1} = E(n \cdot \Delta u, z_1)$ are the discretized fields in the planes at z_0 and z_1, and m, n are integer numbers. The number of grid points is M in both planes and the summation is made over a region, which is symmetric around the optical axis at $m = 0$.

It is readily seen that the sum has the form of the discrete Fourier transform. Comparing Equation (A.1) with the definition of the discrete Fourier transform F_n of a function f_m [149]

$$F_n = \mathrm{DFT}\{f\} = \sum_{m=0}^{M-1} f_m e^{-2\pi i \frac{mn}{M}} \tag{A.2}$$

we see that, apart from the phase factor before the sum, $E_n^{z_1}$ is the Fourier transform of $E_m^{z_0} e^{ik\frac{(m\,\cdot\,\Delta s)^2}{2z}}$. The relation between Δs and Δu can be found from the comparison of the exponentials in Equations (A.1,A.2)

$$2\pi \frac{mn}{M} = \frac{k(m \cdot \Delta u)(n \cdot \Delta s)}{z} \quad \Rightarrow \quad \Delta u = \frac{\lambda z}{M \Delta s}.$$

The only thing we still have to take care of is the ordering of summation which is different in Equations (A.1) and (A.2). Before and after the discrete Fourier transform the fields have to be reordered such, that the optical axis is positioned at $m = 0$ and the summation is performed from $m = 0 \rightarrow m = M$. This reordering operation is known as *fftshift* [149].

If Fraunhofer approximation is valid, the quadratic phase term $e^{ik\frac{(m\,\cdot\,\Delta s)^2}{2z}}$ can be

dropped and

$$E_n^{z_1} = e^{ik\frac{(n\cdot\Delta u)^2}{2z}}\mathrm{DFT}\left\{E^{z_0}\right\}$$

Finally, for the practical evaluation of the discrete Fourier transform (A.1) it is convenient to use the Fast Fourier Transform (FFT) algorithm [149]. On a single core of a modern CPU[1] the two dimensional FFT of a 2048x2048 array of random complex numbers can be performed in less than 50 ms.

A.2 The degree of transverse coherence

The degree of transverse coherence is expressed as (2.31)

$$\zeta = \frac{\iint |\mu(x_1,x_2)|^2 S(x_1)S(x_2)\mathrm{d}x_1\mathrm{d}x_2}{\left[\int S(x)\mathrm{d}x\right]^2}.$$

After the substitution $x = x_1, x' = x_1 + x_2$ we find

$$\zeta = \frac{\int |\mu(x,x'-x)|^2 S(x)S(x'-x)\mathrm{d}x\mathrm{d}x'}{\left[\int S(x)\mathrm{d}x\right]^2}.$$

For a Schell-model beam $\mu(x,x'-x)$ simplifies to $\mu(x')$. In that case the expression above is given by

$$\zeta = \frac{\int |\mu(x')|^2 \left(S\otimes S\right)(x')\mathrm{d}x'}{\left[\int S(x)\mathrm{d}x\right]^2},$$

where $\otimes$ denotes the convolution operation.

Let us now consider a GSM source (2.40,2.41). Apart from the normalization constant, which is present in both the numerator and the denominator, the spectral density $S(x)$ is given by the normalized Gaussian distribution

$$S(x) = \frac{1}{\sqrt{2\pi}\sigma}\exp\left(-\frac{x^2}{2\sigma^2}\right) = N(0,\sigma),$$

where σ is the rms size of the beam. The convolution of two normalized Gaussian distributions $N(0,\sigma_1)$ and $N(0,\sigma_2)$ is known to be also a normalized Gaussian distribution $N(0,\sqrt{\sigma_1^2+\sigma_2^2})$. This yields

$$(S\otimes S)(x) = \frac{1}{\sqrt{4\pi\sigma^2}}\exp\left(-\frac{x^2}{4\sigma^2}\right)$$

in the nominator and $\int S(x)\mathrm{d}x = 1$ in the denominator. As in the GSM the SDC is also Gaussian function $\mu(x') = \exp\left(-x'^2/2\xi^2\right)$, we finally find the degree of transverse

[1] Intel(R) Xeon(R) CPU, X5570 @2.93GHz

coherence in the form

$$\zeta = \frac{\xi}{\sqrt{\xi^2 + 4\sigma^2}}$$

Introducing the parameter $q = \xi/\sigma$ (2.45) for GSM sources yields

$$\zeta = \frac{q}{\sqrt{4+q^2}} \quad \text{and} \quad q = \frac{4\zeta}{\sqrt{1-\zeta^2}}$$

A.3 Simulations of single pulses in the frame of Gaussian statistics

In this chapter we aim to generate an ensemble of individual light pulses with a finite bandwidth and a finite pulse duration. If the fields from different pulses are independent and many pulses are calculated, we approach the limit of Gaussian statistics. We follow up on the idea proposed in [150] to generate partially coherent pulses. The authors of [150] showed through numerical simulations, that they were able to produce ensembles of pulses with the same statistical properties as the pulses generated at free-electron lasers. A similar approach was proposed earlier in [151] to generate chaotic radiation. Here we develop a solid basis for such an approach and extend this method to the spatial domain. Eventually, we will present a method to generate individual partially coherent pulses in space and time.

The idea of the authors of [150] is the following. They generate an initial pulse $E_0(\omega_k) = \sqrt{S(\omega_k)}e^{i\phi(\omega_k)}$, where $S(\omega_k)$ is the average spectrum, $\omega_k = k \cdot \Delta\omega$ gives an equidistant grid of frequencies, and $\phi(\omega_k)$ are independent random numbers in the range $[-\pi, \pi)$ for different ω_k. They multiply the Fourier transform of $E_0(\omega)$ by a filter function, with its width corresponding to the known FEL pulse duration. Finally, the inverse Fourier transform of this product describes a pulse with a finite bandwidth and a finite pulse duration and mimics the statistical properties of FEL pulses.

We start with the initial field $E_0(\omega)$ in the frequency domain. According to the sampling theorem an arbitrary complex valued function with a finite width of its Fourier spectrum T_0 can be written as

$$E_0(\omega) = \sum_k E_0(\omega_k)\mathrm{sinc}(\omega_k T_0 - \omega T_0), \tag{A.3}$$

where $\mathrm{sinc}(x) = \sin x/x$, $\omega_k = k\pi\Delta\omega$, $\Delta\omega = 1/T_0$ and k is an integer. For $\omega = \omega_k$ we find $E_0(\omega) = E_0(\omega_k)$. We choose T_0 to be much larger than the pulse duration. Writing $E_0(\omega)$ as a product of the amplitude and phase $E_0^{(r)}(\omega_k) = A_\omega(\omega_k)e^{i\phi^{(r)}(\omega_k)}$ we determine the Fourier transform of $E_0^{(r)}(\omega)$

$$E_0^{(r)}(t) = \Pi_{T_0}(t) \sum_k A_\omega(\omega_k) e^{i\phi_k^{(r)}} e^{i\omega_k t}, \tag{A.4}$$

where

$$\Pi_{T_0}(t) = \begin{cases} \pi/T_0 & \text{for} \quad |t| < T_0 \\ 0 & \text{elsewhere} \end{cases}$$

is the Fourier transform of $\mathrm{sinc}(\omega T_0)$ and $\phi_k^{(r)} = \phi^{(r)}(\omega_k)$. Now we multiply the field in the time domain $E_0(t)$ by the pulse envelope which is much narrower than T_0 and find the expressions

$$\begin{aligned} E^{(r)}(t) &= A_t(t) \sum_k A_\omega(\omega_k) e^{i\phi_k^{(r)}} e^{-i\omega_k t} \\ E^{(r)}(\omega) &= \sum_k \tilde{A}_t(\omega - \omega_k) A_\omega(\omega_k) e^{i\phi_k^{(r)}} \end{aligned} \tag{A.5}$$

for the field in the time domain and in the frequency domain, respectively. We denote the Fourier transform of an arbitrary function f by $\tilde{f}$.

Using Equations (2.89, 2.90) we determine the MCF and the CSD,

$$\begin{aligned} \Gamma(t_1, t_2) &= A_t^*(t_1) A_t(t_2) \sum_k |A_\omega(\omega_k)|^2 e^{-i\omega_k(t_2 - t_1)} \\ W(\omega_1, \omega_2) &= \sum_k \tilde{A}_t^*(\omega_1 - \omega_k) \tilde{A}_t(\omega_2 - \omega_k) |A_\omega(\omega_k)|^2. \end{aligned} \tag{A.6}$$

In both derivations we have assumed that $\phi_k^{(r)}$ are independent uniformly distributed random numbers in the range $[-\pi, \pi)$ for different r, hence [33]

$$\lim_{N \to \infty} \frac{1}{N} \sum_{r=1}^{N} e^{i(\phi_l^{(r)} - \phi_k^{(r)})} = \delta_{kl}, \tag{A.7}$$

where δ_{kl} is the Kronecker delta. The average intensity, the average spectrum, the CDC and the SDC are given by

$$\begin{aligned} I(t) &= |A_t(t)|^2 \sum_k |A_\omega(\omega_k)|^2 \\ S(\omega) &= \sum_k |\tilde{A}_t(\omega - \omega_k)|^2 |A_\omega(\omega_k)|^2 \\ |\gamma(t_1, t_2)| &= \frac{\sum_k |A_\omega(\omega)|^2 e^{-i\omega_k(t_2 - t_1)}}{\sum_k |A_\omega(\omega_k)|^2} \\ |\mu(\omega_1, \omega_2)| &= \frac{\sum_k \tilde{A}_t^*(\omega_1 - \omega_k) \tilde{A}_t(\omega_2 - \omega_k) |A_\omega(\omega_k)|^2}{\sqrt{\sum_k |\tilde{A}_t(\omega_1 - \omega_k)|^2 |A_\omega(\omega_k)|^2} \sqrt{\sum_k |\tilde{A}_t(\omega_1 - \omega_k)|^2 |A_\omega(\omega_k)|^2}}, \end{aligned} \tag{A.8}$$

The shape of the average intensity is determined by $|A_t(t)|^2$, which means that the initial and final pulse shapes are identical. It is interesting to note that the final spectrum is characterized not only by the initial spectrum $|A_\omega(\omega)|^2$ of the field, but is a convolution

between the initial spectrum and the Fourier transform of $A_t(t)^2$. The coherence time is determined by the inverse width of the initial spectrum of $|A_\omega(\omega)|^2$. As such, the Wiener-Khintchine theorem (2.26) is not valid, if the width of $\tilde{A}_t(\omega)$ is comparable or larger than the width of $A_\omega(\omega)$. This limit appears when the pulse duration is comparable or larger than the coherence time, i.e. for temporally highly coherent pulses. In the other limit, when the pulse duration is much larger than the temporal coherence time the Wiener-Khintchine theorem can be applied.

As an example we assume that the initial pulse shape $|A_t(t)|^2$ and the initial spectrum $|A_\omega(\omega)|^2$ are both Gaussian

$$A_t(t) = a \exp\left(-\frac{t^2}{4T^2}\right) \qquad \text{and} \qquad A_\omega(\omega) = b \exp\left(-\frac{(\omega-\omega_0)^2}{4\Omega_0^2}\right).$$

Substituting these functions in (A.8) we find after some algebra

$$\begin{aligned} I(t) &= I_0 \exp\left(-\frac{t^2}{2T^2}\right), \\ S(\omega) &= S_0 \exp\left(-\frac{(\omega-\omega_0)^2}{2\left[\frac{1}{4T^2}+\Omega_0^2\right]}\right) \\ |\gamma(t_1,t_2)| &= \exp\left(\frac{(t_2-t_1)^2}{2}\Omega_0^2\right) \\ |\mu(\omega_1,\omega_2)| &= \exp\left(-\frac{(\omega_2-\omega_1)^2T^4}{2T^2+\frac{1}{2\Omega_0^2}}\right). \end{aligned} \tag{A.9}$$

Defining the coherence time as $\tau_c = 1/\Omega_0$ we find that Equations (A.9) are identical to

$$\begin{aligned} I(s,t) &= \exp\left(-\frac{s^2}{2\sigma^2} - \frac{t^2}{2T^2}\right) \\ S(s,\omega) &= \exp\left(-\frac{s^2}{2\sigma^2} - \frac{(\omega-\omega_0)^2}{2\Omega^2}\right) \\ \gamma(s_1,s_2,t_1,t_2) &= \exp\left(-\frac{(s_2-s_1)^2}{2\xi^2} - \frac{(t_2-t_1)^2}{2\tau_c^2}\right) \\ \mu(s_1,s_2,\omega_1,\omega_2) &= \exp\left(-\frac{(s_2-s_1)^2}{2\xi^2} - \frac{(\omega_2-\omega_1)^2}{2\Omega_c^2}\right), \end{aligned} \tag{A.10}$$

which describe the statistical properties of GSM pulses for $s_1 = s_2 = 0$.

It is worth mentioning that this model only describes situations, where the CDC depends on the times t_1 and t_2 through the difference $t_2 - t_1$.

This method can be extended to the spatial domain. Applying the sampling theorem in two dimensions an arbitrary two dimensional complex function with finite Fourier

[2] This expression is missing in [150], where $|A_\omega(\omega)|^2$ is considered as the final average spectrum.

spectra in both dimensions can be expressed as

$$E_0^{(r)}(q,\omega) = \sum_{mn} E_0^{(r)}(q_m,\omega_n)\mathrm{sinc}(q_m D_0 - qD_0)\mathrm{sinc}(\omega_n T_0 - \omega T_0), \tag{A.11}$$

where $E_0^{(r)}(q_m,\omega_n) = A_q(q_m)A_\omega(\omega_n)e^{i\phi_{mn}^{(r)}}$. The momentum transfer q is the inverse coordinate of the position s and D_0 is much larger than the extend of the field in the spatial domain. Applying the same procedure as described above we find the field as a function of time t and position s

$$E^{(r)}(s,t) = A_t(t)A_s(s)\sum_{mn} A_\omega(\omega_m)A_q(q_n)e^{i\phi_{mn}^{(r)}}e^{-i(\omega_m t - k_n s)} \tag{A.12}$$

and as a function of the frequency ω and the position s

$$E^{(r)}(s,\omega) = A_s(s)\sum_{mn} \tilde{A}_t(\omega-\omega_m)A_\omega(\omega_m)A_q(q_n)e^{i\phi_{mn}^{(r)}}e^{ik_n s}. \tag{A.13}$$

Here we have introduced the functions $A_q(q)$ and $A_s(s)$ with the widths corresponding to the angular divergence and the source size. The MCF is determined by

$$\begin{aligned}\Gamma(s_1,s_2;t_1,t_2) =& A_s^*(s_1)A_s(s_2)\sum_n |A_q(q_n)|^2 e^{ik_n(s_2-s_1)} \\ & A_t^*(t_1)A_t(t_2)\sum_m |A_\omega(\omega_m)|^2 e^{-i\omega_m(t_2-t_1)}\end{aligned} \tag{A.14}$$

and the CSD can be expressed as

$$\begin{aligned}W(s_1,s_2;\omega_1,\omega_2) =& A_s^*(s_1)A_s(s_2)\sum_n |A_q(q_n)|^2 e^{ik_n(s_2-s_1)} \\ & \sum_m |\tilde{A}_t(\omega-\omega_m)|^2 |A_\omega(\omega_m)|^2.\end{aligned} \tag{A.15}$$

Here we have used

$$\lim_{N\to\infty}\frac{1}{N}\sum_{r=1}^{N} e^{i(\phi_{nm}^{(r)}-\phi_{n'm'}^{(r)})} = \delta_{nn'}\delta_{mm'},$$

which is is equivalent to (A.7)[3]. Although the field of individual pulses $E^{(r)}(s,t)$ does not factorize in spatial and temporal components due to the mutual phase $\phi_{mn}^{(r)}$, the statistical averages do factorize $\Gamma(s_1,s_2;t_1,t_2) = \Gamma(s_1,s_2)\Gamma(t_1,t_2)$ in this model. The

[3] We can rearrange the integers nm into a single integer $j = n\cdot M + m$, where $m = 1,\dots M$. Using the phases $\phi_j^{(r)}$ and $\phi_{j'}^{(r)}$ in Equation (A.7) yields $\delta_{jj'}$. The integers j and j' are equal if and only if $n = n'$ and $m = m'$.

same holds for the CSD. If we assume $A_t(t)$, $A_\omega(\omega)$, $A_s(s)$, and $A_q(q)$ are all Gaussian

$$\begin{aligned} A_t(t) &= a\exp\left(-\frac{t^2}{4T_0^2}\right) \qquad & A_\omega(\omega) &= b\exp\left(-\frac{(\omega-\omega_0)^2}{4\Omega_0^2}\right) \\ A_s(s) &= c\exp\left(-\frac{s^2}{4\sigma^2}\right) \qquad & A_q(q) &= d\exp\left(-\frac{q^2}{4\sigma_q^2}\right), \end{aligned} \tag{A.16}$$

we readily see that, provided $\xi = 1/\sigma_q$, Equations (A.14,A.15) are identical to (2.89,2.90), which describe the coherence properties of GSM pulses now for arbitrary positions s_1, s_2.

A.4 Synchrotron radiation

The far field expression for the radiation field generated by a single electron is given by Equation (28) in [98] or (48) in [82]

$$E_f(\eta, \mathbf{s}, z, \bar{\theta}) \sim \exp\left(iz/2\left[\bar{\theta} - \frac{\mathbf{s}}{z}\right]^2\right)\psi_f\left(\left|\bar{\theta} - \frac{\mathbf{s}}{z} - \eta\right|\right), \tag{A.17}$$

where $\psi_f(x) = \sin(x^2/4)/(x^2/4)$.

The to calculate the cross spectral density let us first consider

$$\begin{aligned} & E(\eta, \mathbf{s}, z, \bar{\theta} + \Delta\theta/2)E^*(\eta, \mathbf{s}, z, \bar{\theta} - \Delta\theta/2) \\ = \;& \psi_f\left(\left|\bar{\theta} + \frac{\Delta\theta}{2} - \frac{\mathbf{s}}{z} - \eta\right|\right)\psi_f\left(\left|\bar{\theta} - \frac{\Delta\theta}{2} - \frac{\mathbf{s}}{z} - \eta\right|\right) \\ & \times \exp\left([i\frac{z}{2}\left[\left|\bar{\theta} + \frac{\Delta\theta}{2} - \frac{\mathbf{s}}{z}\right|^2 - \left|\bar{\theta} - \frac{\Delta\theta}{2} - \frac{\mathbf{s}}{z}\right|^2\right]\right) \\ = \;& \psi_f\left(\left|\bar{\theta} + \frac{\Delta\theta}{2} - \frac{\mathbf{s}}{z} - \eta\right|\right)\psi_f\left(\left|\bar{\theta} - \frac{\Delta\theta}{2} - \frac{\mathbf{s}}{z} - \eta\right|\right)\exp\left(iz\left[\bar{\theta}\cdot\Delta\theta - \Delta\theta\cdot\frac{\mathbf{s}}{z}\right]\right) \end{aligned}$$

Inserting the last expression in (3.3)

$$W(z, \bar{\theta}, \Delta\theta) = e^{iz\bar{\theta}\Delta\theta}\int \mathrm{d}\mathbf{s}\mathrm{d}\eta f_\perp(\mathbf{s}, \eta)e^{-i\Delta\theta\mathbf{s}}\psi_f\left(\left|\bar{\theta} + \frac{\Delta\theta}{2} - \frac{\mathbf{s}}{z} - \eta\right|\right)\psi_f\left(\left|\bar{\theta} - \frac{\Delta\theta}{2} - \frac{\mathbf{s}}{z} - \eta\right|\right).$$

Using the substitution $\phi = \mathbf{s}/z - \bar{\theta} + \eta \;\Leftrightarrow\; \mathbf{s} = z(\phi + \bar{\theta} - \eta)$ we obtain (44) in [98]

$$W(z, \bar{\theta}, \Delta\theta) = e^{iz\bar{\theta}\Delta\theta}\int \mathrm{d}\phi\mathrm{d}\eta f_\perp(z[\phi+\bar{\theta}-\eta], \eta)e^{-i\Delta\theta(\phi+\theta-\eta)}\psi_f\left(\left|\phi - \frac{\Delta\theta}{2}\right|\right)\psi_f\left(\left|\phi + \frac{\Delta\theta}{2}\right|\right).$$

The phase space distribution of the electron bunch can be written as (47,52,53) in [98]

$$f_\perp(\mathbf{s}, \eta) = f_\mathbf{s}(\mathbf{s})f_\eta(\eta)$$

were

$$\begin{aligned} f_{\mathbf{s}}(\mathbf{s}) &= \exp\left(-\frac{s_x^2}{2N_x}\right)\exp\left(-\frac{s_y^2}{2N_y}\right) \\ f_{\eta}(\eta) &= \exp\left(-\frac{\eta_x^2}{2D_x}\right)\exp\left(-\frac{\eta_y^2}{2D_y}\right). \end{aligned}$$

The integration in $\mathrm{d}\eta$ can be carried out analytically and gives in 1D

$$\int \mathrm{d}\eta e^{-i\Delta\theta(\phi+\theta-\eta)}\exp\left(-\frac{(\phi+\theta-\eta)^2}{2N}-\frac{\eta^2}{2D}\right) = \frac{\sqrt{2\pi}}{z^2/N+1/D}\exp\left(-\frac{(\phi+\bar{\theta})^2}{2(N/z^2+D)}-\frac{ND\Delta\theta^2}{2(N/z^2+D)}-i\frac{(\phi+\bar{\theta})\Delta\theta N/z}{N/z^2+D}\right).$$

For the cross-spectral density we obtain

$$\begin{aligned} W(z,\bar{\theta},\Delta\theta) \sim\ & e^{iz\Delta\theta\bar{\theta}}\exp\left(-\frac{N_xD_x\Delta\theta_x^2}{2(N_x/z^2+D_x)}-\frac{N_yD_y\Delta\theta_y^2}{2(N_y/z^2+D_y)}\right) \\ & \times\int \mathrm{d}\phi_x\mathrm{d}\phi_y\exp\left(-\frac{(\phi_x+\bar{\theta}_x)^2}{2(N_x/z^2+D_x)}-\frac{(\phi_y+\bar{\theta}_y)^2}{2(N_x/z^2+D_x)}\right) \\ & \exp\left(-i\frac{(\phi_x+\bar{\theta}_x)\Delta\theta_xN_x/z}{N_x/z^2+D_x}-i\frac{(\phi_y+\bar{\theta}_y)\Delta\theta_yN_y/z}{N_y/z^2+D_y}\right) \\ & \psi_f\left(\sqrt{\left[\phi_x-\frac{\Delta\theta_x}{2}\right]^2+\left[\phi_y-\frac{\Delta\theta_y}{2}\right]^2}\right) \\ & \psi_f\left(\sqrt{\left[\phi_x+\frac{\Delta\theta_x}{2}\right]^2+\left[\phi_y+\frac{\Delta\theta_y}{2}\right]^2}\right) \end{aligned} \tag{A.18}$$

One dimension

As we are interested in the coherence properties in the center of the beam in the hori-

zontal direction. Substituting $\Delta\theta_x = \bar{\theta}_x = 0$ in (A.18) we find

$$\begin{aligned} W(z, \bar{\theta}_y, \Delta\theta_y) \quad \sim \quad & e^{iz\Delta\theta_y\bar{\theta}_y} \exp\left(-\frac{N_y D_y \Delta\theta_y^2}{2(N_y/z^2 + D_y)}\right) \\ & \times \int \mathrm{d}\phi_y \exp\left(-\frac{(\phi_y + \bar{\theta}_y)^2}{2(N_x/z^2 + D_x)}\right) \exp\left(-i\frac{(\phi_y + \bar{\theta}_y)\Delta\theta_y N_y/z}{N_y/z^2 + D_y}\right) \\ & \int \mathrm{d}\phi_x \exp\left(-\frac{\phi_x^2}{2(N_x/z^2 + D_x)}\right) \\ & \psi_f\left(\sqrt{\phi_x^2 + \left[\phi_y - \frac{\Delta\theta_y}{2}\right]^2}\right) \psi_f\left(\sqrt{\phi_x^2 + \left[\phi_y + \frac{\Delta\theta_y}{2}\right]^2}\right). \end{aligned}$$

This is the expression (62) in [98], with the exception that here another Gaussian term is appearing in the $\mathrm{d}\phi_x$ integral. Replacing x by y and vice versa we obtain the coherence properties in the horizontal direction in the vertical center of the beam. This expression is more general than the result in [98], as here no assumptions are made. In [98] it is assumed that $D_x \gg 1$ and $N_x \gg 1$, which is not valid at high brilliance synchrotron sources such as PETRA III for low photon energies.

In the far field (63 in [98], $N \ll z^2 D$) the expression simplifies to

$$\begin{aligned} W(z, \bar{\theta}_y, \Delta\theta_y) \quad \sim \quad & e^{iz\Delta\theta_y\bar{\theta}_y} \exp\left(-\frac{N_y \Delta\theta_y^2}{2}\right) \times \int \mathrm{d}\phi_y \exp\left(-\frac{(\phi_y + \bar{\theta}_y)^2}{2D_x)}\right) \\ & \int \mathrm{d}\phi_x \exp\left(-\frac{\phi_x^2}{2D_x}\right) \psi_f\left(\sqrt{\phi_x^2 + \left[\phi_y - \frac{\Delta\theta_y}{2}\right]^2}\right) \\ & \psi_f\left(\sqrt{\phi_x^2 + \left[\phi_y + \frac{\Delta\theta_y}{2}\right]^2}\right). \end{aligned}$$

A.5 Propagation of a GSM beam through the thin lenses

In this chapter we calculate the propagation of partially coherent radiation through a beamline including one thin optical element (see Figure 4.2). To determine the focus size, the transverse coherence length in the focus and the distance between the lens and the focus we identify in Equations (2.49,4.3)

$$\tilde{\Sigma}_1 = \sigma_f \Delta_f, \qquad \tilde{\Xi}_1 = \xi_f \Delta_f$$

where σ_f is the focus size and ξ_f is the transverse coherence length in the focus. The radius of curvature (2.51) R_f behind the lens and the expansion coefficient (2.50) Δ_f (this parameter describes the difference between the focus size and the size of the beam

behind the lens, see equation above) can be written as

$$\tilde{R}_1 = -z_{f1}\left[1+\left(\frac{2k\sigma_f^2\zeta_f}{z_{f1}}\right)^2\right] \quad \text{and} \quad \Delta_f = \left[1+\left(\frac{z_{f1}}{2k\sigma_f^2\zeta_f}\right)^2\right]^{1/2}.$$

One can rewrite

$$\tilde{R}_1 = -z_{f1}\Delta_f^2\left(\frac{2k\sigma_f^2\zeta_f}{z_{f1}}\right)^2 = -\frac{z_{f1}}{\Delta_f^2}\left(\frac{2k\tilde{\Sigma}_1^2\zeta_f}{z_{f1}}\right)^2 \tag{A.19}$$

which yields

$$\Delta_f^2 = -\frac{\left(2k\tilde{\Sigma}_1^2\zeta_f\right)^2}{z_{f1}\tilde{R}_1}. \tag{A.20}$$

On the other hand Δ_f^2 can be expressed as

$$\Delta_f^2 = 1+\left(\frac{z_{f1}}{2k\sigma_f^2\zeta_f}\right)^2 = 1+\Delta_f^4\left(\frac{z_{f1}}{2k\tilde{\Sigma}_1^2\zeta_f}\right)^2.$$

Comparing the two expressions for Δ_f^2

$$-\frac{\left(2k\tilde{\Sigma}_1^2\zeta_f\right)^2}{z_{f1}\tilde{R}_1} = 1+\frac{\left(2k\tilde{\Sigma}_1^2\zeta_f\right)^4}{z_{f1}^2\tilde{R}_1^2}\left(\frac{z_{f1}}{2k\tilde{\Sigma}_1^2\zeta_f}\right)^2 = 1+\frac{\left(2k\tilde{\Sigma}_1^2\zeta_f\right)^2}{\tilde{R}_1^2}$$

we determine the distance between the focal plane and the lens

$$z_{f1} = -\frac{\tilde{R}_1}{1+\left(\tilde{R}_1/[2k\tilde{\Sigma}_1^2\zeta_f]\right)^2} \tag{A.21}$$

Substituting the focal distance from equation (A.21) in equation (A.20) yields the expansion coefficient

$$\Delta_f^2 = 1+\left(\frac{2k\tilde{\Sigma}_1^2\zeta_f}{\tilde{R}_1}\right)^2 \tag{A.22}$$

A.5.1 The magnification factor

Here we calculate the magnification factor $M = \sigma_f/\sigma$ for an infinite large aperture, $\Omega \to \infty$. An infinite aperture implies that the beam size is not modified by the transmission

through the lens $\tilde{\Sigma}_1 = \Sigma_1$. Using (4.4) we write

$$\sigma_f^2 = \frac{\Sigma_1}{\Delta_f} = \frac{\sigma^2 \Delta_1^2}{1 + \left(\frac{z_{\rm eff} \Delta_1^2}{\tilde{R}_1} \right)^2} = \frac{\sigma^2 \Delta_1^2}{1 + \left(\frac{z_{\rm eff} \Delta_1^2}{R_1} - \frac{z_{\rm eff} \Delta_1^2}{f} \right)^2}$$

and find

$$M^2 = \frac{\Delta_1^2}{1 + \left(\frac{z_{\rm eff} \Delta_1^2}{R_1} - \frac{z_{\rm eff} \Delta_1^2}{f} \right)^2} = \frac{1}{\frac{1}{\Delta_1^2} + \left(\frac{z_{\rm eff} \Delta_1}{R_1} - \frac{z_{\rm eff} \Delta_1}{f} \right)^2} = \frac{1}{\frac{1}{\Delta_1^2} + \left(\frac{z_{10}}{z_{\rm eff} \Delta_1} - \frac{z_{\rm eff} \Delta_1}{f} \right)^2}$$

In the last step we have used (2.50,2.51)

$$R_1 = \frac{z_{\rm eff}^2}{z_{10}} \Delta_1^2$$

The right term of the denominator we express as

$$\begin{aligned} \frac{z_{10}}{z_{\rm eff} \Delta_1} - \frac{z_{\rm eff} \Delta_1}{f} &= \frac{z_{10} f - z_{\rm eff}^2 \Delta_1^2}{z_{\rm eff} \Delta_1 f} = \frac{z_{10} f - z_{10}^2 - z_{\rm eff}^2}{z_{\rm eff} \Delta_1 f} = \frac{z_{10}(f - z_{10}) - z_{\rm eff}^2}{z_{\rm eff} \Delta_1 f} \\ &= \frac{f - z_{10}}{f} \frac{z_{10}}{z_{\rm eff} \Delta_1} - \frac{z_{\rm eff}}{\Delta_1 f} = \left(\frac{f - z_{10}}{f} \right) \left(\frac{z_{10}}{z_{\rm eff} \Delta_1} - \frac{z_{\rm eff}}{(f - z_{10}) \Delta_1} \right) \end{aligned}$$

This yields the magnification factor

$$M^2 = \frac{(f/[f - z_{10}])^2}{\alpha}$$

The denominator can be written as

$$\begin{aligned}
\alpha &= \frac{f^2}{(f-z_{10})^2\Delta_1^2} + \left(\frac{(f-z_{10})z_{10} - z_{\text{eff}}^2}{z_{\text{eff}}\Delta_1(f-z_{10})}\right)^2 \\
&= \frac{f^2 z_{\text{eff}}^2 + ((f-z_{10})z_{10} - z_{\text{eff}}^2)^2}{z_{\text{eff}}^2\Delta_1^2(f-z_{10})^2} \\
&= \frac{f^2 z_{\text{eff}}^2 + (f-z_{10})^2 z_{10}^2 + z_{\text{eff}}^4 - 2z_{10}(f-z_{10})z_{\text{eff}}^2}{(z_{\text{eff}}^2 + z_{10}^2)(f-z_{10})^2} \\
&= \frac{(f-z_{10})^2(z_{10}^2 + z_{\text{eff}}^2) + f^2 z_{\text{eff}}^2 - (f-z_{10})^2 z_{\text{eff}}^2 + z_{\text{eff}}^4 - 2z_{10}(f-z_{10})z_{\text{eff}}^2}{(z_{\text{eff}}^2 + z_{10}^2)(f-z_{10})^2} \\
&= 1 + \frac{f^2 z_{\text{eff}}^2 - (f-z_{10})^2 z_{\text{eff}}^2 + z_{\text{eff}}^4 - 2z_{10}(f-z_{10})z_{\text{eff}}^2}{(z_{\text{eff}}^2 + z_{10}^2)(f-z_{10})^2} \\
&= 1 + z_{\text{eff}}^2 \frac{f^2 - (f-z_{10})^2 + z_{\text{eff}}^2 - 2z_{10}(f-z_{10})}{(z_{\text{eff}}^2 + z_{10}^2)(f-z_{10})^2} \\
&= 1 + z_{\text{eff}}^2 \frac{f^2 - f^2 - z_{10}^2 + 2fz_{10} + z_{\text{eff}}^2 - 2z_{10}f + 2z_{10}^2)}{(z_{\text{eff}}^2 + z_{10}^2)(f-z_{10})^2} \\
&= 1 + \frac{z_{\text{eff}}^2}{(f-z_{10})^2}
\end{aligned}$$

Finally, the magnification factor can be expressed as

$$\begin{aligned}
M^2 &= \left(\frac{f}{f-z_{10}}\right)^2 \left(1 + \frac{z_{\text{eff}}^2}{(f-z_{10})^2}\right)^{-1} \\
M &= \left|\frac{f}{f-z_{10}}\right| \left(1 + \frac{z_{\text{eff}}^2}{(f-z_{10})^2}\right)^{-1/2}
\end{aligned}$$

A.5.2 Distance from the lens to the focus

In the case of an infinite large aperture $\Omega \to \infty$ the focus distance is given by

$$\begin{aligned}
z_{f1} &= -\frac{\tilde{R}_1}{1 + (\tilde{R}_1/[2k\Sigma\zeta_f])^2} = -\frac{\tilde{R}_1}{1 + (\tilde{R}_1/[\Delta_1^2 z_{\text{eff}}])^2} \\
&= -\frac{\Delta_1^2 z_{\text{eff}}^2}{\tilde{R}_1} \frac{\Delta_1^2}{1 + (\Delta_1^2 z_{\text{eff}}/\tilde{R}_1)^2} \\
&= -M^2 \frac{\Delta_1^2 z_{\text{eff}}^2}{\tilde{R}_1} \\
&= -M^2 \left(\frac{\Delta_1^2 z_{\text{eff}}^2}{R} - \frac{\Delta_1^2 z_{\text{eff}}^2}{f}\right) \\
&= -M^2 \left(z - \frac{\Delta_1^2 z_{\text{eff}}^2}{f}\right)
\end{aligned}$$

The difference $z_{f1} - f$ is expressed as

$$\begin{aligned}
z_{f1} - f &= -M^2 \left(z_{10} - \frac{\Delta_1^2 z_{\text{eff}}^2}{f} + f \frac{1 + (\Delta_1^2 z_{\text{eff}}/\tilde{R}_1)^2}{\Delta_1^2} \right) \\
&= -M^2 \left(z_{10} - \frac{\Delta_1^2 z_{\text{eff}}^2}{f} + \frac{f}{\Delta_1^2} + f \left[\frac{\Delta_1 z_{\text{eff}}}{R} - \frac{\Delta_1 z_{\text{eff}}}{f} \right]^2 \right) \\
&= -M^2 \left(z_{10} - \frac{\Delta_1^2 z_{\text{eff}}^2}{f} + \frac{f}{\Delta_1^2} + \frac{f}{\Delta_1^2 z_{\text{eff}}^2} \left[\frac{\Delta_1^2 z_{\text{eff}}^2}{R} - \frac{\Delta_1^2 z_{\text{eff}}^2}{f} \right]^2 \right) \\
&= -M^2 \left(z_{10} - \frac{\Delta_1^2 z_{\text{eff}}^2}{f} + \frac{f}{\Delta_1^2} + \frac{f}{\Delta_1^2 z_{\text{eff}}^2} \left[z_{10} - \frac{\Delta_1^2 z_{\text{eff}}^2}{f} \right]^2 \right) \\
&= -M^2 \left(z_{10} - \frac{\Delta_1^2 z_{\text{eff}}^2}{f} + \frac{f}{\Delta_1^2} + \frac{f}{\Delta_1^2 z_{\text{eff}}^2} \left[z_{10}^2 - 2z \frac{\Delta_1^2 z_{\text{eff}}^2}{f} + \left(\frac{\Delta_1^2 z_{\text{eff}}^2}{f} \right)^2 \right] \right) \\
&= -M^2 \left(z_{10} - \frac{\Delta_1^2 z_{\text{eff}}^2}{f} + \frac{f}{\Delta_1^2} + \frac{f z^2}{\Delta_1^2 z_{\text{eff}}^2} - 2z + \frac{\Delta_1^2 z_{\text{eff}}^2}{f} \right) \\
&= -M^2 \left(-z_{10} + f \frac{1 + (z_{10}/z_{\text{eff}})^2}{\Delta_1^2} \right) \\
&= M^2 \left(z_{10} - f \right).
\end{aligned}$$

The result is

$$z_{f1} - f = M^2 (z_{10} - f).$$

A.6 Numerical mode decomposition

The mode decomposition approach is not limited to the GSM sources. If the CSD of the source is known, integral Equation (2.35) can be used to find the corresponding modes. The numerical solution of the Fredholm integral equation is not straightforward, however, there are techniques to find this solution in certain cases.

We assume that the CSD in the source plane is known and is given as a four dimensional array of complex numbers[4] $W_{ij,kl} = W(x_1^i, y_1^j, x_2^k, y_2^l)$, where $i, j, k, l = 1, 2, \ldots N$. The aim is to find a set of the eigenvalues β_n and the corresponding modes E_{kl}^n, which all satisfy

$$\sum_{i=1}^{N} \sum_{j=1}^{N} W_{ij,kl} E_{ij}^n = \beta_n E_{kl}^n.$$

[4] We assume that the array has the same number of elements in each direction. If the wavefront is flat at the source real numbers can be used.

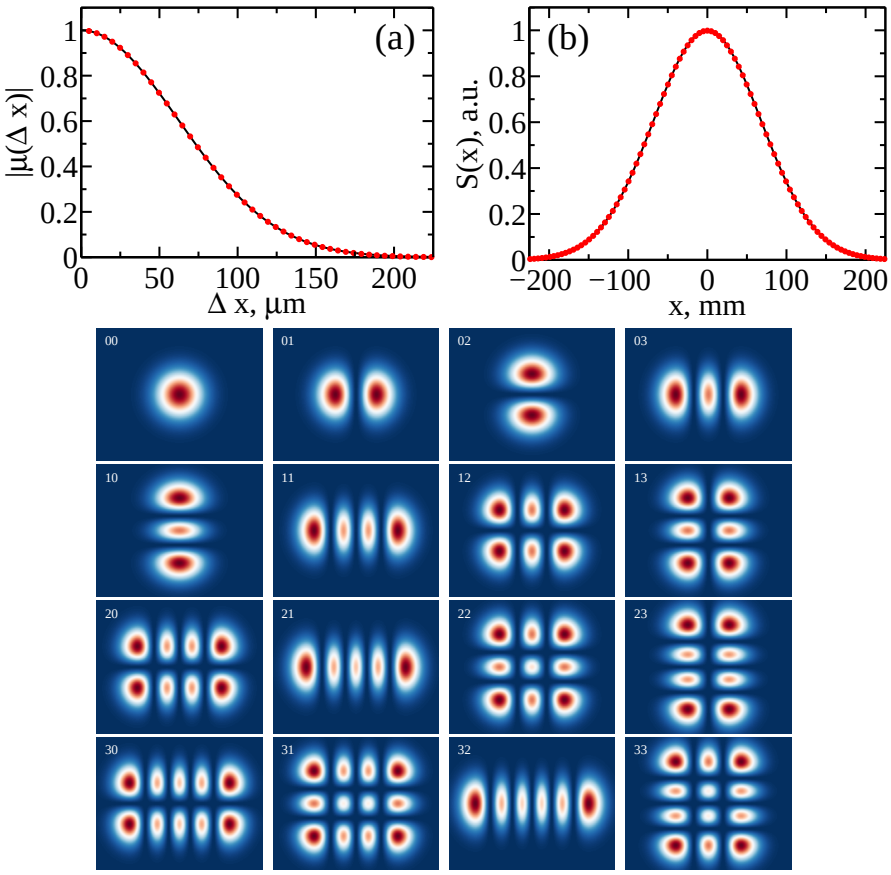

Figure A.1: (a) The modulus of the SDC $|\mu(\Delta x)|$ determined from the initial CSD (black solid line) and from the sum of 25 lowest modes (red dashed line). (b)The spectral density $S(x)$. (c) The intensity distribution of 16 lowest modes.

The double sum can be rewritten as

$$\sum_{q=1}^{N^2} W_{pq} E_q^n = \beta_n E_p^n$$
$$\text{or} \quad \bar{W}\vec{E}_n = \beta_n \vec{E}_n,$$

where $q = iN + j = 1, 2, \ldots N^2$ and $p = kN + l = 1, 2, \ldots N^2$, $\bar{W}$ is the $N^2 \times N^2$ matrix with the elements W_{pq} and $\vec{E}_n = (E_1^n, E_2^n, \ldots E_{N^2}^n)^T$ is a column vector with N^2 elements. Now the solution of the Fredholm integral equation is expressed as an eigenvalue problem. The eigenvalues describe the main properties of linear operators, which appear throughout the whole field of physics, as they correctly describe a vast number of phenomena in the first approximation. As such, the solution of the eigenvalue problem or the diagonalization is very well studied in the field of numerical mathematics.

The eigenvalue problem can be effectively solved by a variety of approaches. In our

case only a small number of modes contribute to the total radiation field and the majority of the eigenvalues are small, i.e $\beta_j/\beta_0 \ll 1$ for almost all j. Then algorithms based on the Lanczos method [152] are effective. They are based on the following idea: due to the fact that W_{pq} is hermitian [46] all eigenvalues are real and the set of the eigenvectors, the modes, forms an orthogonal basis of the parameter space. Therefore, an arbitrary vector $\vec{S}$ can be written as a sum of the eigenvectors $\vec{S} = \sum_n \alpha_n \vec{E}_n$. Applying the operator $\bar{W}$ m times on the vector $\vec{S}$ yields

$$\bar{W}(\bar{W}(\bar{W}\cdots(\bar{W}\vec{S}))) = \bar{W}^m S = \sum_n \beta_n^m \alpha_n \vec{E}_n \approx \beta_0^m \alpha_0 E_0$$

where β_0 is the eigenvector corresponding to the largest eigenvalue β_0. The eigenvector $\vec{E}_0$ and the eigenvalue β_0 are thus given by

$$\vec{E}_0 \approx \frac{\bar{W}^m \vec{S}}{|\bar{W}^m \vec{S}|}, \qquad \beta_0 = \frac{|\bar{W}\vec{E}_0|}{|\vec{E}_0|}.$$

Is the largest eigenvalue found, the next eigenvalue is determined as the largest eigenvalue of the matrix $\bar{W}' = \bar{W} - \beta_0 \vec{E}_0 \cdot \vec{E}_0^T$. Applying these steps consecutively we can determine all contributing eigenvalues and eigenvectors. Since only vector multiplications are involved, the Lanczos method requires only $\mathcal{O}(M)$ operations, where M is the size of the W_{pq} matrix. Moreover, since the number of contributing modes in our case is rather small a fast convergence is possible.

To find the largest eigenvalues and the corresponding eigenvectors we used the matlab routine *eigs*, which is based on the ARPACK library [152]. We performed numerical simulations to find the mode decomposition of a given CSD function with a fixed frequency. Three different CSDs were considered We used the numerical mode decomposition to determine the first 25 modes of a GSM source (2.40,2.41) with the CSD in the form

$$W(x_1, y_1, x_2, y_2) = \exp\left(-\frac{x_1^2 + y_1^2 + x_2^2 + y_2^2}{4\sigma^2} - \frac{(x_2 - x_1)^2 + (y_2 - y_1)^2}{2\xi^2}\right). \qquad \text{(A.23)}$$

Parameters from FLASH $\sigma = 68$ µm, $\xi = 62$ µm (see chapter 3.3.2) were used in this simulation[5]. The modulus of the SDC $|\mu(\Delta x)| = |\mu(-\Delta x/2, \Delta x/2, \Delta y = 0, \Delta y = 0)|$ as a function of the separation Δx is shown in Figure A.1 a. The spectral density $S(x) = S(x, y = 0)$ as a function of the position across the beam in the horizontal direction is shown in the inset of Figure A.1 a. We compared these functions for the initial CSD (black lines) with the same functions determined from the mode decomposition (red dashed lines) using the lowest 25 modes in (2.34). It is readily seen from Figure A.1 a, that the initial CSD and the sum of 25 lowest modes deliver the same intensity distribution and the same modulus of the SDC in the horizontal direction. Due to the symmetry of the initial CSD the same result is obtained in the vertical direction.

The normalized contribution β_n/β_0 of the first 25 modes is shown in Figure A.1

[5] These parameters were determined for a wavelength of $\lambda = 13.5$ nm. The wavelength, however, is irrelevant for the mode decomposition

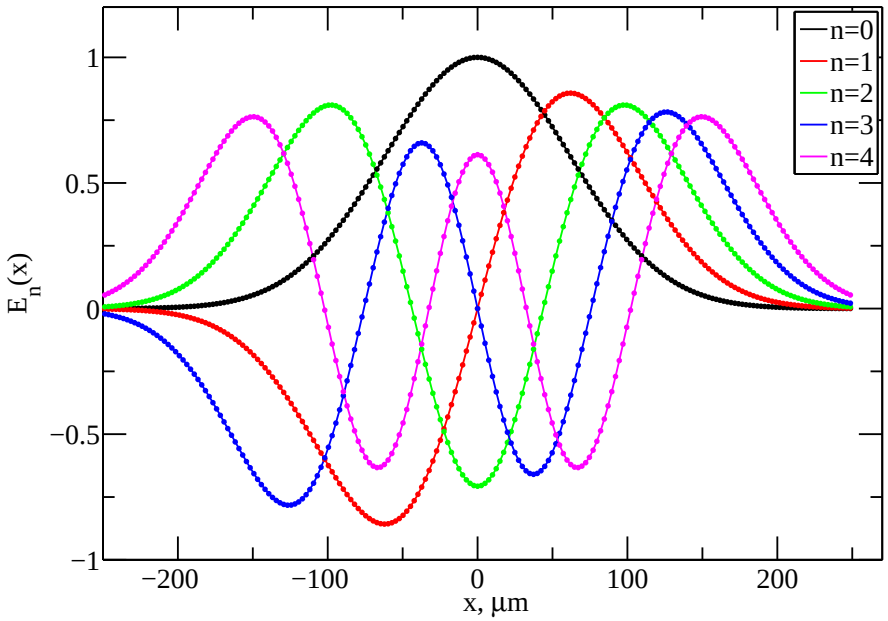

Figure A.2: Coherent modes of the GSM. The comparison between the analytical expression of the modes (2.70) (solid lines) with the modes determined in a numerical mode decomposition (circles). The field $E_n(x) = E_n(x, y = 0)$ as a function of the horizontal position x across the beam is shown. Modes number 1,2,4,7,12 in Figure A.1 are shown.

b. The intensity distribution $|E_n(x, y)|^2$ of the respective modes is shown in Figure A.1 c. In Figure A.2 we present the comparison of the analytic formulas , $E_n^{\mathrm{ana}}(x)$, (2.68) (black line) with the numerically determined modes , $E_n^{\mathrm{num}}(x)$ (dashed lines) modes. This comparison shows excellent agreement. The error $\chi^2 = \sum_i |E_n^{\mathrm{ana}}(x_i) - E_n^{\mathrm{num}}(x_i)|^2 / (\sum_i |E_n^{\mathrm{ana}}(x_i)|^2)$, where the summation is performed over all positions x_i, is also shown in Figure A.2 for $n = 1, 2, \ldots, 5$ and is less than 10^{-6} for all modes.

From these results we conclude, that the mode decomposition is an effective tool to simulate the radiation properties of the FEL sources. The numerical mode decomposition with a decent sampling (the size of the CSD was chosen to be $201 \times 201 \times 201 \times 201$) can be performed in a reasonable time (about two minutes) on a moderate machine[6]. The numerically determined modes can be propagated through an arbitrary arrangement of optical elements using the well developed techniques for wavefront propagation, as demonstrated in the previous chapter.

[6]The machine used for the simulations consists of 8 double core processors (Intel(R) Xeon(R) CPU, X5570 @2.93GHz) and has 71 Gb of Random-Access-Memory.

A.7 Degeneracy parameter

We start with Heisenberg's uncertainty relation for the photons[7] [46]

$$\Delta p_x \Delta x \geq \frac{\hbar}{2},$$

where $\Delta p_x, \Delta x$ are the uncertainties in the momentum and position and $\hbar = h/2\pi$ and h is the Planck constant. Applying similar relations to other conjugate pairs $\Delta p_y, \Delta y$ and $\Delta E, \Delta t$, where E is the photon energy and t is the time, we find

$$\Delta p_x \Delta x \Delta p_y \Delta y \Delta E \Delta t \geq \left(\frac{\hbar}{2}\right)^3,$$

which is a condition for the phase space volume of light. The minimum phase ocupied by light is $V_s = (\hbar/2)^3$ and can be regarded as the space ocupied by a single photon. The degeneracy parameter [66, 46] can be defined as

$$\delta = N_{\mathrm{ph}} \cdot \frac{V_s}{V}$$

where N_{ph} is the total number of photons, $V_s = (\hbar/2)^3$ is the phase space volume ocupied by a single photon, and $V = \Delta p_x \Delta x \Delta p_y \Delta y \Delta E \Delta t$ is the phase space ocupied by all photons.

The uncertainties in x, y directions can be replaced by the beam size σ_x and the divergence σ'_x of a Gaussian Schell-model beam $\Delta x = \sigma_x,\ \Delta p_x = \hbar k \sigma'_x$ and similarly for y direction. The energy uncertainty ΔE is given by $\Delta E = \hbar \sigma_\omega$, where σ_ω is the rms width of the spectrum, and $\Delta t = \sigma_t$ with σ_t being the rms pulse duration. Using $\tau_c = 1/\sigma_\omega$ the phase space volume of the photon beam is given by

$$V = \varepsilon_x \varepsilon_y (2k)^2 \frac{2\sigma_t}{\tau_c} \left(\frac{\hbar}{2}\right)^3.$$

and using Equations (2.61,2.64) we obtain

$$\frac{V_s}{V} = \zeta_x \cdot \zeta_y \cdot \frac{\tau_c}{2\sigma_t}.$$

Finally, the degeneracy parameter can be expressed as

$$\delta = N_{\mathrm{ph}} \cdot \zeta_x \cdot \zeta_y \cdot \frac{\tau_c}{2\sigma_t}. \tag{A.24}$$

If the coherence time is on the order of the pulse duration, the ratio $\tau_c/(2\sigma_t)$ is replaced with ζ_t, which is defined similarly to the normalized degree of cohernce in the spatial

[7] The uncertainty relations are often written with a factor h rather than $\hbar/2$ on the right hand side. The value of the factor depends on the definition of the uncertainties. Here $\hbar/2$ is chosen so that the uncertainties can be described as rms widths of the Gaussian beam.

domain.

A.8 Analysis of the Young's measuremens at LCLS

The analyzed regions shown in Figure 5.2 were divided into vertical slices 10 pixels wide. The number of slices varied from 5 to 10 depending on the pinhole size. The single shot values of $|\gamma_{12}^{\text{eff}}|$, shown in Figure 5.3, are each an average over these slices, with error bars given by the statistical variation (standard deviation) between these slices. The diffraction patterns, where the incoherent background was present in the data in the analyzed region, were identified by a high variation of the fit parameters between different slices. These interference patterns, as well as the patterns with poor signal, were excluded from our evaluation. In Figure A.3 (a,c) the diffraction pattern and the visibility map of an included measurement are presented. Figures A.3 (b,d) show a measurement, where the visibility varies significantly in the analyzed region. It changes its value from about 0.5 to 0.7 and this particular shot was excluded from the analysis.

A.9 Beam width characterization

A.9.1 Measurements at SXR beamline at LCLS

To estimate the average size of the focus, we exploited the shot-to-shot variation in alignment between the beam and the apertures due to instabilities in the beam position

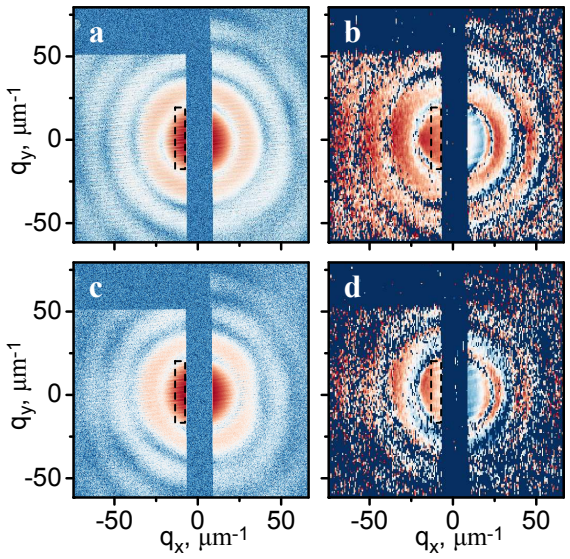

Figure A.3: (a,c) Two diffraction patterns measured a pinhole separation of 8 µm. Corresponding visibility maps (c,d) shown the contribution of incoherent background. Visibility maps were calculated according to Equation (2.84) for all vertical line scans.

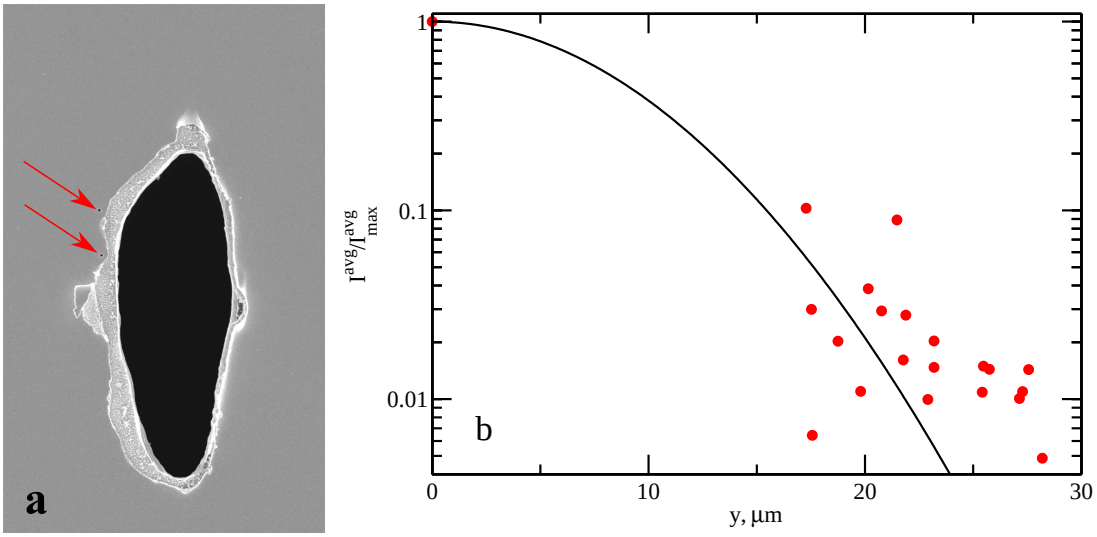

Figure A.4: a) The SEM image of an aperture after exposure to a single LCLS pulse. This particular pulse was not centered on the double pinhole (indicated by red arrows), which lies outside of the damaged region. b) The total scattered intensity of all pulses, which did not destroy the pinholes (red dots) and a Gaussian fit through these points (black line). The numbers are normalized by the maximal total scattered intensity determined for the same pinhole separation. Due to the asymmetry of the beam (the beam is larger in the vertical direction, see SEM image in a) the horizontal direction was rescaled by a factor of 3.1 ± 0.2 to obtain effectively a round beam. The intensities are shown as a function of the distance between the center of double pinhole and the center of the beam, determined as the position with maximal extend of the crater in the vertical and horizontal direction.

and the sample stage in the plane of the sample. Using the coordinates of undamaged pinholes and the corresponding scattered intensities measured as an integrated signal at the CCD we determined a few points on the tails of the intensity distribution curve at the position of the pinholes (see Figure A.4 (a)) . Fitting a Gaussian through these points gives an average beam size of 17.3 ± 2.4 µm FWHM in the vertical direction and 5.7 ± 0.4 µm FWHM in the horizontal, in the plane of the apertures.

A.9.2 Measurements at BL2 beamline at FLASH

To measure the beam profile in the plane of the apertures we analyzed PMMA imprints produced by single FEL pulses with varying degree of attenuation of the beam. Three sets of PMMA imprints with one order of magnitude difference in attenuation were analyzed. Using Gaussian beam approximation a beam width of about 10×10 µm FWHM was determined. In the horizontal direction additional features on the sides of the beam were observed. For the less intense beam, however, round craters, 15 µm in

diameter, indicate that the central part of the beam is more less smooth.

The focus width of the FLASH beam at the BL2 beamline was measured prior to the double pinhole coherence mesurements in November 2010. Imprints on 1 μm thick PMMA film with varying degree of attenuation were recorded and analyzed afterwards by an SEM. The absorbers used in our experiment and the corresponding attenuation are listed in table A.1 for the fundamental ($\lambda = 7.9$ nm), T_f, and for the third harmonic T_3. The ratio P_3/P_f between the contribution of the third harmonic, P_3, and the contribution of the fundamental, P_f, is also shown in table A.1. For the unattenuated beam a ratio of 0.6 % was reported in [47] The PMMA imprints were recorded for all 5 degrees of

	no Att.	100 nm Al	200 nm Al	300 nm Al	490 nm Si
T_f	1	0.076	$0.58 \cdot 10^{-2}$	$0.45 \cdot 10^{-3}$	$0.24 \cdot 10^{-4}$
T_3	1	0.79	0.62	0.49	0.27
P_3/P_f	0.006	0.06	0.64	6.5	67.5

Table A.1: The absorbers and the corresponding degrees of attenuation for the fundamental, T_f, and the third harmonic T_3 radiation at FLASH.

attenuation, however, only the first three produced craters. The SEM images of the craters measured without attenuation, with a 100 nm thick Al absorber and with a 200 nm thick Al absorber are shown in Fig 1.

All SEM images of the imprints are inclined by an angle of about 77.2 degree clockwise with respect to the orientation which was present during the experiment. After the correction of this inclination angle the horizontal crater size, s_h, and the vertical crater size, s_v, was determined from each SEM image. The result of this analysis is sumerized in table A.2.

	no Att.		100 nm Al			200 nm Al	
	s_h/μm	s_v/μm	s_h/μm	s'_h/μm	s_v/μm	s_h/μm	s_v/μm
1	66.2	36.9	41.3	25.2	23.2	13.7	17.2
2	61.3	36.9	44.2	26.5	23.5	12.8	15.5
3	62.9	36	43.6	27.4	23.3	13.1	16.6
4	64.4	38.5	42.7	23.3	23.5	13.5	15.9
5	60.5	41.1	42.9	24.9	24.0		
mean	63.1	37.9	43.0	25.5	23.5	13.3	16.3
std	2.3	2.0	1.1	1.6	0.3	0.4	0.8

Table A.2: The horizontal s_h and the vertical s_v size of the crater determined from the SEM images shown in Figure A.6. Two values are noted for horizontal direction corresponding to the full size of the beam, s_h, and the central part of the beam s'_h, both shown in figure A.6 c.

To estimate the beam size we applied Liu's method [153]. The result of this analysis

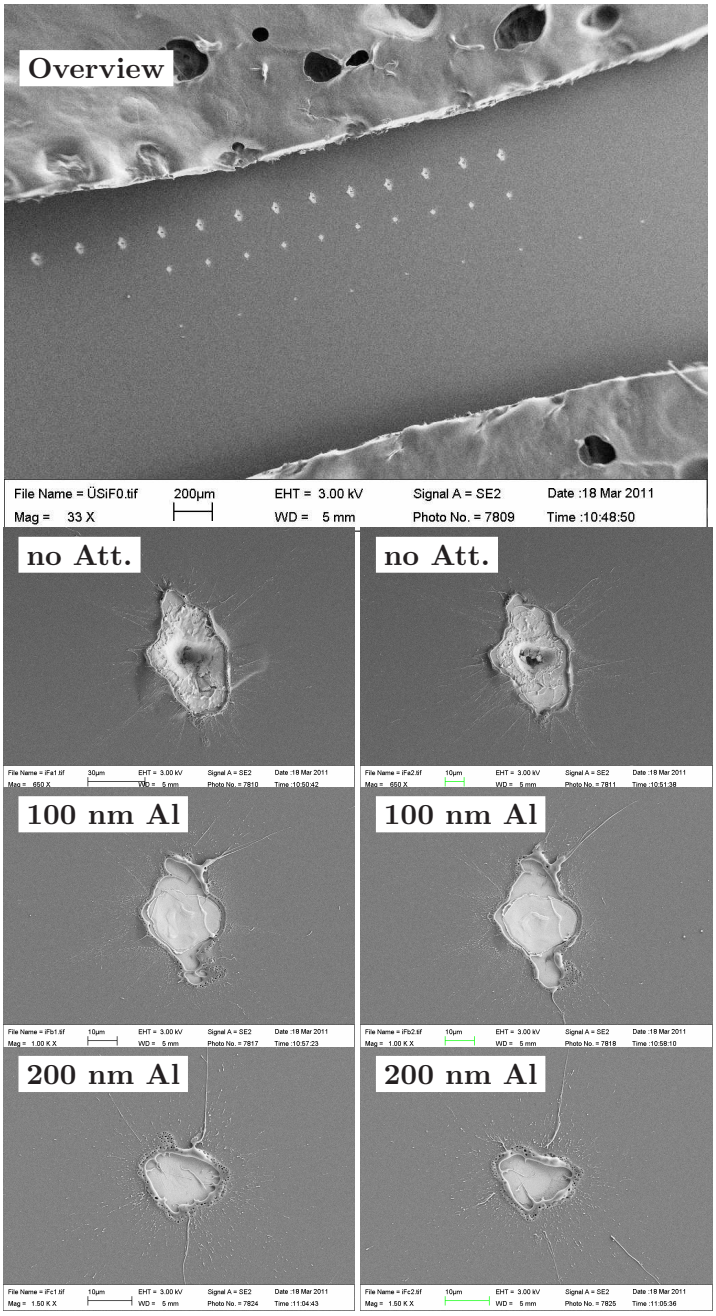

Figure A.5: SEM images of the craters produced by the FEL beam with different absorbers in the beam.

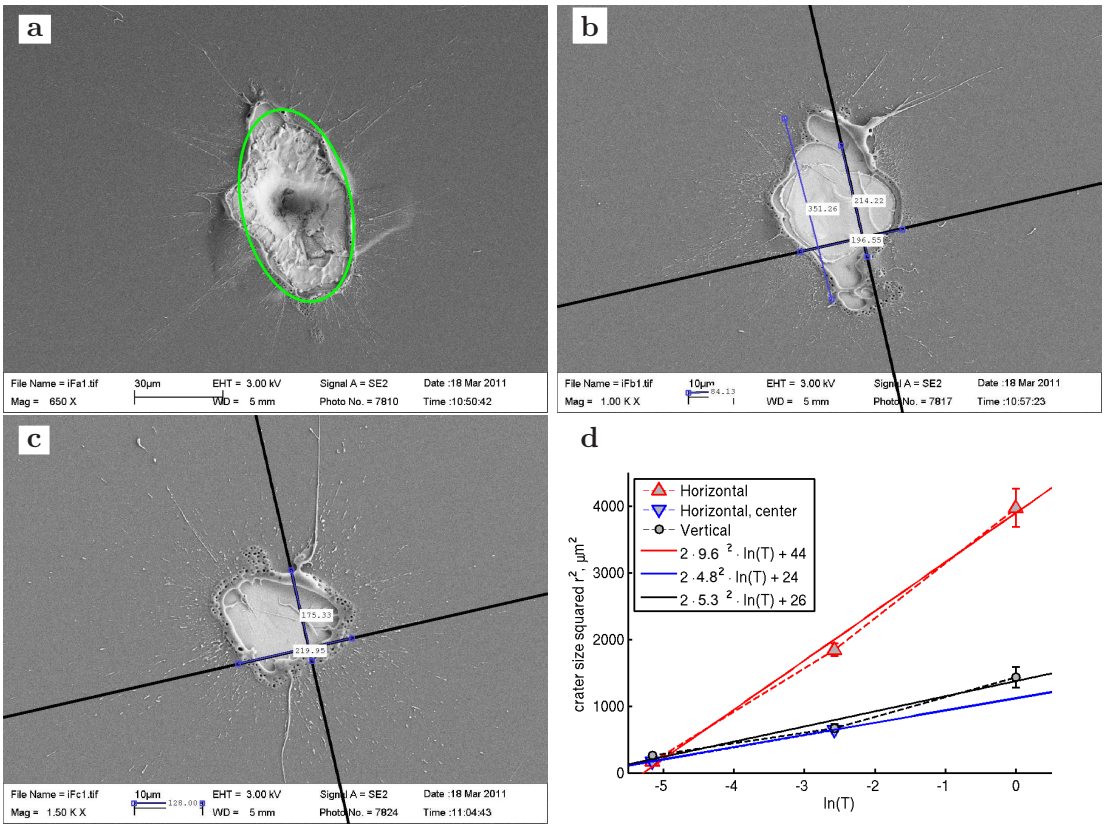

Figure A.6: Analyzed SEM images. a: no attenuator, b: 100 nm Al absorber, c: 200 nm Al absorber. d:The size of the crater as a function of the logarithm of the attenuation (proportional to the intensity). The total crater size in the horizontal direction (red triangles), the size of the central part of the crater in the horizontal direction (blue triangles, see also b) and the crater size in the vertical direction (black circles). The slope of the linear fit is equal to $2\sigma^2$, where σ is the width of a Gaussian function.

is shown in Figure A.6. An rms beamsize of 19.2 μm in the horizontal direction and 10.7 μm in the vertical direction was found. This values correspond to 45 μm x 25 μm FWHM.

The experimental values are adequately described by linear functions. This means that the measured points of the intensity distribution curve can be approximated by a Gaussian function in both directions.

In the SEM images, especially in the images of the imprints recorded with 100 nm Al absorbers in the beam, a non-Gaussian beam shape in the horizontal direction can be directly observed. Additional craters on the left and the right side of the central maximum are visible. If we neglect these additional features which appear to result from strong intensity modulations we can consider the beam to be approximately round.

This approximation yields a focus size of 10 µm×10 µm FWHM.

We analyzed the uncertainty in the position of the beam relative to the center of the double pinhole. We determined the crater center positions produced by the FEL beam in the PMMA (see overview of the craters in Figure A.5) relative to each other. According to motor positions we know how large the relative distance should be. Any deviation corresponds to the positional uncertainty that we aim to recover. Since the multiple aperture frame and the PMMA were mounted on the same sample holder, the beam jitter determined from the SEM images of the damaged PMMA corresponds to the beam jitter on the double pinholes. The analysis yields an rms jitter of 7.4 µm in the horizontal 6.3 µm in the vertical direction. The peak to peak value is 24 µm in the horizontal and 16 µm in the vertical direction.

A.9.3 Measurements at PG2 beamline at FLASH

About twenty single shot intensity profiles were analyzed. The mean values and the standard deviations are presented here. The beam was elongated in the vertical direction due to the use of a horizontal plane grating.

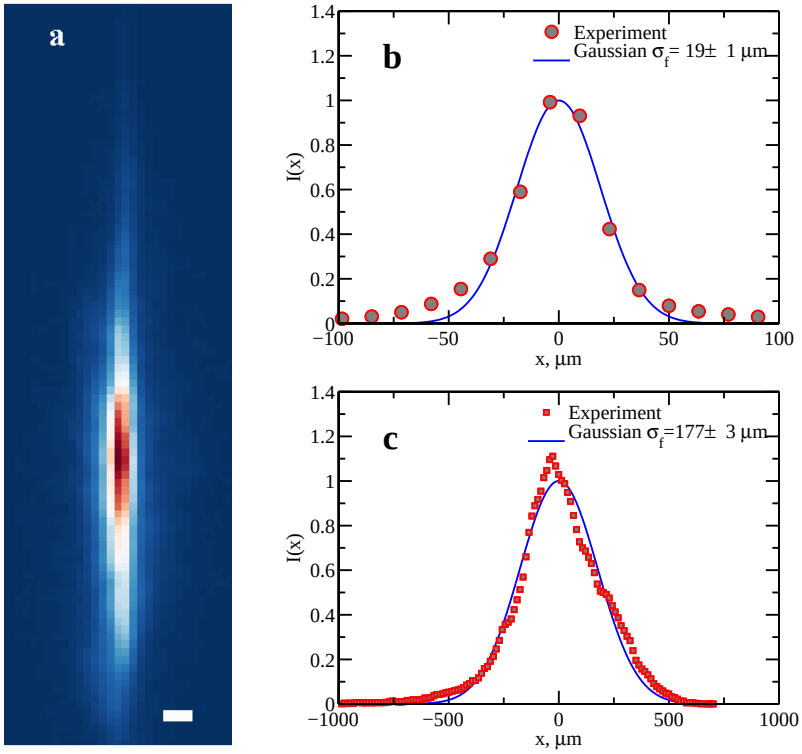

Figure A.7: The intensity profile measured at PG2. (a) A single shot profile recorded with the CCD at a distance of 0.37 m downstream of the focus. The projection of the beam profile in the horizontal (red circles) (b) and in the vertical (red squares) (c). Gaussian fits in (b,c) are shown by blue solid lines. The scale bar in (a) is 50 µm wide.